Rapid-response and High-precision Wide-field Photometry of Transients and Gravitational Wave Counterparts

Thesis

Rapid-response and High-precision Wide-field Photometry of Transients and Gravitational Wave Counterparts

Dean Philip Roberts MPhys(Hons)

A thesis submitted for the degree of

Doctor of Philosophy

in Astrophysics

Supervisors: Dr. Ulrich Kolb & Dr. Simon Clark

School of Physical Sciences,

The Open University

Submitted April 2019

Abstract

This work focuses on the use of the small-aperture PIRATE robotic telescope, built with off the shelf components at a relatively low cost, in the observation of numerous astrophysical objects. This includes both the follow-up of gravitational wave alerts released by the LIGO/Virgo collaboration, but also the long term monitoring of Luminous Blue Variable (LBV) stars in the nearby Triangulum galaxy (M33). A new pipeline was developed to fully automate the follow-up of gravitational wave alerts, which enables PIRATE to respond promptly without human intervention. This resulted in the detailed follow-up of four gravitational wave alerts, all of which were as a result of a binary black hole merger. Although no optical counterparts were detected, upper limits were placed on the magnitude of any potential counterpart. However, this work did produce dozens of serendipitously discovered candidate variable stars; and had it not been due to bad luck, PIRATE would have been able to follow-up the famous binary neutron star merger event GW170817.

Additionally, PIRATE was used to monitor several candidate LBV stars in the Triangulum galaxy for a continuous period of 4 months, to search for signs of an S Dor cycle that's indicative of an LBV. This was used in conjunction with new spectroscopic data taken with the WHT to analyse the behaviour of these stars and reclassify them accordingly. In total, three stars were re-classified as bona fide LBVs as a result of this work, and a further four were given new classifications as Cool Hypergiants. Although no LBV was photometrically observed undergoing an outburst, PIRATE was able to detect several of them in M33 and would have consequently observed such a rare event had one occurred during its observing window.

Acknowledgements

Firstly I would like to start off by thanking my supervisors, Ulrich Kolb and Simon Clark, for all their help and guidance along the way. I could not have asked for better supervisors and they have always been friendly & approachable from day one. I have particularly enjoyed working with Ulrich in the commissioning of the new PIRATE facility in Tenerife, something which gave me great pride to be part of.

I would like to thank the wider Astronomy community at the OU, including Andrew Norton & John Barnes for their comments and feedback during my mini viva; and also everyone in the OpenScience Observatories group who worked with me on any PIRATE related topics. Furthermore, I am grateful to all the technical support that I have received over the years, especially from Geoff Bradshaw who provided invaluable support on the Linux system and Edward Hand who worked closely with me in the early days of commissioning PIRATE.

Over the four years of my PhD I have made many friends along the way, too many to name here, but I would especially like to thank everyone who works, or has worked, in the Astronomy office for their friendship & moral support: Dan Staab, Paul Greer, Ashley Spindler, Pam Rowden, George Pagomenos, Joe Cooper, Andrew Davies, Mark Parker, James Doherty, Heidi Thiemann, Aaron Andrews and Brendan Webster. We had many great times together and created many fond memories in this time, most notably for me were the “Deansoc” games nights and

the random trips out & about around Milton Keynes.

Special thanks goes to Meredith Morrell and Richard Busuttil for their help and guidance with all things PIRATE related over the years. Richard was an invaluable source of knowledge during the early days of my PhD, and it was a pleasure to welcome him back in December 2018 with the roles reversed! As for Meredith, I cannot thank him enough for all the help he has given me along the way, especially when it comes to coding in Python, and I have enjoyed our many conversations together, especially grumbling about computer issues.

I would also like to extend my thanks to my close friends who I've been able to confide in but also to keep my spirits up: Adam Williams, Darren Goddard, Gareth Morgan & Martin Riffel. But extra special thanks goes to my loving parents Ian & Maxine for all their encouragement & support over the years but most importantly their unconditional love, which I have been blessed with since the day I was born.

Lastly, I would like to thank my girlfriend Sim, for all her love and unwavering support over the last three years. She has always been there for me no matter what and I don't think I could have finished my PhD without her; I look forward to what the future holds for both of us.

Contents

List of Figures

List of Tables

Chapter 1

Introduction - Part 1

The overarching questing driving this thesis was "Can a small-aperture robotic telescope be used to follow up time-critical and variable astronomical events, and what can we learn from these observations?" This was to be achieved with the utilisation of a new robotic telescope facility in Tenerife. With the ability to remotely slew to anywhere in the sky at a moments notice, robotic telescopes are regarded as the best way to observe fast fading transients, as they remove the human element from the command chain. In addition to this, their autonomous operation allows them to be placed in very remote locations, such as mountaintops, where access by road is limited but observing conditions are optimal. Autonomous operation means these robotic telescopes are much more cost effective to run than the traditional large telescope facilities because they require less staff to run and maintain them. Furthermore, small aperture robotic telescopes such as the one used in this thesis can be comprised of commercially available hardware, reducing the cost further.

One of the initial goals of this work was to perform a feasibility study into the use of a new robotic telescope facility in performing rapid response follow-up to gravitational wave alerts. In addition to this, the author was tasked with evaluating the ability to perform observations of massive stars in the local group Triangulum

galaxy (M33). Subsequent goals included developing the software necessary to allow PIRATE to respond rapidly to any gravitational wave alerts, and assisting in the commissioning phase of the new telescope facility in Tenerife. One more subsequent goal was to collect historical observations of Luminous Blue Variable (LBV) stars in the Triangulum galaxy, both spectroscopic and photometric; and use them in conjunction with new observations to investigate the long term behaviour of LBV stars with the aim being to reclassify some stars based on this new data.

This chapter, Chapter 1, outlines the new PIRATE robotic telescope facility located in Tenerife, designated PIRATE Mk3, and the author's contributions to its commissioning process in 2016. Along with the current PIRATE installation, this chapter also summarises the previous versions of the same telescope in Majorca and comparable robotic telescope facilities around the globe. Part 2 of the introduction, Chapter 2, introduces the two areas of scientific study in this thesis, and includes an overview of gravitational waves and LBV stars.

The third chapter describes the LIGO alert process for distributing gravitational wave alerts, as well as the PIRATE alert pipeline which was written specifically for the work in this thesis. Lastly in section 3.3 the procedure for scheduling observations with the ABOT telescope control software and OpenScience Observatories (OSO) Scheduler is explained.

Chapter 4 discusses the work undertaken with PIRATE to perform follow-up observations to gravitational wave alerts produced by the LIGO-Virgo Collaboration (LVC) during the second observing run (O2). This includes: listing all the alerts that were followed up in real time, detailing all the observations that were made, describing the method used to search the data for optical counterparts and lastly the results of this search are also given in section 4.3.

Chapter 5 moves on to discuss the analysis of spectroscopic observations made of candidate Luminous Blue Variable stars in the nearby Triangulum galaxy (M33),

with the main aim being to reclassify some of these stars based on their spectroscopic variability.

Chapter 6 builds on this work by presenting the long term monitoring observations made with PIRATE of the Triangulum galaxy. The aim of this was to complement the spectroscopic observations with photometric observations in order to search for variability in LBV candidates and compare these new observations with archival observations.

1.1 Early versions of the PIRATE telescope

The original PIRATE[1] (Physics Innovations Robotic Astronomical Telescope Explorer) Mk1 telescope was built in March 2008 at the Observatori Astronomic de Mallorca (OAM) near Costitx, Mallorca, at an altitude of just 162m above sea level (Busuttil, 2016). It consisted of a 14" Celestron Schmidt-Cassegrain OTA mounted on a Paramount ME German equitorial mount, with an SBIG STL-1001E CCD camera housing a Kodak KAF-1001E CCD chip which had 1024 x 1024 pixels. The FoV of the telescope was 22' x 22' and the CCD pixels were 24 μm across, which corresponded to a plate scale of 1.21"/pixel. Attached to the OTA along with the camera was an Optec TCF microfocuser and an eight position filter wheel that contained Johnson-Cousins BVRI broadband filters and three narrow band filters (Hα, OIII, SII). This was initially housed in a roll-off shed but after receiving extra funding in 2009 a Baader Planetarium 3.5m diameter all-sky clamshell dome was added to house the telescope (Holmes et al., 2011; Kolb, 2014).

In August 2010 the old 14" Celestron OTA was removed and replaced with a 17" PlaneWave CDK17 reflector and a new PlaneWave focuser, but all the other hardware remained unchanged; this increased the FoV to 29' x 29' and became

[1] `http://pirate.open.ac.uk/`

known as PIRATE Mk1.5. A year later in August 2011 the main imaging camera on PIRATE was replaced with an SBIG STX16803 camera that contained a 4096 x 4096 KAF16809 CCD chip, increasing the FoV again to 43' x 43' and the pixel scale to 0.63"/pixel. The CCD camera also housed an internal 5 position filter wheel which contained Baader RGB filters along with a Hα and clear filters (Kolb, 2014). This configuration was known as PIRATE Mk2 (see Kolb et al. (2018)) and remained unchanged for over 4 years until PIRATE was eventually removed from the OAM in November 2015 and temporarily housed at Baader Planetarium in Mammendorf, Germany, until its new permanent home in Tenerife was ready.

PIRATE was moved to Mammendorf to undergo a full service of all the optical hardware to ensure it was operating at peak performance when it reached Teide Observatory. However, as this was not going to be ready until mid-summer 2016, an agreement was made to house PIRATE in an observatory at the Baader Planetarium workshop for the interim period, to enable students to still have access to the teaching telescope until the new site was operational.

The author was given remote access to this observatory to continue preparations on the automated pipeline for rapid response follow-up observations; however, the first LIGO observing run, O1, ended on the 19$^{\text{th}}$ January 2016 which meant there would be no live alerts to respond to. And in addition to this, the previous observatory control software ACP[2] was still in use on PIRATE in Mammendorf, this meant that live testing of the pipeline wasn't possible and instead the author began working on the front end of the pipeline. This involved working on how to receive & process alerts, rather than how to connect with the telescope and push alerts to the observatory, because this would have to wait until the new control software ABOT was up and running. In addition to this, the author had general oversight of the telescope in Mammendorf, testing the setup before it was used by students and

[2] `http://acp.dc3.com/index2.html`

gaining experience with the performance of the new components.

1.2 PIRATE Telescope Mk3

The new observatory site is located on the Canary Island of Tenerife at the Observatorio del Teide (OT), and the foundations were completed by July 2016, at which point PIRATE was transported from Germany and installed up on Mt Teide. This version of PIRATE contained mostly the same hardware as PIRATE Mk2 except the SBIG camera was broken in transit and replaced with an FLI ProLine camera, and a new 10Micron GM4000 mount was installed to attach the OTA to the pier. In addition to PIRATE, The Open University also installed a new telescope facility next door to the PIRATE dome called COAST, and this telescope essentially comprised of the PIRATE Mk1 OTA on a 10Micron mount, all housed in a 3.5m Baader Planetarium clamshell dome.

First light for PIRATE Mk3 (see Figure 1.1) occurred on 26$^{\text{th}}$ July 2016 and from the beginning of August onwards PIRATE entered a 12 month long commissioning phase to iron out any teething problems with the new facility. The commissioning phase came to an end on the 6$^{\text{th}}$ July 2017 when the telescope was inaugurated by the Vice Chancellor of The Open University Peter Horrocks and the director of the IAC Rafael Rebolo López.

The new observing site was chosen for several reasons, but chief among them was its altitude; located 2,390m above sea level this puts OT above the cloud base most of the time, affording the observatory clear unrestricted views of the night sky on a daily basis. This, combined with the low light pollution and excellent seeing conditions, meant Teide Observatory was an ideal location for the placement of both Open University telescopes.

PIRATE's primary function is as a distance learning telescope for use by un-

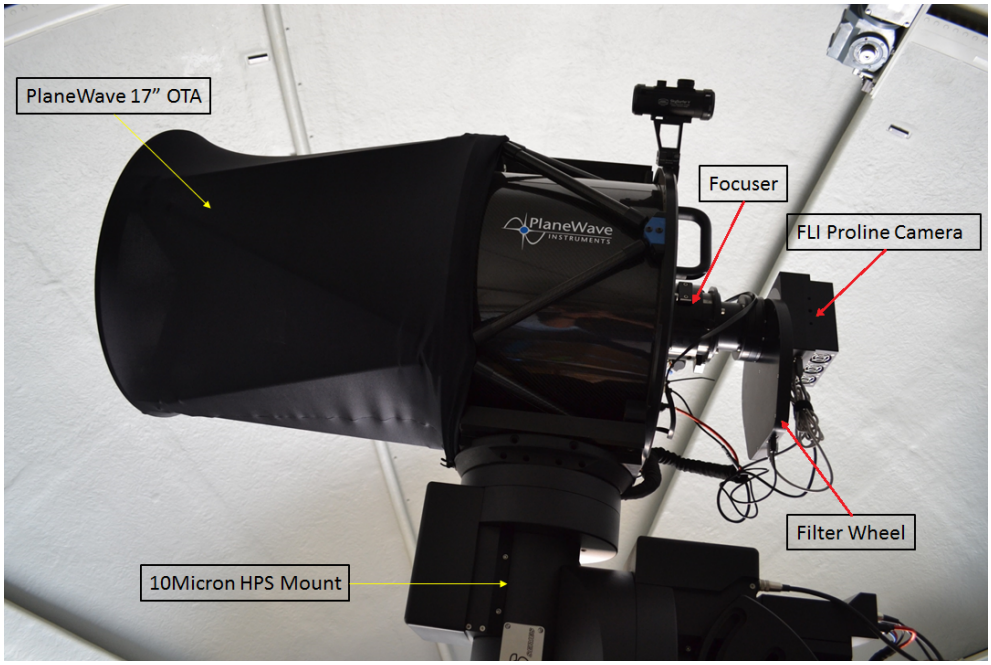

Figure 1.1: PIRATE Telescope (Photo by Author).

dergraduate students for up to 30% of the year, see Holmes et al. (2011), and for the rest of the year it is used as a research telescope studying a variety of objects such as: variable stars, exoplanet transits, supernovae, cataclysmic variables and microlensing events.

PIRATE Mk3 consists of a 17" PlaneWave Corrected Dall-Kirkham (CDK) Optical Tube Assembly (OTA) that is mounted on top of a 10Micron GM4000 HPS mount, which is a German "go to" equatorial style mount. Attached on the end of the OTA are a series of instruments, firstly there is the PlaneWave focuser mounted directly behind the OTA, then there is an FLI (Finger Lakes Instrumentation) filter wheel which contains 3 Baader RGB broadband filters, and 3 narrowband filters (Hα, OIII, SII). And lastly there's an FLI ProLine PL16803 camera that houses a KAF-16803 CCD chip, which has 4096 x 4096 pixels giving a field of view of 43' x 43' and a plate scale of 0.63"/pixel. All this is housed in a Baader Planetarium

all-sky 4.5m clamshell dome (Figure 1.2), which opens up entirely to the night sky, allowing the telescope to view any target without the dome impeding the view.

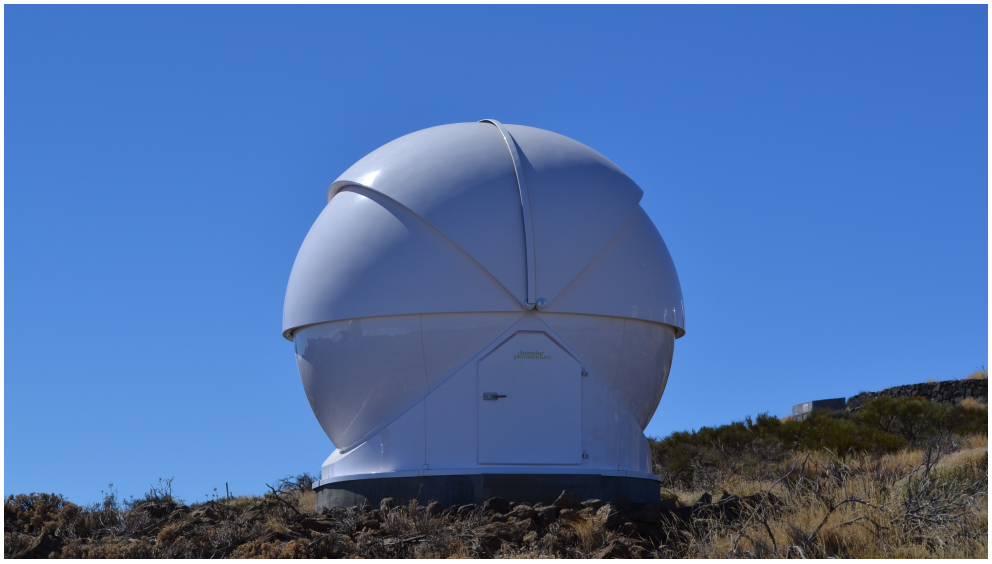

Figure 1.2: PIRATE's 4.5m clamshell dome (Photo by Author).

1.3 Contributions to the Commissioning Process of PIRATE

During the 12 month commissioning process of the new observatory in Tenerife, the author made significant contributions to the development, testing, implementation and overall supervision of the telescope, examples of which are outlined below.

1.3.1 Flat field testing

One of the challenges of operating an autonomous telescope is to be able to gather usable flat field frames (often shortened to "flats"), night after night, without the need for human intervention. Traditionally, at a manual observatory, it is up to

the night duty astronomer to prepare the telescope each evening; including the acquisition of optimal flat field frames. This is achieved by observing a patch of sky of uniform brightness at twilight, before the faint background stars start to appear. The ideal flat field frame contains no saturated pixels and a typical pixel count of between 30-40,000 , to avoid any non-linearity problems. The astronomer on duty can achieve this by slightly tweaking the exposure time for each image in order to hit the sweet spot where pixel counts are maximised.

However, this is not possible at a robotic observatory as no two nights are identical and the time at which flat field observations are possible changes every night as the local sunset/sunrise time changes throughout the year along with the length of dusk/dawn too. In addition to this, the weather conditions change from night to night, and so does the positioning of the Sun during sunset. Given all these variables, it is therefore necessary to set up an automated flat fielding routine for the telescope. In the case of PIRATE, this is done using the ABOT observatory control software and a flatfielding configuration file, which is an XML file that contains instructions for the telescope during twilight to gather these calibration frames.

At the beginning of the commissioning process the default XML file was not making optimal use of the limited time during dusk and dawn twilight. So to improve this, the author investigated the flat field process and determined the optimal filter pattern and ideal exposure times. An example of this analysis is shown in Table 1.1, where 15 flat field exposures were taken using the G filter on PIRATE and the exposure time and number of counts for each one was recorded. The average number of counts was rounded to the nearest hundred and also taken from the centre region of the CCD chip which receives the brightest illumination.

B filter	Evening	10/01/2017	
Number	Exposure Time (s)	Average counts	Time
1	0.05	1780	18:51:48
2	0.89	6255	18:51:54
3	4.95	26700	18:52:00
4	8.46	42700	18:52:11
5	9.13	42800	18:52:24
6	9.69	42500	18:52:39
7	10.3	41900	18:52:54
8	10.99	41500	18:53:09
9	11.71	41200	18:53:25
10	12.6	40300	18:53:43
11	13.58	40300	18:54:01
12	14.67	39800	18:54:20
13	15.89	38800	18:54:39
14	17.27	38500	18:55:01
15	18.86	37700	18:55:24

Table 1.1: Example of the typical CCD counts obtained with different exposure times during the flat fielding process.

The results of this analysis showed that the optimal setup was to allow 3-4 minutes per filter, to obtain up to 15 flat field frames (with the first two always being too short to use) and order them: OIII, SII, Halpha, R, G, B and Clear for dusk, with the order then reversed at dawn twilight. Also, the program was timed to start 5 minutes after sunset every night and 35 minutes before sunrise every morning, with a set maximum exposure time of 30s. Due to the fact that the science frames taken with PIRATE could be taken with either 1x1 or 2x2 binning, this meant that calibration frames had to be available in both options. For the dark and bias frames this isn't a problem as they aren't time limited; however, for the flat field frames this required configuration to alternate between the two types. To achieve this, it was decided that every dusk twilight would be devoted to taking 2x2 binning flats, whereas every dawn twilight would be used for 1x1 binning flats. This was a trade off between maximising the number of flat field frames in each filter and providing a second set of flats with different binning.

Lastly, after discussion with other users, it was agreed that the orientation of the telescope should be altered at twilight to find a more uniform patch of sky, where the light gradient was lowest. To begin with, Sybilla had set the telescope up to gather flat field frames by pointing at 35° altitude; but research by Chromey and Hasselbacher (1996) indicated that pointing the telescope more vertical (towards the zenith) during twilight returned the best quality flat field frames. Therefore, as part of this analysis, the configuration files in ABOT were altered to point the telescope at 80° Altitude - 80° Azimuth at dusk and 80° Altitude - 280° Azimuth at dawn.

1.3.2 Pointing model

Another significant part of the commissioning phase was the completion of the star pointing model on PIRATE. Initially this could only be configured manually in Tenerife, but future improvements to ABOT allowed users to update the pointing

model remotely.

For many telescope applications it is important to achieve sub-arcsec pointing precision. The advanced telescope control software can achieve this, but this is totally dependent upon the telescope being calibrated to a high precision in the first place. This can be achieved by creating a strong pointing model in the telescope mount computer. And from this, along with accurate GPS coordinates, the mount software can be calibrated to determine exactly where the telescope is pointing at any point in time.

The set up of the pointing model is done by moving the telescope mount manually to line the telescope up precisely with a list of individual target stars in the mount database. These stars are among the brightest apparent stars in the night sky and are spread across the entire sky, which enables a selection of them to be observable throughout the year, regardless of sky conditions. Once the target star is dead centre in the CCD image, the coordinates are saved in the pointing model and this is then repeated until enough stars have been obtained. Typically 10-20 stars are enough for a good pointing model to achieve the 0.1" accuracy desired, and with the first PIRATE pointing model approximately 15-18 starts were observed from Tenerife during the first servicing trip in late-September 2016. For comparison, more recent pointing models on PIRATE have included up to 50 stars, further increasing the accuracy all year round.

During this first field trip, the author also helped to manually align the mount with the correct North-South alignment, which would have affected the accuracy of the pointing model. This was done by making small adjustments to the mount fasteners, to ensure the telescope only moved by minute amounts.

Ultimately, this servicing trip provided PIRATE with much improved tracking and centring of objects, thanks to this pointing model and subsequent alignment improvements. Before this, there was significant trailing by stars in the CCD im-

ages as they were poorly tracked by the mount, meaning any exposures over 60s were subject to distorted PSFs and star trails. The improvements in the tracking allowed for more stable observations, with exposures up to 10mins now possible. This enabled PIRATE to take deeper images to find fainter sources and allowed for better source extraction to take place, aiding improved photometric measurements.

1.3.3 Linearity response

Further into the commissioning phase of PIRATE the author began experimenting with the linearity response of the new telescope setup in Tenerife. It was important to gain an understanding of the linearity response of the CCD to the incoming light as this ensures that the photon count by the CCD can be extrapolated into a total flux from a star, without missing any light.

Having a linear CCD response simply means that there's a linear relation between the number of photons incident upon the detector and the amount of electrons produced, which is then converted into digital counts (ADU) by using the gain. However, due to the way CCDs work, this relation is not always linear and it is particularly affected when a CCD nears its saturation point.

In order to determine the linearity response of PIRATE's CCD, an experiment was devised that involved obtaining multiple images of a target star, with increasing exposure times. These images were then calibrated and source extracted to determine the number of counts observed at each time interval. This data was then analysed to determine the point at which the linear relationship between exposure time and counts ceased. This was calculated to be in the region of 55,000-60,000 counts and so it was agreed that the maximum range of linear observations with PIRATE should be 45-50,000 counts to err on the side of caution. This was in line with expectations because, the maximum number of counts of a 16 bit CCD pixel before it is fully saturated is 65,535 and as they approach this limit the pixels become

less responsive to incoming photons; meaning they begin to respond non-linearly. In PIRATE's case, this non-linearity started above 55,000 counts, which therefore meant that for any scientific observations to be accurate, the stars in question could not have any individual pixel counts over this limit, otherwise their linearity could not be relied upon.

1.3.4 Collaborative contributions

The previous commissioning tasks were undertaken almost exclusively by the author. A number of other tasks required close cooperation with technicians and telescope users to achieve the desired results.

Firstly, one of the most difficult tasks during the commissioning phase was to design and implement a queue scheduling system to interact with the new observatory control software (ABOT). This was developed in-house by an OU colleague, Edward Hand, and it would become known as the OpenScience Observatories Scheduler once completed; more details on the scheduler are given later in section 3.3.2.

The author's main contribution to this centred around the testing and implementation of the scheduler's queuing priority system. The logic for this is explained in section 3.3.2, but the practical implications of the proposed algorithm had to be tested to determine what approximate priority ranges corresponded to what cadence of observations, e.g. a priority of ~ 500 would be expected to return 1 observing request per night. In addition to this, the author soon realised that this particular queue scheduling logic wasn't compatible with their goal of rapid response observations; so the author requested an immediate override function be built into the scheduling software (see section 3.3).

The author was also involved in testing the different methods of uploading observing requests to this new scheduler. This included both individual requests submitted via a web form and multiple requests submitted by uploading a CSV file on

to the OSO website. For the rapid response observations, a UNIX command line API was created whereby automated alerts could be sent to the scheduler via cURL uploads containing all the required observing fields in JSON format, to be added to the queue schedule. This was developed at the request of the author, who was also involved in testing the interoperability between the OSO scheduler and the author's Python script, which required rapid automated observing requests to be submitted upon the receipt of an alert from LIGO.

Secondly, there were several issues during the commissioning phase surrounding the automated focusing of the telescope for day-to-day observations. The author spent a considerable amount of time studying the underlying issues. The problem stemmed from the fact that the auto focusing algorithm of the telescope only triggered when the temperature drops more than 5 degrees above or below a known focuser position for a given temperature. These data points were stored in a "focus vault" and ABOT extrapolates this for intermediate temperatures between the existing data points. However, the existing points were taken in the summer, when temperatures were warmest, and once temperatures started to drop, somehow this caused a mis-match between the existing data points/trend and the new ones, causing several observations to be out of focus every night. The initial solution to this was to wipe the focus vault clean and start with fresh focus points, but then this meant that all of the focus positions from warmer temperatures no longer existed.

The next attempted solution involved Edward Hand manually generating a large array of focus values for the focus vault, based off previous focus points and a linear trend fit. This initially worked well but as time went on it became less and less effective and temperatures again moved out of range. So after discussions with the ABOT developers Sybilla, the final solution resulted in reducing the "temperature tolerance" at which ABOT requested a new focus run to 2 degrees and adding some minor changes to the way the focusing logic worked within ABOT.

This concludes the overview of the telescope facility and the author's contributions. Now the topic of discussion moves on to look at the population of small robotic telescopes comparable in size and scope to PIRATE.

1.4 Current Installations of Robotic Telescopes

At the Teide Observatory site there is a new area reserved exclusively for small aperture robotic telescopes, where PIRATE is located alongside its sister facility COAST (IAC, 2017). The other robotic telescopes located here include:

1. MAGEC (Majorca cAnary survey of very fast movinG sky objECts) is an autonomous telescope facility dedicated to observing fast moving objects such as asteroids and comets. The facility itself contains 5 telescopes, two of similar size to PIRATE at 0.45m, one 0.4m telescope, one 0.3m and another 0.17m (Rodríguez and del Puerto, 2015).

2. LCO (Las Cumbres Observatory) is a global robotic telescope network specialising in rapid follow-up of transients and searching for exoplanets, their facility at Teide Observatory currently contains two 0.4m telescopes but this will be expanded in the future (Rodríguez and del Puerto, 2015).

3. Slooh is a robotic telescope service that offers live views of the night sky at a number of sites across the world, the Optical Telescope Array (OTA) at Teide Observatory contains a 0.5m and a 0.35m telescope. Although not the first robotic telescope, Slooh was the first telescope service to offer live views through the telescope via the internet (Gomez and Fitzgerald, 2017).

4. MASTER (Mobile Astronomical System of the TElescope Robots) is a global robotic telescope network operated by the University of Moscow, Russia, and comprises of 8 separate sites around the world, each housing two parallel 0.4m

telescopes. The main research goals of the project include measuring the polarisation and properties of gamma-ray bursts in the optical (Lipunov et al., 2016).

5. The Qatar Exoplanet Survey (QES) is an array of eight 0.1m telescopes mounted on a single platform, with the aim of searching for "hot" exoplanets similar in mass to Jupiter (IAC, 2017).

6. AMOS-CI (All-sky Meteor Orbit System-Canary Islands) is owned by the Comenius University in Bratislava, Slovakia, and consists of two stations (one at OT and another at ORM) containing two sets of cameras that are capable of recording meteors as they enter the atmosphere overhead (Tóth et al., 2015).

Looking slightly further afield at the Observatorio del Roque de los Muchachos (ORM) on La Palma and there is the GOTO[3] (Gravitational-wave Optical Transient Observatory) autonomous telescope facility. This was commissioned in July 2017 and houses a slewing matrix capable of carrying up to 8 OTAs, though there are currently just 4, which provide a combined field of view of 5 square degrees and can detect transients down to 21st magnitude[4]. As the name suggests the primary purpose of this facility is to detect optical counterparts to gravitational wave merger events, similar to the work done with PIRATE in this thesis. Another robotic telescope located at ORM is the Liverpool Telescope, which is a 2m class robotic telescope operated by Liverpool John Moores University in the UK (Steele, 2004). It has a field of view comparable to PIRATE at 40' x 40' but with its larger light collecting area it can reach targets as faint as 21 st magnitude; in a 10 minute exposure with excellent sky observing conditions[5]. It's automated design makes it

[3] https://goto-observatory.org/telescopes/

[4] http://www.iac.es/divulgacion.php?op1=16\&id=1227\&lang=en

[5] https://telescope.livjm.ac.uk/TelInst/calc/

ideal for catching fast fading transients and its large size has enabled it to follow up even fainter targets than the 0.5m class robotic telescope to which PIRATE belongs.

Globally there are many more robotic telescope facilities currently in use, the Robotic Telescope List[6] puts the figure at 133[7], which is too many to name, but some facilities that perform rapid follow-up observations similar to PIRATE are:

1. Super-LOTIS (Livermore Optical Transient Imaging System) is a 0.6m autonomous telescope located at Kitt Peak National Observatory (Arizona, USA) and is capable of rapid slewing with the primary goal of localising gamma-ray bursts. It has a rather small field of view of 17' x 17' but this enables it to follow up much fainter sources, as faint as $m_r = 18.5$ in a 60s exposure (Williams et al., 2008).

2. ROTSE-III[8] (Robotic Optical Transient Search Experiment) is a network of four 0.45m robotic telescopes located in Texas, Namibia, Turkey & Australia, each with a 1.85 x 1.85 degree field of view, purposely designed with a rapid slewing capability in order to follow up gamma-ray burst afterglows (Akerlof et al., 2003).

3. TAROT[9] (Télescopes à Action Rapide pour les Objets Transitoires) is similar to ROTSE in that it was designed to remotely observe optical counterparts to gamma-ray bursts, and it consists of a pair of telescopes, 0.25m in diameter, with one located in the southern hemisphere (La Silla, Chile) and the other one located in the northern hemisphere (Calern, France). The field of view of the TAROT telescopes is 1.86 x 1.86 degrees, with a magnitude limit in the V band of 17 (Klotz et al., 2008). As TAROT has telescopes in both

[6] `http://www.astro.physik.uni-goettingen.de/~hessman/MONET/links.html`
[7] As of 2nd August 2016
[8] `http://www.umich.edu/~rotse/rotse-iii/rotseiii.htm`
[9] `http://tarot.obs-hp.fr/infos/`

hemispheres this meant that they could potentially follow up every transient event in the night sky, regardless of location. But what they lack is the ability to continuously observe from the dark side of the Earth as it rotates.

4. BOOTES (Burst Observer and Optical Transient Exploring System) is a telescope network which operates five 0.6m robotic telescopes at observatories in Spain, New Zealand, China and Mexico. As the name suggests; their primary aim is to quickly follow-up transients and this is achieved by automating the whole process from receiving the alert to moving the telescope. Unlike the TAROT telescopes, BOOTES has telescopes spread across the globe enabling them to make continuous observations of the same target as the Earth rotates (Hiriart et al., 2016).

It's clear from all the telescope facilities discussed that small aperture robotic telescopes are becoming the tool of choice for transient astronomy, due to their capability and low cost. As small robotic telescopes such as PIRATE can be made with off the shelf components, they are not only cheap to build but also cheaper to run; and so this enables smaller institutions to build their own dedicated astronomical observatories. As a consequence, this allows larger institutions to build a network of small robotic telescopes for the same price or less than a typical large multinational observatory. The key benefits of this being the ability to continuously observe transients at any time of the day without being interrupted and thus probing a new area of phase space for variability.

Now the topic of discussion moves onto one of the two main lines of study with the PIRATE telescope, gravitational waves. The next section will discuss their origins in astrophysics, as well as the past and current attempts at detecting them, along with a discussion about their electromagnetic counterparts, particularly in the optical. Lastly this section moves on to the recent confirmed detections by LIGO in 2015 and more recently in 2017.

Chapter 2

Introduction - Part 2

The initial decision to attempt to follow up of gravitational waves with PIRATE was driven by the timing of the start of the Advanced LIGO and VIRGO detectors, without which none of this science would have been possible. Furthermore, the expected error box for the detection of an optical counterpart was over 100s of square degrees, necessitating the collaboration of many of the worlds largest observatories, together with as many smaller scale telescopes as possible. This large collaboration was also necessary due to the time critical nature of the observations, which meant that the longer the delay between GW detection and EM observation, the greater the chance of missing the evolution of the transient and the physics behind it. This is where PIRATE could contribute greatest to the EM follow-up campaign, with it being a robotic telescope it could respond autonomously to any incoming alert and attempt to capture the optical counterpart in its early stages.

The study of Luminous Blue Variable stars with PIRATE was motivated primarily by the autonomous nature of PIRATE, which could be utilised to obtain large volumes of data from monitoring the same population of stars night after night for months on end. This could then be used to look for periods of large scale variability of the candidate LBV stars, indicative of an S Dor outburst. From a scientific

perspective though, the study of these stars was important because of the role they play in stellar evolution with their high mass outflows. The variability of these stars is well known, but the exact behaviour and timescales is poorly understood, thanks in part to their rarity. It was hoped that by using PIRATE in this way, some of the gaps in this understanding could be filled in, at least with small scale variations over large periods of time.

The remainder of this chapter goes on to discuss the science behind both thesis topics in much more detail.

2.1 Gravitational Waves

The foundations for the theory of gravitational waves were laid down when Albert Einstein published his Special Theory of Relativity in 1905 (Einstein, 1905), in this theory he postulated two things: firstly he stated that all inertial reference frames are equivalent and none can be treated specially. Secondly, Einstein postulated that the speed of light in a vacuum must be constant, this cannot be changed as it is a fixed value and a property of light itself, so the speed of light is the same for all observers regardless of the motion of the light source. By combining these two postulates, Einstein came up with the idea of space-time, where the two properties become intrinsically linked to each other and cannot be treated separately, this was shown by using Lorentz transformations (2.1 & 2.2), where the spatial and temporal coordinates depend on time and space respectively.

$$x' = \gamma(x - vt) \tag{2.1}$$

$$t' = \gamma(t - vx/c^2) \tag{2.2}$$

Where (x, t) and (x', t') are the space-time coordinates of two inertial frames moving with a velocity v relative to each other and $\gamma = 1/(1-v^2/c^2)^{1/2}$ is the Lorentz factor.

However, after formulating his Special Theory of Relativity Einstein realised that the apparent equivalence of inertial and gravitational mass meant that gravity could not be included in his theory. Newton's law on gravitation had stood firm for hundreds of years and seemed to work perfectly, but there was a problem with this law that made it incompatible to Einsteins new theory. Newton assumed that gravity acted instantaneously across the universe, something Einstein had shown impossible if he was right about the speed of light being the speed limit of the universe. Also, Newton hadn't taken into account that gravity can be caused by energy not just mass. Eventually Einstein realised that gravity should not be treated as a force but it is in fact indistinguishable from acceleration, something that he called his principle of equivalence.

It is from this that Einstein went on to write his General Theory of Relativity in 1915 which helped describe gravity in the context of space and time (Einstein, 1916). From his equivalence principle he deduced that gravity was just the physical manipulation of the curvature of space time (Camp and Cornish, 2004). In this new theory Einstein drew up ten field equations that described the behaviour of gravity resulting from the interactions of space-time with mass and energy; these may be represented as a tensor in the following form:

$$R_{\mu\nu} - \frac{1}{2} g_{\mu\nu} R + g_{\mu\nu}\Lambda = \frac{8\pi G}{c^4} T_{\mu\nu} \tag{2.3}$$

Where $R_{\mu\nu}$ is the Ricci curvature tensor, R is the scalar curvature, $g_{\mu\nu}$ is the metric tensor, Λ is the cosmological constant, G is Newton's gravitational constant, c is the speed of light and $T_{\mu\nu}$ is the stress-energy tensor. Alternatively, this can be written in a more compact form known as the Einstein Tensor:

$$G_{\mu\nu} = \frac{8\pi G}{c^4} T_{\mu\nu} \tag{2.4}$$

Where G_N is Newtons gravitational constant and $T_{\mu\nu}$ is the stress energy tensor.

In mid-1916 Einstein produced a paper that followed directly on from General Relativity and in it he presented linearised approximations for his field equations, introducing gravitational waves for the first time. However, Einstein was forced to look again at these results as he had used the wrong kind of tensor in his calculations that wasn't invariant under coordinate transformation, thus explaining why no one else could reproduce his results. Another conclusion that Einstein made from this result was that radiation of gravitational energy from monopoles was permitted, something that Max Abraham had ruled out a few years earlier when he was carrying out his own work on a relativistic theory of gravitation in 1912.

After mistakes in his original paper, Einstein released another copy on his 1916 paper two years later (Einstein, 1918), with alterations to the problematic pseudo-tensor and more importantly a revised radiation formula that for the first time considered quadrupole radiation (Steinicke, 2005). Also he mentioned how he came to realise that no single coordinate system was preferable over another. Instead he said that the choice of reference coordinates greatly effects what results you find, and that it should be recognised none is preferable over any other.

To understand why gravitational waves are produced by quadrupole radiation; it's important to firstly understand why it cannot be produced with monopole or dipole sources. Monopole radiation can only be created by a spherically symmetric change to the source, meaning the change would have to originate from a single point, hence the term "mono-pole". An example of this would be a pulsating sphere moving in and out or a source disappearing and reappearing in the field. However, this would violate conservation of mass and charge laws. Dipole radiation on the other hand occurs when there is an acceleration of the source along one axis (with two poles) but it's still axially symmetric, an example being a particle moving back and forth along a straight line. This is permissible in electromagnetism due to there

being two opposite charges, however as gravity is purely an attractive force then doing this would violate conservation of momentum laws. Quadrupole radiation is generated when a source accelerates in two axes (with four poles), typically this involves a circular motion (or orbit) of two masses around each other, an example being a binary star system. Thus, a quadropole is the lowest permitted multipole for gravitational radiation.

2.1.1 First gravitational wave detectors

The first type of detectors used to look for gravitational waves were called resonant bars (later known as Weber bars after the man who invented them Joseph Weber), these were solid aluminium bars about two meters in length and they were designed to measure the strain of a passing gravitational wave. The strain value (h) is a dimensionless amplitude that is a measurable parameter of a gravitational wave, as shown in equations 2.5 & 2.6. It can be derived from the gravity gradient (g') which is the difference in gravity (Δg) between two points divided by their distance (d). As gravity is just another form of acceleration, this can be integrated twice with respect to time to give an instantaneous change in displacement as a function of time.

$$g' = \frac{\Delta g}{d} \tag{2.5}$$

$$h = \frac{2\Delta d}{d} \tag{2.6}$$

By using these resonant bars Weber hoped to measure the strain of gravitational waves passing by the Earth coming from nearby stars with a strain of the order 10×10^{-16} (Weber, 1960). However, the equipment he was using (a 2x1m solid aluminium cylinder bar suspended on steel wires with piezoelectric crystals attached to convert the vibrations into electric signals) was very rudimentary and ultimately not capable of ever detecting gravitational waves.

Between 1967 and 1974 Weber published several papers (Weber, 1968, 1969; Lindley, 2005) claiming to have detected gravitational waves with his resonant bars; however, other groups tried and failed to replicate his results, such as Drever et al. (1973) who were a group was led by Ron Drever at Glasgow University that built an enhanced version of the Weber bar. They tried to recreate Weber's results but were unable to detect any gravitational waves.

The use of resonant bars continued throughout the 20^{th} century and culminated in the formation of the International Gravitational Event Collaboration (IGEC). This was an international collaboration formed of five members spread across the globe: ALLEGRO, AURIGA, EXPLORER, NAUTILUS and NIOBE. The reason such a network was formed was because of the need to make a coincident detection at multiple sites and thus rule out any local transient noises. Each member of the collaboration housed a resonant bar that ranged in size from 1500kg to 2296kg, and these were all cryogenically cooled close to absolute zero in order to reduce thermal noise (International Gravitational Event Collaboration, 2003). This network was operational for three years and during this time they were unable to make any detections of gravitational waves (Prodi et al., 2000), as they were ultimately limited by the sensitivity and type of detector.

2.1.2 Interferometer era

Having reached the limit of what a resonant bar could do, a new type of detector was necessary in order to improve the sensitivity of the detector by several orders of magnitude. In fact Weber had already thought about this and one of his students, Robert Forward, was the first to operate an interferometer in the late 1960s (Kennefick, 2007) along with the Soviet scientists Mikhail Gertsenshtein and Vladislav Pustovoit. The big improvement these interferometer detectors made over the resonant bars was that they allowed for the positioning of two "test masses" a significant

distance apart (not just in the same laboratory but many hundreds of meters away), thus increasing the sensitivity of the detector and the signal range they were sensitive to. However, to achieve the necessary sensitivity of the laser interferometer many technological challenges would need to be overcome.

Interferometers are named as such because they involve measuring an interference pattern caused by the merging of two light sources. Laser interferometers are used in gravitational wave detectors because of the properties of laser light, such as high collimation and strong coherence, that allow them to be used over great distances and still maintain a powerful and coherent beam.

The basic set-up of an interferometer involves just five key components. Firstly there needs to be a light source(laser), this light then passes through a beam splitter that sends the light beam up the two arms of the detector that are perpendicular to each other. At each end of the arms are highly reflective mirrors that bounce the light back to the beam splitter where the two beams merge again and form an interference pattern on a photodetector. These interferometers are tuned so that once the laser beams travel up and down each arm, when they recombine at the beam splitter they will be in anti-phase and produce destructive interference thus canceling each other out. Any slight deviation to the length of these arms and the laser beams will recombine out of phase and this change can be seen by the detector at the end of the beam pipe.

This design allows for the detector to be very sensitive to slight changes in the path length of the laser which could be caused by a passing gravitational wave. However, all other external factors need to be excluded beforehand, such as seismic vibrations and anthropogenic noise (Waldman, 2011).

Another early adopter of interferometer technology was Rainer Weiss; who built and ran an interferometer at his home institution of MIT as early as 1967. Weiss then went on to work with Ronald Drever in Glasgow and Hans Billing in Garching

on building prototype gravitational wave interferometers. Their combined efforts led to vast improvements in interferometer technology in the late 1970s and early 1980s with large improvements to the overall power and sensitivity of their instruments. Working in parallel with this technological development was Kip Thorne and a group of theoretical physicists at Caltech, where they worked on theoretical predictions of gravitational waves based on Einsteins work on general relativity (Thorne and Weiss, 2016).

In the years that followed the groups at MIT and Caltech formed a close working bond, and the final outcome of this partnership resulted in the two institutions forming a joint bid for funding from the National Science Foundation (NSF) for the construction of a Laser Interferometer Gravitational Wave Observatory (LIGO) in 1989. This new observatory was spread over two sites; each housing a 4km long interferometer using technology developed at MIT (Thorne and Weiss, 2016).

2.1.3 LIGO

LIGO was built between 1994 and 1998 at two sites in the USA, one at Livingston, Louisiana and another at Hanford, Washington. Initially three interferometers were installed across the two sites, with one at the Livingston facility (L1) and two at the Hanford facility (H1) & (H2) but the second Hanford interferometer was only half as long as the main one.

Shown in Figure 2.1; the fundamental design of the interferometers built for LIGO were fairly unchanged from the first generation of detectors built in the 1970s, they still included the basic set up of: four mirrors, a beam splitter, a laser and a photodetector. However, to reduce the background noise in the detectors a number of extra measures were needed to isolate the system. One of these was to keep the entire interferometer inside a vacuum in order to remove any air turbulence inside the arms that might affect the position of the mirrors or the light path of

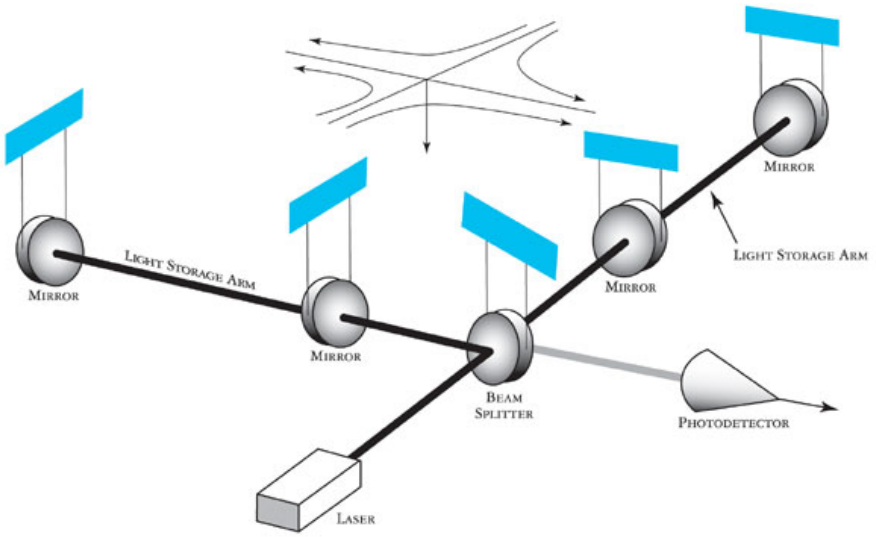

Figure 2.1: Interferometer design used at LIGO. Image credit: LIGO

the laser beam. In addition to this, the effects of seismic noise on the detector were reduced by adding an external hydraulic system to isolate surface vibrations; and also suspending a heavy (10kg) mirror with a pendulum system helped to isolate the system further.

The first engineering test run of LIGO was conducted in October 2000 and subsequent tests were carried out for a further 18 months until the detector became stable enough to operate (Abbott et al., 2004a). The first proper science run (S1) of LIGO was performed between 23rd August and 9th September 2002 (Abbott et al., 2004a). From the very beginning LIGO was designed to be upgraded over time in order to benefit from the latest technological improvements. As a result of this LIGO did not run at initial design sensitivity straight away (solid black line in Figure 2.2), instead it took several upgrades over many years to reach the desired strain sensitivity.

Strain sensitivity, as used in Figure 2.2, is an amplitude spectral density (as opposed to characteristic strain). The amplitude spectral density is the square root of

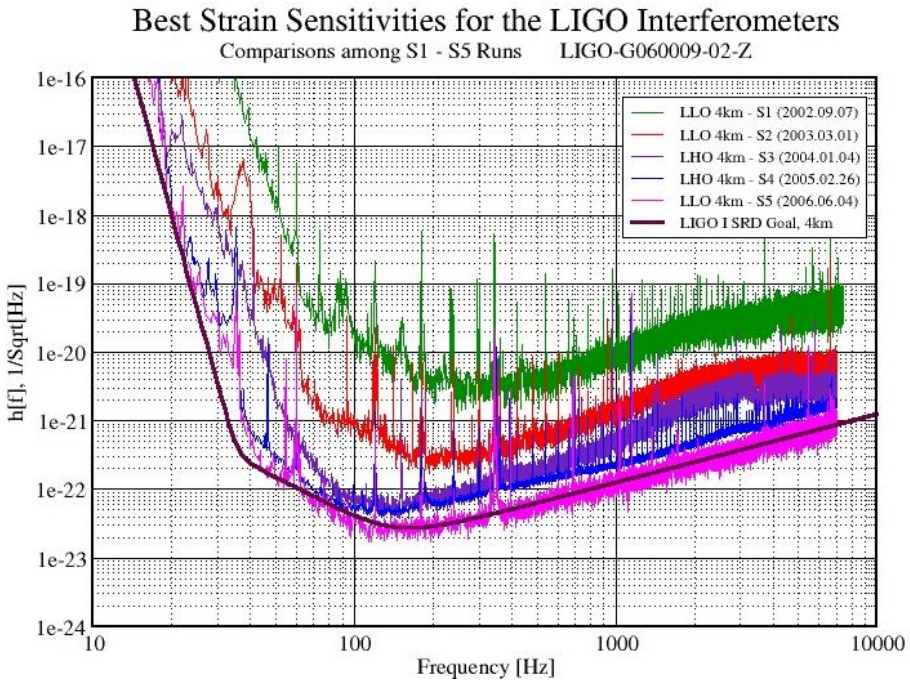

Figure 2.2: Comparison of LIGO detector sensitivity (strain) over the initial 5 science runs with the initial design sensitivity (Abbott et al., 2006).

the power spectral density; which if integrated over all positive frequencies gives the mean square amplitude of the noise in the detector. Conversely, the characteristic strain is a way of modifying the amplitude to take into account how the signal adds up over time, then the area between the characteristic strain of the source and the detector sensitivity curve gives a measure of the signal-to-noise ratio (SNR) of the signal (Moore et al., 2015).

The exact shape of this sensitivity curve is dictated by two broad noise effects and several smaller noise sources. For instance, the sensitivity at lower frequencies (<60Hz) is dominated by seismic noise, while at the higher end (>100Hz) it is the photon shot noise in the laser that dominates (LIGO Scientific Collaboration et al., 2015). In Figure 2.3 the total strain noise is broken down into its component parts:

1. Quantum noise incorporates photon shot noise with the radiation pressure fluctuations from the laser.

2. Seismic vibrations can include anything from earthquakes and vehicle movement to the wind and even ocean waves.

3. Newtonian gravity (also known as terrestrial gravity) noise relates to fluctuations in the local gravitational field around the mirrors (test masses) caused by density perturbations as a result of seismic displacement.

4. Suspension thermal noise arise primarily from thermal variations in the steel wires used to suspend the mirrors.

5. Mirror coating Brownian noise is the dominant of the three thermal noises emanating from the test masses, this comes about because of mechanical dissipation in the coatings of the mirrors due to the Brownian motion of the molecules. A similar process occurs in the mirror substrate.

6. Mirror coating thermo-optic noise is a result of the relaxation of a temperature differential between the mirror substrate and coating layers that is generated by the laser hitting the mirrors surface.

7. Residual gas left in the evacuated beam pipes still interferes with the beam path and alters the refractive index, resulting in different optical path lengths (LIGO Scientific Collaboration et al., 2015).

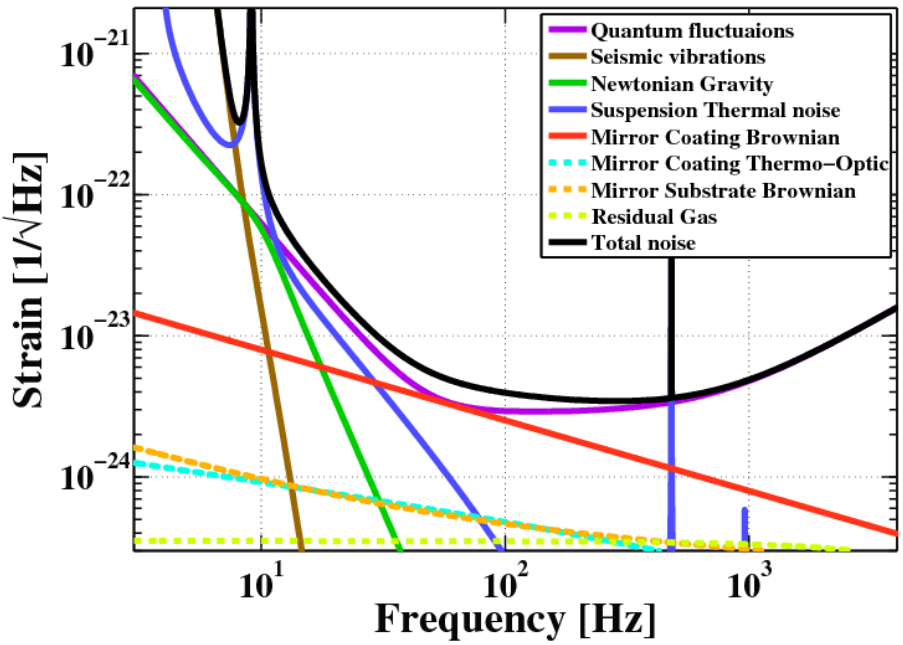

Figure 2.3: Main contributors to the strain sensitivity curve noise floor (LIGO Scientific Collaboration et al., 2015).

In addition to these broad noise effects there are also numerous spectral peaks, some are caused by vibrational modes in the mirrors' suspension wires but most of the large spikes are caused by power line harmonics where the magnetic field around the power lines couple directly to the magnets used to control the mirrors. For example, the first harmonic occurs at 60Hz which is the operating frequency of the US national grid, the second harmonic occurs at 120Hz.

Since its inaugural science run in 2002, LIGO embarked on four further science runs over the subsequent five years to steadily improve the strain sensitivity of the detector (Abbott et al., 2004b, 2005, 2006, 2007). This culminated in November 2005 with the commencement of S5 which was the first science run to operate at design sensitivity (Abbott et al., 2009), as shown in Figure 2.2. S5 lasted for almost two years and during the second half of this run LIGO was joined by the Virgo detector (see subsection 2.1.5) in Italy for the first joint run between the two large

interferometer observatories.

After the initial 5 science runs of LIGO were completed (called "Initial LIGO" hereinafter), a second phase of operations called "Enhanced LIGO" commenced and this involved incremental upgrades to the detectors. These upgrades included: higher-power lasers, a new output mode cleaner and a new readout scheme. The aim of these upgrades was to increase the strain sensitivity by a factor of two from Initial LIGO (Smith and LIGO Scientific Collaboration, 2009).

During Enhanced LIGO (also called S6) both LIGO detectors were operating at an increased sensitivity and they coordinated their operations to join up with the Virgo detector during its second and third science runs, and also the Swift gamma-ray satellite (Abadie et al., 2012). This sixth science run started in July 2009 and concluded in October 2010 with the resulting analysis of the data showing that no gravitational waves were detected during this joint run (Abadie et al., 2012); however, they were able to achieve an improvement in the strain sensitivity as shown in Figure 2.4.

Succeeding Enhanced LIGO was the third iteration of the detectors called Advanced LIGO, this used the same buildings and vacuum pipes as the original LIGO but everything else was removed and replaced meaning that it took over 5 years to fully reconstruct the interferometers in preparation for Advanced LIGO. One of the major changes to the hardware in Advanced LIGO was with respect to the mirrors and suspension system. As mentioned previously the original LIGO design used 10kg mirrors at either end of the beam pipes, whereas for Advanced LIGO these were upgraded to 40kg and in addition to this they were suspended from a quadruple pendulum system using fused silica fibres. The aim of these three improvements were to: reduce noise from radiation pressure on the mirrors, lower the suspension thermal noise in the wires and reduce seismic vibrations by further isolating the suspension system.

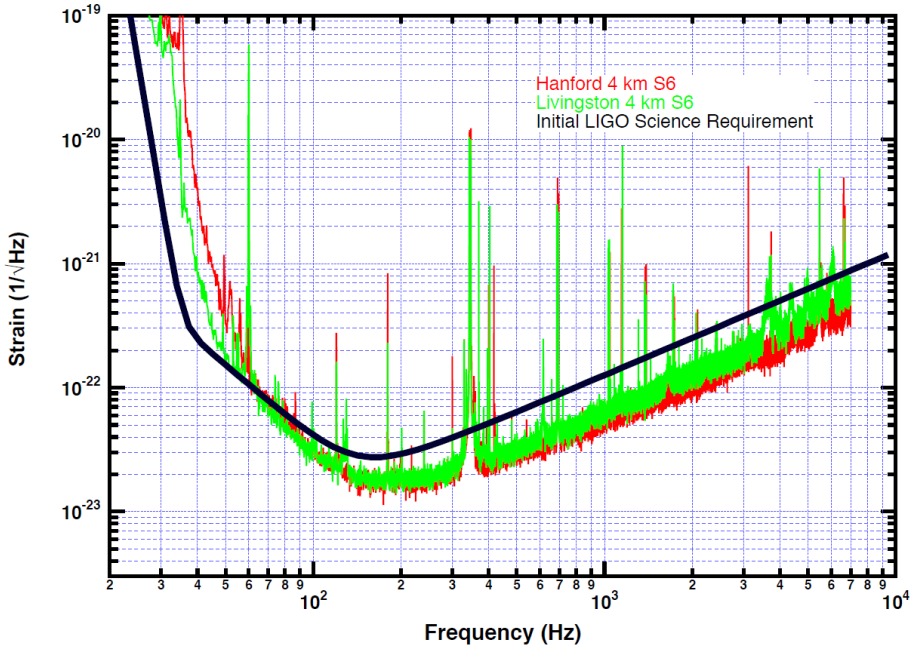

Figure 2.4: Strain sensitivity improvement with Enhanced LIGO (Abadie et al., 2012).

The overall aim of Advanced LIGO is to improve the sensitivity of the detectors by a factor of 10 (see Figure 2.5); however, like the Initial LIGO project it did not run at full sensitivity straight away. For the first observing run (O1) in 2015 it was only operating at around a third of design sensitivity.

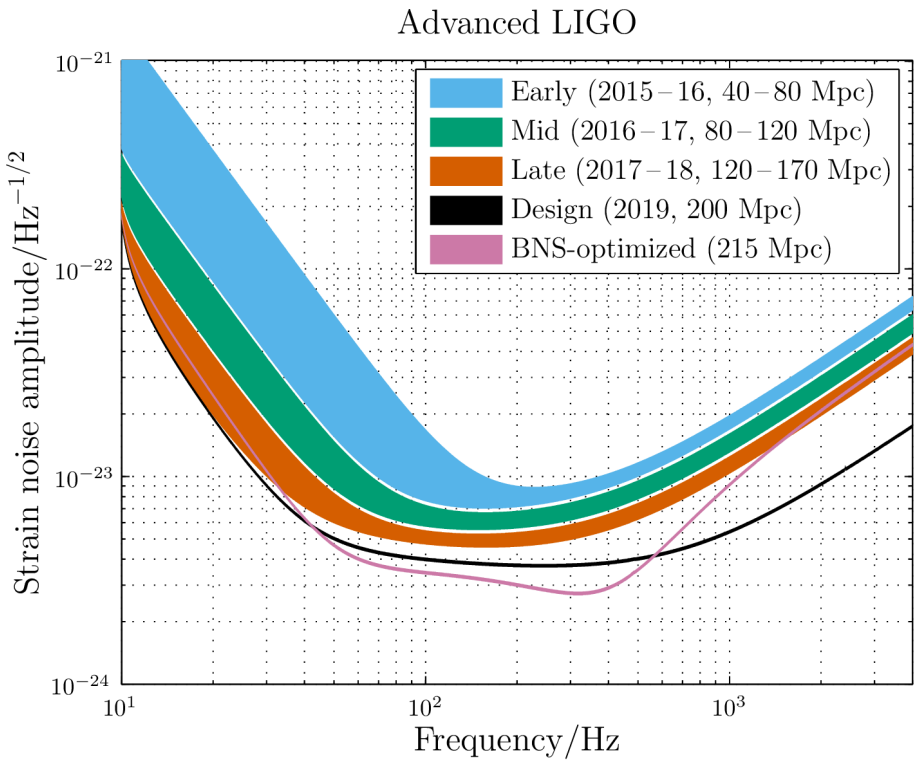

Figure 2.5: Target strain sensitivity for the Advanced LIGO detectors (Abbott et al., 2016d).

Even though it wasn't operating at design sensitivity during O1 the two LIGO detectors were still able to achieve the first positive detection of a gravitational wave (discussed in section 2.1.7).

2.1.4 LIGO Collaborations

Throughout its history LIGO has always been keen to collaborate on the search for gravitational waves and after the success of the IGEC network they teamed up with the TAMA300 detector in Japan to perform the first inter-collaboration search for gravitational waves. At the time the LIGO network consisted of two 4km long interferometers "H1" & "L1" and a 2km long one called "H2". By collaborating

with their Japanese colleagues, they were effectively able to include the 300m long TAMA300 interferometer near Tokyo in their network (Abbott et al., 2005).

Although TAMA300 is less sensitive than the LIGO detectors, it made up for this with its high running time (called duty cycle) of over 80%. During the period of S2 that they were collaborating for they were unable to detect gravitational waves but were able to place an observational upper limit on the rate of binary neutron star coalescence with masses between $1 - 3M_{\odot}$ of 49 events per year per Milky Way Equivalent Galaxy (MWEG) at 90% confidence level. In addition to this, the LIGO collaboration noted that this joint venture with TAMA300 helped them gain experience of doing inter-collaboration searches and develop tools that would come in useful for such collaborations in the future, starting with GEO600 (Abbott et al., 2006).

A European effort to obtain a long baseline interferometer for observing gravitational waves was initiated not long after LIGO was formed, and it started out as two separate projects by scientists at Glasgow University and Max-Planck Institute for Gravitational Physics in Garching. The Max-Planck group applied to the German funding agencies for a 3km long interferometer in 1985 but were refused the funding. Similarly in Glasgow the British team had applied to the UK funding council for a similar project in 1986 but they too were refused. It was at this point the two teams decided to join up and pool their resources to form the GEO collaboration in 1989. They managed to eventually attain funding for a 600m long interferometer in 1994, to be located near Hanover. Construction began a year later and the detector, now called GEO600, was ready for operational use by the end of 2002 (Hornung, 2016).

From the very start the two groups (GEO600 and LIGO) formed a close working relationship which became known as the LIGO Scientific Collaboration (LSC) and this collaboration is still ongoing. After TAMA300 was decommissioned in 2004 they were the only two large interferometer projects running until the completion

of the Virgo detector in 2007. So it was only natural that they conducted their first engineering run in parallel with an engineering run of the LIGO detectors in January 2002. This was soon followed by the first science run between August and September 2002 for 17 days (Abbott et al., 2004a).

2.1.5 Virgo

The Virgo project started out as a joint venture by the French CNRS (National Centre for Scientific Research) and Italian INFN (National Institute for Nuclear Physics) in the early 1990s and since then has been joined by the Dutch NIKHEF, Polish POGRAW, and Hungarian RMKI institutions. The site of Cascina in Italy near the city of Pisa was selected, and construction on the 3km long interferometer started in 1996. In 2000 the Virgo project was given a parent institution called the European Gravitational Observatory (EGO) which became responsible for the construction and future operations of the detector. The construction was completed in 2003 and it took four more years of testing before Virgo became fully operational and started taking data (Hasler, 2003).

Before the first science run of Virgo (VSR1) commenced in 2007, the EGO signed an agreement with LIGO to collaborate on gravitational wave searches, just like they had done with TAMA300 and GEO600 in the past. This collaboration would become known as the LVC (LSC-Virgo collaboration) and allowed all members to access the data from both machines when they were operational. The first time they ran jointly together was late into LIGO Science Run 5 (S5) in October 2007, this was the first time five gravitational wave detectors were operational at the same time (LIGO, GEO600 and Virgo).

The addition of Virgo to the LVC network was much more significant than when GEO600 joined because it was more similar in size and sensitivity to the American LIGO detectors (see Figure 2.6); and in addition to this the location and alignment

of the interferometer arms meant that it covered areas of the sky that were poorly covered by the LIGO detectors (Abadie et al., 2010a).

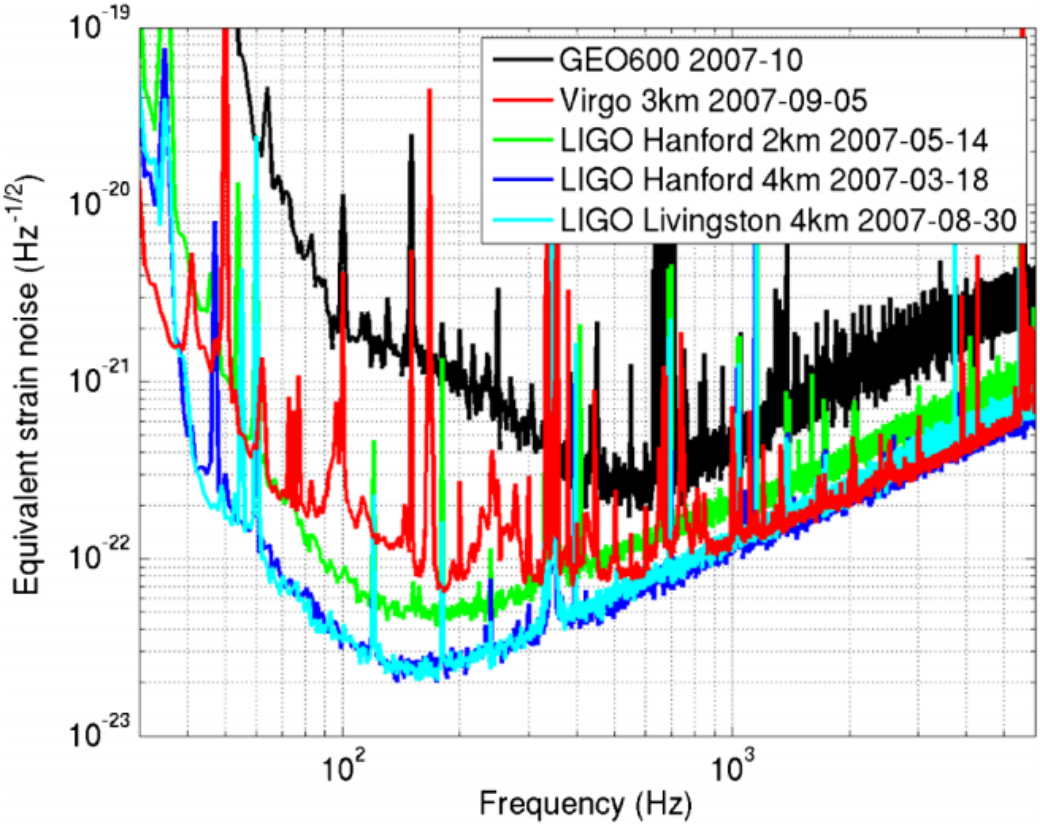

Figure 2.6: Comparison of detector sensitivities as a function of frequency (Hz) (Abadie et al., 2010a).

Detector sensitivity & orientation

The localisation of gravitational wave sources relies upon the triangulation of the signal using two or more detectors and measuring the time delay between the sites. Therefore the accuracy of the localisation is dominated by the separation distance between the two sites, as well as the timing accuracy, which for a single site is given as:

$$\sigma_t = \frac{1}{2\pi\rho\sigma_f} \tag{2.7}$$

where ρ is the signal-to-noise ratio (SNR) of the given detector and σ_f is the effective bandwidth of the signal in the detector (Abbott et al., 2016d; Fairhurst, 2014). This equation ignores many uncertainties that affect the time of arrival measurement in the detectors, but as these errors are common between all detectors they can go largely ignored and this triangulation approach is therefore a good leading order estimate for sky localisation (Abbott et al., 2016d).

With only a two-detector network this timing of arrival approach results in the source localisation being confined to an annulus on the sky, which can be split into two large ellipses if further information such as the spin degeneracy of the signal is known. However, for a triple detector network the localisation is greatly reduced and can be confined to two distinct areas on the sky where the timing of the signal at all three detectors overlap. This can also be confined further if the exact amplitude of the gravitational wave signal in each of the detectors is known, resulting in a single source localisation region on the sky (Fairhurst, 2014).

The sensitivity of each of the detectors in the network varies depending on the direction and orientation of the incoming gravitational wave signal. The detectors respond optimally to a signal coming along the z-axis, from either directly overhead (zenith) or directly underneath (nadir) the detector. As gravitational waves are polarised transverse waves (+ or $\times$) there are four regions on the sky where each detectors aren't sensitive to either polarisation, these are called nodes and they can be seen in Figure 2.7. In addition to this, the orientation of the merging system towards the Earth affects the strength of the signal seen by the detectors (Keppel, 2009). But for simplicity, the antenna patterns shown in Figure 2.7 are all modelled on a face on binary neutron star merger, which is the simplest signal to calculate because the inclination angle is zero.

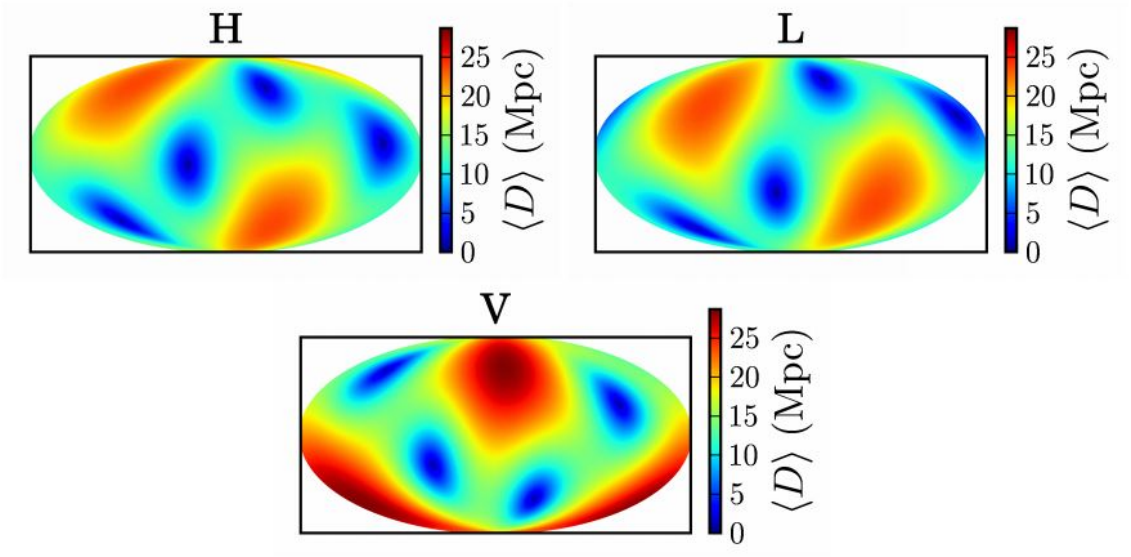

Figure 2.7: Antenna patterns for the LIGO and Virgo detectors, showing their individual blind spots due to the orientation of the interferometer arms (Keppel, 2009).

The addition of the Virgo detector (to the two LIGO detectors) reduces the size of some of these blind spots/nodes because of the location and orientation of the Virgo interferometer arms is significantly different to that of the LIGO detectors, which is evident in Figure 2.7. However, this doesn't necessarily remove the blind spots altogether as it is still necessary for two detectors to be able to see an incoming gravitational wave and therefore have overlapping sensitivity regions. A combined sensitivity map of all three detectors (HLV) is shown in Figure 2.8 where the blind spots have reduced but not disappeared.

In addition to this, the localisation accuracy across the sky varies depending on the origin of the signal. For sources lying on or close to the plane connecting the two (or even all three) detectors, the difference in the time of arrival between the sites is very small, resulting in a very poor source localisation (as shown in Figure

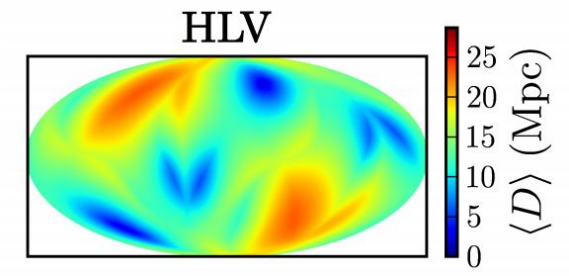

Figure 2.8: Combined antenna patterns for the LIGO and Virgo detectors, showing their combined sensitivity as a triple-detector network (Keppel, 2009).

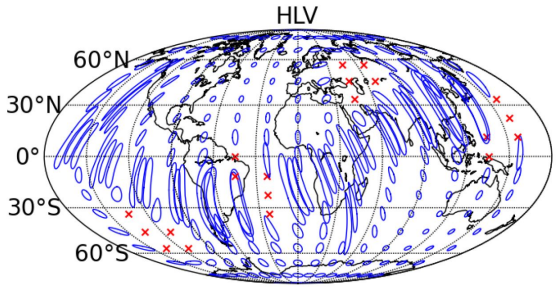

Figure 2.9: The localisation ellipses for the LIGO-Virgo 3-detector network up to 90% confidence. (Fairhurst, 2014).

2.9) (Fairhurst, 2014).

The results of the joint S5/VSR1 gravitational wave searches failed to find any plausible gravitational wave candidates but did place a more constrained upper limit on the number of burst events detectable per year in the 64-2048 Hz band at 2.0 events per year with 90% confidence (Abadie et al., 2010a). Similar results were published for the search for gravitational waves produced from compact binary inspirals, where no detections were made during S5/VSR1 (Abadie et al., 2010b).

The second joint LIGO-Virgo science run occurred in 2009 when the LIGO detector operated its sixth science run (S6) from 7$^{\text{th}}$ July 2009 to 20$^{\text{th}}$ October 2010 and Virgo operated its second and third science runs (VSR2 & VSR3) from 7$^{\text{th}}$ July 2009 to 8$^{\text{th}}$ Janury 2010 and 11$^{\text{th}}$ August to 20$^{\text{th}}$ October 2010 respectively

(Abadie et al., 2012). The total observing time was 207 days, this included 84.5 days when just the two LIGO detectors were running and 52.2 days when all three detectors were observing simultaneously; this is a 50% increase in the accumulated observation time compared to the first LIGO-Virgo run. However, the sensitivity of the detectors had remained fairly constant so it was therefore no great surprise that no candidate gravitational waves were found during this run. Nevertheless, upper limits were obtained for the rate of gravitational waves incident on the Earth, in the 64-1600 Hz band this was reduced from 2.0 to 1.3 yr^{-1} and from 2.2 to 1.4 yr^{-1} for the 1.6-5 kHz band (Abadie et al., 2012).

The fourth and final science run (VSR4) before Virgo's comprehensive upgrade lasted from 3rd June 2011 to 5th September 2011 with a down time of 19%, effectively giving 76 full days of observational data.

Date	Event
1996	Construction on 3km long interferometer began.
2000	European Gravitational Observatory is created.
2003	Construction of detector completed. Commissioning period started.
2007	First science run of Virgo (VSR1) commenced.
October 2007	First joint operation of LIGO and Virgo detectors during S5/VSR1.
7th July 2009	Virgo commenced second science run VSR2 in conjunction with LIGO S6.
8th January 2010	End of second Virgo Science Run (VSR2).
11th August 2010	Start of third Virgo Science Run (VSR3).
20th October 2010	Conclusion of VSR3 and S6 joint science runs.
3rd June 2011	The fourth Virgo science run (VSR4) commenced.
5th September 2011	Completion of VSR4 in preparation for advanced Virgo upgrades.

Table 2.1: Virgo Timeline

Another noteworthy collaboration was made between LIGO, Virgo and IceCube. This is a high energy neutrino observatory built into the Antarctic ice cap near the

South Pole. Because the strongest gravitational signals originate from cataclysmic events, such as supernovae, it is plausible to expect neutrinos to also be produced by such events, especially in the case of Gamma-ray bursts. The three observatories worked together on and off for three years between 2007 and 2010 and subsequently published their findings with no successful coincident event detections. However, they did publish an upper limit to the number of transient event sources with a GW emission energy of $10^{-2}M_{\odot}c^2$ at 150Hz and a high energy neutrino emission of 10^{51} erg to below $1.6 \times 10^{-2}Mpc^{-3}yr^{-1}$ (Aartsen et al., 2014).

2.1.6 Pulsar Timing

Pulsar timing should not be confused with long-term pulsar observations like those made by Hulse & Taylor in the 1970's and 80's (Taylor and Weisberg, 1989). Their method relied upon measuring the time-of-arrival (TOA) of the pulses from a binary pulsar (PSR 1913+16) over a period of 14 years. By analysing the initial pulses from this system they were able to determine the parameters of the system such as its orbital elements and masses of both the pulsar and companion star. Knowing these values they could make accurate predictions for the TOA of these pulses and how they would change over a long period of time, according to general relativity. Their resulting work (along with Taylor's student Weisberg) found that the orbit of this system was losing energy at a rate within 1% that predicted by Einstein's general relativity (see Figure 2.10), and therefore this was evidence that gravitational waves did indeed exist, and were responsible for radiating the gravitational energy away from the system.

The way modern pulsar timing arrays work is to observe very rapidly spinning millisecond pulsars; that rotate up to 170 times per second; and then monitor the TOA of the pulses they produce and compare them to the models to get a timing residual. As these millisecond pulsars are very stable the pulses they emit can be

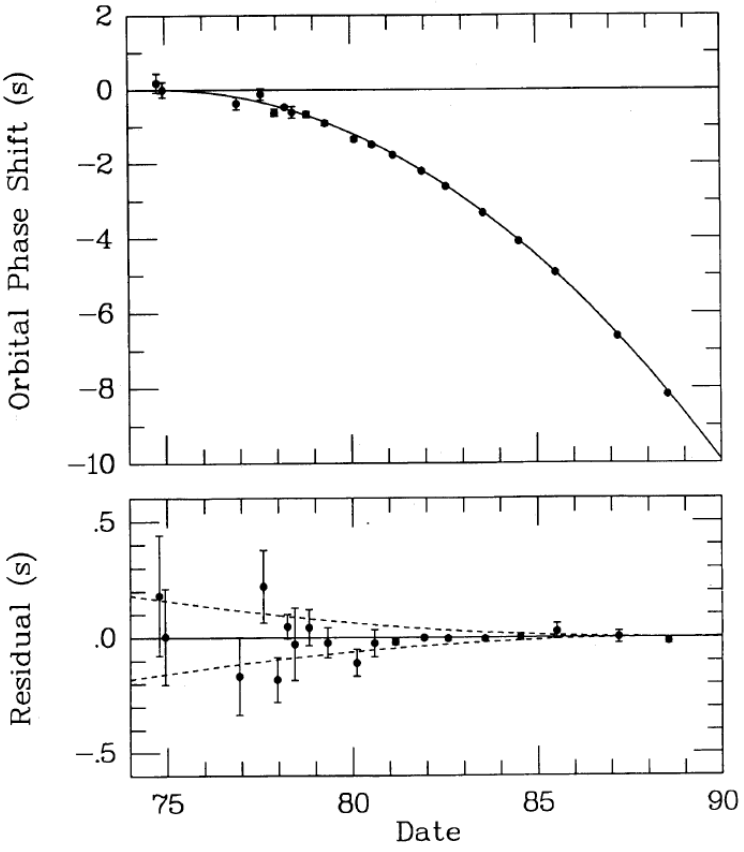

Figure 2.10: Orbital decay of the binary pulsar PSR 1913+16, as measured by pulsar timing techniques (Taylor and Weisberg, 1989).

modelled precisely so that any slight deviation of the received pulse TOA from the expected TOA can be recorded. As general relativity predicts that space-time should stretch and squash as a gravitational wave passes through, the pulses received from these pulsars should arrive ever so slightly later or sooner at the pulsar timing array (Hobbs et al., 2010).

The arrays themselves are made up from the largest radio telescopes in the world: the Parkes Pulsar Timing Array (PPTA) in Australia uses the 64m Parkes radio telescope, the North American Nanohertz Observatory for Gravitational Waves (NANOGrav) uses the 100m Green Bank telescope in West Virginia and the 305m

Arecibo telescope in Puerto Rico and the European Pulsar Timing Array (EPTA) uses the 76m Lovell telescope in the UK and 100m Effelsberg telescope in Germany. Together these three collaborations come under the umbrella of the International Pulsar Timing Array (IPTA) which, like the LVC of interferometers, brings together the research efforts of these three projects and allows them to share valuable knowledge while sharing the same ultimate aim of detecting gravitational waves (Hobbs et al., 2010).

Pulsar timing is not a direct competition with interferometers because they are not expecting to be able to detect gravitational waves emanating from compact binary mergers, instead they are looking to probe a much lower frequency range (see Figure 2.11) where the stochastic gravitational wave background is expected to exist (Hobbs et al., 2010, 2009).

This illustration in Figure 2.11 has not been updated since the Advance LIGO upgrades, however it does show a comparison between the different frequency regimes that the three distinct detector types are able to monitor. These three types include: pulsar timing arrays, space based interferometers (such as LISA) and ground based interferometers (such as LIGO). As shown in this figure, these pulsar timing arrays will be able to probe the ultra-low frequency (10^{-9} to 10^{-8} Hz) range for gravitational wave signals, and within this range there are expected to be gravitational waves emanating from super-massive black hole mergers and the stochastic gravitational wave background.

There is also the possibility of joint operations between the three different types of detectors. For example, if there was a binary black-hole system initially detected by LISA in the coalescence phase, this could be followed into higher frequencies before being detected by a ground based interferometer such as LIGO. This is significant for two reasons: firstly it could mean scientists are alerted to the impending merger sooner and secondly it would add to the total detection statistics so if a

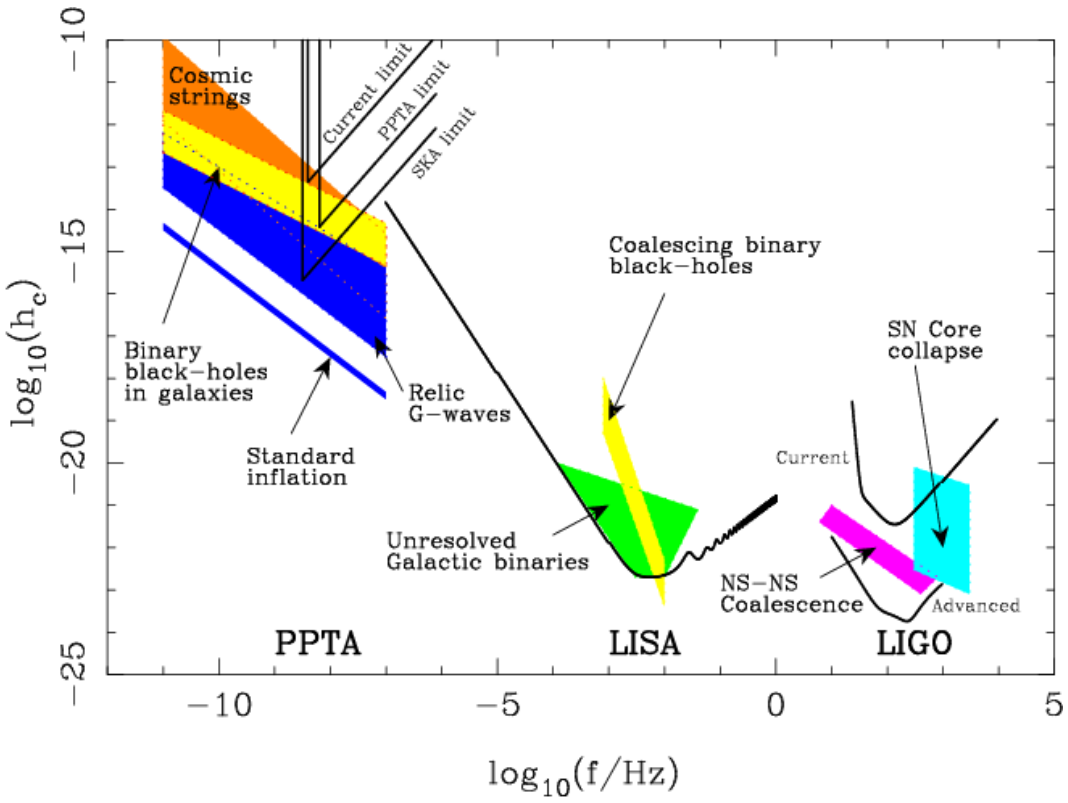

Figure 2.11: An illustration of the characteristic strain sensitivity probed by different types of detectors as a function of gravitational wave frequency (Hobbs, 2011).

weak detection is made in one detector, then the addition of data from another detector could increase the statistical significance of the detection enough to make it a confirmed 5 sigma detection.

As seen in Figure 2.11 there were several sources of gravitational waves illustrated; however, the most significant ones for current detectors and this project are compact binary mergers. That is why they will be discussed more in the next section, with particular attention on what type of electromagnetic counterparts might be associated with them.

2.1.7 Gravitational Waves detections 2015-present

The first confirmed detection of gravitational waves was made by Abbott et al. (2016b) when they announced the detection of gravitational waves from a binary black hole merger. The discovery itself was made on the 14$^{\text{th}}$ September 2015 during an engineering phase of both LIGO detectors. The signal detected had a strain of 10^{-21} and a frequency rising from 35-250 Hz, this occurred in the most sensitive range of the LIGO detectors which is between 100 Hz and 300 Hz (The LIGO Scientific Collaboration and The Virgo Collaboration, 2016). The signal was first seen at the Livingston detector (L1) and $6.9^{+0.5}_{-0.4} ms$ later at the Hanford detector (H1), with the signal lasting approximately 0.2 seconds (Figure 2.12).

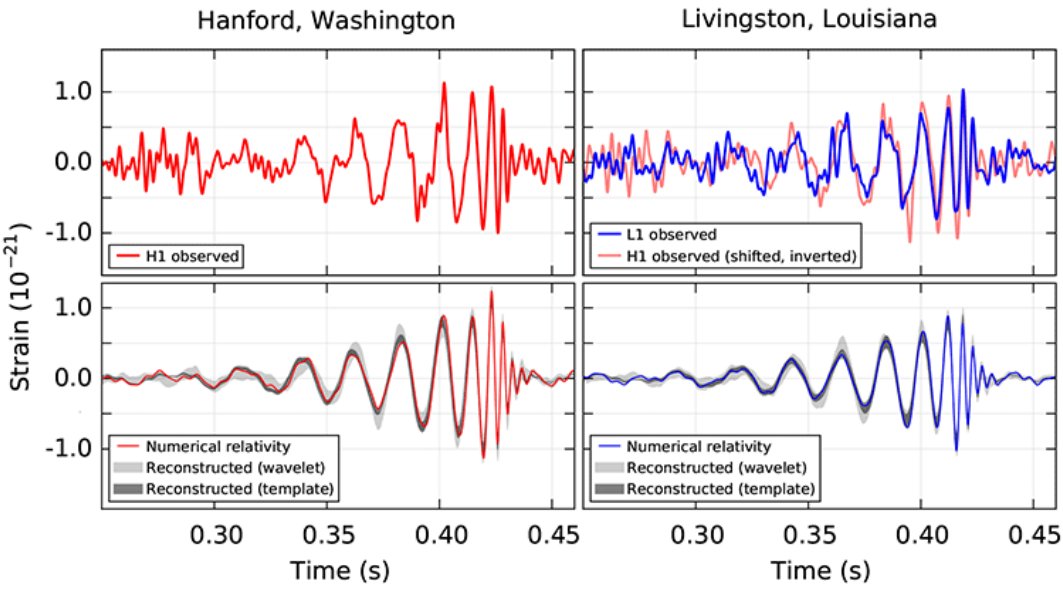

Figure 2.12: Detector strain for the event GW150914 at both LIGO sites (The LIGO Scientific Collaboration and The Virgo Collaboration, 2016).

This was one of two confirmed detections announced by LVC during O1, the other being a binary black hole merger (Abbott et al., 2016). One of the key scientific

finding from these two events was that there is a population of stellar mass black holes with masses far larger than any previously measured, which has implications for the stellar evolution models of the early universe. One of the first groups to try and simulate this was Belczynski et al. (2016) who constructed a simulation of two low metallicity main sequence stars of $96.2M_{\odot}$ & $60.2M_{\odot}$ and evolved them into two black holes with the exact masses detected by LIGO at the point of merger ($36.5M_{\odot}$ & $30.8M_{\odot}$). The model found that the most likely progenitors for the system were formed when the universe was only 2 billion years old and these progenitors had masses between 40-100 $M_{\odot}$ and metallicites around 10% of solar metallicity. The sequence of events is shown in Figure 2.13, and one of their main assumptions was that the stars collapsed directly to black holes and didn't go supernova. There are alternative models to this which don't assume direct collapse, but they generally have to increase the initial metallicity of the progenitors to account for the mass lost during a supernova (Mirabel, 2016).

After O1 the LIGO detectors were shut off for 10 months to enable planned upgrades to the detector hardware such as lasers, electronics and optics; and these modifications increased the sensitivity of the detectors by up to 25%. After a month long engineering run the LIGO detectors were ready to begin O2 observations and on the 30$^{\text{th}}$ November 2016 they transitioned from engineering mode to observation mode[1].

This second observing run (O2) of the two LIGO detectors (H1 & L1) ran from the 30$^{\text{th}}$ November 2016 up until the 25$^{\text{th}}$ August 2017 and was joined by the Virgo detector on the 1$^{\text{st}}$ August 2017. During this 9 month period the LIGO detectors collected 117 days of simultaneous observing time, and were able to detect 3 binary black hole mergers: GW170104 (Abbott et al., 2017a), GW170608 (Abbott et al., 2017b) & GW170814 (Abbott et al., 2017c) and one binary neutron star merger

[1] `https://www.ligo.org/news.php`

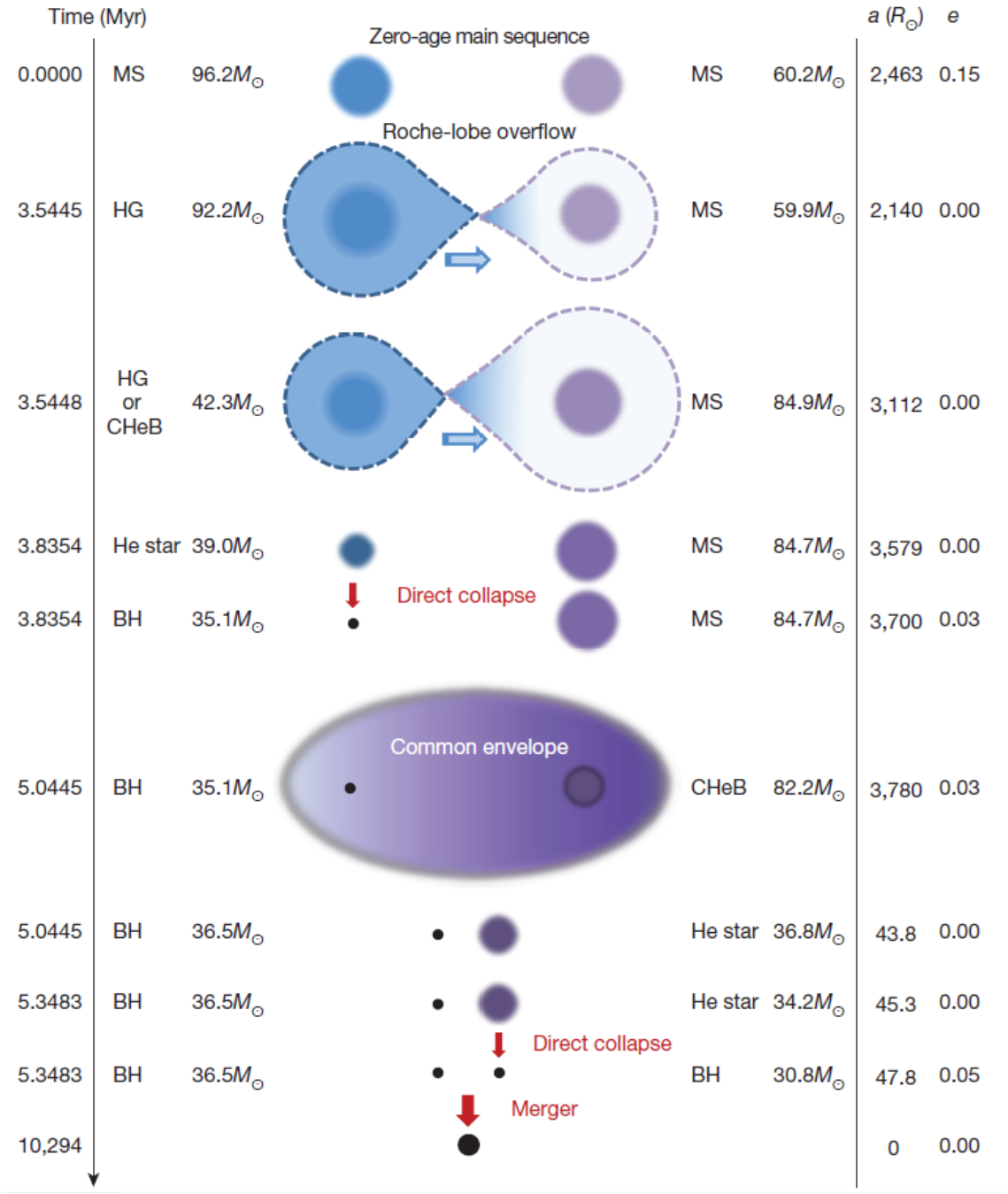

Figure 2.13: A simulation by Belczynski et al. (2016) of a massive binary star evolution that leads to a pair of Black Holes with mass similar to those belonging to the GW150914 event detected by LIGO Abbott et al. (2016b).

GW170817 (Abbott et al., 2017d). In addition to these 4 confirmed detections LIGO also released several candidate alerts for observational astronomers to follow up (Abbott et al., 2019), these are discussed in more detail in chapter 4.

The detection of a binary neutron star merger by LIGO & Virgo on the 17th August 2017 was quickly followed by independent detections of gamma-rays by the Fermi Gamma-ray Burst Monitor (Fermi-GBM) 1.7s later; and multiple detections ensuing in the optical with ground based telescopes. The combined LIGO & Virgo detections were precise enough to localise the source to an area of 31 deg^2 on the sky, and a distance of 40^{+8}_{-8} Mpc. This was a vast improvement on the original alerts from 2015 when the localisation was only 600 deg^2 at best. This improvement meant the electromagnetic (EM) follow-up partners had an easier job searching for a counterpart and it took less than 11 hours for the One-Meter, Two Hemisphere (1M2H) team to detect a new optical transient (SSS17a/AT2017gfo) on the edge of the NGC4993 galaxy (Coulter et al., 2017). Given its location within the LIGO localisation region, and given the fact that NGC4993 is $\sim$40 Mpc away (Freedman et al., 2001), this transient was widely accepted to be the one linked with the binary neutron star merger witnessed by LIGO & Virgo.

Over the course of the next two weeks over 60 more ground-based and space-based observatories followed up this transient, in every wavelength of the EM spectrum, as its colour evolved and brightness faded. This evolution, along with broad spectral features, indicated that this transient was in fact the long predicted "kilonova", which can be distinguished by their rapid reddening and fading brightness (Metzger and Berger, 2012). The exact mechanics behind this evolution will be discussed in the next subsection, along with the physical properties of kilonovae and short gamma-ray bursts.

2.1.8 EM counterparts

Firstly it's important to describe the counterparts associated with different types of compact binary mergers. Given there are only two types of compact objects currently detectable by LIGO (black holes and neutron stars) this means that there are just three distinct types of merger events that are possible: black hole-black hole (BH-BH), black hole-neutron star (BH-NS) and neutron star-neutron star (NS-NS) mergers. In the case of binary black hole (BBH) mergers there isn't expected to be any corresponding EM emission; as (Savchenko et al., 2016, p.14) explains:

> There is no theoretical work to date predicting electromagnetic emission from the coalescence of two non-charged back holes in vacuum. Indeed, it is not possible to create photons in a system with no matter outside of the gravitational horizon and only gravitational interaction involved, without invoking effects of quantum gravity, a theory which has not been developed, yet.

However, the possibility cannot be ruled out and there have been simulations made to try and recreate such a scenario where EM emission is present. One of the more elaborate scenarios proposed by Malafarina and Joshi (2016) involves a naked singularity that would be exposed for a split second after the two black holes merge, and potentially release matter onto an accretion disk around the residual black hole. But a more likely scenario would be that of an accretion disk being present around one or both of the black holes before merger, which would likely originate from an in-falling star that approached close enough to be gravitationally bound to the BBH system and get ripped apart by tidal forces. Although, due to the extremely long merger times this scenario is still very unlikely.

The other type of compact binary merger events involve at least one neutron star (NS-BH or NS-NS) and these are dissimilar to black hole mergers chiefly because

they contain baryonic matter that can interact in the visible universe[2] and emit strong electromagnetic signals during a merger event. These signals can include gamma-ray bursts, fast radio bursts and kilonovae afterglows.

Given that five out of the six confirmed gravitational waves originated from binary black hole mergers it wasn't expected that any EM counterparts would be found, yet astronomers still followed up these events in the hope of seeing something to challenge this prediction. The closest indication that BBH mergers weren't completely "dark" events came about straight after the first LIGO detection back in 2015 (GW150914) when the Fermi satellite detected a faint gamma-ray burst (GW150814-GBM) 0.4s after the merger time; however, this event had a very weak signal and it's statistical significance is a hot topic of debate (Connaughton et al., 2018). If the gamma-rays did indeed originate from the merger of two black holes then this could indicate something else is happening when these black holes merge, but only time will tell if this was a one off coincidence or the first of many examples where BBH mergers are accompanied by a short burst of gamma-rays.

The discovery of the binary neutron star merger (GW170817) and its EM counterpart (AT2017gfo) in 2017 has transformed the field of EM counterparts from theory to observation overnight. However, it is still important to consider the theoretical models of these merger events because we cannot view or examine these objects up close, and must rely on computational models to fit the observational data before we can learn anything about the physical processes going on. These merger events have two separate physical processes associated with them; resulting in two separate EM counterparts, namely Short Gamma-ray Bursts and Kilonovae, but depending on viewing angle and time since merger they wont both always be seen.

[2]In this context the visible universe is any part of the physical universe that exists outside the event horizon of a black hole.

Short Gamma-ray Bursts

Short Gamma-ray Bursts (SGRBs) are very short (under 2 seconds) bursts of high energy gamma-radiation. They are powered by accretion onto a central compact object, and produce highly relativistic collimated jets flowing out the poles of the central object. These jets have a very narrow opening angle so they can only be observed when the observer is looking top down into the jet. This directional dependence lowers the detection probability of these SGRB's as they cannot be seen at every inclination, although the recent detection of GRB 170817A challenges this "top hat" model and suggests fainter off-axis observations might be possible (Goldstein et al., 2017b).

Observations of SGRBs are characterised by a bright powerful flash of gamma-ray radiation; followed by a fading afterglow which fades through the different bands of the EM spectrum from X-ray to radio (D'Avanzo, 2015). This afterglow alone can be used to indicate the presence of a BNS merger event even if the initial SGRB was missed; or more likely because it wasn't directed towards Earth due to the narrow beaming effect. However the afterglow itself is still significantly beamed, covering as little as 10% of the sky, so the detection probability is still heavily dependent on the viewing angle (Metzger and Berger, 2012).

The physical processes powering the optical afterglow is believed to be caused by a relativistic outflow from the SGRB powering through the surrounding circumburst environment and creating a forward shock. This shocked material then produces synchrotron radiation, leading to an optical afterglow that lasts for a few minutes. In addition to this there is a reverse shock which produces an "optical flash" when it interacts with the ejecta but this only lasts for tens of seconds (Granot, 2007).

Kilonovae

The second optical counterpart that is associated with these neutron star merger events is known as a kilonova. The name comes about because these events are up to a thousand times brighter than ordinary novae outbursts, but not as luminous as supernovae. They are produced when the neutron-rich ejecta from these neutron star mergers undergoes rapid neutron capture (r-process) nucleosynthesis to produce neutron rich heavy elements such as gold and platinum (Metzger, 2017). Even though the r-process only lasts a few seconds, it produces enough radioactive heavy elements that can sustain nuclear fission and beta decay for a much longer period ($\sim$ days), resulting in a bright optical/near infrared emission once the opacity drops enough for photons to escape, this is what powers the kilonovae (Tanaka, 2016). Unlike the SGRB afterglow, kilonovae are both isotropic and independent of the density of the circumburst environment, so they are expected to be visible in every instance where there has been a merger of one or two neutron stars in a binary (Chu et al., 2016). However, as recent observations and theoretical models have shown, this isotropy might not necessarily equate to monochromatic emission. The exact composition of the radioactive heavy elements produced in a merger is uncertain, which led to many differing views on what colours, durations and even luminosities to expect from a kilonova (Arcavi et al., 2017). Although, there has now been the first confirmed kilonova detection associated with a neutron star merger, it will require many more discoveries before anything can be said about the nature of these objects and their population as a whole.

In his review of kilonovae Metzger (2017) goes on to discuss the prospects of a twofold kilonova involving strong blue emission at early times ($\sim$ hrs) caused by lanthanide-free emission, and a more traditional redder kilonovae at later times due to high-opacity neutron rich lanthanides being present, as shown in Figure 2.14. The behaviour of AT2017gfo seems to suggest that it was dominated by this "blue

kilonova" process at early times, which according to Metzgers models is indicative of a NS-NS merger observed towards the polar regions. This also agrees with the weak Gamma-ray observations made with Fermi, which is evidence of an off-axis GRB viewed at an angle closer to the pole than the equator (Goldstein et al., 2017b).

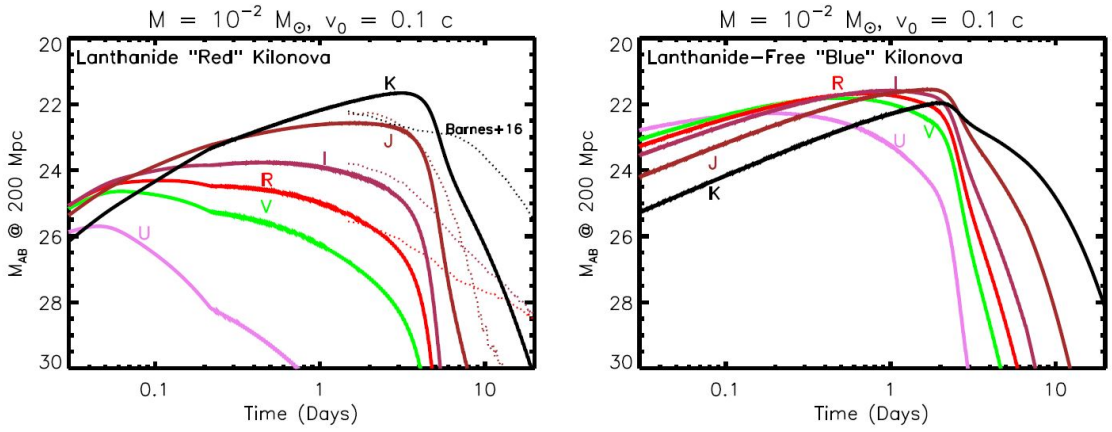

Figure 2.14: "Red" & "blue" kilonova light curves, caused by the difference in abundance of the heavy lanthanide elements (Metzger, 2017).

The behaviour of a single kilonova cannot be used to generalise the entire object class, many more events will need to be observed to build up a significant population database before anything substantial can be inferred about them. Nevertheless, the detection and subsequent observations of AT2017gfo have shown that although some of the behaviour was unexpected, the general pattern that the evolving transient followed was close to what had been predicted for many years previously.

To summarise, there is a combination of EM counterparts that could accompany a binary neutron star or black hole-neutron star merger, with the biggest constraint on observability, after distance, being the inclination angle of the binary towards the observer. But with low-latency high-precision gravitational wave searches and high cadence large survey telescopes, it should be possible to at least observe some if not all of these counterparts every time. An illustration of where these different

counterparts are produced in relation to the post-merger compact object is shown in Figure 2.15, with the central compact object labelled as (BH) and surrounding that the different EM emission mechanisms.

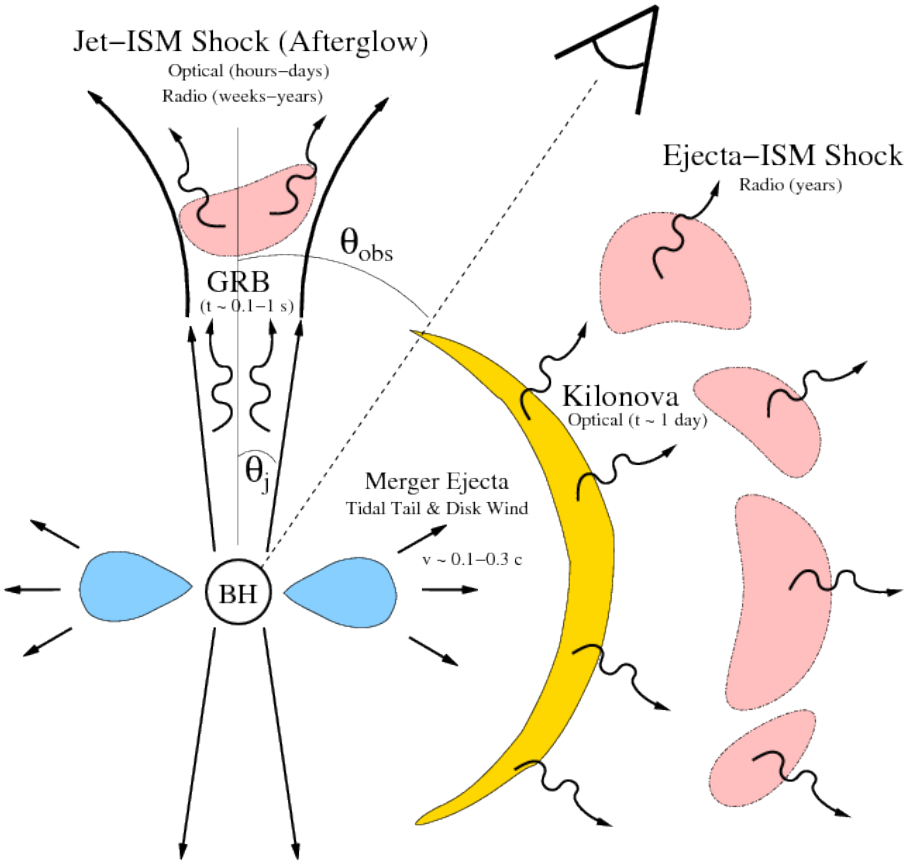

Figure 2.15: An illustration of the potential EM counterparts emanating from a post-merger compact object (Metzger and Berger, 2012).

The topic of discussion now moves on to the other half of this thesis work to do with Luminous Blue Variable stars, and massive stars in general. The background to this work is set out in the following section.

2.2 Massive stars

The distinction between what qualifies as a high mass star and a low mass star is the fate of the star at the end of its life. The vast majority of stars are low mass stars ($< 8M_{\odot}$) that live uneventful lives and culminate with a similarly unremarkable death, ending up as an electron degenerate core known as a white dwarf. However, for the 1% of stars that have an initial mass $> 8M_{\odot}$ there is a wider range of evolutionary paths they could follow, and thus a broader ranger of stellar phenomena. For massive stars with initial masses $> 8M_{\odot}$ they will develop an iron core large enough to collapse past the Chandraskhar limit for a white dwarf and explode in a supernova (Woosley et al., 2002). There are several types of supernova and these are classified by their spectral lines and photometric behaviour rather than the physical processes behind those features. These supernovae explosions can be responsible for triggering star formation in nearby molecular clouds and therefore creating a new generation of stars; a study by Boss and Keiser (2010) into radioactive isotopes in the solar system concluded that it was likely our Sun was formed as a consequence of a supernova explosion of a nearby star. Given the short lifespans of these massive stars, they have less time to move away from their formation region and so when they go supernova they would do so in close proximity to their birthplace. Therefore, massive stars, and by extension supernovae, play a crucial part in the star formation processes within galaxies.

The proportion of massive stars being created in a galaxy is determined by the initial mass function (IMF) and for the Milky Way the most commonly used one has been the Salpeter IMF (Salpeter, 1955) which gives a value of around 1% (Crowther, 2012). The overall lifetimes of massive stars are very short ($\sim 5 - 20$Myr) due to their high luminosities (driven by high fusion rates in the core) and mass loss rates (powered by strong stellar winds); therefore, their death rate is comparable to their birth rate of the IMF. This makes them very rare objects in the galaxy; however, they

are among the most important stars in any galaxy due to their powerful stellar winds and chemical composition which help to influence the dynamics and composition of the interstellar medium (ISM) (Crowther, 2004).

The majority of massive stars form in a cluster within a molecular cloud, sometimes referred to as a star forming nebula, such as the Orion Nebula; and as the distribution of star formation follows a power law, this requires a cluster mass large enough to produce a full spectrum of stellar masses all the way up to $> 8M_{\odot}$ and beyond. Therefore, it is very difficult for low mass star clusters ($\sim 100M_{\odot}$) to form massive stars, instead it requires much larger cluster masses, such as the Orion Nebula Cluster which is $\sim 2000M_{\odot}$ and has formed stars up to $\sim 40M_{\odot}$ (Crowther, 2012). As a result of their short lifespan and high fusion rates, massive stars are important inhabitants of molecular clouds as they can enrich the environment with metals such as oxygen and carbon which enables stars to form with higher metallicities in the future. This is magnified by the fact that when these stars explode as supernova they produce even more elements (heavier than iron), further enriching the surrounding environment.

One of the defining characteristics of massive stars are their high bolometric luminosities, this is because the luminosity of a star increases proportionally to the mass; this is called the mass-luminosity relation and it scales to the power 3 for low mass stars and 1.3 for high mass stars (Crowther, 2012), with the crossover point around $40M_{\odot}$. For example, an O type star that is 20 times more massive than the Sun, would be approximately 10,000 times more luminous. As a result, they are a predominant source of light within galaxies, even though they are very few and far between. They emit most of their radiation in the ultraviolet part of the spectrum, but this also heats up dust that re-emits the light in the far-IR, making them the dominant source of light at these wavelengths in galaxies (Maeder and Conti, 1994). In addition to this, the ultraviolet radiation they emit is ionising,

resulting in the ionisation of gas in the surrounding circumstellar environment. This also links back to how they can affect the composition of the ISM in their immediate vicinity, especially in close proximity to a hydrogen nebula, resulting in H II regions (Crowther, 2004); these can thus be used as a tracer for massive star formation within a molecular cloud.

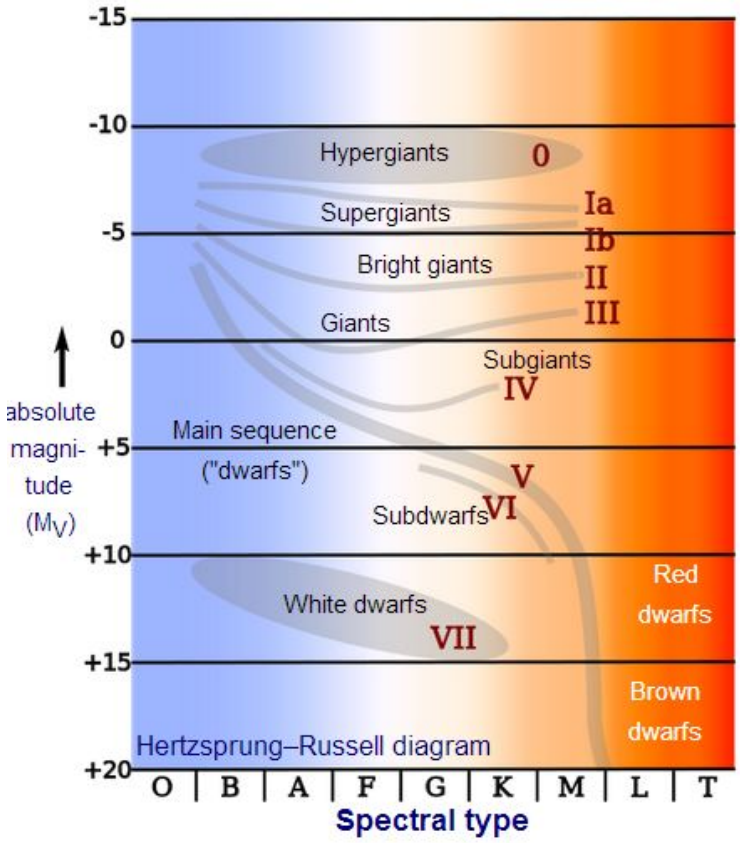

Figure 2.16: Illustration of the Hertzsprung-Russell diagram with the Harvard Spectral Classification scale and Morgan-Keenan luminosity class. Image Credit: Wikipedia/Spacepotato

Figure 2.16 shows the Hertzsprung-Russell diagram, with absolute magnitude along the y-axis and spectral type along the x-axis. This spectral type is defined

by the Harvard Spectral Classification scale, and this classifies stars based on their surface temperature. Main-sequence massive stars are classified as either B-type or O-type stars with effective temperatures of between 10,000-30,000 K and >30,000 K respectively. However, this doesn't distinguish between main-sequence stars and post-MS supergiants very well as it can't differentiate between stars of similar temperature but different luminosities, so to distinguish between them and other stages of evolution the Morgan-Keenan luminosity class is used as well. This is labelled with Roman numerals from I-V, and this can also be seen in Figure 2.16 where the main-sequence stars assigned a luminosity class of V, sub-giants are assigned IV and giants are given I-III depending on their luminosity. With the brightest supergiants assigned the classification of I. O-type stars for example, are the hottest Hydrogen fusing and most luminous stars in the galaxy, but also the rarest.

There are several unique categories of massive stars that are defined by their behaviour and appearance but also what evolutionary stage they are at. These include: OB stars, yellow supergiants (YSGs), red supergiants (RSGs), Wolf-Rayet stars (WR) and Luminous Blue Variables (LBVs); these will all be discussed in the next subsection.

2.2.1 Evolution sequence

Massive stars begin life on the Main Sequence (MS) as an O or B-type star (collectively referred to as OB star) by fusing hydrogen into helium, but at a much quicker rate than their low mass cousins, which results in their rapid evolution. This core fusion is dominated by a process called the CNO cycle which fuses hydrogen at a much faster rate than the proton-proton chain by using carbon, nitrogen and oxygen as catalysts in the reaction (see Figure 2.17). The p-p chain reaction still occurs in massive stars, but the CNO cycle begins to dominate the energy production of MS stars with a mass greater than $\sim 1.3 M_{\odot}$ or when the core temperature reaches

$\sim 1.7 \times 10^7 K$ (Arnett, 1996).

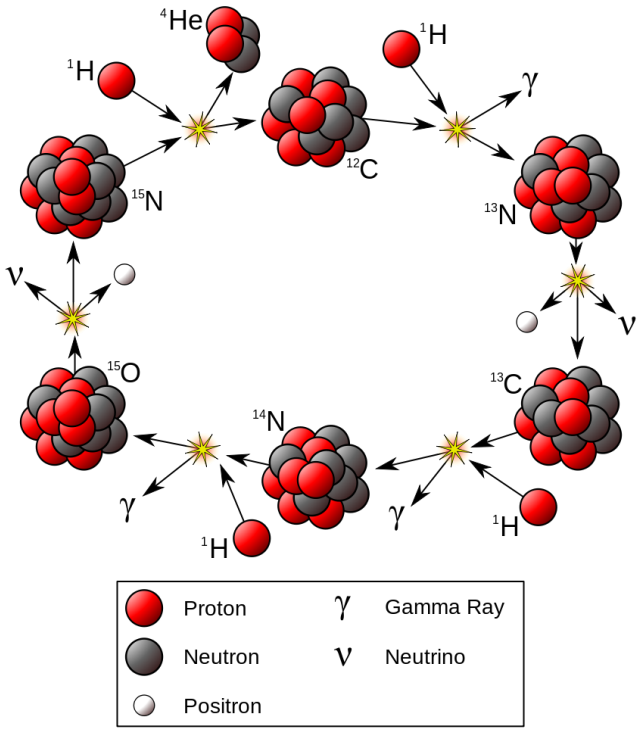

Figure 2.17: Illustration of the CNO cycle in main-sequence stars converting Hydrogen to Helium. Image Credit: Wikipedia/Borb

The main consequence of the CNO cycle is that it releases energy at a much higher rate than the p-p chain and this leads to the formation of convective zones in the core that can distribute the energy more efficiently than radiative zones, and in the most massive stars these convective zones can reach all the way to the surface (Salaris and Cassisi, 2005). This has further implications for the evolution of massive stars because it effects the metallicity in the outer atmosphere of the star.

In addition to the initial mass of a star, there are several parameters that determine the evolution of a massive star, these include: metallicity, rotation rate and binarity (Groh et al., 2014). Aside from the initial mass, which has already been shown to have a significant affect on the luminosity and energy production of a star,

the metallicity is the second most important factor dictating the evolutionary path of a star and hence why these deep convective zones are an important factor.

The metallicity of a star is depicted by the mass fraction of metals (taken as all elements more massive than helium) within the star, usually denoted by the letter Z, with hydrogen (X) and helium (Y) making up the rest of the mass fraction calculation. For example, the surface metallicity mass fraction of the Sun is 0.0134 (Asplund et al., 2009) which is often used as a standard unit of metallicity by astronomers for comparison along with solar mass and solar luminosity. But in addition to this, chemical abundance ratios are also used as a measure of the metal abundance within stars, and this typically involves the ratio of iron to hydrogen:

$$[Fe/H] = \log_{10}\left(\frac{N_{Fe}}{N_H}\right)_* - \log_{10}\left(\frac{N_{Fe}}{N_H}\right)_\odot \tag{2.8}$$

The effects of metallicity on evolution will be seen more in the subsection on Wolf-Rayets, where the strong stellar winds are more sensitive to changes in the opacity of the atmosphere, and the effects of rotation will also be discussed in the following subsection. But as for binarity, up to 70% of massive stars exist in binaries (Sana et al., 2012) with a strong preference for close in systems with orbital periods of the order a few days (de Mink et al., 2014). Simulations by de Mink et al. (2014) estimated that up to 30% of massive stars are involved in binary interactions, which includes 8% that are the products of mergers (see Figure 2.18). This significantly effects both the evolutionary path and ultimate fate of both stars in the system.

The binary interactions can be broken down into three different types, as shown in Figure 2.18; the mergers of a massive star with its binary companion has the largest effect of all on the evolution. The products of these mergers usually have extended lifetimes as they are revitalised by fresh fuel being injected as a result of merging with the companion. The other main type of interaction involves mass-transfer by which the companion star starts stripping the massive host star of material; this is known as Roche lobe overflow and occurs when one star fills its Roche

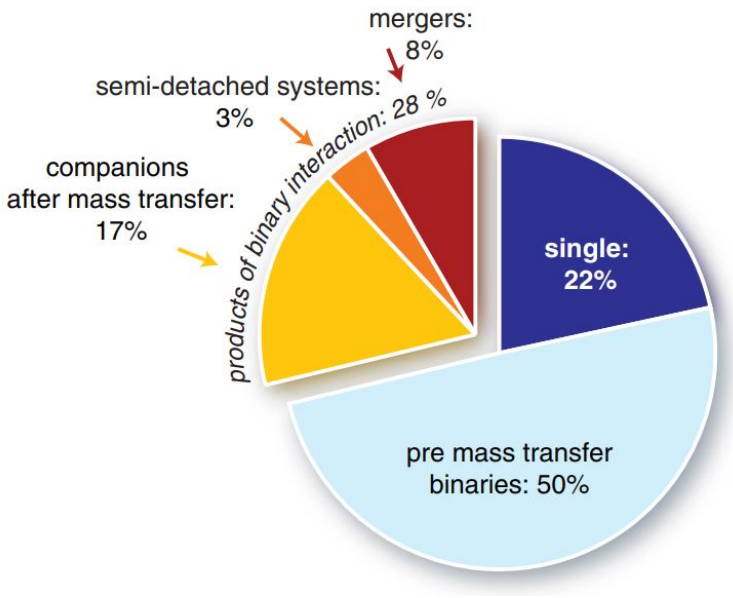

Figure 2.18: Pie chart showing the percentages of interactions for massive stars in simulations by de Mink et al. (2014).

lobe (Morris, 1994). This is the teardrop-shaped region around a star that is defined by the space within which material is bound to the star by gravity.

This mass transfer can become more pronounced as they cool and expand after they leave the main-sequence, because they would begin to expand into the orbit of their companion star which in turn could begin stripping the outer layers of the host star via mass-transfer (Sana et al., 2012). The effects of binarity on a massive star's evolution are significant but not as important as the initial mass or metallicity because they do not occur in all massive stars.

A star reaches the end of the main sequence once it has exhausted most of its hydrogen fuel and begins the fusion of helium in its core. This is called the main-sequence turn off point and is characterised on the H-R diagram by a turn towards cooler temperatures (denoted by the black dashed line in Figure 2.19). This is a result of the increased power output of the core by switching from hydrogen to

helium as the primary source of fuel, and the onset of hydrogen shell burning on top of this, resulting in the outer layers of the star expanding and cooling.

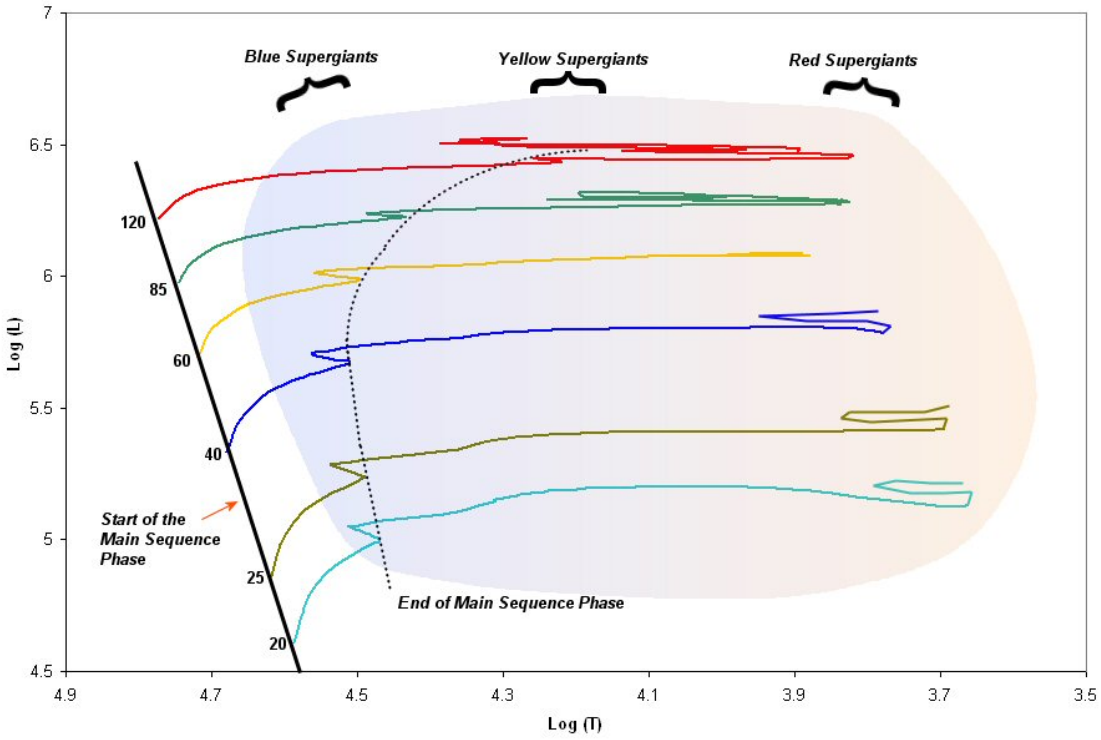

Figure 2.19: Hertzsprung-Russel diagram highlighting the three supergiant phases as a massive star moves off the main sequence. Image Credit: Siobahn Morgan.

Red Supergiants

Post-MS massive stars ($8-40M_{\odot}$) typically evolve into red supergiants (RSG), in the case of extremely high mass stars ($> 40M_{\odot}$) they can evolve directly into Luminous Blue Variables, as shown later. During the transition across the H-R diagram from the hot blue end of the MS to the cooler red section, these massive stars will pass through a yellow supergiant (YSG) phase. This is typically only a few thousands to tens of thousands of years long and therefore these stars are extremely rare (Massey,

2013); however, as their flux peaks at visible wavelengths these stars are among the most visibly brightest in the galaxy. Once these stars cool and expand in size they reach the red end of the H-R diagram where they are classed as red supergiants (RSG). They are named as such because of their red appearance and large size as a result of an expanded envelope. RSG's are powered by helium fusion in the core, but it is still uncertain where along the post-MS evolution this begins.

What happens to these stars next is mainly dependent on their mass loss rates, which is governed by the strength of the stellar winds; the quicker they loose mass, the more likely they are to evolve "backwards" along the H-R diagram and re-enter the YSG phase. This can be seen in Figure 2.20 where Ekström et al. (2012) generated evolutionary tracks for 24 stellar models of varying mass; and not only is there a visible reversal of temperature for stars over $25M_{\odot}$, but for the most massive stars in the simulations ($> 50M_{\odot}$) they never even reach the RSG phase at all. This is due to their extreme mass loss rates which are associated with Wolf-Rayet stars and Luminous Blue Variables.

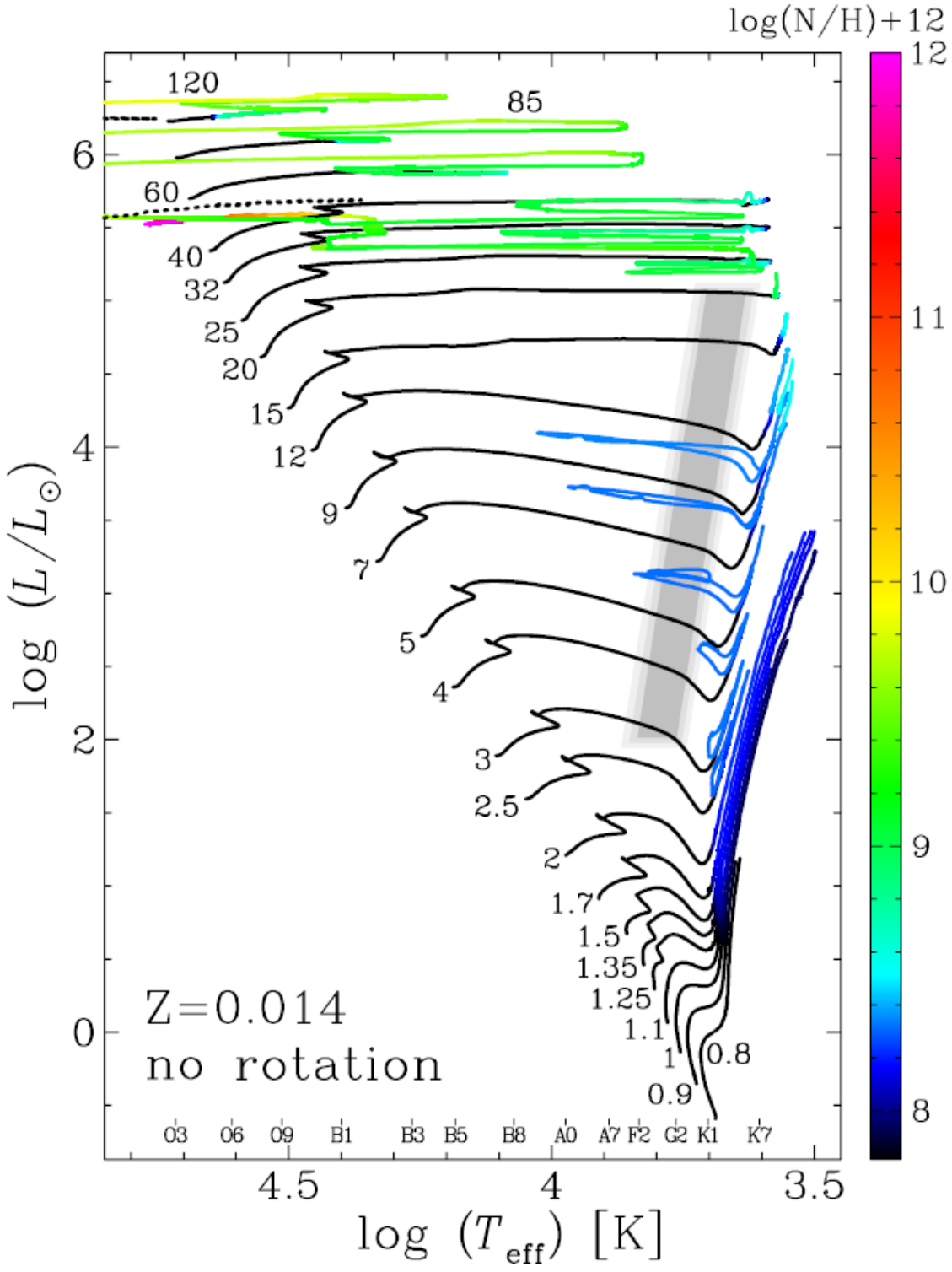

Figure 2.20: HR diagram containing evolutionary tracks of 24 non-rotating stellar models, with a clear shift in evolutionary behaviour above $40 M_{\odot}$ (Ekström et al., 2012).

As will be shown shortly in the Wolf-Rayet & Luminous Blue Variable phases of evolution, the mass loss rate of a massive star is governed largely by its metallicity, which significantly impacts its evolution. However, another factor to consider is the rotation of the stars, as some B[e] supergiants have been observed to have non-spherical winds caused by strong rotation (Lamers, 2013). These are slightly different from classical B[e] stars (Rivinius et al., 2013) undergoing rapid rotation and producing Keplerian disks, because supergiant B[e] stars produce an outflowing disk instead(Lamers, 2013).

The modelling of stellar winds by including rotation is very complex and therefore the majority of stellar evolution models use simplified non-rotating models. But when rotation is taken into consideration in the models, it is found that in general stars with lower initial masses ($20 - 25 M_{\odot}$) can begin to evolve backwards towards hotter temperatures. The evolution tracks produced by Ekström et al. (2012) shown in Figure 2.21 show the effects rotation has on the evolution of massive stars when compared to their non-rotating counterparts in Figure 2.20. This is primarily caused by the rotation feeding the core with fresh hydrogen fuel and allowing it to extend its lifetime on the Main Sequence by up to 25%.

In addition to this, rotation also causes enhanced mass loss by enriching the surface metallicity (Hirschi et al., 2004). This is because the same mixing processes that feeds fresh fuel to the core also brings up heavier fusion products to the surface and this has a knock on effect on the mass loss rates as will be shown in the following subsection on Wolf-Rayet stars.

Wolf-Rayets

Wolf-Rayet (WR) stars are evolved massive stars that have had their outer hydrogen layers stripped away by stellar winds and also by potentially going through an LBV phase. This exposes the hydrogen fusion products such as helium and nitrogen which

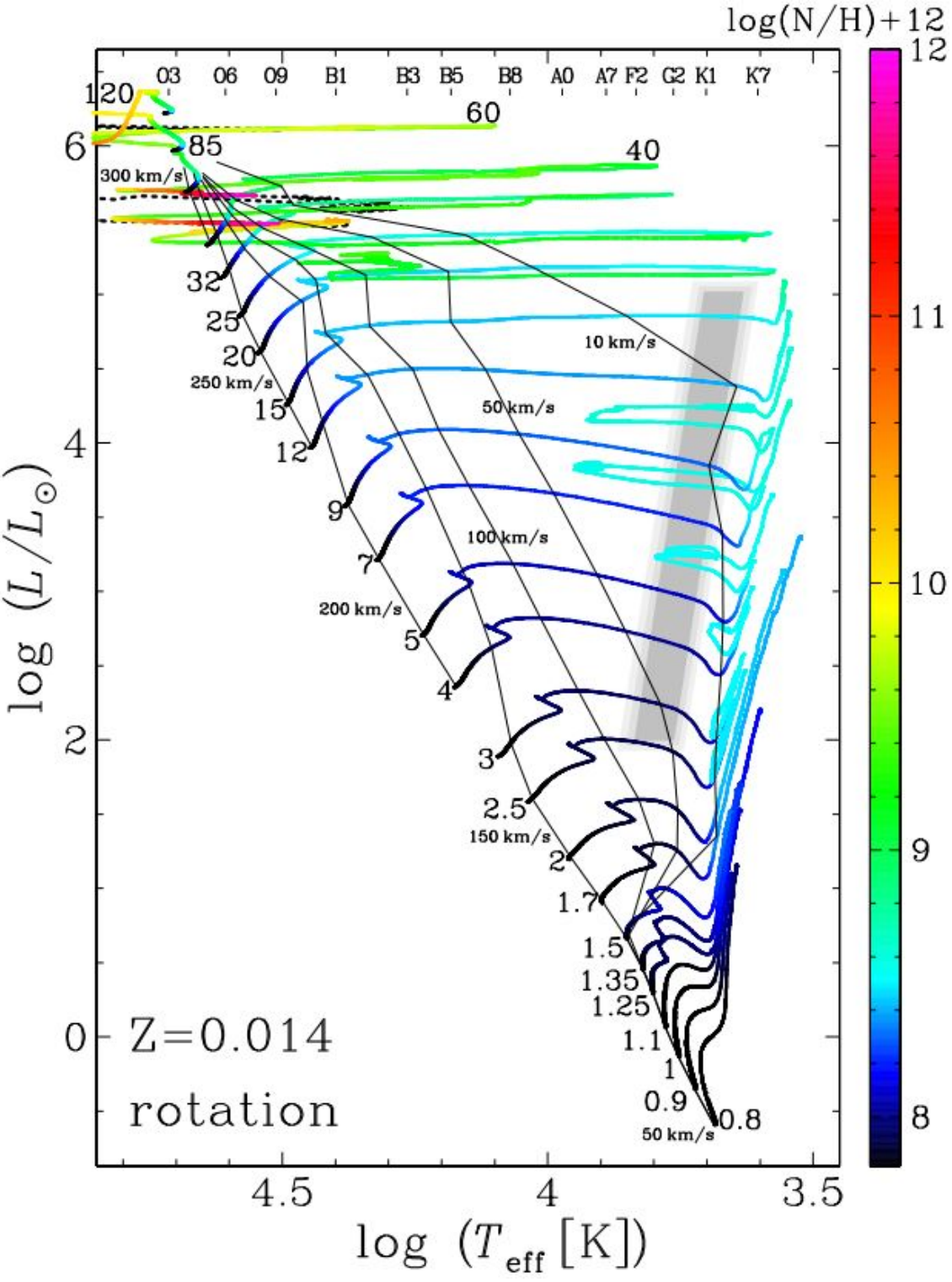

Figure 2.21: HR diagram containing evolutionary tracks of 24 rotating stellar models (Ekström et al., 2012).

can be seen as strong emission lines in the spectra of these stars; these are classified as WN-type Wolf-Rayet stars because their spectra is dominated by nitrogen. As these stars continue to loose mass via strong stellar winds, they eventually expose more of the core elements, such as carbon and oxygen. This can again be identified in the spectra with strong emission lines; stars with dominant carbon lines are designated WC-type Wolf-Rayet stars. Where oxygen lines dominate the spectra these can be classified as WO-type Wolf-Rayets (Massey, 2013); however, these are rare and very few have been identified.

WRs have very high mass-loss rates driven by strong stellar winds, but the exact mass-loss rates are still highly uncertain, due in part to the optically thick winds and circumstellar material that prevents astronomers from penetrating through to observe the stellar core. However, recent advances in sub-mm observatories, such as ALMA, have enabled astronomers to probe deeper into the galacitc plane and observe stellar mass loss rates of massive stars, such as those of the Westerlund 1 cluster by Fenech et al. (2018).

Another problem with studying WRs in the past has been due to the rarity of these stars prohibiting the usual technique of studying an entire stellar population born at the same time in a cluster, this was because there were so few massive stars that covered a wide enough range of masses. However, recent studies of the Scutum-Crux arm by Rosslowe and Crowther (2018) and the Arches cluster by Clark et al. (2018) have been able to utilise the low extinction in the near-IR to study a significant number of massive stars within each young cluster. This is important because as all the stars formed in the cluster at approximately the same time it means that their co-evolution can be studied in detail and their evolutionary progression mapped out. Furthermore, Fenech et al. (2018) were able to confirm that there is a significant increase in mass-loss rates as massive stars transition from OB supergiants to WRs by either an LBV and/or cool hypergiant phases.

The mass loss rates of WR are about 10 times higher than OB stars of similar luminosity on the main-sequence (Massey, 2013), but this varies significantly depending on a number of contributing factors. As these stellar winds are powered by line interaction, the spectral line opacity is the key factor in determining the radiation pressure of a star, and thus the mass-loss rates.

Line driven winds involve the absorption and rapid emission of a photon by a bound electron in an ionised atom. The energy of the individual photon must match that of the energy level of the atomic transition to excite the electron to a higher level momentarily. Once this electron is de-excited it re-emits a photon and results in a net transfer of momentum in the radial direction that causes the gas to expand, dragging other particles with it (Muijres, 2010). The net result of this process throughout the entire star is the creation of a stellar wind that flows radially out from the star.

The opacity of a star is governed by the number of possible absorption lines which in turn is determined by the chemical composition of the stellar atmosphere (metallicity). Therefore stars with an increased metallicity will have higher opacities and consequently higher mass-loss rates than equivalent stars of lower metallicity. The surface metallicity of these stars is a combination of their initial metallicity (from the composition of the nebula they originated from) and core fusion products dredged up by deep convection layers in the star; and as shown previously, this can be accelerated by the rapid rotation of the star. Nugis and Lamers (2000) use this surface metallicity in their mass-loss rate equation to describe the effect luminosity & metallicity have on mass-loss rates of massive stars, this is given as:

$$\log \dot{M} = -11.0 + 1.29 \log \left(\frac{L}{L_{\odot}} \right) + 1.7 \log Y + 0.5 \log Z \tag{2.9}$$

where $\dot{M}$ is the empirical mass-loss rate and Y & Z represent the surface mass fractions for helium and metals respectively. Although this rate can be applied to

any type of WR star it should be noted that this relationship was derived from a sample of Galactic WR stars.

2.2.2 Luminous Blue Variables

The final category of massive stars, with the highest known mass-loss rates of any star, are Luminous Blue Variables (LBV). These stars are characterised by their high luminosity and photometric & spectroscopic variability, which includes undergoing periodic outbursts of intense mass-loss (Humphreys and Davidson, 1994). The current understanding is that for stars with initial masses of around $20 - 25 M_{\odot}$ LBVs are the final stage of evolution after the WR phase, before going supernova (Groh et al., 2013). However, for more massive stars ($> 30 - 40 M_{\odot}$) simulations have shown that they can form directly from, or just at the end of, the main-sequence. This is because as their temperature cools, the opacity of the lines increases and for very massive stars this results in the radiation pressure increasing beyond the force of gravity which is when high mass loss rates occur (Massey, 2013), stripping the star of its outer hydrogen layers and revealing some of the nuclear processed layers underneath.

Luminous Blue Variables are distinct from Wolf-Rayet for a number of reasons. Firstly, they are less evolved stars and so are observed with higher hydrogen abundances, but their main distinction is that they have been observed to violate the Humphreys-Davidson limit (see Figure 2.22) during their "eruption" phase and release up to $10^{-2} M_{\odot}\ yr^{-1}$ compared to mass loss rates of $10^{-5} - 10^{-6} M_{\odot}\ yr^{-1}$ expected for O-type main-sequence stars (with mass loss rates typically an order of magnitude lower again for solar mass sized stars). These eruptions are photometrically characterised by a dip in apparent temperature (see Figure 2.22), from around 12,000-30,000K down to 7,000-8,000K (Humphreys and Davidson, 1994), and an increase in visual luminosity of up to two magnitudes. It was previously thought

that as they move to cooler temperatures they maintain a constant bolometric luminosity, represented in Figure 2.22 as horizontal lines, and but new studies by the likes of Clark et al. (2009) have shown this not to be entirely true.

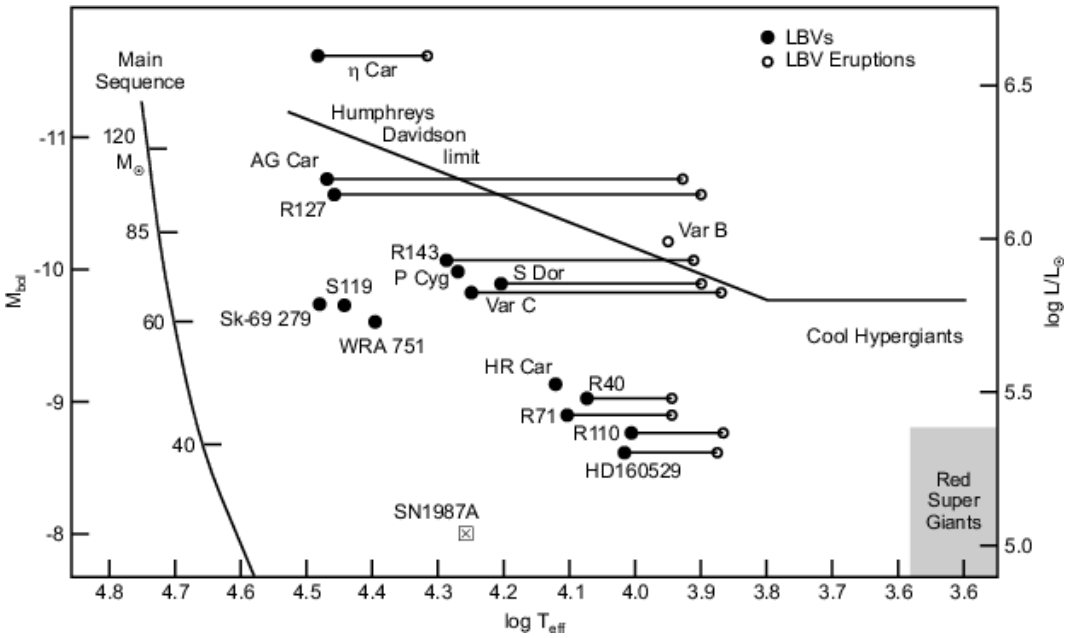

Figure 2.22: Representation of the Humphreys-Davidson limit on a Hertzsprung–Russell diagram, showing how certain LBVs violate this limit by lowering their effective temperature while maintaining a constant luminosity (Weis and Duschl, 2002).

In their research, Clark et al. (2009) analysed over a decade of observations of the LBV AFGL 2298 and found it to vary by over 1.6 magnitudes in the near-IR. However, it also changed its bolometric luminosity by a factor of 2, which is in contention with the previous observations of S Dor and AG Car during outburst. The most likely explanation for this variation in bolometric luminosity was attributed to the expansion and contraction of the photosphere of the star at near constant temperature.

Another way of identifying LBVs is through the presence of P Cygni profiles

(named after another well known LBV star) in their emission lines, see Figure 2.23 for an example. This line profile is caused by a combination of broad emission and narrower absorption of the same line. The reason behind this unusual shape is due to the high velocity winds emanating from the star in the line of sight of the observer, creating a blue-shifted absorption lobe of the same line, which causes this distinct shape. A number of emission lines first identified with LBVs were ones such as the H,He I,Fe II and [Fe II] emission lines (Humphreys and Davidson, 1994).

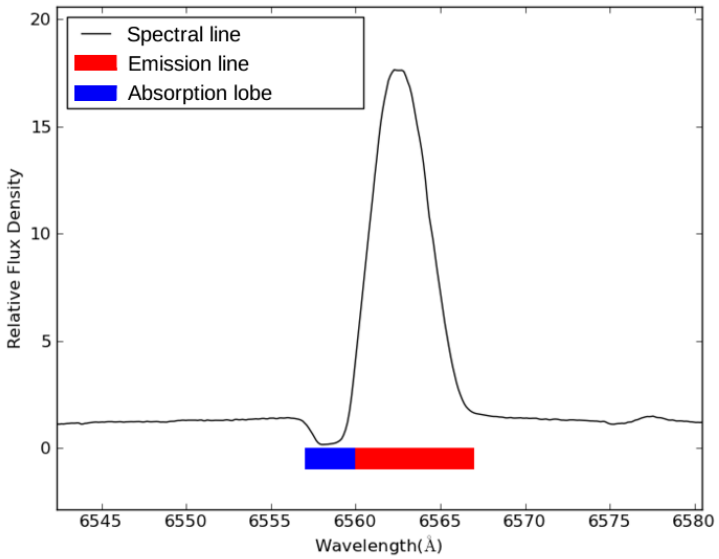

Figure 2.23: An illustration of a simple P Cygni profile with blue-shifted absorption lobe and broad emission features in the stellar continuum. Image Credit: Sailbystars/Wikipedia

2.2.3 Humphreys & Davidson limit

The Humphreys-Davidson limit is an empirical luminosity boundary in the upper right corner of the Hertzsprung-Russell diagram (see Figure 2.22) that was determined from observations of massive stars in the Milky-Way and Magellanic Clouds.

What these observations showed was that there was a lack of cool supergiants above $M_{Bol} \simeq -9.5$ for $T_{eff} < 8000K$, suggesting that stars above some critical mass ($\sim 40 - 50M_{\odot}$) do not evolve into this region. The reason for this is thought to be due to instability of high mass stars during their post-main sequence evolution phase, that limits their evolution to cooler temperatures due to high mass loss rates (Humphreys and Davidson, 1994). Recent models have shown (Figure 2.20) that stars above this empirical limit will actually start evolving back towards hotter temperatures, as this extensive mass loss strips away the cool outer layers of the star leaving the hotter inner regions visible.

Unfortunately estimates for the mass-loss rates for very massive stars are few and far between due to their rarity; consequently, further estimates would greatly improve the accuracy of stellar evolutionary models (Ekström et al., 2012). They are so rare that less than 100 are known to exist in our own galaxy (**?**), and galactic extinction hampers the discovery and study of further examples. This is why using infrared wavelengths (such as the Spitzer space telescope) to study LBVs in the galaxy is preferred to optical wavelengths because they suffer only 1 magnitude extinction in the K-band ($2.2\mu m$) compared to up to 10 magnitudes of extinction in the V-band (500 nm) (Rieke and Lebofsky, 1985). Infrared surveys such as Spitzer have been used to hunt for dusty ring nebulae surrounding massive stars (Clark et al., 2003), the existence of which would show that these stars had undergone significant mass-loss events in their recent past. More recently, Hutsemékers et al. (2013) reported on their discovery of a large dust ring around the yellow hypergiant Hen 3-1379 using the Herschel space observatory.

In addition to searching for LBVs in the Milky Way, recent studies have turned their focus to nearby galaxies in the local group such as M31 or M33, indeed this very thesis does just that. The main benefit this gives is to avoid the heavy extinction in the galactic plane when looking at optical wavelengths, and thus avoiding the need

to use expensive space based observatories to help populate a catalogue of bona fide LBVs.

2.2.4 Photometric & Spectroscopic variability of LBVs

What these LBV studies involve is monitoring the photometric and spectroscopic behaviour of massive stars to determine if they are undergoing an LBV phase in their evolution. The variability of LBVs has been studied for many years (Conti, 1984; Humphreys and Davidson, 1994; van Genderen, 2001; Clark et al., 2005; Smith and Owocki, 2006; Smith et al., 2011; Smith, 2014), and although the physical mechanism behind their variability is still unknown, several things can be inferred about their behaviour. The standard picture of LBVs is that they can be observed in one of two phases: (i) an S Dor cycle during which the visual brightness varies by up to 2 magnitudes over a timescale of about 10-40 years & the bolometric luminosity remains fairly constant and (ii) an outburst phase involving a giant eruption causing the stars luminosity to increase & the visual magnitude to rise by several orders of magnitude. The timescales of these outburst phases are still poorly constrained due to their rarity (Clark et al., 2009).

S Dor cycle

The S Dor cycle is named after the namesake star S Doradus, located in the Large Magellanic Cloud. It is characterised by an increase in brightness by up to two magnitudes in the visual and maintaining a relatively constant barometric luminosity. The timescale of this cycle is typically about 10-40 years but this varies from star to star. The source of this variation arises from changes to the stellar radius and temperature as a result of instabilities within the star (van Genderen, 2001). This cooling of the surface temperature shifts the Plank curve, and thus colour of the star, resulting in changes to the visual brightness which are seen as the S Dor

variability.

An example of an S Dor cycle is shown in Figure 2.24 which displays a lightcurve of the LBV AG Car taken over a period of 22 years and includes two minimum phases of the cycle. What this shows is that the size and duration of these minima are not equal, indicating that the stellar parameters such as temperature, wind velocity and mass-loss rate were also different (Groh et al., 2009).

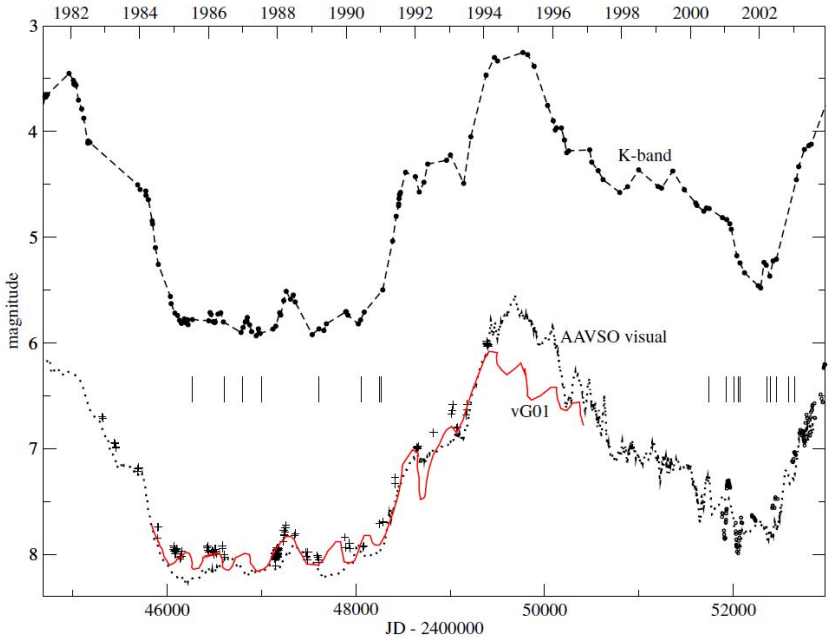

Figure 2.24: AG Car lightcurve from 1982-2004, encompassing two minimum phases (Groh et al., 2009).

During this cycle the star undergoes a transition from hot to cold on the HR diagram (see Figure 2.22), often crossing the Humphreys-Davidson limit in the process, and displaying changes in their spectra from O-type to late G or F-type stars Massey (2013). This leads to the classifying of the two phases within the S Dor cycle, namely a "hot" LBV phase and a "cool" LBV phase.

This "hot" phase is also known as the quiescent phase as it occurs during the minimum of the S Dor cycle and relates to the period of lowest activity. During a

"hot" LBV phase these stars typically show emission lines of : [Fe II], He I and the Balmer hydrogen lines Massey (2013). In addition to this, these spectral lines often display signs of a P Cygni profile (discussed in section 2.2.2), which is as a result of high velocity outflows; this is a good indicator of an LBV star but a small number of massive stars spectra can contain P Cygni profiles as well.

In contrast, the "cool" phase is associated with an increase in brightness as the star moves to cooler temperatures in the HR diagram, indicating it is undergoing an outburst. During this cool phase the star is thought to undergo envelope inflation (Gräfener et al., 2012) which changes the spectra to resemble that of a cool A-F type supergiant with strong Balmer emission lines.

During this outburst the mass-loss rates increase up to 10^{-5}–$10^{-4} M_{\odot}/yr$ (Humphreys and Davidson, 1994), this is powered by strong stellar winds which interact with old stellar ejecta from previous outbursts and winds (Burggraf et al., 2015). This is then dragged out away from the star with the strong winds, forming a small circumstellar nebulae such as the one shown in Figure 2.25 but on a smaller scale.

The presence of strong Balmer lines (specifically $H\alpha$) in the optical spectra of LBVs undergoing an outburst means that they are a good diagnostic tool for calculating the mass-loss rate during an outburst.

Giant eruptions & Eta Carinae

Giant eruptions are distinguished from the S Dor cycle because the star increases in visual brightness by several order of magnitude, much more than the 2 mag variation seen in the S Dor cycle. In addition to this, the bolometric luminosity of the star also increases (Clark et al., 2009) during a giant eruption; however, the exact timescales of these events are still uncertain due to their rarity, Humphreys and Davidson (1994) estimate a few hundreds to thousands of years as a reasonable frequency to these events.

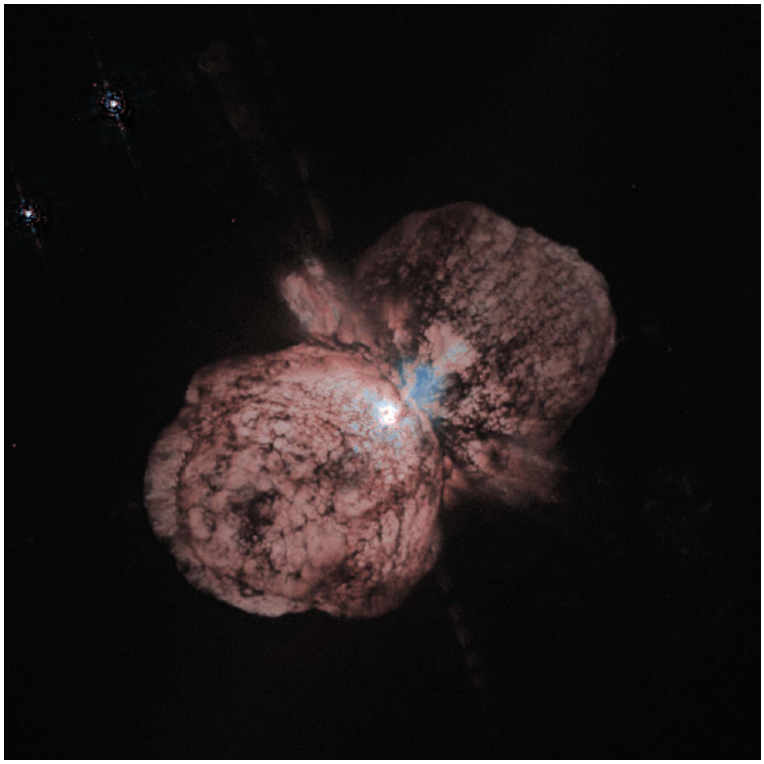

Figure 2.25: Eta Carinae surrounded by the Homunculus Nebula. Imgae Credit: NASA/ESA

The most well known giant eruption is the great eruption of Eta Carinae (η Car) which occurred between 1837 and 1860, temporarily becoming the second brightest star in the sky by increasing its bolometric luminosity by two magnitudes and the visual brightness M_v by 5-7. This spectacular eruption resulted in the ejection of about $15M_\odot$ of material from the star, accounting for approximately 10% of the entire stellar mass (Davidson and Humphreys, 2012a,b). This can still be seen to this day in the form of the bipolar Homunculus Nebula (see Figure 2.25), which consists of two lobes and completely surrounds η Car and its companion star. As a result, it absorbs most of the light from the system and re-emits it in the infra-red.

The fact that η Car survived this was surprising at the time because it was so bright that it was though to be a supernova eruption (now known as a supernova

impostor, see subsection 2.2.5), but the star survived and still lives to this day.

Such extreme mass-loss events are now thought to play an important role in the evolution of massive stars as they enable evolution models to be brought closer in line with observations. However, the exact mechanism behind these great eruptions remains uncertain. The quantities of mass ejected in these great eruptions appears to straddle a grey area between strong stellar winds and non-destructive explosions. The current understanding is that it must be caused by one of these two methods, but both have shortcomings that are difficult to explain away.

The traditional explanation for these great outbursts involves an energetic radiative luminosity from within the star which powers strong continuum driven winds, pushing it past the Eddington limit and this results in heavily mass-loaded winds (Smith et al., 2018). The biggest setback to this scenario is that it is hard to explain how a star can persist for so long in violating the Eddington limit (20 years in the case of η Car's great eruption) with strong winds powered by an unknown but powerful luminosity source.

The alternative scenario involves a hydrodynamic explosion, similar to a novae or supernoave eruption but one that is non-terminal. The mechanism that carries away matter from the star is explosive in nature, rather than radiative, although the radiation is a byproduct of the explosion by heating the circumstellar medium with a shock-wave. This would have to be a low energy explosion originating in the stellar envelope as anything deeper within the star would either not escape the surface, or rip the star apart. This scenario does help explain the duration of such outbursts, because the primary source of luminosity is the shock ploughing through the dense circumstellar medium (CSM), which can sustain the luminosity over many years if the CSM is dense and deep enough. However, the main limitation of this scenario is it's inability to explain the root cause of such a powerful explosion inside the star (Smith et al., 2018).

This leave the mystery of LBV's giant eruptions still unsolved, and because of their rarity it is very difficult to resolve the gaps in the theory. One possibility is the role binary companions could play in such eruptions, they are hard to detect due to the overpowering luminosity of LBVs but the could go a long way to explain the behaviour of stars like η Car during a giant eruption. Smith et al. (2018) proposed a 2-stage scenario to explain this, that involved significant binary interaction over decades before the eruption itself. But ultimately this required some additional energy injection to initiate the large increase in luminosity observed in the great eruption between 1837 and 1860.

Giant eruption events like the one seen with η Car might provide evidence for an impending supernova eruption, which is why they are some of the prime candidates for supernova progenitors in the galaxy. In addition to this, the giant eruptions themselves have become known as supernova impostors, especially in distant galaxies, due to their supernova like behaviour.

2.2.5 Supernova impostors & progenitors

These giant LBV eruptions pose a significant inconvenience to transient astronomers searching for core-collapse supernova events as the large increase in brightness, combined with their rapid rise rate and similar spectra, means they are often mistaken for supernovae eruptions, hence why they are called supernova impostors.

As discussed in the previous subsection, these giant eruptions (such as η Car) are supernova-like in their behaviour because they increase in brightness by several orders of magnitudes and decay or plateau in brightness over a much longer timescale. However, they are distinct from bona fide supernova in that the star survives the eruption and isn't ripped apart by the energetic mechanism that powers the rapid rise in luminosity.

When they are first labelled as a supernova, they are given the classification as

a Type IIn supernova. This is due to the presence of strong but narrow H I lines in their spectra (hence the "n" designation), which are caused by the relatively slow moving winds/ejecta (Schlegel, 1990; Filippenko, 1997).

In external galaxies it is very difficult to determine if a star has survived a supernova (therefore making it a supernova impostor); however, for eruptions in our own Milky Way galaxy it has been possible to resolve a star left over post-eruption. Only two such eruptions have taken place in the Milky Way in recorded history, the mid 19^{th} century great eruption of η Car and the eruption of P Cygni in 1600 AD. In both instances the progenitor star has been observed after the eruption is over (Smith et al., 2011).

There are several observational properties that can be used to try and distinguish between a supernova and a supernova impostor, these include: peak absolute magnitude, spectral morphology, outflow velocity, fading time and progenitor properties; but what Smith et al. (2011) found is that there is no clear correlation between any of these and supernova impostors occupy essentially all the parameter space between classical novae and supernovae. This means it is impossible to say for certain with just one observational parameter if a supernova is an LBV undergoing a giant eruption, the only infallible way of determining this is by observing the progenitor star post-eruption.

Instead, it requires analysing multiple observation parameters to determine if a supernova is indeed an LBV eruption. One such example is supernova 2008S, through a combination of low peak luminosity, slow outflow speeds, slow luminosity decline at late-times and differences in spectral evolution, Smith et al. (2009) concluded that SN 2008S was actually a supernova impostor in the form of an LBV.

Supernoa Progenitors

The relationship between Type IIn supernovae (SN) and LBVs is not just limited to their confusion as supernova impostors, it is also theorised that LBVs could be the progenitors for some Type IIn SN too. This is a result of their appearance, which seems to suggest that Type IIn SN are expanding into a dense circumstellar medium, which would be a result of a high-mass loss phase of evolution.

This observational interpretation is at odds with stellar evolution theories that place LBVs as a post-main sequence phase but not as a pre-SN phase (Maeder and Meynet, 2008). This is because the LBV phase is always succeeded by a hydrogen poor Wolf-Rayet phase in these theories, due to the need for the LBVs to loose their hydrogen envelope before evolving into Wolf-Rayets (Dwarkadas, 2011). However, models by Groh et al. (2013) showed that the 20 $M_{\odot}$ & 25 $M_{\odot}$ rotating star models had spectra very similar to LBVs right before they exploded as a supernova (see Figure 2.26), although they actually suggest that they are Type IIb SN instead.

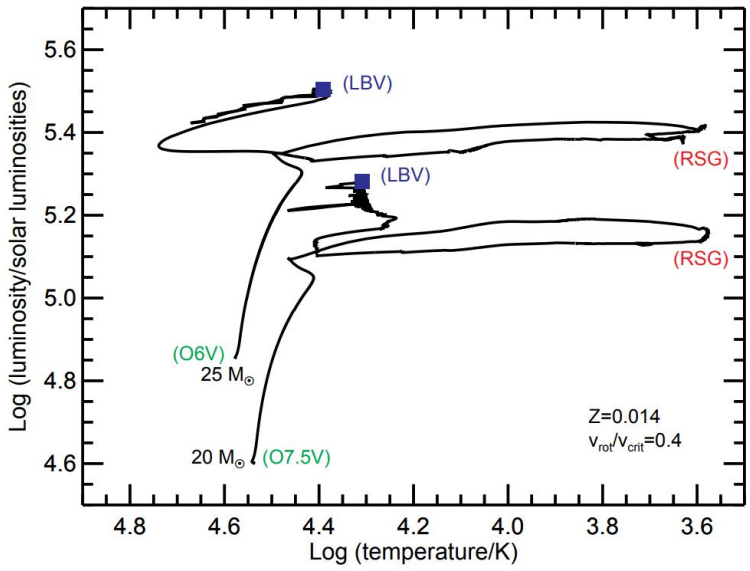

Figure 2.26: Evolutionary tracks of rotating models with initial masses of 20 $M_{\odot}$ & 25 $M_{\odot}$ showing the LBV phase as the pre-SN stage of evolution (Groh et al., 2013).

What the authors noticed in their models was that the pre-SN phase produced spectra that contained strong optical emission lines such as: H, He I and N II, along with P-Cygni profiles. They also point out that these models weren't tuned to produce LBV-like spectra and so the results are serendipitous which makes them more robust. Another interesting result from this paper is that Groh et al. (2013) found LBVs could be divided into two sub-classes based on luminosity, with the low-luminosity LBVs being the terminal phase of stellar evolution before exploding as a supernova and the high-luminosity LBVs could evolve further into WRs.

These models provide theoretical support for a pre-SN phase of LBVs, which could be as short as $\sim$ 5000 years, but they appear to be slightly inconsistent with the previous assertion by Dwarkadas (2011) that they form Type IIn supernovae and not Type IIb. However, this short lived pre-SN stage would be consistent with the apparent rarity of LBVs.

A relatively new phenomena in the field of transient astronomy are superluminous-supernovae (SLSN), these are typically classified as SN with an absolute magnitude greater than -21 in the optical (Moriya et al., 2018). They are classified into two different spectral types, Type IIn with narrow hydrogen emission and Type Ic devoid of hydrogen emission. As the Type Ic SLSN are thought to be powered by a jet fallback mechanism onto a black hole, they will not be discussed any further. But as for the Type IIn SLSN, there are three explanations that have been postulated for their existence, these include: nuclear decay of Nickle-56, spin down of magnetised neutrons stars (magnetars) or the interaction between supernova ejecta and a dense circumstellar material (Moriya et al., 2018).

It is this last scenario that is of most interest in the context of this chapter, because there are links that can be made between Type IIn SLSN and LBV stars. This is because LBVs undergo huge mass-losses which is a possible explanation for the dense circumstellar environment around these SLSN.

This circumstellar material model is based on the interaction between the SN ejecta and a dense circumstellar medium, whereby a shock wave is formed as the two interact. This leads to a transfer of kinetic to thermal energy which is then radiated at different wavelengths, powering the increased luminosity of SLSN. Light curves of these SLSN have shown a diverse range of shapes and timescales, which is thought to originate from a varying circumstellar medium around each progenitor.

It is not entirely clear if these SLSN Type IIn are a separate population of SN or are just more luminous versions of Type IIn SN, and there have been a few SN IIn that bridge the gap between standard SN luminosity peaks and SLSN. This could hint that they aren't a separate population but are in fact just at the bright end of a SN Type IIn luminosity function, which could be explained due to their rarity.

In summary, LBVs have been shown to be a plausible candidate for SN progenitors, especially in the case of Type IIn SN with narrow hydrogen emission and high luminosities in the case of SLSN. This relates closely to the work on gravitational waves because as well as compact binary coalescence (CBC) events, LIGO is also aiming to detect these "burst" events originating from supernovae eruptions. The discovery of such a burst event would trigger a detailed search of the sky in multiple wavelengths, as well as in archival data, to try and identify any previous outburst history or in the case of a nearby galaxy even a potential progenitor star.

The next chapter will shift the focus back onto the gravitational wave follow-up work performed by PIRATE and the procedures used to achieve this.

Chapter 3

Gravitational Wave follow-up method

This chapter focuses on the methods used in the follow-up of gravitational wave alerts, from initial GW detection through to telescope observations. The section begins by outlining the internal LIGO alert process, from identification of candidate events in the detectors to the distribution of alerts to EM partners via the GCN (Gamma-ray Coordination Network) Network. Also included in this chapter is an overview of the different independent search channels employed by LIGO to search for gravitational waves. Lastly, this is followed by an overview of the PIRATE alert pipeline, which was developed specifically by the author to utilise the robotic nature of the telescope and quickly follow-up gravitational wave alerts.

3.1 Identifying gravitational wave candidates with LIGO

The LIGO alert pipeline gathers and analyses all the data coming from the online interferometers and copies them to the computing centres for processing (see Figure

3.1 for a flowchart of this process). They use a variety of real-time and low-latency search channels to identify any candidate events that were coincident in at least two of the three detectors[1]. These can be broadly split into two categories: the first search technique is a Compact Binary Coalescence (CBC) search using a matched filter technique, which involves generating a database of waveforms that can be matched to signals from compact binary systems in real time. The alternative search method uses a more generic transient search pipeline with minimal assumptions to look for so-called "burst" events, which are short duration transient signals in the detectors. The different binary coalescence search pipelines used by LIGO are presented in Table 3.1.

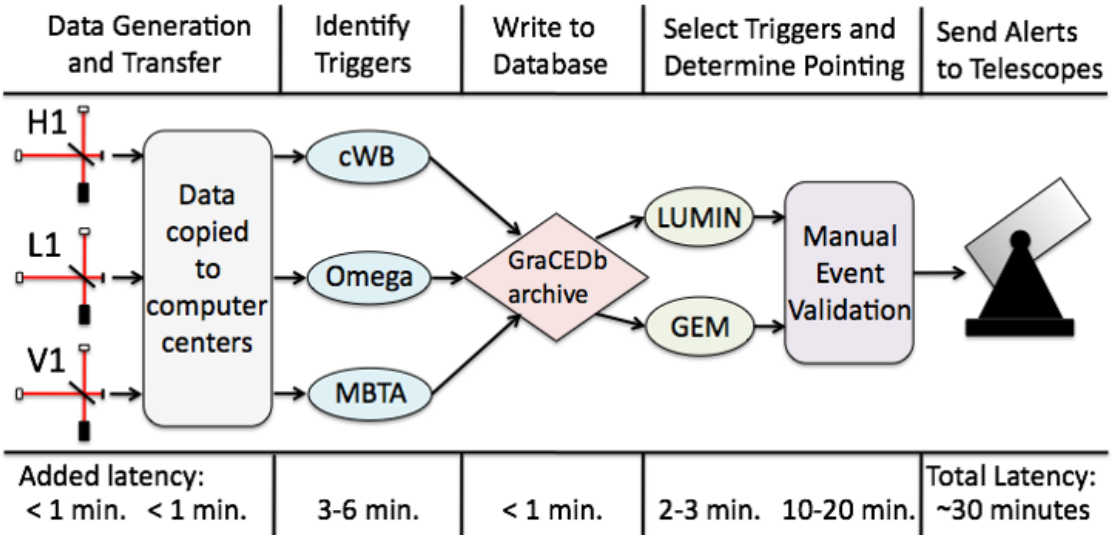

Figure 3.1: The LIGO alert process from data generation to alert distribution, with corresponding time requirements (LIGO Scientific Collaboration et al., 2012). The Omega trigger was discontinued before the beginning of Advanced LIGO in 2015.

[1]Two out of the three detectors includes both LIGO and one Virgo detectors.

Pipeline	Reference
Compact Binary Coalescence	
PyCBC (Python Compact Binary Coalescence)	(Canton T. D. et al., 2014; Usman et al., 2016; Nitz et al., 2017)
MBTA (Multi-Band Template Analysis)	(Adams et al., 2016)
LALInference	(Veitch et al., 2015)
GstLAL (GStreamer LSC Algorithm Library)	(Cannon et al., 2012)
Burst Search	
cWB (Coherent Wave Burst)	(Klimenko et al., 2016)
LIB (LAL Inference Burst)	(Essick et al., 2015)
BayesWaves	(Cornish and Littenberg, 2015)

Table 3.1: A Summary of the search pipelines used by LIGO during O2.

3.1.1 Compact Binary Coalescence Searches

Compact binary mergers such as black hole-black hole mergers produce a sinusoidal signal (or waveform) that intensifies over time and also increases in frequency. The exact shape of this waveform depends on the masses and spin of the merging objects but this can be modelled using the "effective-one-body formalism" (Buonanno and Damour, 2000). This "effective-one-body formalism" is a combination of different techniques of general relativity, namely post-Newtonian (PN) expansion, black hole perturbation theory and numerical relativity (Abbott et al., 2016b).

Using this effective-one-body approach as the basis for the compact binary models, a database of waveforms are generated that correlate to signals from compact binary systems with an individual mass range of $1 - 99M_{\odot}$. In total this database stores approximately 250,000 waveform templates to cover this large mass range (Abbott et al., 2016b). The matched-filter search is performed by comparing the live detector data with these waveform templates, and calculating a matched-frequency signal to noise (SNR) (see Allen et al. (2012) for more details).

The template with the highest SNR is then designated as a "trigger" (see Figure 3.2 for a comparison between a template and strain signal) and this trigger then

undergoes more statistical analysis, such as a chi-squared test. The purpose of such a test is to determine if the data in several different frequency bands are consistent with the waveform template. The final test is to determine the temporal coincidence between the detectors (in the case of when just the two LIGO detectors are operating); to achieve this, the algorithms search a narrow window (15ms) in the data of both detectors to look for the exact same waveform template from the other detector. This window is determined by the light propagation time between the two sites (10ms) plus uncertainties (5ms), so any gravitational wave passing through both detectors must occur within this time window for it to be considered a real event. If the trigger passes all these tests then it is selected as a candidate event, and must be assigned a detection statistic value that determines the significance of the candidate gravitational wave.

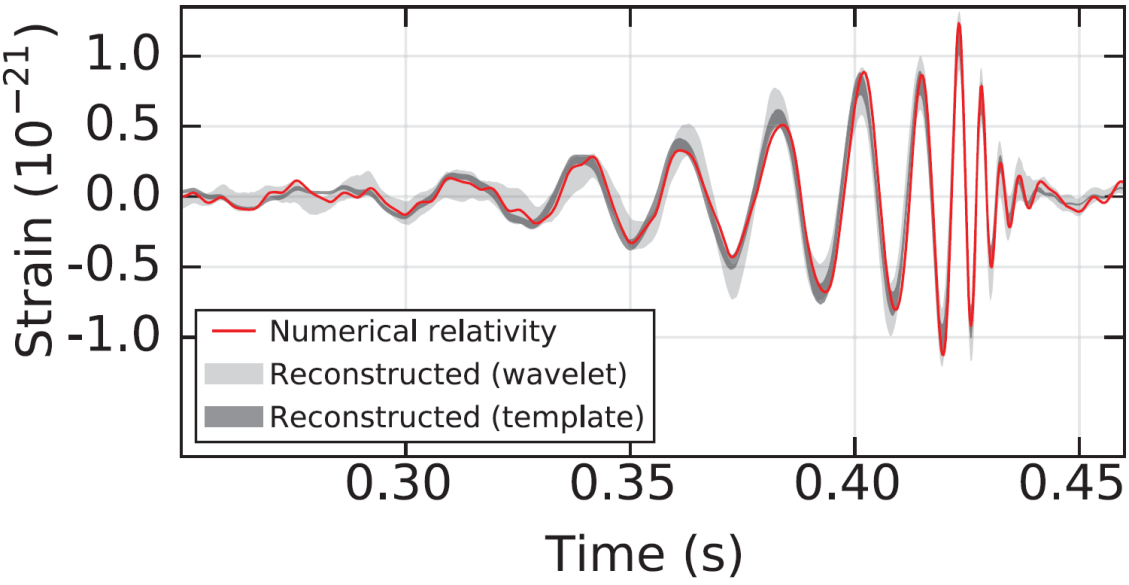

Figure 3.2: Gravitational wave strain in the H1 detector (solid line), along with two independent waveform reconstructions. One (dark grey) uses a binary black hole waveform template, the other (light grey) doesn't use any astrophysical modelling but instead uses a combination of sine-Gaussian wavelets (Abbott et al., 2016b).

False Alarm Rate To determine the significance of a gravitational wave event, also known as the False Alarm Rate (FAR), the signal must be compared with the detector background noise. The FAR is an average rate, usually given as a number of events per month, at which noise fluctuations in the detector would create events of similar significance. For example, the threshold for alerts to be sent out to EM partners during O1 & O2 was a FAR of 1 per month or higher. Calculating the background noise is a non-trivial process because the detectors cannot be shielded from the gravitational wave background, and this background noise contains both non-stationary and non-Gaussian components in the form of transient "glitches" in the data caused by the complex interactions between the instruments and their environment. An example of such a glitch can be seen in Figure 3.3, which occurred due to "a saturation in the digital-to-analogue converter of the feedback signal controlling the position of the test masses" during the detection of the gravitational wave event GW170817 (Abbott et al., 2017d).

Several papers have been published on different ways to estimate the background noise in the LIGO detectors (Smith and Thrane, 2018; Astone et al., 2000), but they all use a process of time-shifting the data to empirically calculate the background noise. This is achieved by shifting the data by a significant amount of time compared with the intersite propagation time, allowing for unrelated instrumental noise to be isolated from the correlated background signal between two detectors (Abbott et al., 2016b).

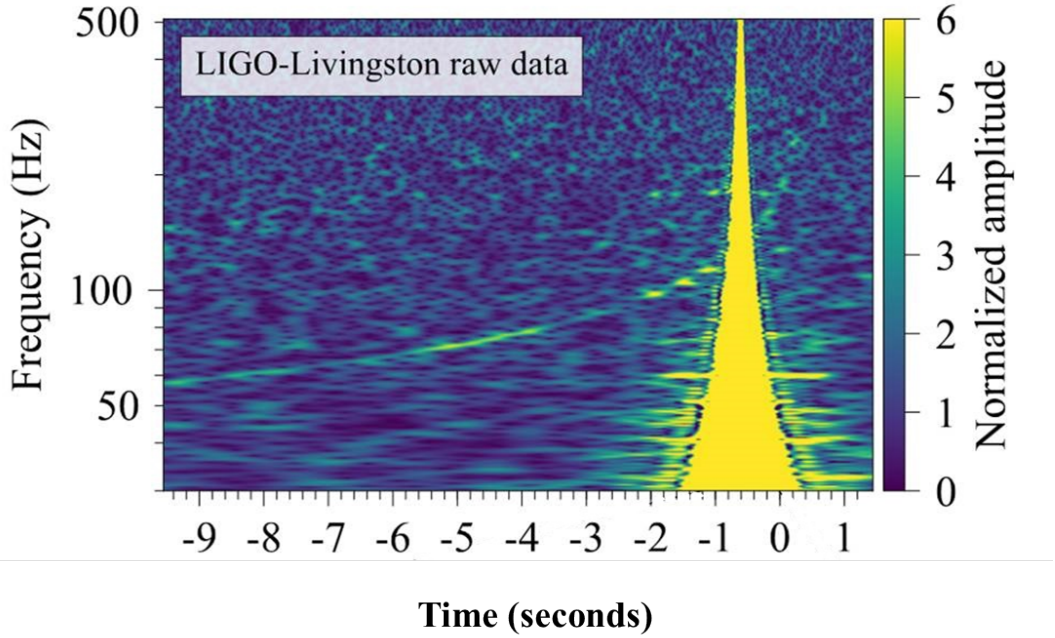

Figure 3.3: An illustration of a glitch in the LIGO strain data, taken from the GW170817 detection paper (Abbott et al., 2017d).

3.1.2 Burst Searches

In addition to the matched-filter template searches, there are also generic transient search pipelines which look for transient events known as bursts. Instead of searching for a specific waveform, these burst search pipelines perform time-frequency analysis of the signal to look for any excess power in both detectors, making minimal assumptions. Using LALInference and LIB as a comparison, the main difference between binary coalescence and burst pipelines is that the burst pipelines are using a single sine Gaussian waveform to filter the data, rather than a long waveform that changes in frequency (Figure 3.2) (Essick et al., 2015). In addition to this, these burst searches don't assume any particular direction, orientation, morphology or timescale (Abbott et al., 2016c). However, this can cause problems when searching the time-frequency space because there are many non-astrophysical sources of burst

noise in the detectors, which can be removed by applying the correct thresholds to the excess power, but this then reduces the ability to detect fainter astrophysical sources. Because of this, detecting time-coincident signals between detector sites is more important for these burst events than it is in the compact binary mergers. The background noise for these burst searches is estimated in the same way as the binary coalescence searches; using a time shifting procedure.

Since the beginning of the Advanced-LIGO era in 2015 five pipelines have triggered a candidate gravitational wave alert : MBTA, gstlal, LIB, PyCBC & CWB. Of those only CWB, PyCBC and gstlal detected a confirmed gravitational wave.

Generating Skymaps For the burst searches they have internal processes that can constrain the source localisation, such as a constrained likelihood algorithm in the case of cWB (Klimenko et al., 2016) or a Markov chain Monte Carlo (MCMC) parameter estimation method in the case of LALInferenceBurst (LIB) (Aasi et al., 2013). However, this isn't the case in the binary coalescence searches, as their output is first uploaded to GraceDB (Gravitational Wave Candidate Event Database), from where it is then analysed with a rapid Bayesian position reconstruction code called BAYESTAR (BAYESian TriAngulation and Rapid localisation). This was written by Singer and Price (2016) to rapidly process a candidate trigger and produce a probability Skymap to constrain the sky localisation of the source. To do this it uses the time, amplitude and phase information passed on by the trigger pipeline to generate a probability distribution map (see Figure 3.4) of the entire sky. Analysis by Singer and Price (2016) showed that with a 32-core system running 32 threads in parallel, BAYESTAR took between just 4-13s to analyse the data and produce a sky localisation map. When all overheads are taken into account this is comparable to the other stages of the LIGO alert process, and thus ultimately allowing astronomers to receive a comprehensive Skymap within a few minutes of the detection.

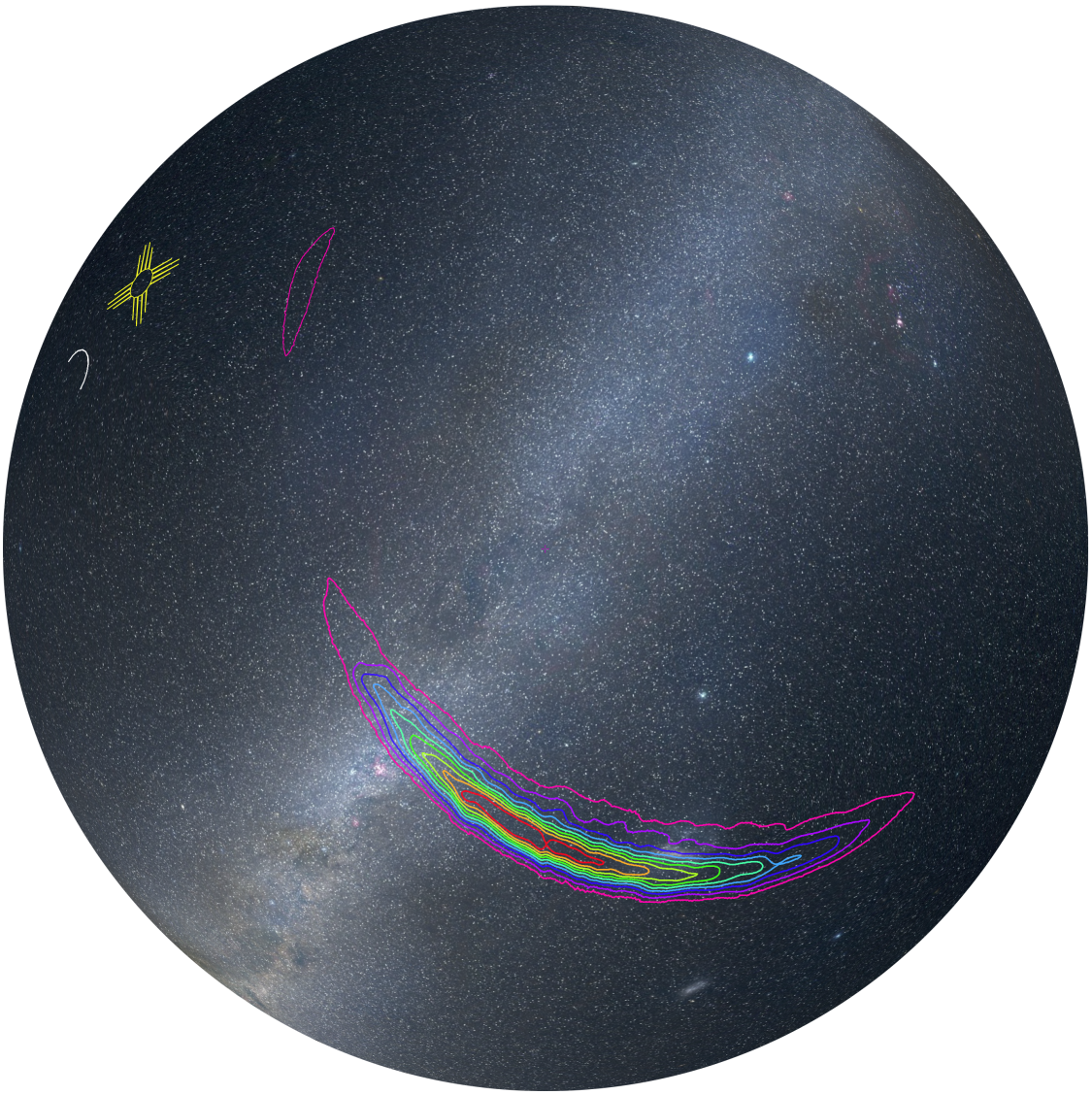

Figure 3.4: The Skymap produced by LIGO for the gravitational wave event GW150914 (Abbott et al., 2016a), showing 10%(red)-90%(purple) confidence regions. This is a global projection, showing one side of the observing sphere, with indications for the positions of the Sun & Moon too.

3.1.3 LIGO Alert Distribution

Before an alert can be distributed it must be vetted by a human, in order to avoid erroneous alerts going out and wasting valuable observing time on some of the worlds best observing facilities. Hence the data streams are monitored 24/7 by experts at each detector site control room, so when an alert is triggered they check the data for any obvious anomalies or disturbances at the time of detection and reject any that do. As pointed out in Figure 3.1 the target latency for this procedure was 10-20 min; however, in reality during O2 this latency was frequently exceeded.

Events which pass this vetting process are finally distributed to the partner EM observatories for follow-up imaging. This is done using the GCN (Gamma-ray Coordination Network) Network, which is a public alert system hosted by NASA and part of the broader VOEvent system (run by the International Virtual Observatory Alliance) (Allan et al., 2016). An illustration of this distribution network is shown in Figure 3.5 where the "author" in this case would be LIGO-Virgo collaboration, the "broker" is what mediates the system which in this case is on a NASA server, and the "subscriber" would be the PIRATE user.

This GCN alert system was designed, and is still used, as a public alert system to enable everyone from professional to amateur astronomers to receive the follow-up alerts of gamma-ray bursts or supernovae. However, because LIGO alerts were private during O1 & O2; anyone wishing to listen in to them had to sign the Memorandum of Understanding (MoU) with the LVC before they could receive these private alerts.

The main type of GCN alerts are called GCN Notices, these are machine readable alerts that contain key information regarding the time and characteristics of a gravitational wave candidate. In addition to these there are also GCN Circulars which are human written bulletins delivered by e-mail directly to the EM observers, these are then used as a way of communicating follow-up observations and any potential

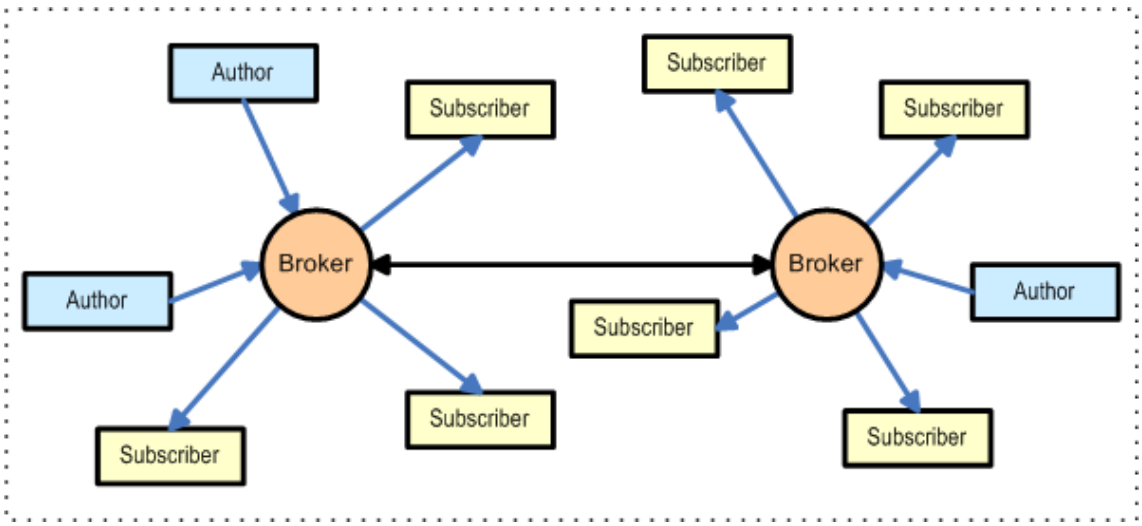

Figure 3.5: Illustration of the GCN alert network, part of the VOEvent network for astronomers. Credit: International Virtual Observatory Alliance (Allan et al., 2016)

counterpart discovery among EM partners.

There are two main methods by which GCN Notices are currently distributed to users: internet sockets and e-mail. The socket method involves maintaining a connection between two computers over the same network so alerts can be received, these alerts are then delivered as XML files that contain all the necessary information about an event. The email method allows observing sites without automated instruments to also receive the GCN Notices, albeit with a slightly longer delay time. These can be configured to be more human-readable or simply deliver a carbon copy of the XML file sent out via the sockets method. Both of these methods are described on the GCN website[2].

GCN Notices

As described above, a GCN Notice is a machine readable alert that contains key information regarding the time and position of a gravitational wave candidate, in

[2] `https://gcn.gsfc.nasa.gov/gcn_describe.html`

addition to this they also include a URL link to a copy of the relevant sky localisation map (Skymap). An example of what one of these GCN notices looks like is shown below in Figure 3.6; this particular alert was sent via e-mail so it appears more human-readable; however, it contains all the exact same data as the XML files distributed over the socket method.

Figure 3.6: Example of a GCN-Notice "Initial" alert produced by the LIGO-Virgo consortium (Singer, 2015).

The structure of these notices start off with identification information such as: date, time, type of alert and alert ID. Then there is also the LIGO observation data such as: trigger type, search pipeline, false alarm rate (FAR), chirp mass and maximum distance. In addition to this there are links to the associated Skymap and event web-page, these are important for the follow-up observations as without a Skymap the EM partners cannot react to the alert.

Firstly there are four different types of GCN Notices that can be distributed to EM partners, this is shown in (Figure 3.6) as the "NOTICE_TYPE", these are: "Test", "Preliminary", "Initial" and "Update". The first one is self-explanatory but the other three form part of the real world alerts that LIGO produce when they have detected a candidate gravitational wave. A "Preliminary" alert is issued as soon as possible with a latency of a few minutes after the trigger verification, it contains just

basic information of the time and significance of the event, but crucially there is no Skymap attached. The aim of this is to give astronomers as much warning as possible to stop any current observations and prepare the telescope to start observations of an incoming Skymap. The "Initial" alert is sent with a latency of several minutes, this is due to the time needed for a Skymap to be generated by the detection pipelines, but this is still fast enough for the vast majority of observatories that participate in the EM follow-up of these events. Lastly, an "Update" alert is issued if offline analysis pipelines have computed a more accurate sky localisation map than the original alert. Typically these are sent several hours or even days after the initial event. Conversely, a retraction alert can also be issued if offline analysis shows that the statistical significance of the event is lower than first predicted (Barthelmy, 2015).

In addition to the four types of alert just mentioned, there are also two different types of event that an alert can be assigned. These are labelled as "GROUP_TYPE" in the GCN Notices and they can be one of two events, either a Compact Binary Coalescence (CBC) or a Burst event. Including this group type in alerts allows astronomers to filter out the alerts they don't want to receive; for example, if they are only interested in CBC alerts then the burst alerts can be filtered out.

Lastly, a new addition to the GCN Notices for O2 was the inclusion of a parameter that indicated the probability that one or more of the CBC objects was a neutron star, labelled as "PROB_NS", with a range of 0-1 (Singer, 2016). This further empowers astronomers with the ability to filter out unwanted binary black hole (BBH) mergers, and only focus on receiving alerts where at least one of the objects, if not both, are a neutron star. The reasons for this were discussed in Chapter 1, but essentially there aren't predicted to be any EM counterparts to these BBH mergers, and given their frequency they could soon consume a lot of the observing time designated to follow-up telescopes, if they aren't filtered out.

Skymaps The most important component of these alerts is the URL link to the Skymap, because this is the key piece of information that directs astronomers as to where they should perform their follow-up observations. As mentioned previously, this rapid sky localisation map (Skymap) is produced with a latency of a few minutes once a gravitational wave has been detected and the link to this is provided in the "Initial" GCN notice under the title "SKYMAP_URL". These Skymaps are 2D projection of the entire sky (see Figure 3.4) mapped in the HEALpix (**H**ierarchical **E**qual **A**rea iso**L**atitude **Pix**elation of a sphere) format (see Figure 3.7), this type of map was chosen for statistical reasons because the entire sphere of the sky needs to be represented with pixels of equal size but not necessarily identical shape (Górski et al., 2005). The resolution of the Skymap varies, as the HEALPix design is a hierarchical map with resolution increasing where the probability increases. Starting out from an initial 3072 pixels, the pixels containing the top 25% probability is subdivided into four smaller pixels, and this process is repeated up to the 8^{th} order. The number of total pixels used to generate the Skymap varies but it cannot exceed $5\text{x}10^6$, and the number of pixels with distinct non-zero values is approximately 1% of these. More details on this adaptive sampling are given in Singer and Price (2016).

These Skymaps can be either machine read or viewed through a HEALpix viewer in a browser, an example of the latter is shown in Figure 3.4. This particular Skymap was produced in relation to the first ever detected gravitational wave (GW150914), and what it shows is a multi-layer visualisation common to all Skymaps viewed on the LIGO website. In the background there is an all-sky projection to help illustrate the position of the target area and on top of this is a layer that consists of nine contour plots that each encircle an area on the sky with a probability density ranging from 10-90%. However in the machine readable version of these there is no need for any visualisation layers so it simply sends out a copy of the raw probability data for all the pixels.

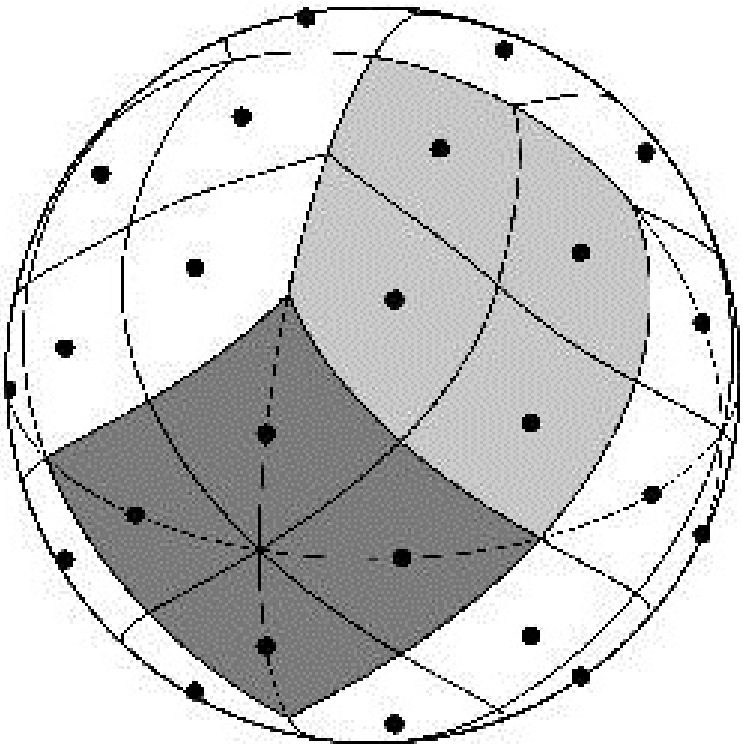

Figure 3.7: A HEALpix grid displaying the pixels of equal area on a sphere (Górski et al., 2005).

3.2 PIRATE Alert Pipeline

The PIRATE alert pipeline (see Appendix A) is written in Python (Rossum, 1995) and is based upon the LIGO-Virgo EM follow-up tutorial script written by Leo Singer[3,4] (Singer, 2015). This is itself based upon an older version written by Singer that processed generic GCN alerts, but since the LIGO-Virgo alerts weren't public, the process to receive them was more specialised. This tutorial script was aimed at LIGO-Virgo EM follow-up partners to enable them to receive, filter and process gravitational wave candidate alerts. The author made use of all these functions and added extra functions to communicate with the PIRATE telescope scheduler; thus creating one all-encompassing pipeline.

The final version of the script requires several additional python packages to run, these include: **pygcn** (to connect to the GCN network)(Singer, 2018), **requests** (enable HTTP downloads in Python)(Reitz, 2011), **healpy** (to process HEALPix images)(Górski et al., 2005), **astropy** (for several observing tools)(Astropy Collaboration et al., 2013), **numpy** (Van Der Walt et al., 2011) and **matplotlib** (for plotting tools)(Hunter, 2007), **subprocess** (to run Bash scripts from Python) and **math** (for mathematical functions). The code itself can be separated into it's three main tasks, these are: connecting to the GCN Network, processing incoming alerts and passing observing requests on to PIRATE.

3.2.1 Connecting to the GCN Network

The LIGO-Virgo gravitational wave candidate alerts are distributed via the GCN Network (as described in subsection 3.1.3), therefore to be able to receive these it is

[3] `http://nbviewer.jupyter.org/github/lpsinger/ligo-virgo-emfollowup-tutorial/blob/master/ligo-virgo-emfollowup-tutorial.ipynb`

[4] A more up to date tutorial has now been published to prepare for public alerts during O3, this can be found at `https://emfollow.docs.ligo.org/userguide/index.html`

necessary to connect to the network. To do this requires a new site configuration[5] which was only initially accessible to groups that signed the MoU with the LVC. In addition to this the pipeline also requires a "robot password" to be able to receive confidential files from GraceDB once an alert has been received. This is a crucial step that must be renewed every 12 months when the robot password expires and a new one should be generated. To use this with the script a new ".netrc" file has to be created on the host PC which contains all the credentials required to access the GCN Network.

Connecting to the network requires just one line of code to run, this is the very last line of Appendix A which starts with the function "**gcn.listen**". There are three arguments sent with this function and these include: the IP address of the host GCN server to connect to[6], the designated port number for private LVC alerts (in this case 8096) and lastly the "handler" argument tells the code what function should be run once an alert is received, and in this case it is the "**process_gcn**" function, which will be described in the next subsection.

Once the code is set running it should automatically connect to the designated server and listen out for incoming alerts; if it has failed to connect an error message will be displayed saying the connection timed out. The output should remain silent until an alert is received, but once one arrives it will be processed and the alert properties will be displayed in the terminal. The code will continue to run and listen for other alerts until it is terminated by the user.

3.2.2 Processing GCN Alerts

The next stage of the pipeline involves processing the alert after it has been received; to do this there are multiple functions within the script. Starting with

[5] `https://gcn.gsfc.nasa.gov/lvc\textunderscoreconfig\textunderscorebuilder.html`

[6] `https://gcn.gsfc.nasa.gov/voevent.html#tc2`

"**process_gcn**", this function saves the alert as an XML file on the host PC, using the GraceDB ID as the filename, and also prints a copy of the alert to the terminal. This step is done for all alerts, regardless of type; however, in the following lines of code the user has the ability to swap between processing test events or real events. This is useful for testing purposes as there are automated test alerts sent from the same servers every 4-5hrs. These lines can be suppressed or included in the code, depending on the needs of the user; but if no filtering is applied, all alerts will be passed on to the next stage of the pipeline.

The filtering of events by type, e.g. "CBC" or "Burst" events was removed from the original tutorial script because the author was interested in following up all types of alert but these can be re-included at any point. All parameters in the XML file are filterable so there's also the possibility to introduce a filter for the new 'PROB_NS" parameter mentioned in subsection 3.1.3, this would enable the script to filter out all alerts except CBC alerts containing at least one neutron star.

The next step in this function is to call another function in the script called "**get_skymap**", this enables the pipeline to locate and download the relevant skymap corresponding to each alert. It uses a "root.find" command to look up the URL of the skymap in the XML file created earlier, and then uses the "requests" package to send a HTTP request for the skymap. Once the script has obtained a copy of the skymap it then saves it as a .fits file and passes it back to "**process_gcn**". From there the skymap is sent in HEALPix form to another function within the script called "**tabletest**".

The aim of this function is to filter out unwanted pixels from the skymap and convert the observable ones into RA & Dec observing fields. To do this it begins by inspecting the metadata for the skymap, and assigning each pixel of the skymap a unique RA & Dec value. This is then collated in a table with the following four headers: Pixel Number, Probability, RA & Dec. Next the pixels below -40° Decli-

nation are removed as they are below the observing limit of the PIRATE telescope in Tenerife. Subsequent steps remove all pixels below a certain probability threshold set by the user and re-sort them by descending probability, in this instance the threshold is set at 6.67%; meaning only the top 6.67% of pixels in the skymap are kept. Then the script saves a CSV copy of this table before proceeding any further to enable users to check which and how many pixels are trying to be observed.

Following on from this is a process to convert the pixels into observing fields, this is made more complicated by the fact that the resolution of the pixels is higher than the FoV of PIRATE. To get around this a new array of "observed" pixels is created from the previous table by only including pixels that are at least 42arcmin away from another pixel in either RA or Dec. This results in a table of observing tiles that shouldn't overlap by more than a few arcminutes with any adjoining pixels, maximising the coverage of the skymap. The script again saves a CSV copy of this output before passing it on to another function called "OSO_API_Uploader" which uploads them immediately to the telescope's schedule. Ideally the script would also filter pixels based on their observability at the current epoch; but this task was performed by the OSO scheduler anyway (see subsection 3.3.2).

```
params = {
                'key': '51272f354a2b2131534d2a3f77',
                'name': 'Kappa_%d' % x,
                'observatory': 'pirate',
                'isTimed': 'false',
                'ra': RA,
                'dec': DEC,
                'atoms': 'R:100',
                'priority':prio,
                'binning': 1,
                'altLimit': 20,
                'repeats': 2,
                'immediate': 'true',
                'maxRepeats': 3,}
```

Figure 3.8: An example of the JSON file uploaded to the OSO Scheduler by the follow-up pipeline, containing all the input fields for the telescope.

The final stage of the pipeline involves uploading observations from the script to the telescope via the OSO scheduler. The is done by generating a unique ID and priority for each observing tile, this ensures that no two fields are identical. For each observing tile a unique observing request can be generated in the form of a JSON file (see Figure 3.8); containing all the necessary observing information such as: exposure time, filters, repeats etc. Each individual JSON file can then be uploaded via URL to the OSO Scheduler API using the correct hyperlink and hashkey. The script is programmed to return text to the terminal so the user knows if the observing requests have been successfully uploaded to the scheduler. Lastly, one more command is required by the OSO scheduler to prompt it to request a new schedule, this is called a "Clear Queue" command, and it is required to force the telescope to request a new schedule, containing the new observing requests.

3.3 Scheduling observations on PIRATE

The PIRATE telescope itself is run by an observatory control software called ABOT, which was initially developed for the Solaris Project (Sybilski et al., 2014) and now sold commercially by Sybilla Technologies. To aid the delivery of student modules and improve the accessibility of the telescope to researchers, an in-house scheduler was also created by staff at The Open University's OpenScience Laboratory; this became known as the OpenScience Observatories (OSO) Scheduler.

All regular scheduled observations are made using the OSO Scheduler, the only time when this is not used is either when undergraduate students are using ABOT for real-time control, for testing procedures or if a special observing request is made (e.g. defocused images). There are two types of scheduled observations that can be submitted to the OSO Scheduler, "Timed" and "Filler" requests, described later. The latter is used in most instances, especially in the follow-up of transients as they

have unpredictable behaviour, however the "Timed" requests are more useful for exoplanet transits and periodic variables because they have predictable periods. All the requests submitted to the OSO Scheduler for this thesis were accomplished using the "Filler" request, although a special category was created just for the follow-up of LIGO alerts. "Immediate" requests, as they were known, were given an infinitely high priority in the queue so they would be added to the schedule straight away, which allowed for rapid follow-up observations to be performed.

3.3.1 ABOT

ABOT is an observatory control software developed by Sybilla Technologies that runs on the Microsoft .NET framework and is aimed specifically at robotic telescope facilities (Sybilski et al., 2014). In close liaison with OU stake holders, Sybilla developed a bespoke software package for the OpenScience Observatories, in coordination with Baader Planetarium (who provided the hardware). This package built upon their work on Project Solaris in which the first version of ABOT was developed to control a network of up to 5 telescopes fully autonomously. An overview of the internal structure of ABOT is shown in Figure 3.9, from the telescope hardware all the way up to the Microsoft Azure cloud service.

The core work of ABOT is done within the Robotic Services layer, this is where all the control software for the observatory sits. These are split into 5 different "hubs" called: Audio Visual, Sensor Hub, Device Hub, Broker Hub and Hardware Manager. In addition to this, the web services provide a platform for outwards facing interfaces, such as the ABOT dashboard and AstroDrive file storage site.

The Hardware Manager in ABOT controls all the hardware within the observatory, including: the 4 dome segments, telescope mount, focuser, filter wheel and camera (including shutter). This allows ABOT to control every aspect of the observatory, and together with feeds from the Sensor Hub, it has the ability to monitor

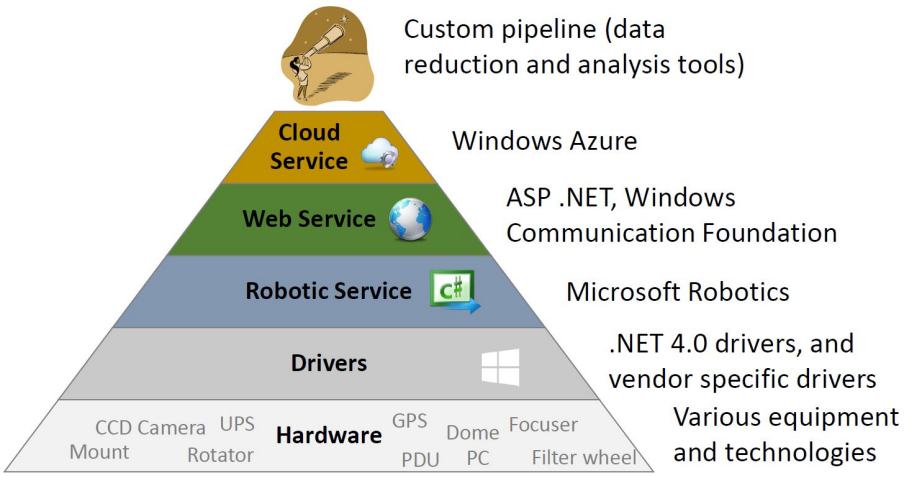

Figure 3.9: An overview of the ABOT command and control system, showing the various subsystem layers within ABOT, along with all the technologies used in each layer (Sybilski et al., 2014).

the weather and close the dome when it deteriorates.

The Sensor Hub receives input from numerous sensors located around the observatory site, these include a Reinhardt weather station containing: cloud, temperature, humidity, wind speed and wind direction sensors. There are also two temperature and humidity sensors inside the dome and an AllSky camera on the weather mast which contains a star counting algorithm. Altogether these sensors help ABOT build up a picture of the local weather conditions in Tenerife; informing the system on the next steps to make. ABOT won't open the dome unless all sensors are working and sensor values are within limits, for example if the temperature drops below 0°C then the dome won't open until the temperature rises again.

In addition to this, Sybilla designed a new dashboard in coordination with the OpenScience Observatories, with the primary purpose to provide students with a user-friendly environment to monitor and control the telescope remotely during their observing sessions. The ABOT dashboard integrates live webcam streams, as well as

live weather data from the observatory site and presents them in a user friends GUI (graphical user interface). This provides remote users with all the tools they need to take manual control over the telescope and submit observing requests directly to it, instead of having to submitting requests via the scheduler. There are two main advantages for this, it allows users to fine tune their observations (e.g. exposure time and focus position) and it also enables them to sidestep the scheduler and submit as many observations as they require.

The dashboard is all hosted by cloud servers that help to deliver this interface to many users across the globe at any given time; furthermore, these cloud servers also host AstroDrive, which is an online storage space that receives raw images from the telescope immediately after they have been taken. This allows telescope users to download their images from the observatories in real time.

Returning to the ABOT scheduler, there are two types of queues in this, an "object queue" and "immediate queue". All observing requests, regardless of origin, end up in the "immediate queue" as this is the queue that is fed directly into the telescope. However, there are different paths requests can take to get there. Firstly they can come directly from the ABOT dashboard, which is where all the requests from users in control of the telescope end up, either by submitting a single request or a block of multiple requests, this is known as the "object queue". The second path involves any observing requests saved on the local server, which can be loaded into the immediate queue with the click of a button (load work). And lastly there is the "Azure Queue" that uses the Microsoft Azure cloud service, which for the OpenScience Observatories connects to the OSO Scheduler located on campus in Milton Keynes and allows ABOT to receive the daily observing schedule at the start of every night. This is usually an automated process but a new schedule can be requested in ABOT via the dashboard using the "load web work" command.

3.3.2 OSO Scheduler

The OSO Scheduler is written in PHP (PHP: Hypertext Preprocessor) and provides telescope users at The Open University with a means of scheduling observations on the robotic telescopes in Tenerife many weeks in advance. The scheduler was created by Edward Hand who worked closely with a small group of expert telescope users, including working with the author, to determine what scheduling logic to use, and how the priority of targets would be established.

This prioritisation equation:

$$P_{Total} = P_{user} * T_{wait}^{1.2} * N_{requests}^{0.8} * \Phi_{night}^{-1} * \Phi_{year}^{-1} \tag{3.1}$$

shows how several factors are taken into account when calculating an individual targets priority P_{Total}. Here P_{user} is the user defined priority, T_{wait} is the total time a request has been waiting in the queue for, $N_{requests}$ applies when the same target has been requested more than once, Φ_{night} is a fraction of the night a target is observable for and Φ_{year} is the fraction of the year that the target is observable for.

Once a priority of a target it calculated, the scheduler then generates an optimum schedule for the night. This works downwards from the top of the priority list, and assigns an observing slot based on the slot with the highest score given by:

$$Score = (T_S - T_0)^{-1} * \sigma^{-2.7} \tag{3.2}$$

Here T_S is the time of the observing slot, T_0 is the current time and σ is the airmass value. This equation is heavily weighted towards airmass value, because observations with a low airmass are the most desirable.

On top of these individual target priority values, it was agreed that "timed" requests as a whole would always take priority in the schedule, with the exception of gravitational wave alerts, as these had a defined observing window in which they

could be observed; and the remaining observing time would be used for "filler" requests, which are not time-specific and can be observed at any time. Gravitational wave alerts processed by the author's pipeline and passed on to the OSO Scheduler would designated as "immediate" requests, so that they were imaged without delay. This was achieved by assigning them with a priority of $1x10^{30}$ and clearing the current schedule from the queue to replace it with one containing the new observations.

The observation requests can either be uploaded via a web form like the one shown in Figure B.1 in Appendix B, or they can be submitted using a command line interface via HTTP POST requests. All of the observing requests used for the work in this thesis were submitted using the second method, using an API to interface with the output from the alert pipeline discussed at the start of this section.

Once a request has been submitted it will be added to the list of observations that are sorted in priority order, and it will be automatically added to the schedule at some point in the future. As well as containing prioritisation algorithms the scheduler also has a built in algorithm to avoid observing: anything within 10 degrees of the moon, directly at planets or anything below 20 degrees altitude at any given time. It is at this stage that all gravitational wave follow-up observations requested would be filtered to check their visibility from Tenerife with PIRATE.

Lastly, at the beginning of every night ABOT requests a new schedule to carry out, so the OSO Scheduler sends a copy of it's schedule for the next few hours to the telescope to be observed. This is then refreshed throughout the night, whenever the telescope runs out of requests and needs to get more from the scheduler.

Now that the methods and processes surrounding the follow-up observations to gravitational wave alerts have been discussed, the topic will move on to the next chapter where the results from the first PIRATE observing run will be presented.

Chapter 4

Results from first PIRATE observing run

This section focuses on the observations made with the PIRATE robotic telescope in response to gravitational wave alerts released by the LIGO-Virgo Collaboration (LVC) during the second observing run of the LIGO detectors (O2). Detailed descriptions of all follow-up observations are given, regardless of the eventual significance of the initial alert, followed by a description of the analysis methods used to search the images for an optical counterpart. Lastly there is a discussion of the results of observations from a select few alerts that had sufficient good data to be processed and were not retracted.

Details of the second LIGO observing run are given in section 2.1.7 but in summary the LIGO collaboration reported observing gravitational waves from a further 3 binary black hole (BBH) mergers and more importantly, in conjunction with the Virgo detector, they were able to observe the signal of a pair of merging neutron stars for the first time. In addition to these 4 events, 10 further candidate triggers were released to EM follow-up partners by the LVC over the 9 month long observing run (Abbott et al., 2019).

The discovery of an electromagnetic counterpart to the gravitational wave event GW170817 was a breakthrough moment in astronomy as it was the first time that multi-messenger observations were made of the same object. Unfortunately PIRATE was not able to take part in the historic follow-up observations of this neutron star merger event, this was due to the location in the sky being below the altitude limit of the telescope. However, the reported detection magnitude of $17.46 \pm 0.03 mag_r$ (Valenti et al., 2017) was bright enough that it would have been above the magnitude limit of PIRATE, meaning that it was just the random location in the sky that prevented PIRATE from contributing to this historic detection. Nevertheless, this proves that the work performed with PIRATE during the rest of the O2 follow-up campaign was justified and further vindicates this project as a viable option for performing rapid-response follow-up observations to gravitational wave alerts.

4.1 Observations during O2

The second observing run (O2) of the two LIGO detectors began on the the 30^{th} November 2016; however, it wasn't until the 4^{th} January 2017 when the first gravitational signal was detected by LIGO (Abbott et al., 2017a). This would prove to be one of nine CBC alerts sent out during this 9 month period, and one of only three to have a high enough statistical significance to be considered a confirmed event. In addition to this, the other five alerts from O2 were classified as "burst" events, meaning they didn't detect a compact binary waveform in the data but instead observed an excess in the gravitational wave strain for a very short period. PIRATE was set up to receive all types of alerts from the LVC detectors, primarily due to the need to test the connectivity between the authors pipeline and the telescope hardware during its commissioning phase. Additionally it was unknown how many alerts there would be in total throughout O2, and the probability of seeing an

EM counterpart to the burst events was also non-zero, so the decision was made to respond to each and every event PIRATE was capable of following up.

A summary of all the alerts released during O2 is given in table 4.1, where the corresponding alert type and time is also given, along with the date and time of the first PIRATE observations. Of these, there are 10 alerts that PIRATE was able to follow up but also 4 that it was not. For G277583 the telescope wasn't available for research use as it was being used in its primary role as a teaching telescope for undergraduate students. In the case of G288732 (which became GW170608 after confirmation) the sky localisation was located in the daytime sky, making optical observations impossible from Tenerife at that time of year. With the addition of the Virgo detector in August 2017, the skymaps for G297595 (GW170814) and G298048 (GW170817) were much smaller than previous alerts, and with them both being located in the Southern Hemisphere it made observing them with PIRATE virtually impossible; the entire skymap for G297595 was located below PIRATE's safe observing limit and the skymap for G298048 was only just above the horizon at twilight at the time of year it was detected.

The reaction times achieved by PIRATE during O2 are also provided in table 4.1 and averaged 22.5hrs (excluding GW170104 and GW170814 which were both delayed due to other factors[1]). This delay far exceeds the author's initial ambitions and also the required response times to obtain the most important scientific data. However, for the large part, the causes of this delay were outside the author's control. Comparisons between the delay of manual and automated follow-up observations are hard to make due to these external factors such as LIGO and the weather in Tenerife, which make a like-for-like comparison very difficult. Of the three automated follow-

[1]Manual observations of GW170104 were delayed due to the author being on vacation and GW170814's delay doesn't reflect the fact that this was initially outside PIRATE's FoV, and only became visible after an Update alert was sent out.

up observations that weren't affected by bad weather, all 3 were observed within 18hrs of the initial trigger, and considering these alerts were all received between 8am-2pm, there was no situation where the observations could be made as soon as the alert was received. In fact, the fastest reaction time during the whole of O2 was done manually within 4hrs by the author upon receipt of an email alert.

Name	Type	Trigger Date (UTC)	Notice Date (UTC)	Observed Date (UTC)	Delay (dd:hh:mm:ss)
G268556 GW170104	CBC	2017/01/04 10:11:58	2017/01/04 16:47:00	2017/01/09 01:59:14	04:15:47:16
G270580	Burst	2017/01/20 12:31:00	2017/01/20 13:38:31	2017/01/21 07:00:13	00:18:29:13
G274296	Burst	2017/02/17 06:05:53	2017/02/17 23:05:19	2017/02/17 23:39:33	00:17:33:40
G275404	CBC	2017/02/25 18:30:21	2017/02/25 18:55:03	2017/02/25 22:18:55	00:03:48:34
G275697	CBC	2017/02/27 18:57:31	2017/02/27 19:24:45	2017/02/27 23:50:25	00:04:52:54
G277583	Burst	2017/03/13 22:40:09	2017/03/13 23:10:43	Not Observed	
G284239	Burst	2017/05/02 22:26:07	2017/05/03 14:29:04	2017/05/03 20:38:24	00:22:12:17
G288732 GW170608	CBC	2017/06/08 02:01:16	2017/06/08 17:19:35	Not Observed	
G296853	CBC	2017/08/09 08:28:21	2017/08/09 09:17:20	2017/08/10 02:24:29	00:17:56:08
G297595 GW170814	CBC	2017/08/14 10:30:43	2017/08/16 13:55:14	2017/08/17 04:45:22	02:18:14:39
G298048 GW170817	CBC	2017/08/17 12:41:04	2017/08/17 13:08:17	Not Observed	
G298389	Burst	2017/08/19 15:50:46	2017/08/19 19:02:51	Not Observed	
G298936	CBC	2017/08/23 13:13:58	2017/08/23 16:49:36	2017/08/24 02:09:23	00:12:55:25
G299232	CBC	2017/08/25 13:13:37	2017/08/25 13:39:05	2017/08/28 23:28:33	03:10:14:56

Table 4.1: This table summarises all the alerts sent out to EM partners by the LVC, along with the time of the event (Trigger Date), alert distribution time (Notice Date), the time it was first observed by PIRATE (Observed Date) and the delay time between Trigger and Observed dates. A more detailed table is available in the Abbott et al. (2019) paper.

4.1.1 GW170104 Observations

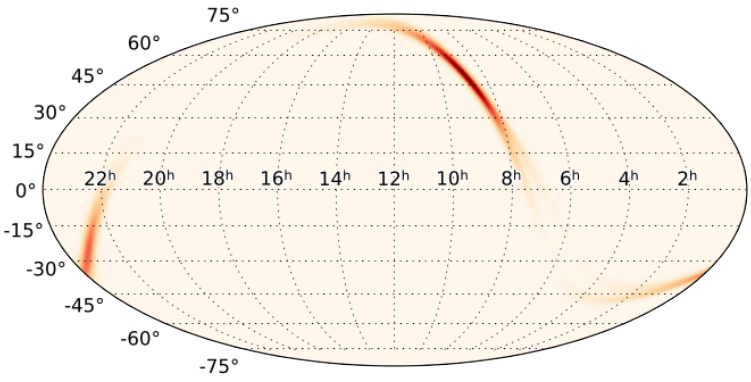

Figure 4.1: The Skymap produced by BAYESTAR for gravitational wave alert G268556, with Right Ascension (RA) along the x-axis and Declination (Dec) on the y-axis.

The gravitational wave alert G268556 was initially sent out by the LVC to EM partners at 14:35 UTC on the 4$^{\text{th}}$ January 2017, over 4hrs after the event occurred. It was described as a CBC event with a 0% chance of containing a companion below $3M_{\odot}$, in other words it was 100% likely to be a binary black hole merger event. It had a false alarm rate (FAR) of about 1 in 6 months, which was above the threshold of 1 per month, and a skymap was produced by BAYESTAR (see Figure 4.1) that covered 1600 deg^2 for the 90% confidence region (LIGO Scientific Collaboration & Virgo Collaboration, 2017a). At the time the PIRATE alert pipeline wasn't operational and it took 4 days for the author to manually schedule an observation of one field within the error box at coordinates RA: 08:58:21 Dec: +51:43:26. This

was observed for a total of 7 nights starting from the 9$^{\text{th}}$ January at 2am UTC, with exposures of 120s taken in the B & R filters and ending on the 18$^{\text{th}}$ January at 23:57 UTC.

On the 1$^{\text{st}}$ June 2017 Abbott et al. (2017a) published a paper announcing that the candidate (G268556) had been elevated to a confirmed gravitational wave detection (GW170104) following further analysis. The paper showed that this gravitational wave signal was produced by the merger of two stellar mass black holes with masses of $31.2^{+8.4}_{-6.0}M_{\odot}$ and $19.4^{+5.3}_{-5.9}M_{\odot}$ at a distance of 880^{+450}_{-390} Mpc. Several other groups contributed in the follow up of this event but only a handful published any results and none of them were by optical telescopes.

Goldstein et al. (2017a) reported that Fermi detected no candidate electromagnetic counterpart with either of its GBM or LAT instruments during their observations of GW170104. Savchenko et al. (2017) reported on the INTEGRAL follow-up observations, which included scanning the entire skymap up to the 90% confidence level, and they constrained some upper limits in the 75 keV - 2 MeV energy range of $F_{\gamma} = 1.9 \times 10^{-7} erg/cm^2$ to $F_{\gamma} = 10^{-6} erg/cm^2$ respectively. They were also unable to confirm a claim by the AGILE group (Verrecchia et al., 2017) that reportedly detected a γ-ray (E2) in conjunction with the LIGO observations. In their paper, Verrecchia et al. (2017) described how the MCAL instrument on AGILE detected a weak event (called E2) occurring $0.46 \pm 0.05s$ before T_0, with a e post-trial probability of being temporally associated with GW170104 of $2.4\sigma - 2.7\sigma$. Lastly, ANTARES Collaboration et al. (2017) reported that the neutrino telescope ANTARES didn't detect any neutrino candidates within $\pm 500s$ of the GW event.

4.1.2 Candidate alert G270580 observations

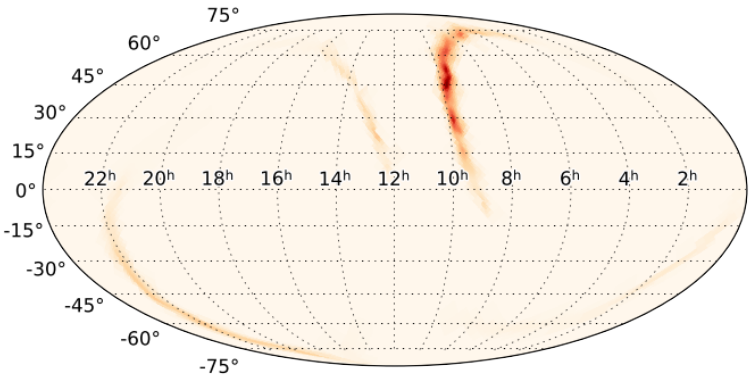

Figure 4.2: The Skymap produced by LIB for gravitational wave alert G270580, with Right Ascension (RA) along the x-axis and Declination (Dec) on the y-axis.

Sixteen days after the last alert, the LVC released another GCN notice to EM partners on the 20$^{\text{th}}$ January 2017 at 13:38 UTC, just over an hour after it was detected, but this time the interferometers had detected what looked to be a burst event instead. The false alarm rate (FAR) of this event was fairly low at 1 in 2.4 months; however, as it was above the minimum threshold it was distributed to EM partners. The skymap accompanying the alert was produced by the LIB search pipeline (see Figure 4.2) and contained a 90% credible region covering 3100 deg^2, located mainly in the northern celestial hemisphere (LIGO Scientific Collaboration & Virgo Collaboration, 2017b).

At this time the alert pipeline was still incomplete and as this alert arrived in the daytime immediate observations with PIRATE weren't possible. Furthermore,

bad weather at the observatory meant that the first images weren't obtained until the night of the 22nd January, meaning the initial follow-up response was delayed by two days. A total of 212 frames were taken on the first night of observations (112 in B and 100 in R filters), with an exposure time of 100s, covering 28 separate fields of view in the sky (these were labelled as the "Sectors" fields). Repeat observations of the same fields took place on the 23rd, 24th, 25th and 26th January.

Many EM observing partners were able to follow-up this event, including several optical telescope like PIRATE; however, on the 28th June 2017 the LVC retracted the alert due to data quality issues stemming from snow ploughing in the area at the time of the detection. For this reason further data analysis of this event was discontinued (LIGO Scientific Collaboration & Virgo Collaboration, 2017k).

4.1.3 Candidate alert G274296 observations

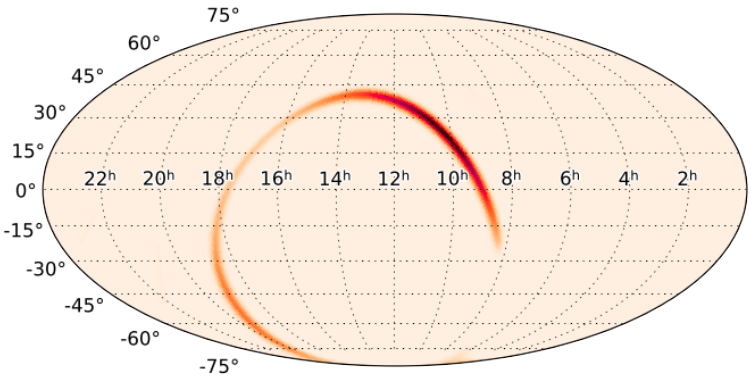

Figure 4.3: The updated Skymap produced by cWB for gravitational wave alert G274296, with Right Ascension (RA) along the x-axis and Declination (Dec) on the y-axis.

On the 17$^{\text{th}}$ February 2017 the LVC reported a new candidate gravitational wave event (G274296) emanating from another burst event (LIGO Scientific Collaboration & Virgo Collaboration, 2017c). This event was initially assigned a false alarm rate of one in two months and even though the candidate event occurred at 06:05 UTC the alert containing a skymap wasn't sent out via the GCN network until 23:05 UTC, this was attributed to a data processing issue. The skymap itself was produced by the cWB pipeline and once the alert was received, prompt follow-up observations with PIRATE were initiated manually as the alert pipeline was still incomplete. The first follow-up observations were taken with PIRATE at 23:39 UTC, just over 17.5hrs after the initial alert was received.

On the first night of observations PIRATE was able to image four separate fields of the cWB skymap (labelled Eggington), taking a total of 96 frames using the R filter with 100s exposures. Observations continued 2 days later due to bad weather, and in total the Eggington fields were observed for 5 out of the 8 nights following the alert. Follow-up observations ceased when a new alert was received from the LVC on the 25$^{\text{th}}$ January.

An updated skymap (see Figure 4.3) was produced again by cWB and released by LVC to EM partners on the 29$^{\text{th}}$ June 2017 (LIGO Scientific Collaboration & Virgo Collaboration, 2017j), improving on the previous sky localisation map with 90% confidence regions spanning 1153 deg^2. This event is currently still in the candidate stage and with an updated false alarm rate of one per six months, it is still unlikely to be reclassified as a significant detection.

4.1.4 Candidate alert G275404 observations

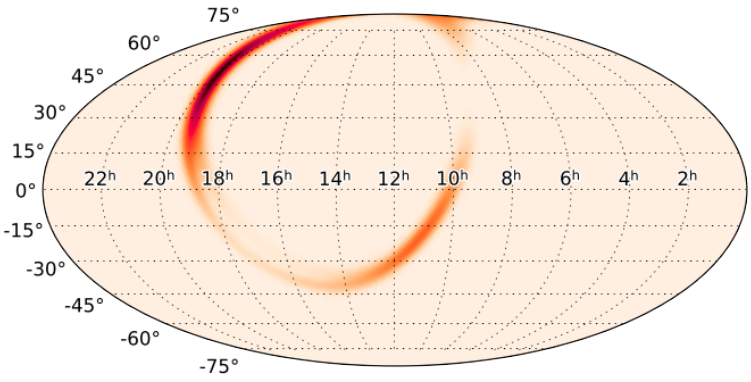

Figure 4.4: The Skymap produced by BAYESTAR for gravitational wave alert G275404, with Right Ascension (RA) along the x-axis and Declination (Dec) on the y-axis.

The next candidate gravitational wave alert (G275404) was sent by the LVC to EM partners on the 25th January 2017 at 18:55 UTC, with a latency of just 25 minutes after a CBC signal was detected in the LIGO detectors. This allowed enough time to manually plan for observations with PIRATE on Tenerife; which commenced at 22:18 UTC. This particular event was close to the FAR threshold of 1 per month and it was reported that if this was astrophysical in origin then the probability that one or more of the compact objects was a neutron star was 100% (LIGO Scientific Collaboration & Virgo Collaboration, 2017d).

Initial sky localisation was provided by BAYESTAR which generated a skymap (see Figure 4.4) that spanned 2100 deg^2 with 90% confidence regions. This covered

a huge range of latitudes from +90° to -45° declination due to the banana shape of the skymap (LIGO Scientific Collaboration & Virgo Collaboration, 2017d). Because this skymap spanned such a huge area it was possible to select two separate regions to follow up with PIRATE at different parts of the night. One region (Alpha) focused on the southern arc stretching down from the celestial equator at RA≈ +10hr, while a second region (Omega) was chosen on the northern arc where the highest probability pixels were located. For each region a total of 49 (Alpha) and 50 (Omega) separate fields of view were observed by PIRATE, each with 60s exposures in the R filter.

Manually scheduled observations with PIRATE started less than 4hrs after the event at 22:18 UTC; however, the first observations were incomplete as the telescope didn't slew to any of the targets and instead observed the same field 386 times in one night, this was due to human error. Observations continued from the 26$^{\text{th}}$ February until 6$^{\text{th}}$ March when the telescope was needed for scheduled curriculum activities. A total of 569 images were obtained across the 99 fields observed during the follow-up of this alert.

An updated skymap produced by BAYESTAR was sent out to EM observing partners by the LVC on the 8$^{\text{th}}$ March 2017 with more conservative assumptions leading to the 90% credible region expanding to cover 17000 deg^2 (LIGO Scientific Collaboration & Virgo Collaboration, 2017f). Many other groups also contributed to the follow-up of this alert and reported their observations to the LIGO-Virgo EM collaboration via GCN Circulars; however, on the 5$^{\text{th}}$ April the LVC provided an update on the offline analysis of this trigger and deemed that it was no longer a trigger of interest due to its low significance (LIGO Scientific Collaboration & Virgo Collaboration, 2017g).

4.1.5 Candidate alert G275697 observations

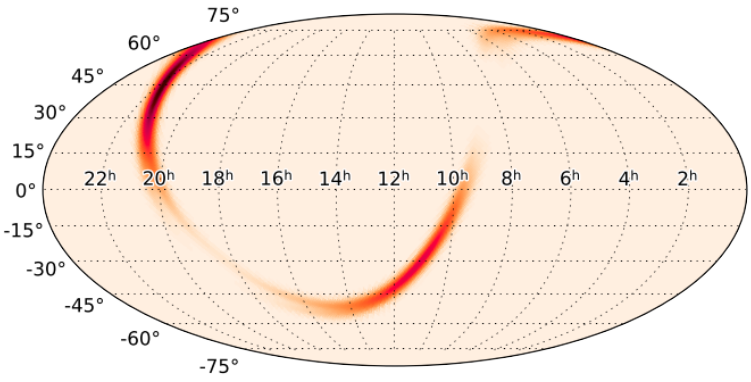

Figure 4.5: The Skymap produced by BAYESTAR for gravitational wave alert G275697, with Right Ascension (RA) along the x-axis and Declination (Dec) on the y-axis.

Just two days after the previous alert the LVC sent out another alert identifying the third candidate CBC merger event (G275697) of O2 so far. At 19:24 UTC on the 27$^{\text{th}}$ February 2017, less than half an hour after the event was detected, the GCN notice for the event was distributed to EM follow-up partners; the first time this had been achieved during O2. Again like the previous alert this had a low false alarm rate of about one in two months, and was also given a 100% chance of containing at least one neutron star if the event was astrophysical in origin (LIGO Scientific Collaboration & Virgo Collaboration, 2017e). Thus representing another candidate event with the potential to contain an electromagnetic counterpart that warranted rapid and extensive follow-up observations. With only two detectors online at the

time, the size of the sky localisation area was still extremely large at 1800 deg^2 up to 90% confidence regions, and this again spanned both the Northern and Southern Hemispheres, as shown in Figure 4.5.

PIRATE was able to monitor 18 fields of view (labelled Beta) in the southern arc of the skymap, in addition to the 99 it was already observing for G275404. Observations began less than 5hrs after the event at 23:50 UTC and consisted of 100s exposures taken solely in the R filter. Observations continued for 14 nights, with two nights lost to bad weather; and in total 452 frames were obtained with PIRATE covering each individual field between 21 and 28 times.

Similarly to the previous alert the significance of this event was reanalysed offline and it was determined that the signal detected at the time of the alert wasn't significant enough to warrant further follow-up observations; this was also sent on the 5^{th} April 2017 (LIGO Scientific Collaboration & Virgo Collaboration, 2017h).

4.1.6 Candidate alert G284239 observations

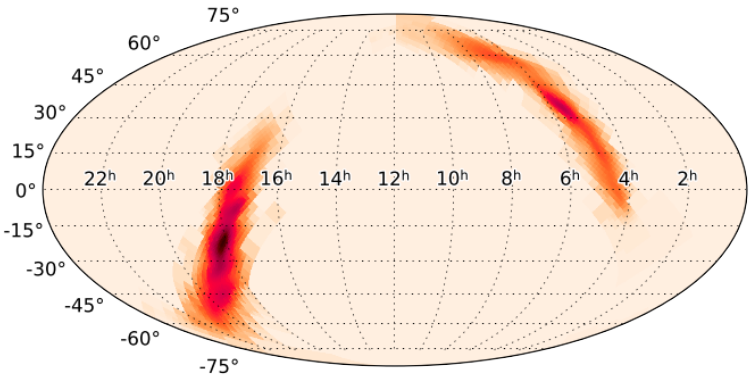

Figure 4.6: The Skymap produced by LIB for gravitational wave alert G284239, with Right Ascension (RA) along the x-axis and Declination (Dec) on the y-axis.

The next gravitational wave alert that PIRATE responded to was G284239 which was a burst event detected by both LIGO detectors at 22:26 UTC on the 2nd May 2017. The alert itself was not sent by the LVC until 14:29 UTC due to technical problems (LIGO Scientific Collaboration & Virgo Collaboration, 2017i), which resulted in PIRATE not being able to perform follow up observations for over 22hrs after the event. The LALInference Burst (LIB) search pipeline generated a skymap for the event which covered an area of 3593 deg^2 with a 90% confidence region, see Figure 4.6.

When PIRATE was finally able to start follow-up observations on the night commencing the 3rd May, it began monitoring 12 different fields of view (labelled May) in the southern arc of the skymap and 7 fields in the northern arc. Each field

was imaged up to four times a night for five consecutive nights, with every exposure being 100s long and taken in the R filter. In total 160 frames were collected in the follow up of this alert, covering the 19 separate fields. Observations ceased on the 8^{th} May to allow for urgent repairs to be made to the telescope's shutter.

For several weeks the iris shutter on PIRATE had been sticking and resulted in an under-exposure of all but the very central pixels on the CCD chip. This caused problems with the science and, more importantly, calibration images. For this reason the data taken from this alert wasn't analysed, and further follow-up observations after the telescope's repair weren't performed.

4.1.7 Candidate alert G296853 observations

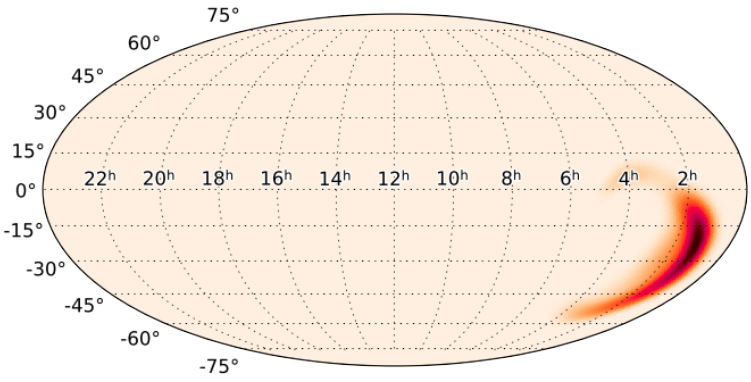

Figure 4.7: The Skymap produced by BAYESTAR for gravitational wave alert G296853, with Right Ascension (RA) along the x-axis and Declination (Dec) on the y-axis.

On the 9th August 2017 the LVC reported detecting another candidate gravitational wave event (G296853) at 08:28 UTC (with the alert being sent out to EM partners in under an hour). This event was identified as a binary black hole merger by three CBC search pipelines (gstlal, cWB and MBTA), and it was assigned a false alarm rate of one in four years by gstlal. In addition to this, a skymap was generated using the BAYESTAR source localisation algorithm (see Figure 4.7) that spanned a region of 1155 deg^2 up to 90% confidence levels, located almost entirely in the Southern Hemisphere (LIGO Scientific Collaboration & Virgo Collaboration, 2017l).

In the 3 months since the last alert the author was able to complete the auto-

mated alert pipeline which went live around mid-July 2017; hence, all the follow-up observations from now on were scheduled autonomously by the pipeline. For this particular event, as the alert was received early in the morning it allowed plenty of time to manually adjust the pipeline output and attempt to maximise the efficiency of the tiling process.

The first follow-up observations to this alert with PIRATE weren't made until 02:24 UTC on the 10^{th} August, almost 18hrs after the event. PIRATE was able to observe 34 fields (labelled Sigma) covering the top 6.67% of probability pixels in the skymap, the coordinates of all these fields are given in Table 4.2. Observations consisted of pairs of 60s exposures taken up to two times per night with the R filter, for 8 days following the initial alert; each field was observed between 16 and 30 times over this period. In total 767 frames were obtained during the follow-up of this alert, and these were all passed on to the data processing stage to be processed by the author and search for any potential optical counterpart. The method for this is described in the next section, and the results of all these counterpart searches are presented section 4.3.1.

Field	RA (deg)	DEC (deg)	RA (hh:mm:ss)	Dec (dd:mm:ss)
Sigma_1	16.5250000	-28.8011111	01:06:06	-28:48:04
Sigma_2	16.5250000	-27.7844444	01:06:06	-27:47:04
Sigma_3	16.5250000	-26.7772222	01:06:06	-26:46:38
Sigma_4	16.7000000	-25.6130556	01:06:48	-25:36:47
Sigma_5	16.8750000	-24.4602778	01:07:30	-24:27:37
Sigma_6	17.0500000	-23.3180556	01:08:12	-23:19:05
Sigma_7	17.5791667	-22.1852778	01:10:19	-22:11:07
Sigma_8	17.7541667	-27.9530556	01:11:01	-27:57:11
Sigma_9	17.7541667	-26.9444444	01:11:01	-26:56:40

Table 4.2 continued from previous page

Field	RA (deg)	DEC (deg)	RA (hh:mm:ss)	Dec (dd:mm:ss)
Sigma_10	17.7541667	-28.9716667	01:11:01	-28:58:18
Sigma_11	17.7541667	-30.0000000	01:11:01	-30:00:00
Sigma_12	17.7541667	-21.0619444	01:11:01	-21:03:43
Sigma_13	17.9291667	-25.7786111	01:11:43	-25:46:43
Sigma_14	18.1041667	-24.6244444	01:12:25	-24:37:28
Sigma_15	18.2791667	-23.4805556	01:13:07	-23:28:50
Sigma_16	18.2791667	-19.9466667	01:13:07	-19:56:48
Sigma_17	18.8083333	-18.8394444	01:15:14	-18:50:22
Sigma_18	18.8083333	-22.3466667	01:15:14	-22:20:48
Sigma_19	18.9833333	-27.1119444	01:15:56	-27:06:43
Sigma_20	18.9833333	-21.2216667	01:15:56	-21:13:18
Sigma_21	18.9833333	-28.1222222	01:15:56	-28:07:20
Sigma_22	19.1583333	-25.9444444	01:16:38	-25:56:40
Sigma_23	19.1583333	-17.5827778	01:16:38	-17:34:58
Sigma_24	19.3375000	-24.7886111	01:17:21	-24:47:19
Sigma_25	19.5125000	-23.6433333	01:18:03	-23:38:36
Sigma_26	19.5125000	-20.1055556	01:18:03	-20:06:20
Sigma_27	20.0375000	-22.5080556	01:20:09	-22:30:29
Sigma_28	20.0375000	-18.9972222	01:20:09	-18:59:50
Sigma_29	20.2166667	-17.8961111	01:20:52	-17:53:46
Sigma_30	20.2166667	-21.3819444	01:20:52	-21:22:55
Sigma_31	20.7416667	-16.8019444	01:22:58	-16:48:07
Sigma_32	20.7416667	-20.2644444	01:22:58	-20:15:52
Sigma_33	21.2708333	-18.2100000	01:25:05	-18:12:36

Table 4.2 continued from previous page

Field	RA (deg)	DEC (deg)	RA (hh:mm:ss)	Dec (dd:mm:ss)
Sigma_34	21.7958333	-17.1138889	01:27:11	-17:06:50

Table 4.2: Coordinates of all Sigma fields observed during the follow up of G296853.

4.1.8 GW170814 Observations

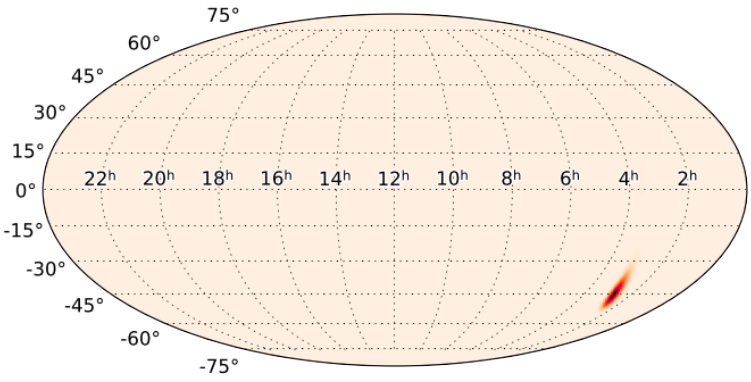

Figure 4.8: The Skymap produced by BAYESTAR for gravitational wave alert G297595, with Right Ascension (RA) along the x-axis and Declination (Dec) on the y-axis.

Just five days after the previous alert, on the 14$^{\text{th}}$ August 2017 the LVC sent out an alert identifying another candidate binary black hole merger (G297595), this time with an extremely low false alarm rate of 1 in 80 000 years. For the first time since the start of O2, Virgo was also able to detect a faint signal in conjunction with the two LIGO detectors, and this had big consequence on the size of the initial skymap sent to EM partners, see Figure 4.8. This skymap was produced by BAYESTAR and sent along with the initial alert at 11:01 UTC, and was confined to a region of 97 deg^2 up to 90% confidence (LIGO Scientific Collaboration & Virgo Collaboration, 2017m). The location of this skymap was too far south to be observed with PIRATE; however, two days later at 13:55 UTC the LVC released a second skymap (see Figure 4.9) that

was generated using LALInferece instead and this spanned an area approximately twice the size. This meant that the northern tip of this new skymap was visible from Tenerife, and although it was a lower probability region, it was decided that PIRATE should still perform follow-up observations regardless.

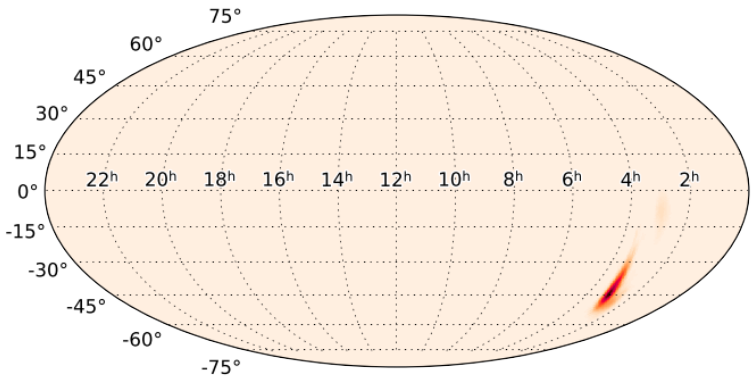

Figure 4.9: The Skymap produced by the LALInference pipeline for gravitational wave alert G297595, with Right Ascension (RA) along the x-axis and Declination (Dec) on the y-axis.

Automated observations were scheduled immediately after receiving the updated skymap; but as this arrived during the daytime it was a further 15hrs before PIRATE took its first images at 04:45 UTC on the 16th August 2017. Although PIRATE was scheduled to observe 34 fields (labelled Nu) it only ended up monitoring 14 of those fields due to their proximity to the horizon limit of the telescope, a list of these fields is given in Table 4.3. The images consisted of 100s exposures taken with the R filter and due to the low declination, are at a relatively high airmass value. Observations

Field	RA (deg)	DEC (deg)	RA (hh:mm:ss)	Dec (dd:mm:ss)
Nu_8	48.38378906	-34.77202020	03:13:32.11	-34:46:19.27
Nu_11	48.77929688	-33.73403586	03:15:07.03	-33:44:02.53
Nu_13	48.99902344	-32.70846106	03:15:59.77	-32:42:30.46
Nu_16	49.48242188	-31.60690457	03:17:55.78	-31:36:24.86
Nu_17	49.65820313	-34.90836627	03:18:37.97	-34:54:30.12
Nu_19	50.05371094	-33.86870460	03:20:12.89	-33:52:07.34
Nu_21	50.27343750	-32.84155510	03:21:05.63	-32:5029.60
Nu_24	50.66894531	-31.82615778	03:22:40.55	-31:49:34.17
Nu_25	50.71289063	-30.82180969	03:22:51.09	-30:49:18.51
Nu_28	51.06445313	-29.78486982	03:24:15.47	-29:47:05.53
Nu_29	51.28417969	-34.22886633	03:25:08.20	-34:13:43.92
Nu_30	51.59179688	-33.19745409	03:26:22.03	-33:11:50.83
Nu_33	51.89941406	-32.17805154	03:27:35.86	-32:10:40.99
Nu_34	51.89941406	-31.12635112	03:27:35.86	-31:07:34.86

Table 4.3: Coordinates of all Nu fields observed during the follow up of GW170814.

lasted for 5 nights and a total of 116 images were collected before a new alert took priority and telescope time was reallocated. These EM observations were uploaded to GraceDb on the 29$^{\text{th}}$ August and a GCN Circular was distributed to EM partners containing a summary of PIRATE's follow-up observations on the 15$^{\text{th}}$ September (Roberts, 2017).

On the 6$^{\text{th}}$ October 2017 Abbott et al. (2017c) announced that they had detected a binary black hole merger on the 14$^{\text{th}}$ August 2017 and had renamed the candidate alert GW170814. This was the first triple detector discovery, and also the first confirmed gravitational wave event that PIRATE followed up. Like previous

alerts, several EM partners contributed to the follow-up of this trigger, even in the knowledge that it was unlikely to contain an EM counterpart; a list of all contributions can be found on the GCN web page dedicated to this event[2] where all the GCN Circulars regarding this event are published.

Similar to the data from the previous alert, the data obtained with PIRATE from the follow-up of this alert was also processed to look for any optical counterparts with the results given in section 4.3.2.

[2] https://gcn.gsfc.nasa.gov/other/G297595.gcn3

4.1.9 Candidate alert G298936 observations

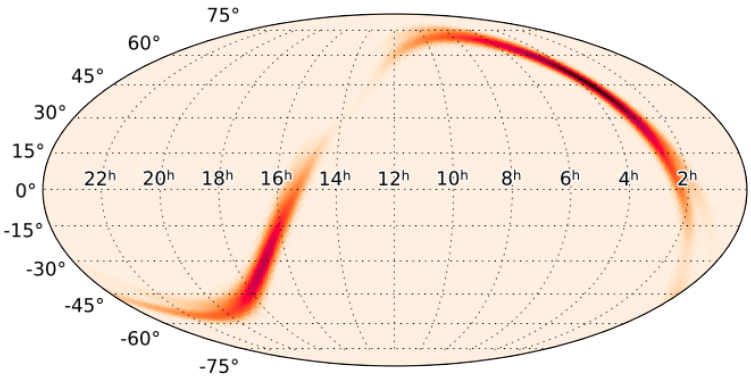

Figure 4.10: The Skymap produced by BAYESTAR for gravitational wave alert G298936, with Right Ascension (RA) along the x-axis and Declination (Dec) on the y-axis.

The next candidate gravitational wave alert that PIRATE responded to was G298936, which was a CBC event detected by the gstlal search pipeline at 13:13 UTC on the 23rd August 2017. The first alert that was sent at 13:33 UTC was just a preliminary alert and so it didn't contain a skymap; however, the initial alert sent 3 minutes later did contain a skymap produced by BAYESTAR and this covered an area of 2145 deg^2 up to 90% confidence regions, see Figure 4.10 (LIGO Scientific Collaboration & Virgo Collaboration, 2017n).

PIRATE's automated alert pipeline identified 13 fields in this skymap to observe in the coming night; however, a third "update" alert was sent by the LVC at 16:49 UTC containing a second updated skymap (see Figure 4.11). This new skymap was

released after the Virgo data was inspected and re-analysed offline using the PyCBC pipeline, leading to a more precise sky localisation of 1219 deg^2 (LIGO Scientific Collaboration & Virgo Collaboration, 2017o). The automated alert pipeline again processed this alert and skymap to produce another set of observing requests, this time only 5 fields (labelled Iota) were targeted (see Table 4.4) with PIRATE and observations began at 02:09 UTC (13hrs after the initial trigger).

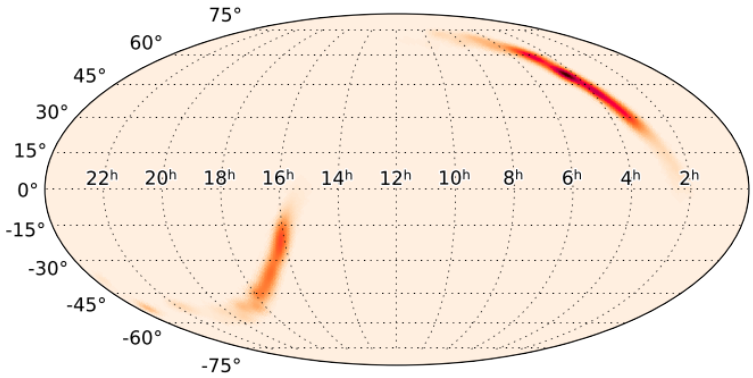

Figure 4.11: The Skymap produced by BAYESTAR for gravitational wave alert G298936 with the addition of the Virgo detector data. The Right Ascension (RA) is along the x-axis and Declination (Dec) on the y-axis.

Observations consisted of pairs of 100s exposures taken with the R filter, and they only lasted for two days due to the arrival of a subsequent gravitational wave alert taking priority. As a result PIRATE only acquired 38 frames, imaging each of the 5 fields up to 4 times a night. This was still enough data to be able look for a rapidly fading transient; however, the luminosity of the transient would have to

Field	RA (deg)	DEC (deg)	RA (hh:mm:ss)	Dec (dd:mm:ss)
Iota_1	65.67285383	49.79970220	04:22:41.48	49:47:58.93
Iota_2	66.17045455	48.92279516	04:24:40.91	48:55:22.06
Iota_3	66.77083333	49.70239033	04:27:05.00	49:42:08.61
Iota_4	67.18160377	50.48004426	04:28:43.58	50:28:48.16
Iota_5	67.86374134	49.60504813	04:31:27.30	49:36:18.17

Table 4.4: Coordinates of all Iota fields observed during the follow up of G298936.

change considerably in between observations to be identifiable after two days. The results of this search campaign are also presented in section 4.3.3.

On the 29$^{\text{th}}$ August the LVC released another updated sky localisation map, this time produced by LALInference, with a decrease in the 90% confidence region from 1219 to 952 deg^2; however, as PIRATE targeted the top 6.67% pixels these observations still fall within this new refined skymap (LIGO Scientific Collaboration & Virgo Collaboration, 2017q). The next day on the 30$^{\text{th}}$ August the author reported PIRATE's observations to the EM follow-up community in the form of a GCN Circular (LIGO Scientific Collaboration & Virgo Collaboration, 2017r).

4.1.10 Candidate alert G299232 observations

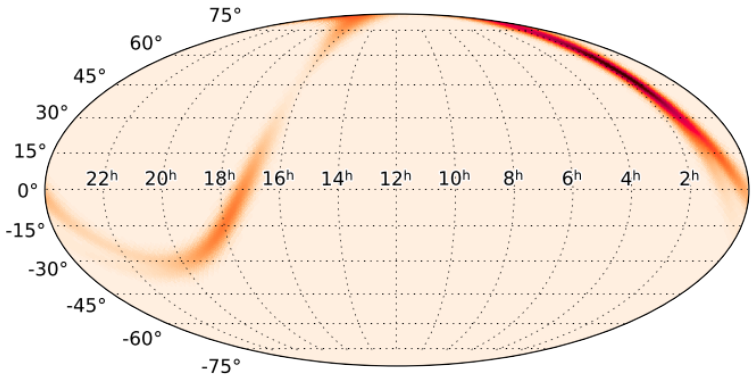

Figure 4.12: The Skymap produced by BAYESTAR using LIGO & Virgo data for gravitational wave alert G299232, with Right Ascension (RA) along the x-axis and Declination (Dec) on the y-axis.

The last candidate gravitational wave alert for O2 was sent just two days after the previous alert and on the very last day of O2 operation; on the 25th August 2017 at 13:13 UTC the LIGO & Virgo detectors identified a CBC merger candidate with a false alarm rate of just over one per two months, making it a marginal detection just above the threshold. If this event was astrophysical in origin then the object's properties appeared consistent with the merger of a black hole and a neutron star (LIGO Scientific Collaboration & Virgo Collaboration, 2017p).

The initial GCN Notice alert was sent by the LVC to EM partners at 13:39 UTC; however, the link was forbidden and EM partners couldn't access the skymap on GraceDB, so a GCN Update was issued at 14:20 UTC containing a valid skymap

Field	RA (deg)	DEC (deg)	RA (hh:mm:ss)	Dec (dd:mm:ss)
Kappa_1	30.7625	38.6822222	02:03:03	38:40:56
Kappa_2	31.1125	39.4508333	02:04:27	39:27:03
Kappa_3	31.4666667	40.2280556	02:05:52	40:13:41
Kappa_4	31.8166667	41.0144444	02:07:16	41:00:52
Kappa_5	32.1666667	41.8102778	02:08:40	41:48:37
Kappa_6	32.3208333	42.6097222	02:09:17	42:36:35

Table 4.5: Coordinates of all Iota fields observed during the follow up of G299232.

link. This skymap was produced by BAYESTAR and was constrained to an area of 2040 deg^2 up to 90% confidence regions, as shown in Figure 4.12. The automated alert pipeline was running at the time so once the skymap was received it was able to calculate 6 fields (labelled Kappa) to observe with PIRATE for the coming night, in the highest 6.67% probability region. The exact coordinates of these fields are shown in Table 4.5.

Observations with PIRATE didn't begin until 23:28 UTC on the 28^{th} August due to bad weather in Tenerife. During the intervening three days, one of the other EM follow-up groups, MASTER (Lipunov et al., 2016), identified a potential transient object while searching for an optical counterpart to this alert. They assigned it an identity (MASTER OT J033744.97+723159.0), and noted that its location was on the edge of the galaxy NGC1343 (Lipunov, 2017a,b). Given its unfiltered detection magnitude of 17, it was expected that this object could be visible from Tenerife with PIRATE and so the object was added to the scheduling queue to be observed every night.

PIRATE monitored the 6 fields (Kappa) plus the MASTER transient for 7 nights continuously from the 28^{th} August to 4^{th} September, with exposures of the 6 fields

(Kappa) lasting 100s in the R filter and images of the MASTER transient requiring 300s exposures in the B & R filters. The author informed the EM community of PIRATE's observations with a GCN Circular on the 29th August (Roberts et al., 2017), this also included an estimated magnitude of the MASTER transient in the R & B filters of 16.49 ± 0.06 and 17.11 ± 0.11 respectively. Observations of the 6 fields (Kappa) then ceased, but PIRATE continued to monitor the MASTER transient for a further 11 weeks as it had been subsequently classified as a Type IIb supernova (Jonker, 2017; Copperwheat and Steele, 2017).

In total PIRATE obtained 234 images in the follow up of the initial 6 fields (Kappa) and a further 339 from the observations of the MASTER supernova discovery. All images from the follow-up of this alert were processed using the method outlined in the next section, with the exception of the MASTER supernova images which were analysed separately given the coordinates of the target were already known. The results from both the gravitational wave search and the supernova follow-up are given in section 4.3.4.

4.1.11 Summary of Observations

Of these ten alerts that PIRATE followed up, there were only four that had high quality data or were not later withdrawn by the LVC, the analysis of these four alerts is given in section 4.3. For illustrative purposes all four sets of follow-up observations are displayed on one plot in Figure 4.13. These consisted of 1155 individual exposures in total, taken across 59 regions on the sky, which covered four LVC alert triggers: G296853 (Sigma), G297595 (Nu), G298936 (Iota) & G299232 (Kappa). As all these observations were taken in August, the distribution of these fields across the sky is primarily confined by the position of the Sun at that time of year, prohibiting observations in the daytime half of the sky. The individual confinement of the observations is dictated by the individual sky localisation map

(skymap) from each alert, these can be seen in Figures 4.7, 4.9, 4.11 and 4.12.

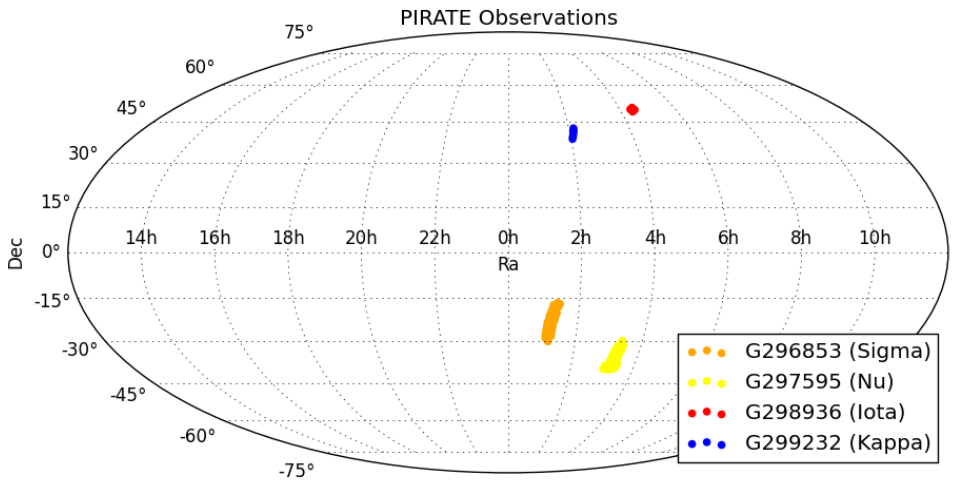

Figure 4.13: The Skymap produced by BAYESTAR for gravitational wave alert G298936 with the addition of the Virgo detector data.

A timeline of all the follow-up observations made with PIRATE during O2 is displayed in Figure 4.14, spanning 11 months throughout 2017. The names for these individual observing campaigns were initially meant for internal reference only, and could not contain the LIGO alert name for confidentiality reasons; but to avoid confusion, these names have been kept for continuity purposes. There was no particular pattern to this naming convention but Greek letters were often used as a memorable way to refer to each follow-up campaign.

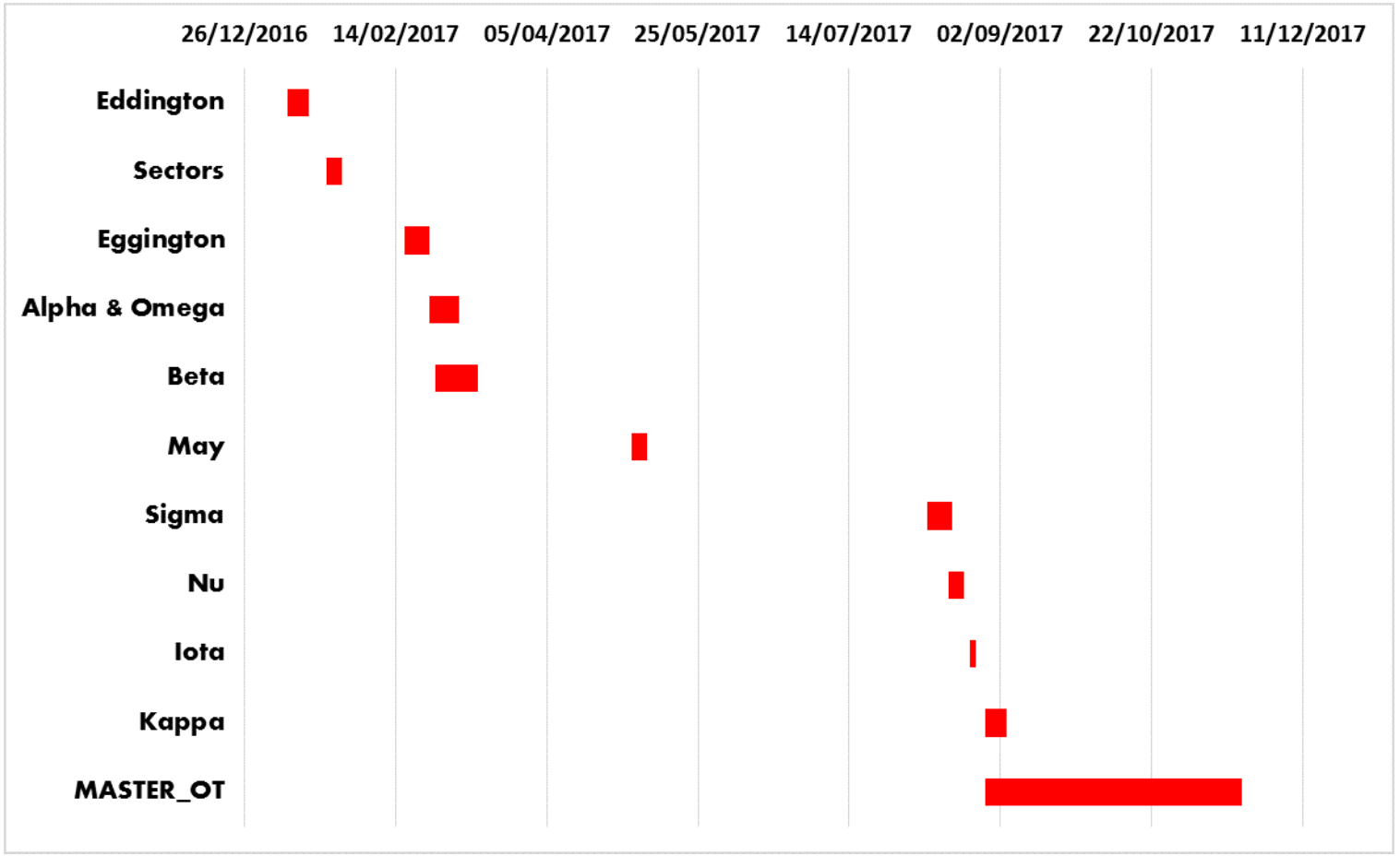

Figure 4.14: Timeline of follow-up observations made with PIRATE during O2.

As mentioned at the beginning of this chapter, PIRATE just missed out on observing the optical counterpart to the first ever detected Binary Neutron Star merger. However, given the resulting limiting magnitudes obtained during the other follow-up observations were in the region of 17.5 magnitude at 100s exposure time, it's not too difficult to assume that given the right observing conditions (good seeing, low airmass etc.) the optical counterpart to GW170817 would have been within the detectable range of PIRATE with a SNR greater than 5-10. This is based on the assumption of a detection magnitude of 17.46 in the R band that was reported by Valenti et al. (2017) 11 hours after the merger event. Given that the measured decay rate was 1.1mag/day (Valenti et al., 2017), it's also possible to assume that observations been possible sooner, that the transient would have been even brighter within the first few hours after merger.

For a small telescope the size of PIRATE, there would be limited opportunity to revisit the transient to take further measurements, due to this rapid decline in luminosity, especially if the telescope was still in autonomous mode and the data containing the transient detection had not yet been processed. This limits the scientific value PIRATE is able to gain from a source at the edge of it's detection capabilities. But given the initial priority of all EM partners was to detect a source, PIRATE has proved that it was capable of at least detecting the EM counterpart to a GW merger event; which given that at the time the sky localisation was very poor, signifies a valuable contribution to the combined EM follow-up efforts by observatories all over the world.

4.2 Method for searching for optical counterparts

Described here is the method used to search for optical counterparts to gravitational wave alerts, more specifically using the data obtained with PIRATE during its follow-up observations. This process involves a number of stages and starts with simple image reduction and calibration, followed by the extraction of individual sources in each image, the plotting of a light curve for every star in each image across the entire data set, and concludes with a manual identification process.

4.2.1 Image Calibration

To convert raw images into usable science data all images obtained with the telescope must be calibrated to account for optical and instrumental defects. The pipeline employed to do all the calibration of the data in this chapter was written by a colleague specifically for PIRATE data and it follows a standard calibration procedure. The individual steps in the process are outlined below:

1. Remove overscan regions on all images by removing 40 pixels from each side of the image.

2. Stack all bias frames together to create a master bias.

3. De-bias each individual dark frame to remove readout noise.

4. Scale each dark frame down to 1s and stack to create a master dark.

5. De-bias each flat.

6. Scale up master dark to each flat and subtract.

7. Stack each set of flats by filter and divide by the median counts to produce master flats for each filter.

8. Calibrate science frames using all three master calibration frames.

Once all the science images are calibrated then the last step is to plate solve the images to obtain WCS coordinates. The plate solve script in the pipeline uses a local version of the Astrometry.net[3] source catalogues to solve for each image in the data-set; with the correct WCS coordinates in place it is then possible to extract all the sources in the image.

4.2.2 Variability Search Toolkit (VaST)

After several tests with alternative software packages it was decided that the most suitable one to use was VaST[4], which is a variability search toolkit developed by Sokolovsky and Lebedev (2018) to search for variable objects in a series of images.

VaST works by identifying all the individual sources in an image using SExtractor (Bertin and Arnouts, 1996), and cataloguing each object's pixel coordinates and instrumental magnitude. This is performed on all images in the series to produce a set of catalogues, which are then cross-matched using a linear transformation of the images, with the first image of the series acting as the photometric and astrometric reference image. The software is then able to track individual sources throughout all the images in the data-set and ultimately produce a lightcurve for each one.

When plotting a lightcurve, VaST uses the first image in the series as a detection image and only generates lightcurves for objects detected in this image. This assumes that any transient observed by PIRATE would be at least detected in the first image given that they are expected to fade over time. However, this might not be the case if the seeing or airmass quality is very poor in the first image. This is hard to mitigate against when the location, and indeed the magnitude, of a potential transient is unknown. In cases where a second image was taken in quick succession,

[3] `http://nova.astrometry.net/`

[4] `http://scan.sai.msu.ru/vast/`

it could be possible to run VaST again without the poor quality image, but in most cases the telescope wont return to the same patch of sky for several hours as it tries to cover a large area of the skymap. Furthermore, it's reasonable to assume that if the first image had poor seeing or airmass, then a subsequent image taken immediately after would not have significantly improved observing conditions.

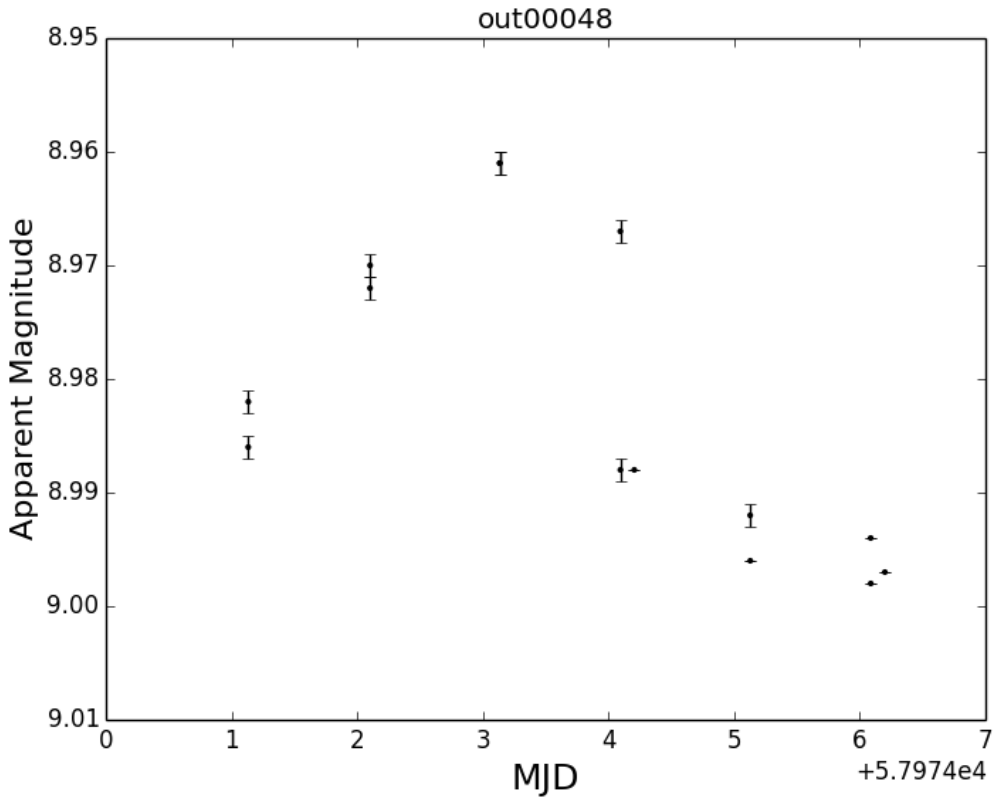

Figure 4.15: This is a sample lightcurve produced by VaST, this this case of an object identified in the Sigma_25 field in the follow up of LIGO candidate alert G296853.

In order to produce a reliable lightcurve the variations between images must be accounted for. Typically this is achieved using differential photometry between target stars and reference stars that show little variability; however, with VaST this

is done by matching stars from each image to the reference image and correcting the magnitude scales for all the images to the instrumental magnitude scale of the reference image. This means all the images in the data-set should be fairly self-consistent with each other, but not necessarily calibrated to an astronomical standard catalogue.

The lightcurves themselves are plotted using the instrumental magnitude & magnitude error provided by SExtractor, and the Modified Julian Date (MJD) provided by the FITS header of each image, as shown in Figure 4.15. Then for each object "VaST computes a number of variability indices characterising the scatter of magnitude measurements and/or smoothness of the lightcurve" (Sokolovsky et al., 2017). These indices use a variety of methods to highlight variability in an object's lightcurve. These indices can be broadly grouped together into the following categories, based on their purpose:

1. Quantifying the scatter of a lightcurve by calculating statistical distribution values such as Standard Deviation (σ), Robust Median Statistic (RoMS) (Rose and Hintz, 2007), Median Absolute Deviation (MAD) (Sokolovsky et al., 2017; Zhang et al., 2016) and Interquartile Range (IQR) (Sokolovsky et al., 2017).

2. Quantifying the smoothness of a lightcurve such as $1/\eta$ or the Variability Detection Statistic (S_B) (Sokolovsky et al., 2017).

3. Using a combination of the above methods, for example: Stetson's J index or Stetsons L index (Sokolovsky et al., 2017; Stetson, 1996).

4. Characterising the strength of a periodic signal in the lightcurve, using a periodagram for example.

Historically transients (and variable stars) would be detected by "blinking" a pair of images to identify any changes between them; however, this technique is inefficient

and only works well when both images are of comparable quality. An alternative is scatter searches, such as the ones used by VaST to calculate the statistical distribution of the values in a lightcurve, but these didn't work well when erroneous data points were included in the lightcurves as they failed to remove outliers. So highly erroneous data points would make some lightcurves appear more variable than they truly are.

Variability Index: Ratio of the mean square successive difference to the variance

After assessing the performance of the different variability indices in VaST with data from long term observations with PIRATE it was decided that the best index to use in the search for transients was $1/\eta$ where η is the ratio of the mean square successive difference over the variance. A test was also conducted with the observations taken of the MASTER Type IIb supernova target, where VaST was run on the data to produce a variability plot using the $1/\eta$ index to determine if it would highlight such a transient. The results of this test can be seen in Figure 4.16, where the object in question stands out against all other objects in the image with a $1/\eta$ value of 64.9.

This particular statistical method was developed by von Neumann (1941) to apply to observations/measurements taken when the standard deviation of a population remained constant but the mean varied gradually between observations, resulting in a long term trend that could be missed by conventional methods. Shin et al. (2009) have a more detailed explanation of this method and how it can be applied to large astronomical data-sets.

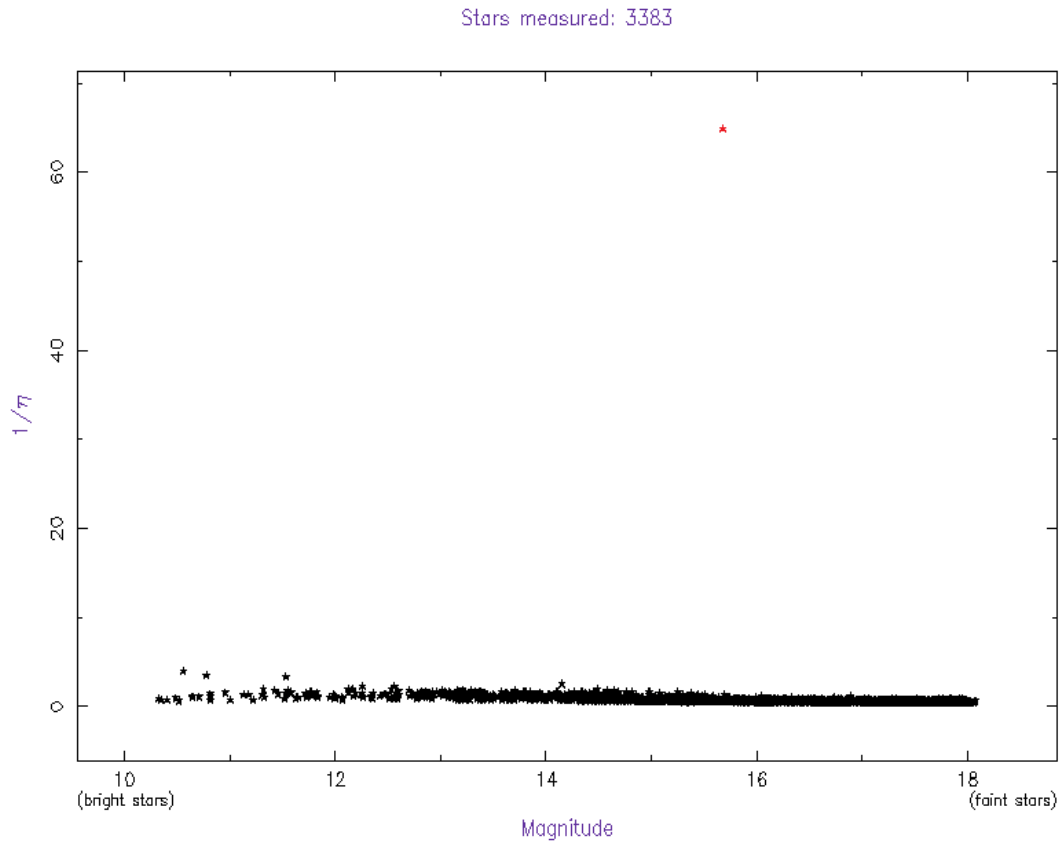

Figure 4.16: A plot showing the $1/\eta$ value as a function of magnitude for all the objects in a single image. The standout object (red star) is the MASTER Type IIb supernova, which varies in brightness significantly over time.

The ratio of the mean square successive difference to the variance computes the ratio of two independent variance values δ^2 and s^2, where

$$\delta^2 = \frac{\sum_{i=1}^{n-1}(x_{i+1} - x_i)^2}{n-1}, \tag{4.1}$$

is the mean square successive difference and

$$s^2 = \frac{\sum_{i=1}^{n}(x_i - \bar{x})^2}{n}, \tag{4.2}$$

is the square of the standard deviation. The δ^2 value differs from the variance in that it calculates the difference from the previous value in the data set, rather

than the difference from the mean. What this means is that when comparing two observations with identical means & variance, if one has a gradual change over time compared to the other, then this will be highlighted by difference in the δ^2 value; or more specifically, the ratio between the mean square successive difference and the variance

$$\eta = \frac{\delta^2}{s^2}. \tag{4.3}$$

This is exactly the sort of scenario that would occur when looking for a transient object in an image among thousands of non-varying stars with some scatter but no overall trend. Using the η ratio (more precisely $1/\eta$) enables VaST to identify which objects have a gradual but significant change in their brightness when compared to stars with similar or lower variance. What the tests with the supernova lightcurves showed was that using the $1/\eta$ variability index was a much more reliable way to identify these transients when compared to other variability indices such as IQR, MAD, Stetson's J index etc. The output of these variability indices from the test can be found in appendix C.

4.2.3 Magnitude Calibration

This last step in the calibration process is performed by VaST internally, and it is necessary in order to compare the results from this work to other publications and catalogues, using the apparent magnitude scale. This involves converting the instrumental magnitudes produced by SExtractor and calibrating them with a comprehensive star catalogue. For narrow fields of view (FOV) or short exposures this is usually achieved using the nearest standard star (assuming one is visible) of similar magnitude to the one being measured in order to calibrate the magnitude to it; however, with larger FOVs containing many thousands of stars a star catalogue can be used to determine the offset between the two data-sets. Correcting for this offset involves plotting line of best fit between the instrumental magnitudes and catalogue

magnitudes from the APASS (AAVSO Photometric All-Sky Survey) catalogue, this function is typically linear but VaST can also try to fit a parabola or "photocurve" to the data. By fitting a function through all the data points VaST is able to accurately compute a magnitude scale for each image so the instrumental magnitudes of the objects can be converted into apparent magnitudes, and these are what get plotted in the final output of the variability search process.

4.2.4 Manual identification process

The final stage in this search process is for the user to manually identify any significant detections that could represent a potential transient in the data by eye. To help with the visual search, predefined limits were agreed before the analysis of the data began. It was decided that the threshold used in this project would be a $(1/\eta)$ value of 2 or higher, except in cases where there were no objects above this limit in which case the top 3 would be included instead. This is a relatively low limit compared to the variability expected from transients such as the supernova discussed earlier; however, there is a significant enough deviation from the rest of the data set to justify further investigation of these variables. Even if a transient isn't discovered, they are more than likely going to be highly variable stars of some kind, some of which may not have been observed before.

After each object's lightcurve is viewed by eye, a classification is assigned to the object depending on the morphology of the lightcurve; there are four categories created by the author and these are explicit definitions for this work and not to be confused with an external classification scheme. These categories are: long period variable, (short) variable, faint star or transient and examples of these four types are shown in Figure 4.17. In addition to this classification, every object was cross matched in SIMBAD[5] to try and identify any known sources; if an object was

[5] `http://simbad.u-strasbg.fr/simbad/sim-fid`

identified then its identifier was used instead of a classification, and these come under the cross-matched sources header in Table 4.6. The criteria for classifications is given below:

Long Period Variable These are defined by a distinctive long-term trend in the lightcurve and have relatively tight error bars, lower than the variation of the data. They are distinct from variables in that they have an incomplete period over the timescale of observations. "Long" in this context, is anything longer than the timescale of a given set of observations.

Variable These objects vary a lot within the observation period, sometimes with a distinct pattern, but some can be more erratic. To qualify for this category, they must include an entire period within the duration of observations, otherwise they will be classified as a long period variable.

Faint Star Lightcurves that are dominated by large error bars as a result of low SNR data are classified as faint stars. This is because these lightcurves are essentially flat when the error bars are taken into account but the software finds them hard to distinguish from true variables due to this noise. Any magnitude cut of the data to avoid this could have missed a faint transient in the data.

Transient These objects appear to fade over time, typically with an exponential or linear trend. The crucial distinction from long period variables is that the brightest data point comes first, with subsequent points equal or fainter in magnitude.

These classifications are a qualitative means to narrow down the results into a handful of potential transient candidates, disregarding any variables that were also identified. It was necessary to take this manual step due to the large uncertainties

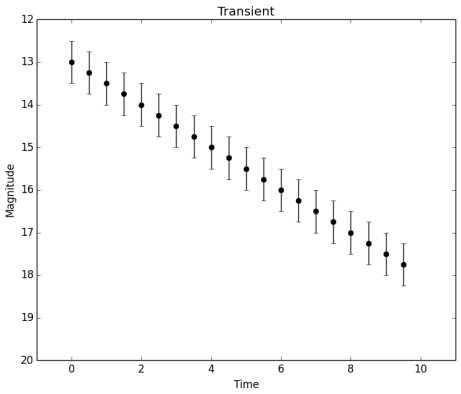

(a) Example of a transient lightcurve.

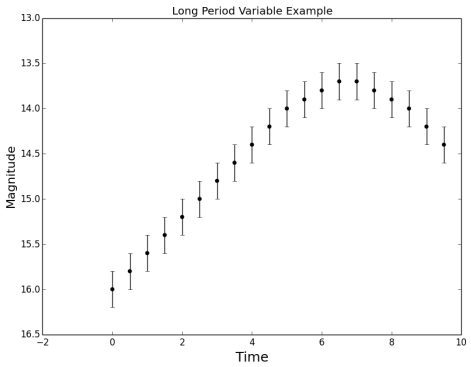

(b) Example of a long period variable lightcurve.

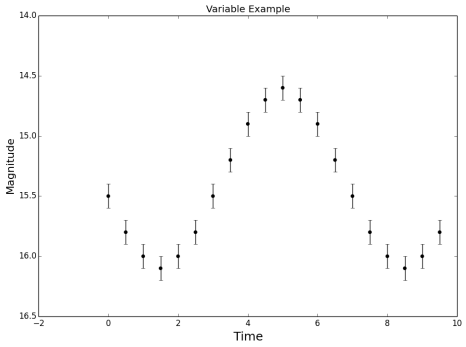

(c) Example of a variable lightcurve.

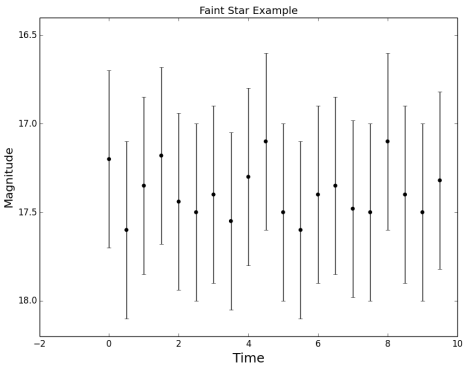

(d) Example of a faint star lightcurve.

Figure 4.17: Examples of the four categories of lightcurve classification used in this analysis.

surrounding fainter sources, which results in a significant number of false positives. In addition to this, the low number of observations (especially in the case of the Iota fields) results in poorly sampled lightcurves that make it very difficult to interpret any kind of variable behaviour. Also, the "transient" classification doesn't necessarily mean that one has been discovered, merely that the lightcurve in question behaves in a similar way. Closer inspection of the source and cross-matching with other catalogues will be able to determine if it is indeed a new object in the sky or not.

4.3 Results

In total VaST was used to generate variability plots of objects in 59 fields containing a total of 1155 images covering the follow up of 4 LVC alerts; a visual search was conducted on the variability plots from each field and each object was subsequently given a classification. A summary of all the classifications are given in Table 4.6 where the outcome of all four follow-up searches are presented. Across these four searches there were a total of 259 objects identified that met or exceeded the variability requirements mentioned in subsection 4.2.4. A selection of the most interesting targets from these searches are presented in this section, for a full list of objects see Appendix D and the individual lightcurves in Appendix E.

Name	Fields observed	Duration (Nights)	Cross-matched sources	Long Period Variable	Variable	Faint stars	Transients
Sigma	34	8	34	24	28	26	0
Nu	14	5	9	30	7	12	1
Iota	5	2	4	32	5	18	0
Kappa	6	7	6	5	17	1	0

Table 4.6: Summary of the classification of the 259 objects of interest identified across the 59 separate fields.

4.3.1 G296853 lightcurves

The analysis of the Sigma fields, observed during the follow-up of the candidate gravitational wave alert G296853, resulted in the identification of 112 objects of interest out of over 11 400 sources in total, spread across the 34 fields observed by PIRATE; these objects are presented in Table D.1 in Appendix D. The magnitude limits of these observations ranged from 16.3-17.2 mag in the R band, as shown in Appendix F.

Within this data set of 112 objects are 34 sources that have been cross-matched with objects in SIMBAD, these are typically the brighter or more variable objects in each image that have a higher chance of being studied by other telescopes or surveys. In Figure 4.18 are a selection of lightcures of objects that were cross-matched with SIMBAD, they include a Mira variable (Figure 4.18a), W UMa variable (Figure 4.18c) and a rotatinoally variable star (Figure 4.18d). The detection of variable stars with VaST is no surprise, especially variables such as W UMa type objects that have a smooth lightcurve variation for which the $1/\eta$ index is more sensitive to; moreover, these short period variables are more easy to detect in a short period of time, such as the 8 days these observations lasted for, because their full variation period can be captured.

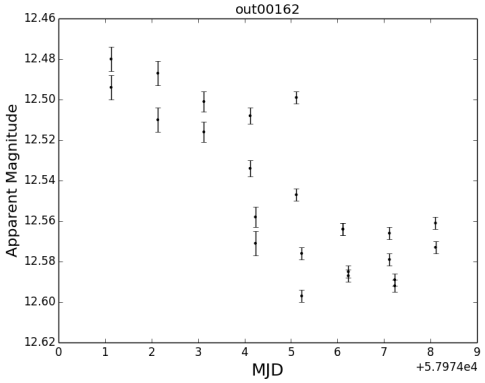

(a) A lightcurve of U Scl, which is a Mira variable star with a period of 333 days (Samus' et al., 2017).

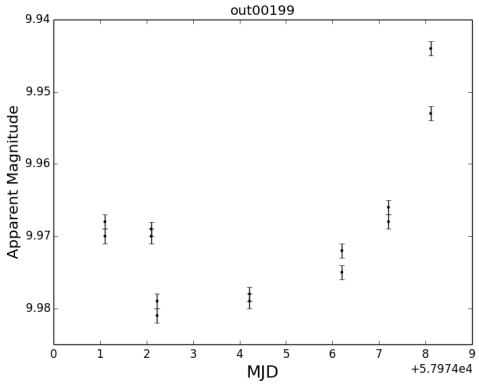

(b) A lightcurve of CD-25 473, a star that doesn't appear in the GCVS.

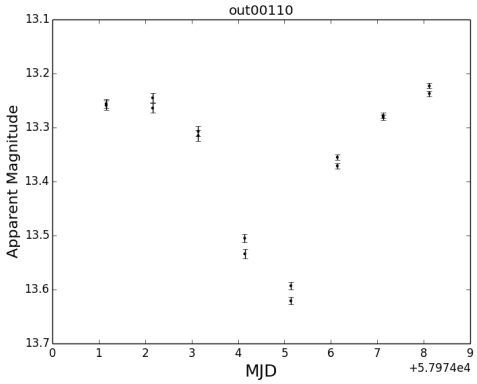

(c) A lightcurve of CRTS J012032.0-174732 , which is a W UMa type eclipsing binary.

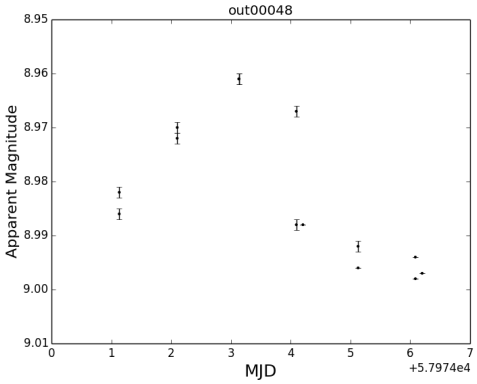

(d) A lightcurve of CD-24 564, a rotationally variable star.

Figure 4.18: A selection of R filter lightcurves from the Sigma fields with cross-matched sources in the SIMBAD archive (Wenger et al., 2000).

Out of the remaining 78 objects there are a combination of: faint objects, variable objects and objects identified as long period variables (summarised in Table 4.6). A sample of these lightcurves is shown in Figure 4.19; they all exhibit a gradual change in brightness from day to day. None of these objects could be cross-matched with the SIMBAD database or the General Catalogue of Variable Stars (GCVS) hence why they are referred to by their VaST designation for reference.

While these variable objects are interesting, they are not unexpected as in any given set of observations there are going to be variable stars, all stars vary to some degree and on different timescales. However, the most important outcome of these observations and subsequent data analysis was that there was no object identified as a transient that could be linked with the gravitational wave alert G296853. Given that this candidate event was classified as a binary black hole merger it is unsurprising that no optical counterpart was discovered by PIRATE or any other EM partners.

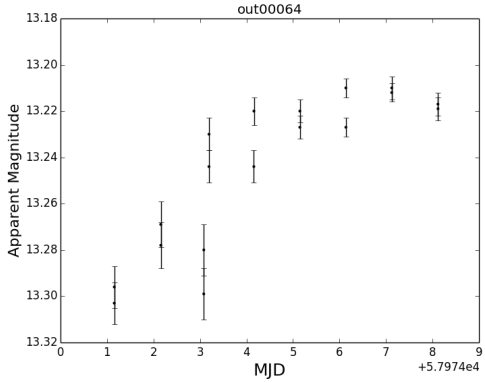

(a) The lightcurve of (out00064) from the Sigma_17 field, classified as a long period variable.

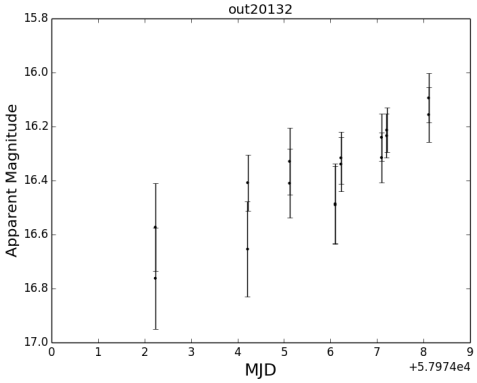

(b) The lightcurve of (out20132) from the Sigma_22 field, classified as a long period variable.

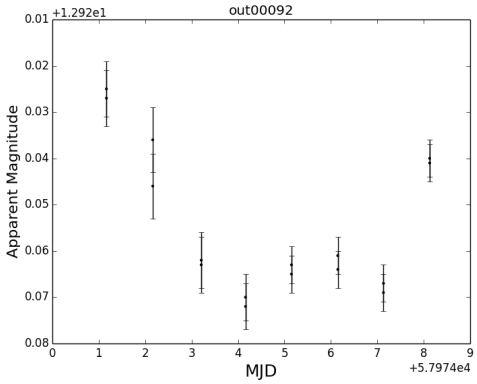

(c) The lightcurve of (out00092) from the Sigma_23 field, classified as a long period variable.

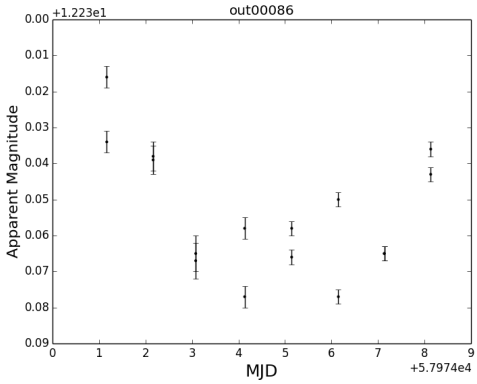

(d) The lightcurve of (out00086) from the Sigma_31 field, classified as a long period variable.

Figure 4.19: A selection of R filter lightcurves of objects identified as potential long period variable stars that had no cross-matched source in SIMBAD.

4.3.2 GW170814 lightcurves

The analysis of the 14 Nu fields, observed during the follow-up of the gravitational wave event GW170814, resulted in the identification of 59 objects of interest out of 4797 objects in total. The lightcurves of these objects were then classified into one of four categories which can be seen in Table D.2 of Appendix D, with the individual lightcurves themselves given in Appendix E. Due to the infrequent and short timespan of these particular observations, the true lightcurve shape for each object was hard to determine. With so few data-points it is difficult to obtain a precise pattern in the lightcurve so therefore there were a greater number of objects classified as "long period variables" based on a simple extrapolation of the few data points available. The magnitude limits varied from 16.7-17.1 in the Nu fields, as shown in Figure F.5 & F.6 in Appendix F.

Cross-matching the coordinates of all the 59 objects with SIMBAD resulted in 9 objects with known identifiers, four of these are presented in Figure 4.20 and include two stars from the Tycho-2 catalogue (Høg et al., 2000) as well as NGC 1339 (Figure 4.20c which is an elliptical galaxy within a galaxy cluster. In addition to this, the object out00191 was identified as the star 2MASS J03161395-3336024 and displays a clear dip in brightness which might indicate some periodic variability; however, according to the General Catalogue of Variable Stars this star isn't listed as being a variable and so it would be an interesting target for future follow-up observations.

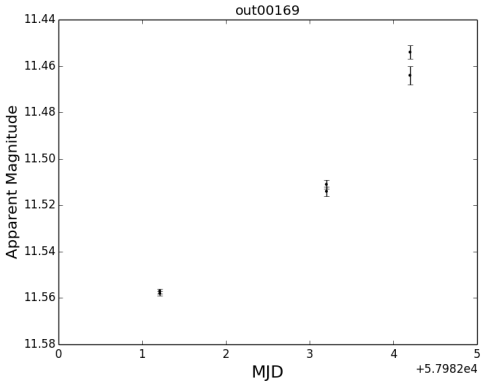

(a) A lightcurve of the TYC 7021-782-1, a star that doesn't appear in the GCVS.

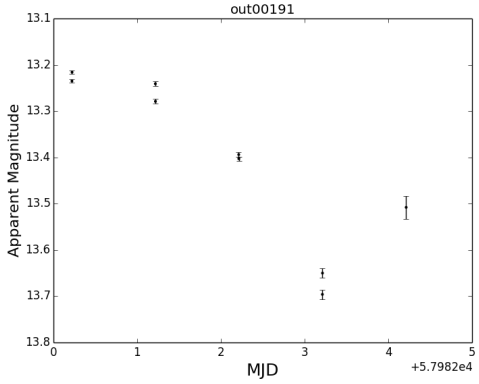

(b) A lightcurve of 2MASS J03161395-3336024, a star that doesn't appear in the GCVS.

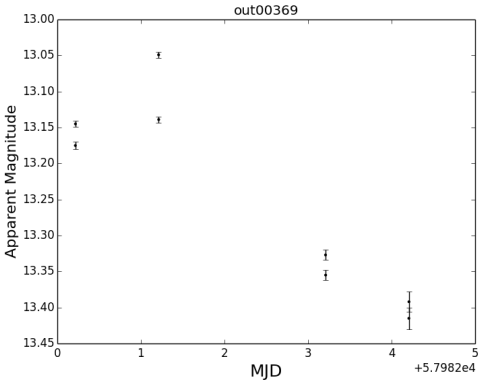

(c) A lightcurve of NGC 1339, which is a galaxy in a group of galaxies.

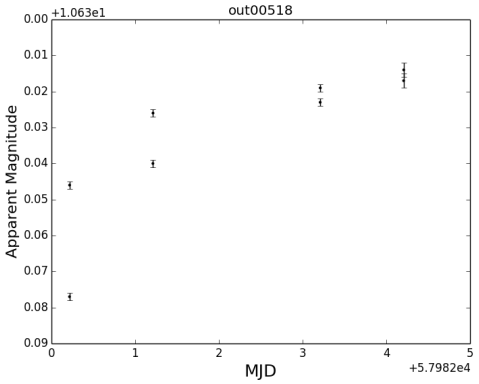

(d) A lightcurve of TYC 7021-102-1, a star that doesn't appear in the GCVS.

Figure 4.20: A selection of R filter lightcurves from the Nu fields with cross-matched sources in the SIMBAD archive (Wenger et al., 2000).

Of the remaining 40 objects the majority were classified as long period variables or faint stars, but there was one object classified as a transient (see Figure 4.21). Initial inspection of this object's lightcurve suggested there was a dimming of around 0.2 mag over four days; however, the large error bars on the last data point in particular mean that the uncertainties surrounding this declining trend are large and the object could easily be non-variable. In addition to these large error bars, the poor sampling of the lightcurve as a whole makes it difficult to extract a long term trend from so few data points.

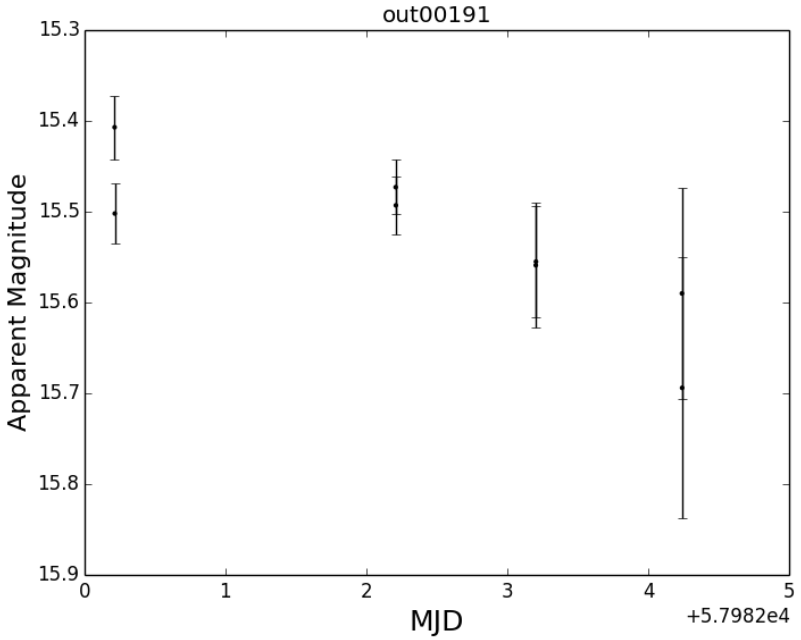

Figure 4.21: The R filter lightcurve of (out00191) from the Nu_13 field, an object classified as a transient due to its declining lightcurve, but identified in VizieR to be Gaia star 5054555592560016640.

In order to disprove this finding, the coordinates of the object were cross matched in VizieR[6] with several thousand source catalogues, resulting in a source being

[6] http://vizier.u-strasbg.fr/viz-bin/VizieR

identified in several catalogues less than 1 arcsecond from it's position. Using the Gaia DR1 data (Gaia Collaboration et al., 2016) as an example, see Table 4.7, the position and magnitude of the star "5054555592560016640" matches almost exactly with the object given in Table D.2. The R filter magnitude from the PIRATE observations was 15.5 ± 0.1 and the Gaia G filter magnitude was 15.6. Therefore it has been shown that after further analysis, the object identified initially as a transient is actually a star present in several catalogues.

Distance (arcsec)	RA (J2000)	DEC (J2000)	Gaia ID	Gmag
0.543	03 14 27.5150	-32 35 35.7995	5054555592560016640	15.601

Table 4.7: Gaia DR1 catalogue entry for suspected transient object.

A selection of the rest of the unidentified objects from the Nu fields are shown in Figure 4.22, with all four objects classified as "long period variables". These lightcurves suffer from the same limitations and uncertainty as the ones previously mentioned, therefore it is very difficult to draw any conclusions from their appearance. None of these objects could be cross-matched with the SIMBAD database or the General Catalogue of Variable Stars (GCVS).

Given that this alert was eventually confirmed as a real gravitational wave event, any optical counterparts identified in the PIRATE follow-up data could potentially have been connected with the merger event; however, as with the previous alert this event was also a binary black hole merger and so no electromagnetic counterparts was expected. The observations with PIRATE were consistent with this, as no counterpart was detected within the observed fields down to a limiting magnitude of 16.9 in the R filter.

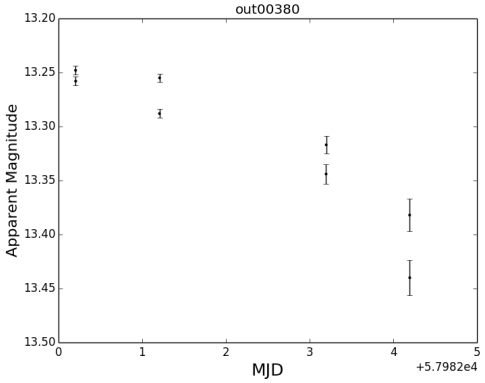

(a) The lightcurve of (out00380) from the Nu_16 field, classified as a long period variable.

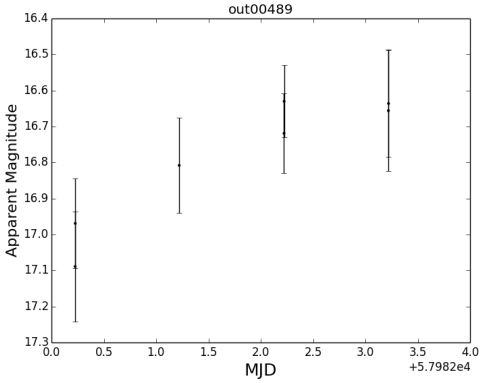

(b) The lightcurve of (out00489) from the Nu_19 field, classified as a long period variable.

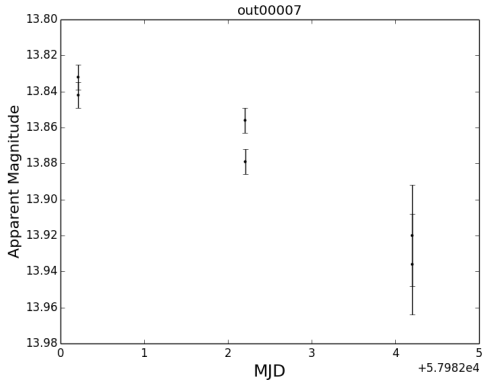

(c) The lightcurve of (out00007) from the Nu_24 field, classified as a long period variable.

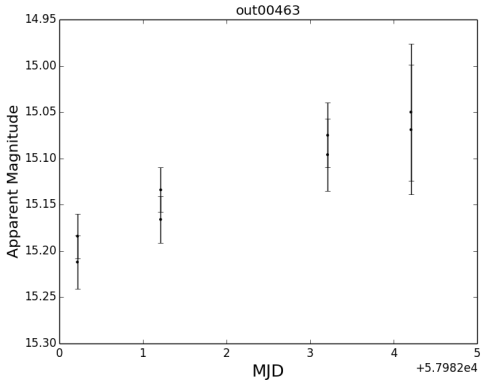

(d) The lightcurve of (out00463) from the Nu_33 field, classified as a long period variable.

Figure 4.22: A selection of R filter lightcurves of objects identified as potential long period variable stars in the Nu fields that had no cross-matched source in SIMBAD.

4.3.3 G298936 lightcurves

The analysis of the Iota fields, observed during the follow-up of the candidate gravitational wave alert G298936, resulted in the identification of 59 objects of interest out of over 19 200 objects in total, spread across the 5 fields observed by PIRATE; these objects are presented in Table D.3 of Appendix D, and the individual lightcurves themselves are in Appendix E.

All the lightcurves computed for this alert are of poor-quality as there aren't enough observations to draw any conclusions about the behaviour of these objects. These lightcurves only span two days, with a maximum of four data points per lightcurve; however, they weren't discarded in case PIRATE detected a glaringly obvious transient that would have decreased in brightness significantly between observations. No such transient was found, but each source identified as variable by VaST was classified into one of the four categories from subsection 4.2.4. The magnitude limits for these short observations were relatively good, from 17.0-17.3 in the R band, as shown in Appendix F.

Four sources were identified by cross-matching with SIMBAD and these are shown in Figure 4.23. Two of these were objects originally identified by Høg et al. (2000) in the Tycho 2 catalogue (Figures 4.23a & 4.23d), one was first identified by Cannon and Pickering (1918) in the Henry Draper catalogue (see Figure 4.23c) and the last one was identified by the 2MASS survey (Cutri et al., 2003) (Figure 4.23b).

The remaining 55 objects couldn't be cross-matched with SIMBAD and were classified mainly as long period variables or faint stars. The size of the error bars make it difficult to constrain any real trend in the lightcurves, with the exception of out01761 which has a much higher signal to noise ratio which can be seen in Figure 4.24c where the error bars are significantly lower than the overall change in brightness. Three other lightcurves taken from this dataset are presented in Figure 4.24.

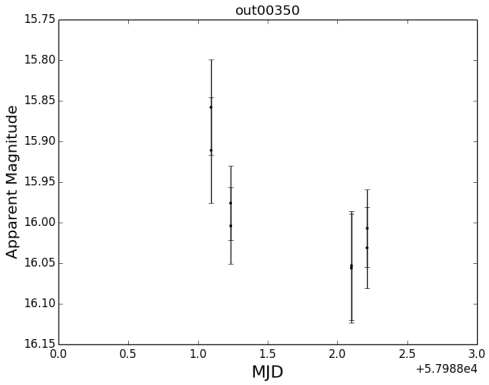

(a) A lightcurve of the TYC 3337-1159-1, a star that doesn't appear in the GCVS.

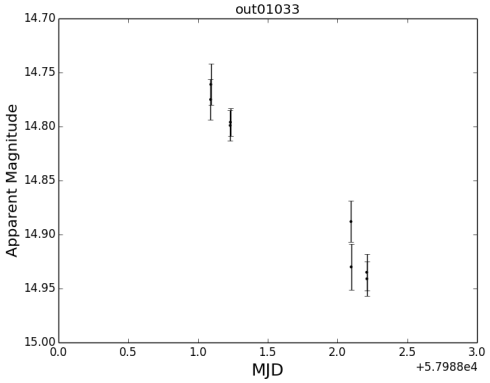

(b) A lightcurve of 2MASS04301894+4944024, a star that doesn't appear in the GCVS.

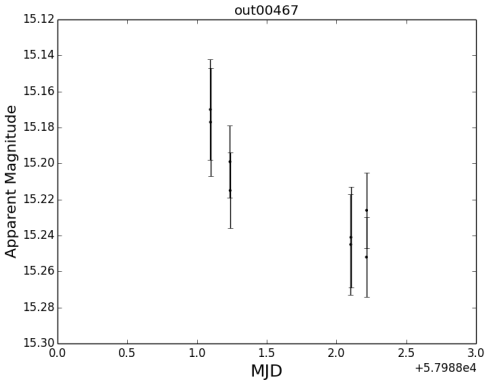

(c) A lightcurve of HD 27968, a star that doesn't appear in the GCVS.

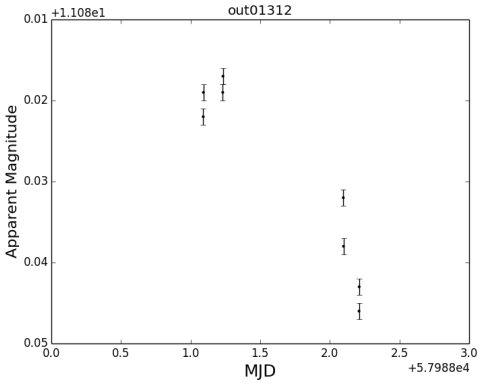

(d) A lightcurve of TYC 3350-827-1, a star that doesn't appear in the GCVS.

Figure 4.23: A selection of R filter lightcurves from the Iota fields with cross-matched sources in the SIMBAD archive (Wenger et al., 2000).

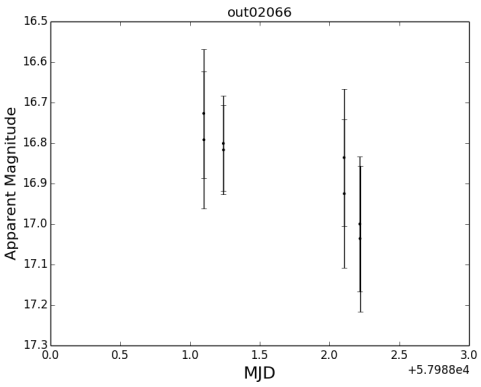

(a) The lightcurve of (out02066) from the Iota_2 field, classified as a faint star.

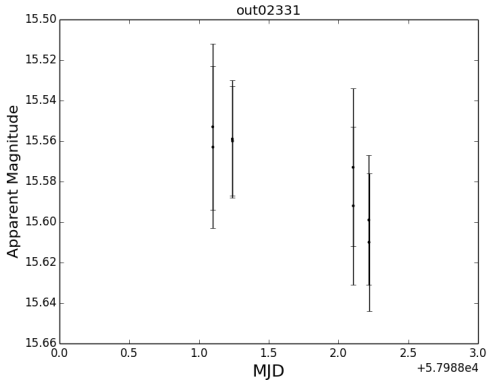

(b) The lightcurve of (out02331) from the Iota_2 field, classified as a long period variable.

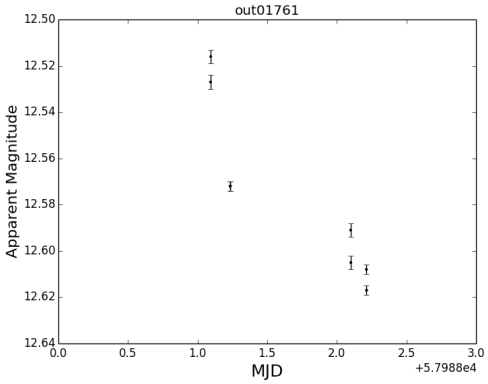

(c) The lightcurve of (out01761) from the Iota_3 field, classified as a long period variable.

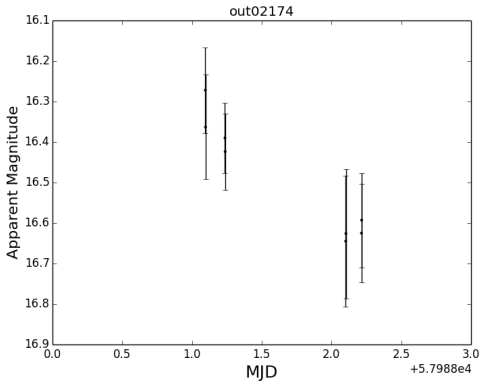

(d) The lightcurve of (out02174) from the Iota_4 field, classified as faint star.

Figure 4.24: A selection of R filter lightcurves from the Iota fields containing objects classified as long period variables or faint stars, with no cross-matched source identified in SIMBAD.

4.3.4 G299232 lightcurves

The analysis of the Kappa fields, observed during the follow-up of the candidate gravitational wave alert G299232, resulted in the identification of 29 objects of interest out of 11 460 total objects, spread across the 6 fields observed by PIRATE; these objects are presented in Table D.4 in Appendix D. The magnitude limits for these observations varied from 17.5-17.9 in the R band, as shown in Appendix F. These were among the best quality observations taken with PIRATE during the EM follow-up phase.

Within this dataset of 29 objects are 6 sources that have been cross-matched with objects in SIMBAD, four of these are shown in Figure 4.26. The Kappa fields were observed for 7 nights in most cases and so the lightcurves displayed in Figure 4.26 are much more well sampled than previous follow-up observations, this helps to detect patterns of variability over similar timescales. For example, lightcurve 4.26a appears to be a type of eclipsing binary with a period of near constant flux proceeded by a sudden dip of up to 0.1 magnitudes. This particular star was identified in the Tycho-2 catalogue (Høg et al., 2000) as TYC 2829-403-1 but when the coordinates were cross-referenced with the GCVS no variable star was reported at that location, leading to the possibility that this is a newly discovered variable star.

Another eclipsing binary was also identified in this search, the W UMa type star known as V0755 Andromeda (see Figure 4.26b) which has a period of 0.366 days (taken from GCVS catalogue (Samus' et al., 2017)) was observed by PIRATE several times over 7 days at different points in its phase, varying in between approximately 13.0-13.6 magnitudes. A periodagram for this lightcurve was computed using the Lomb-Scargle technique and it displayed in Figure 4.25; it shows that the two foremost periods are 0.550 and 0.366 days, with the latter in agreement with the GCVS data. Historical observations in the Tycho-2 catalogue (Høg et al., 2000) give a B-V colour of 0.55 ± 0.11 which indicates this is probably a yellow F-type star with a

surface temperature around $T \sim 6000K$. This translates to an approximate mass of $1.15M_{\odot}$ for a Main Sequence star. In addition to this, parallax measurements taken with the Gaia satellite and converted into distance estimates by Bailer-Jones et al. (2018), estimate the distance to the star system to be $657^{+23}_{-22}pc$.

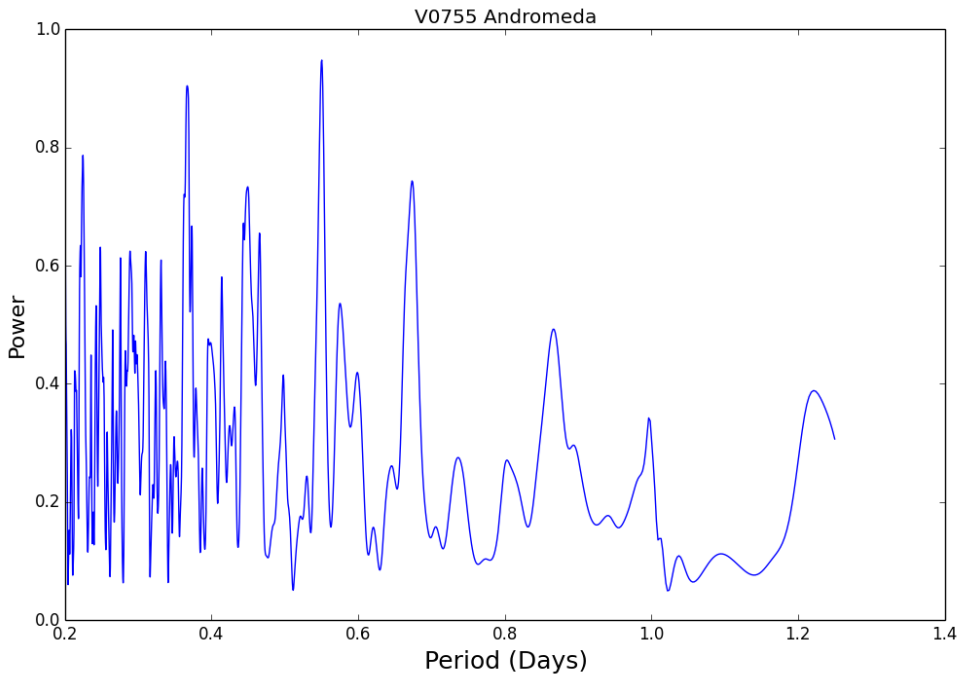

Figure 4.25: A periodogram of the W UMa variable V0755 And, displaying the most prominent periodicity's in the PIRATE data. The two foremost periods are 0.550 and 0.366 days.

Of the other two lightcurves presented in Figure 4.26, one is of the Mira variable V* AH Andromeda (Figure 4.26c) and the other is of the barred spiral galaxy 2MASX J02084017+4253336 (Figure 4.26d as identified by Huchra et al. (2012).

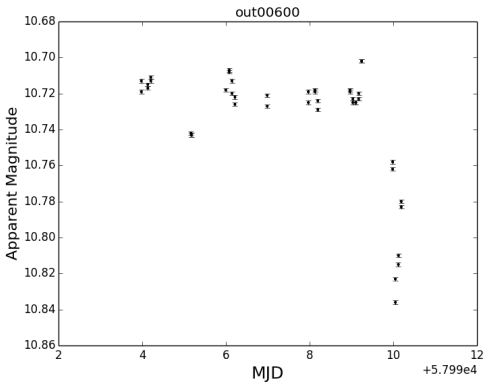

(a) A lightcurve of the TYC 2829-403-1, a star that doesn't appear in the GCVS.

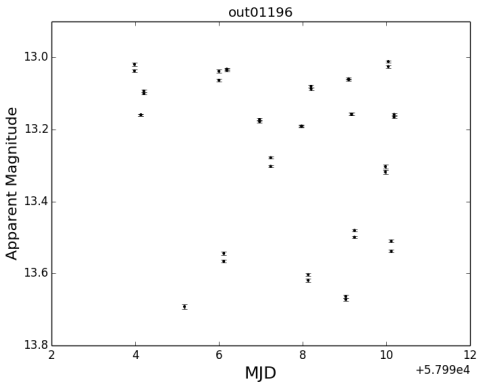

(b) A lightcurve of V0755 Andromeda, a W UMa type star with a 0.366 day period (Høg et al., 2000).

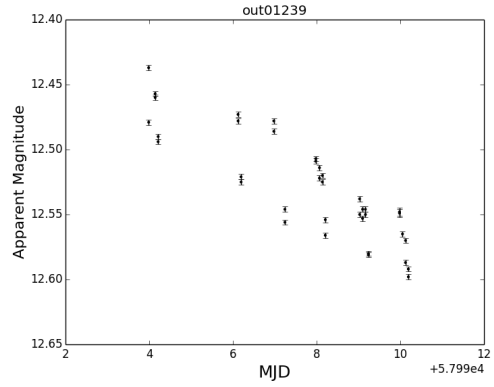

(c) A lightcurve of V* AH Andromeda, a variable star of the Mira type.

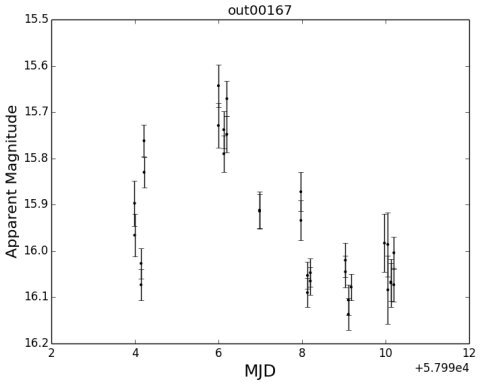

(d) A lightcurve of 2MASX J02084017+4253336, a galaxy with a barred spiral.

Figure 4.26: A selection of R filter lightcurves from the Kappa fields with cross-matched sources in the SIMBAD archive (Wenger et al., 2000).

Of the remaining 23 sources that weren't identified in SIMBAD, the vast majority (17) were classified as variables with just one classified as a faint star. The lightcurves displayed in Figure 4.27 are some of the more interesting objects identified in the Kappa fields, with one, out01440 (Figure 4.27a), being classified as a long period variable due to its long continuous dimming trend; and the other three all classified as variables due to their irregular or un-periodic nature. Object out20043 (Figure 4.27d) for instance appears to display the behaviour of another eclipsing binary, with a potential eclipse of 1.5 magnitudes depth in just a few hours.

MASTER Supernova candidate

As mentioned in section 4.1.10, PIRATE also followed up a supernova candidate detected by the MASTER collaboration[7] (Lipunov et al., 2016) less than 48hrs after the initial discovery notice was sent out to EM astronomers (Lipunov, 2017a). The initial MASTER OT unfiltered detection magnitude on 27$^{\text{th}}$ August 2017 at 00:01UTC was 17.0, and the initial uncorrected detection magnitudes taken with PIRATE at 23:51UTC on the 28$^{\text{th}}$ August were R=16.49$\pm$0.06 and B=17.11$\pm$0.11. Further uncorrected filtered observations were reported by KU collaboration (2017a) on 27$^{\text{th}}$ August of r=16.67 $\pm$ 0.03 and i=16.71 $\pm$ 0.03, which are consistent with PIRATE's observations taken the next day.

The resulting lightcurves, taken in both red and blue filters, are shown in Figure 4.28. What was rare about this target was that thanks to MASTER's early detection, PIRATE was able to start observing this supernova for about a week before it reached it's peak luminosity; and PIRATE was able to monitor this target for over 65 days before it eventually faded beyond its magnitude limit.

PIRATE was not alone in taking observations of this target, several other groups also observed it (KU collaboration, 2017a; Lipunov, 2017c; Jonker, 2017; KU col-

[7] `http://master.sai.msu.ru/static/OT/033744.97723159.0.png`

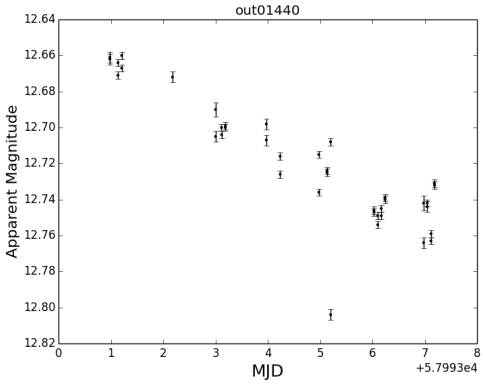

(a) The lightcurve of (out01440) from the Kappa_2 field, classified as a long period variable.

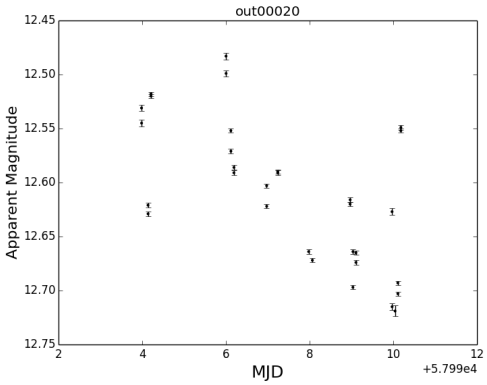

(b) The lightcurve of (out00020) from the Kappa_3 field, classified as a variable.

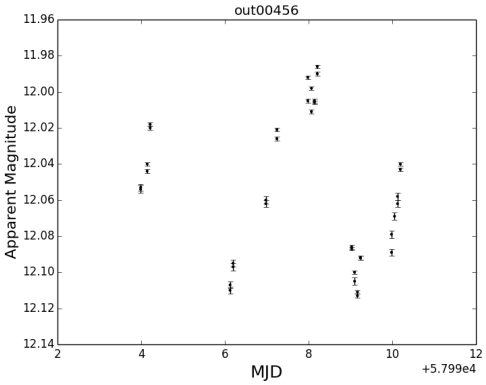

(c) The lightcurve of (out00456) from the Kappa_4 field, classified as a variable.

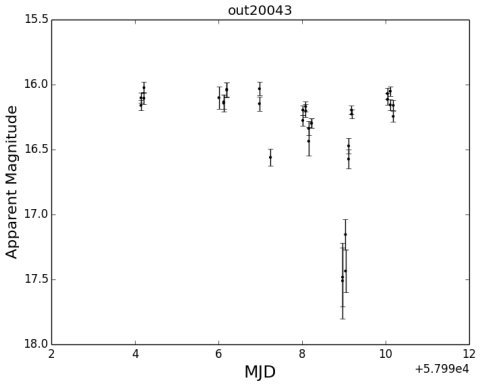

(d) The lightcurve of (out20043) from the Kappa_5 field, classified as a variable.

Figure 4.27: A selection of R filter lightcurves from the Kappa fields containing objects classified as: long period variables, variables or faint stars, with no cross-matched source identified found in SIMBAD.

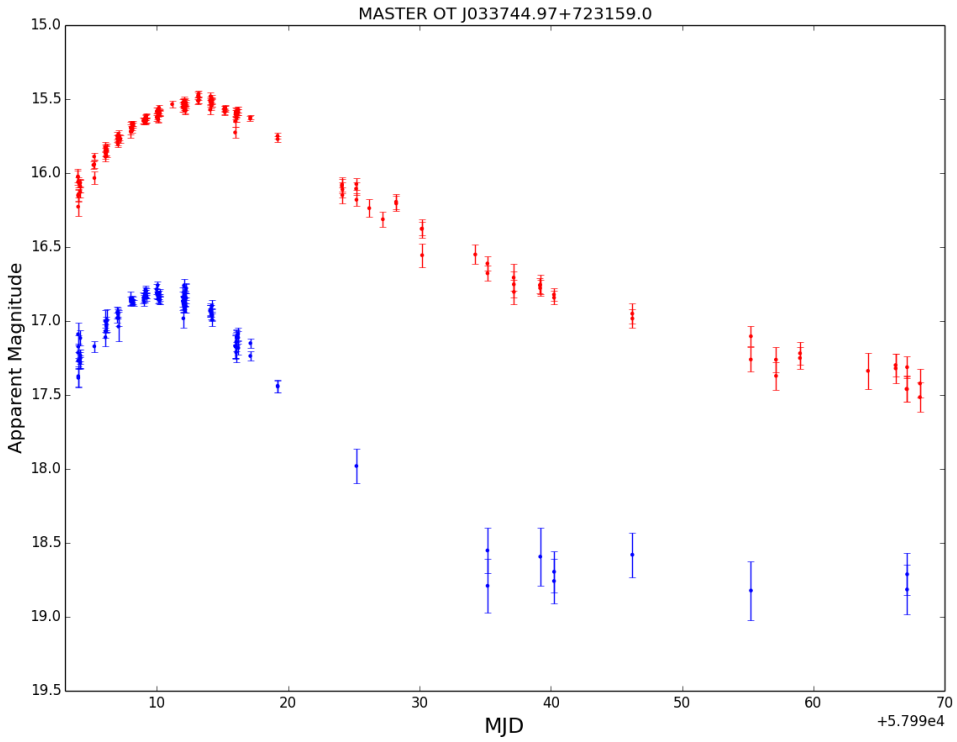

Figure 4.28: A lightcurve of the supernova candidate MASTER OT J033744.97+723159.0, with images taken by PIRATE in both the red and blue filters.

laboration, 2017b; Watson, 2017; Lipunov, 2017d; Copperwheat and Steele, 2017; Emery, 2017) and from the initial observations it was determined that the host galaxy for the supernova was NCG1343. What they also observed was that this supernova occurred at a very large distance from it's galactic centre at ∼20kpc (Lipunov, 2017e). Some of these groups also obtained spectroscopic observations of this supernova (Jonker, 2017; Copperwheat and Steele, 2017; Lipunov, 2017f) and the consensus was that this resembled a Type IIb core-collapse supernova before maximum. Type IIb supernova typically display weak hydrogen lines in their initial

spectra but these disappear quickly and helium lines become more dominant, this suggests the progenitor only contained a thin hydrogen layer.

The PIRATE observations agree with this, they show slight reddening as the supernova developed, with a max luminosity in the blue filter occurring a day or two before the red filter. The shape of the lightcurve also suggests this supernova was beginning to plateau before it became to faint to observe with PIRATE; further observations would be needed to confirm this.

The most unusual aspect of this supernova was that it occurred so far out in its host galaxy, far away from the main star formation regions in the galactic disc. This poses the question of how such a massive star got there in the first place, or was it the result of one or maybe multiple merger events of smaller stars that culminated in a star massive enough to undergo core-collapse and form a supernova? Although not directly related to gravitational waves, this event shows how similar events could be detected serendipitously when using global astronomical observatories to search vast areas of the sky in such a sort time. It also proved very useful as a test event for PIRATE and all the new calibration & reduction software implemented to hunt for optical counterparts.

4.3.5 Limiting Magnitude

Estimates of the limiting magnitude of these observations were obtained using the variability data generated in VaST (see Appendix F). Specifically, the standard deviation of the faintest detectable star was used as a basis to estimate the signal-to-noise ratio, this value was recorded along with the magnitude of the faintest star in each field (see Appendix F), with an example for the Kappa fields given below in Table 4.8.

What these values show is the magnitude of the faintest detectable star observed in each field with VaST and the corresponding Standard Deviation of the lightcurve

Field	Magnitude	SD	SNR
Kappa 1	17.59	0.205	5.30
Kappa 2	17.62	0.0212	5.13
Kappa 3	17.47	0.185	5.88
Kappa 4	17.93	0.215	5.06
Kappa 5	17.54	0.188	5.78
Kappa 6	17.69	0.207	5.25

Table 4.8: Example of the faintest detectable magnitudes in each field.

calculated by VaST. However, this is not an absolute magnitude limit of the raw data, this is a cut off based on the source extraction parameters set in VaST, which can be quite strict. These signal to noise ratios are all above SNR of 5 whereas it would be expected that an SNR of 3 would still be detectable against the background noise with a more powerful/sensitive source extraction software. Therefore, the true magnitude limit will be slightly lower than these values taken from VaST, but they provided a good first estimate.

The SNR values were calculated by taking the standard deviation value of the lightcurve of the faintest star in each field, and using a simplified version of the CCD equation:

$$\sigma_{mag} = \frac{1.0875}{SNR}, \tag{4.4}$$

Where the figure 1.0875 is a correction term for the error in electrons and same error in magnitudes Howell (2006).

4.4 Discussion

In total, the follow-up observations performed by PIRATE during O2 resulted in over 3000 images being obtained in the follow up of ten alerts released by the LVC; of these, four data sets had enough good quality data to process and look for transients. This process resulted in the production of hundreds of lightcurves with variability across the time frame of the observations, but most of these objects were deemed to be either variable or very faint stars.

Across the entirety of the O2 follow-up observing campaign, only one object's lightcurve (out00191 from the Nu13 field) was identified as being a potential transient; however, this was found not to be a transient but a regular star (Gaia 5054555592560016640). As a result, there were no confirmed transients/optical counterparts identified by PIRATE in response to the four candidate alerts that were followed up and had high enough quality data for analysis. Nevertheless, upper limits on a detection magnitude can be applied based on these observations, for which any potential optical counterpart must have appeared fainter than. For these follow-up observations that limit varied from 16.3-17.9 mag in the R filter, with 60-100s exposures. This could have been improved by taking longer exposures and thus increasing the signal-to-noise of faintest stars in the image but this would've been at the expense of covering more area of the sky or reducing the cadence of subsequent follow-up observations.

In addition to this, all the follow-up observations were taken solely with the R filter on PIRATE, and the original justification for this was to maximise sky coverage in the immediate time following an alert. However, this could have been relaxed after the initial search period was over and repeat images were being taken, this could have then allowed for more colour images to be taken. This would have certainly been the case if EM follow-up partners had detected a candidate counterpart source that required further follow-up observations. But as for the initial detection work,

maximising the sky coverage by limiting the observations to one filter made the most sense.

Also, the duration of the follow-up campaigns for each alert were relatively short in hindsight, and although this was sometimes caused by multiple alerts in quick succession, or student use of the telescope, there were some instances when the follow-up campaigns were prematurely cut short on the assumption that any optical counterpart would have faded by that time, or if it was a binary black hole merger, there was no optical counterpart to look for.

Since the completion of the O2 observing run in August 2017, there have been three more announcements by the LVC regarding the re-classification of a candidate alert into a confirmed detection. One of these was GW170814 (formally known as G298046), announced by Abbott et al. (2017c), which was a binary black hole merger detected on the 14^{th} August 2017 by all 3 LIGO/Virgo detectors. The sky localisation was constrained, using all three detectors, to just $60deg^2$ which enabled EM partners to perform much more targeted follow-up observations than had previously been possible. However, as with previous binary black hole mergers this one wasn't expected to produce an EM counterpart; despite this, 25 observatories reported follow-up observations to the EM follow-up community via the GCN Circulars (Abbott et al., 2017c). These observations were made in gamma-rays, x-rays, optical, near infrared and neutrinos; but none reported detecting any EM counterpart in conjunction with the gravitational wave alert (G298046) issued by the LVC. This includes PIRATE, which was also unable to detect an EM counterpart to this binary black hole merger, but this is consistent with the current understanding of binary black hole mergers.

The identification process could be improved in the future to not just rely on SIMBAD for cross-referencing with known stars but also using the VizieR library to cross-reference with thousands of astronomical databases. Using VaST to search for

transients was a quick an effective method that was already prepackaged and ready to use, this includes its internal SIMBAD & VSX cross matching tools. But using another bespoke search tool that produces more user friendly output files might have been easier to upload and cross-reference with VizieR.

One further improvement to this identification process could have been to the way in which the variable objects were classified. The human nature of this process meant it was entirely subjective and no qualitative way was used to classify these objects.

Chapter 5

Analysis of spectra from candidate LBVs in M33

The discussion now returns to the massive star aspect of this thesis, specifically the analysis of spectra taken with the WHT looking for variability indicative of Luminous Blue Variable stars in the Triangulum galaxy (M33).

From the background set out in the Introduction Chapter (Chapter 1), it is clear that the evolutionary picture of massive stars is still uncertain. Furthermore, the classification of objects such as LBVs is not trivial; they contain a diverse collection of stars with differing properties, and compounding this is their rarity which limits the number of similar galactic stars for comparison. All together this makes LBVs relatively poorly understood objects and any further study or observations that can add to this sum of knowledge is very important.

This is evident in the literature surrounding the classification of LBVs, as there remains disagreement over how and what to classify as LBVs (Aadland et al., 2018). This seems to centre around the frequent usage of the term "LBV candidates" to describe massive stars who's spectra closely resemble that of confirmed LBVs but have not yet been observed to photometrically vary during an outburst or "cold"

phase. This can lead to confusion when trying to collate all the known bona fide LBVs as some authors leave off the "candidate" from their published tables of LBVs.

In this chapter the author will attempt to reclassify some LBV candidates in the Triangulum Galaxy (M33) based on changes to their spectral lines, following a similar method to Clark et al. (2012) in reclassifying them based on spectral morphology. These will be complimented with archival data from which comparisons can be drawn and the long term behaviour analysed but also by comparing them with prototypical stars of each class, such as the LBV's P Cygni and Romano's Star.

Succeeding this, in the next Chapter, the author will present photometric observations of some of these stars that were taken over several months using the PIRATE robotic telescope, and comment on what implications these have for their current classifications.

5.0.1 Historical Observations of LBVs in M33

As was discussed in the Introduction Chapter, the ability to study galactic LBVs is severely hindered by the presence of dust in the galactic plane, especially at optical wavelengths. Therefore, the galaxies of the Local Group serve as a good alternative to study nearby galaxies for their massive stars such as LBVs and Wolf-Rayets.

And the Triangulum galaxy is one of the best such galaxies to study because it is face on to the Milky Way, allowing deeper and clearer images to be taken with less contamination from dust, and it has a well defined distance which improves the accuracy of the physical properties of the stars studied in this galaxy. Furthermore, the different metallicity of stars in M33 allow astronomers to test evolutionary models as a function of metallicity, using these stars as an extra-galactic laboratory.

The majority of research published on the LBV candidates in M33 has been done by Philip Massey (Massey et al., 1996, 2007, 2016), who has been studying massive stars in M33 for almost 40 years. Others who have published research on LBVs in

M33 include Humphreys et al. (2014b, 2017, 2014a) and more recently Sholukhova et al. (2018). In addition to this, Clark et al. (2012) also published their findings in 2012 with their paper on candidate LBVs in M33, and it is this paper that the work in this thesis is largely based on, adding a new epoch of spectral observations to those taken in 2010.

5.0.2 Searching for candidate LBVs

There were 18 LBV candidates studied by Clark et al. (2012); displayed in Table 5.1; and these were originally taken from the Massey et al. (2007) paper which published a comprehensive list of 37 candidate LBVs in M33. And so by cross-matching this list with the most up to date list of candidate LBVs found in the Massey et al. (2016) paper, it was found that there were five new candidate LBVs and one re-classified as a LBV candidate since the Massey et al. (2007) was published; these are displayed in Table 5.2. This leads to a grand total of 43 candidate and confirmed LBVs within M33.

The data used in this thesis originates from the spectra taken by Clark et al. (2012) in 2010, and combines this with spectra taken three years later in 2013. Of the 18 candidates listed in Table 5.1, 13 of these had spectra from both 2010 and 2013; these stars are all presented in section 5.1. In addition to this, a further 12 massive stars that had spectra obtained in 2013 but not in 2010 were given new identifications as either Wolf-Rayets or Cool Hypergiants, this was out of a total of 44 stars with spectra obtained in 2013; the remaining spectra were either featureless, too noisy or unchanged from previous observations; these are presented in section 5.2.

LGGS J#	Aliases	Classification	Telescope	V
013242.26+302114.1	-	Iron Star	WHT	17.44
013324.62+302328.4	-	Iron Star	WHT	19.58
013350.12+304126.6	UIT212	Iron Star	WHT, Keck	16.82
013406.63+304147.8	UIT301	Iron Star	WHT	16.08
013357.73+301714.2	-	B hypergiant	WHT	17.39
013416.44+303120.8	-	B hypergiant	WHT	17.10
013422.91+304411.0	-	B hypergiant	WHT	17.22
013424.78+303306.6	-	B hypergiant	WHT	16.84
013429.64+303732.1	-	B hypergiant	WHT	17.10
013339.52+304540.5	B517	P Cyg LBVc	WHT	17.50
013341.28+302237.2	[HS80] 110-A	P Cyg LBVc	WHT	16.28
013416.07+303642.1	-	P Cyg LBVc	WHT	17.95
013309.14+303954.5	UIT045	Ofpe/WNL	WHT	17.91
013327.26+303909.1	UIT104	Ofpe/WNL	WHT	17.95
013509.73+304157.3	Romano's Star	Ofpe/WNL	WHT	18.04
013349.23+303809.1	Var B	LBV	Keck	16.21
013335.14+303600.4	Var C	LBV	WHT, Keck	16.43
013416.10+303344.9	UIT 341	LBVc	WHT	17.12

Table 5.1: List of candidate LBVs analysed by Clark et al. (2012).

LGGS J#	V	Type
013229.03+302819.6	18.998	cLBV:
013303.09+303101.8	16.994	cLBV
013317.05+305329.9	18.921	cLBV
013344.79+304432.4	18.151	cLBV:
013349.28+305250.2	19.043	cLBV
013429.64+303732.1	17.105	B8Ipec/cLBV

Table 5.2: List of new candidate LBVs identified in Massey et al. (2016).

5.0.3 Classifications

As previously mentioned, the classification of stars in this chapter will follow a similar method to Clark et al. (2012). In their paper, they describe a 5 morphological classifications for the candidate LBV stars being studied, namely: P Cygni, Ofpe/WNL, bona fide LBV, Iron Star & Blue Hypergiant. The first 3 of these were all taken straight from Massey et al. (2007) and are well defined spectral types; however, in their paper they als used the terms hot and cool LBV candidates to describe the remaining stars. Clark et al. (2012) took issue with this as it implies a distinct phase in the evolutionary period; so instead, they used these terms Iron Star & Blue Hypergiant to replace these.

Iron Star

The definition of an Iron Star as described in Clark et al. (2012) is entirely based upon the spectral appearance of the star. The spectrum of these stars contain many metallic emission lines, such as Fe II, Mg II & N III; and they also display strong emission lines in the Balmer series. The Fe II emission line spectra of LBVs are highly variable, and so LBV stars can appear as an Iron Star during the optical

maximum of the S Dor cycle, but then change appearance to appear as a B[e] star.

Iron stars are like B[e] stars in that they are rotating fast enough to have a disk like component, leading to different spectral lines from the polar regions; however, Iron stars are are much closer to the Eddington limit, and so therefore they don't need to rotate as fast to produce a disk like structure at the equator, and hence why these are referred to as supergiant B[e] stars (Zickgraf et al., 1985).

Another way to distinguish Iron Stars is to take IR photometric observations and produce colour-colour plots of these stars. This can be used to identify stars with a large IR excess that are likely to be supergiant B[e] stars, with the strong IR excess is likely to be caused by hot circumstellar dust and Fe II emission lines, originating in the circumstellar disc.

Blue Hypergiants

As for Blue Hypergiants, these stars are classified by Clark et al. (2012) as cool hypergiants demonstrating a combination of strong absorption and emission lines, similar to Var C in its cool phase. This includes the presence of several metal lines in absorption. Again, there is a degeneracy between LBV stars undergoing an S Dor event and moving to cooler temperatures, and yellow hypergiants that are stable for several decades.

Due to their cool photospheres, the spectra of these stars contain several metallic absorption lines, in addition to this, the Balmer series of Hydrogen lines are typically in absorption.

5.0.4 Observations

The data for these new observations were taken under observer led time in 2013 using the 4.2m William Herschel Telescope (WHT) at the Observatorio del Roque de los Muchachos (ORM) which is located in La Palma, Spain. The spectra themselves

were taken using the AutoFib2 plus Wide Field Fibre Optical Spectrograph (AF2-WYFFOS) instrument; this was a multi-object, wide-field, fibre spectrograph that was decommissioned on 31st July 2017[1]. This data acquisition follows a similar process by Clark et al. (2012) 3 years previously, where they obtained spectroscopic observations of 17 target stars over four consecutive nights on the WHT.

The reduction of the raw spectroscopic data was performed in IRAF using the pipeline provided on the AF2 webpage[2]. The first step in this process involves the usual CCD image processing procedures such as obtaining good quality dark and bias frames in order to correct for the dark current and bias. Additionally a flat-field is required and for spectra this is usually acquired using a uniform light source such as a lamp. This can then be used to create a normalised flat frame along the dispersion direction. Following on from this, the overscan region has to be cropped to remove any spurious data from the spectrum and any cosmic ray hits or bad pixels should be removed from the frames to enable an accurate flux calibration to take place. Next, the object and sky background need to be located in order to continue with the reduction process by identifying the spectra and subtracting the sky background before it can be extracted. Lastly, the spectrum undergoes wavelength calibration is using a calibration lamp (such as Neon or Helium), to correctly assign the wavelength values to the spectrum based on prominent wavelength features.

Before these spectra were given to the author to use, they were also normalised with respect to the continuum in order to easily identify absorption and emission features.

[1] `http://www.ing.iac.es/PR/inst.php?inst=WYFFOS`

[2] `http://www.ing.iac.es/astronomy/instruments/af2/reduction.html`

5.1 Spectroscopic Analysis-Part1

In this section the analysis of 13 potential LBV candidates is presented. These 13 stars were selected from the Clark et al. (2012) paper because they all had corresponding spectra taken from 2013 which are presented in this thesis for the first time. In total over 40 stars in M33 were observed in 2013 as part of the observer led time that resulted in the spectra presented in this thesis; however, the majority of these didn't have corresponding spectra taken in 2010 from the Clark et al. (2012) paper and so therefore are presented on their own in section 5.2.

LGGS J#	Other ID	Classification
J013242.26+302114.1		Iron Star
J013324.62+302328.4		Iron Star
J013335.14+303600.4	Var C	LBV
J013339.52+304540.5	B517	P Cygni LBVc
J013341.28+302237.2	101-A	P Cygni LBVc
J013350.12+304126.6	UIT 212	Iron Star
J013357.73+301714.2		BHG
J013406.63+304147.8	UIT301	Iron Star
J013416.07+303642.1		P Cyg LBVc
J013422.91+304411.0		BHG
J013429.64+303732.1		BHG
J013459.47+303701.9		Iron Star
J013509.73+304157.3	Romano's Star	LBV

Table 5.3: List of 13 LBV candidates analysed in this section, with spectra from both 2010 and 2013. The classifications displayed come from Clark et al. (2012).

5.1.1 LGGS J013242.26+302114.1

This star was first classified as an Iron Star by Clark et al. (2012) and in their analysis of its spectra they concluded that it didn't "unambiguously demonstrate behaviour characteristic of the LBV phenomenon". Massey et al. (2007) classified this star as a "hot LBV candidate" because of its strong emission in the lower Balmer series and the presence of singly ionised metals, resembling the prototype of this class, Var C.

As previously discussed in section 5.0.3, the term Iron Star is used to describe LBV candidates with metallic emission lines present in their spectra. They are also classified by their strong IR excess, which is why some of these stars form a sub-category of stars known as supergiant B[e] stars (sgB[e]), thought to be similar in appearance to classical B[e] stars that display a circumstellar disc due to rapid rotation.

The two epochs of spectral data presented in Figure 5.1 show: a significant increase in the strength & ratio of the Balmer series lines; this replicates what Clark et al. (2012) saw in their spectra, in the $\sim$ 4 year period in-between their observations. There is also a noticeable narrowing of their wings, which indicates a reduction in Thompson scattering due to a lower density stellar wind. In addition to this, there was also a strengthening of the [O III] nebular lines over the 3 year period. This is likely caused by worse atmospheric seeing when these observations were taken, which results in more nebular emission being included in the spectrum. And in addition to this, poor seeing conditions can result in lower signal-to-noise spectra unless this is compensated for with longer exposures. These nebular lines are not directly related to the stars activity, but originate in either a circumstellar nebula or a diffuse gas cloud associated with nearby star formation.

Although there are significant changes in the spectra displayed in Figure 5.1 between 2010-2013, most notably with the width of the Hβ wings and stength of the [O III] emission lines, these by themselves do not offer enough evidence of an

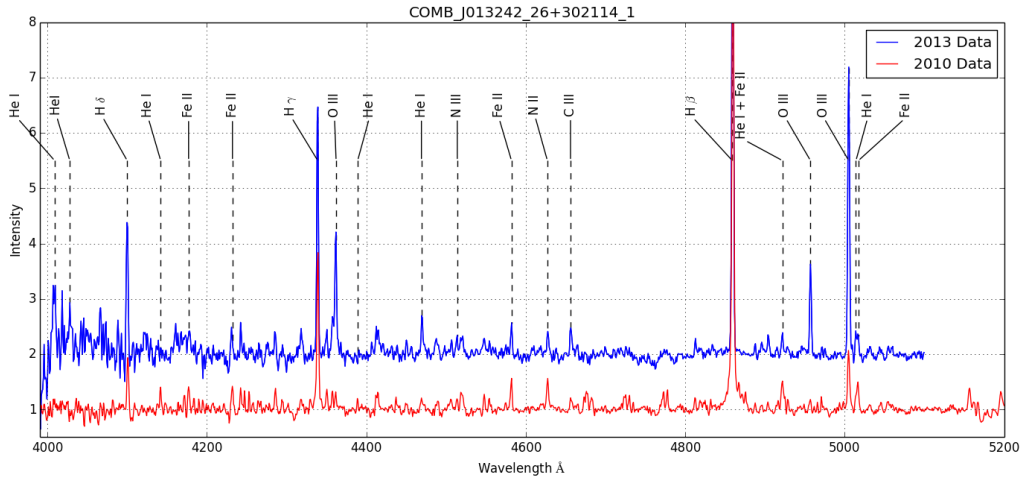

Figure 5.1: Spectra of LGGS J013242.26+302114.1, classified as an Iron Star by Clark et al. (2012).

LBV. To be considered an LBV, a clear change in temperature would also have to accompany these changes, something already described as an important indication of an S Dor cycle.

5.1.2 LGGS J013324.62+302328.4

Along with the previous star, this was also classified as a "hot LBV candidate" by Massey et al. (2007) and an Iron Star by Clark et al. (2012). In addition to assigning it the classification of an Iron Star, Clark et al. (2012) also studied IR photometry and concluded that the large IR excess of this star, along with its apparent variability, indicated that it may belong to the sgB[e] sub-type of Iron Stars. While the exact physical mechanism behind this sub-type is uncertain, it is thought to be similar to that of the classical B[e] stars, where rapid rotation rates drive the formation of a circumstellar disc.

Returning to the spectra of LGGS J013324.62+302328.4, what's distinctive about it is the appearance of the Balmer series, with a modest Hβ line, negligible Hγ and an absorption dominated Hδ but this is only prominent in the 2010 spectra (red) from Figure 5.2.

One of the most noticeable change between the 2010 and 2013 spectra is that the Balmer ratio ($H\beta/H\gamma$) has increased, this reverts the significant decrease in $H\beta$ observed by Clark et al. (2012) in their observations between 2006-2010. In addition to this, there was also a notable increase in the strength of the He I emission lines ($4011\mathring{A}4122\mathring{A}4358\mathring{A}4922\mathring{A}5016\mathring{A}$). Furthermore, there are still strong [Fe II] lines in 2013, which have increased slightly over the three years in between observations. In summary, although the star has developed new spectra features, there isn't enough evidence to change the classification from an Iron Star.

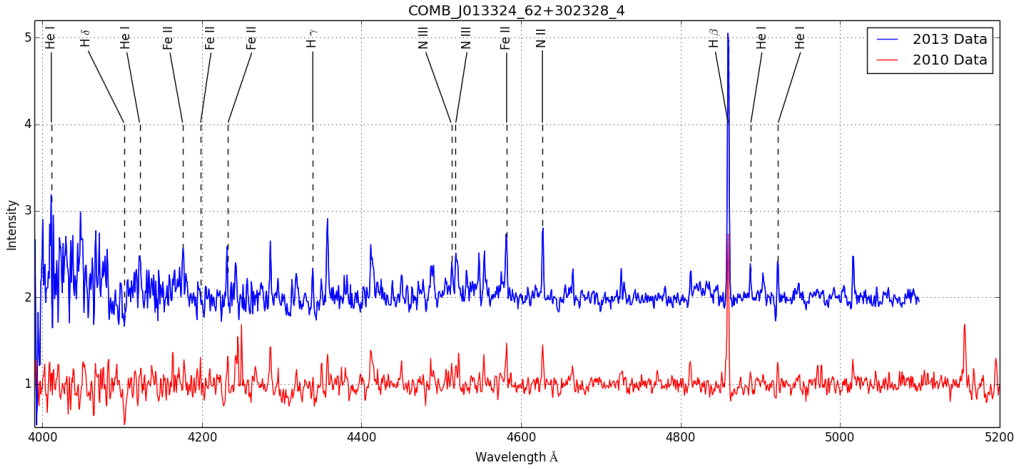

Figure 5.2: Spectra of LGGS J013324.62+302328.4, classified as an Iron Star by Clark et al. (2012). Prominent Helium lines include (4011$\mathring{A}$4122$\mathring{A}$4358$\mathring{A}$4922$\mathring{A}$5016$\mathring{A}$). Balmer series lines: $H\beta$ at 4860$\mathring{A}$ & $H\gamma$ 4339$\mathring{A}$

5.1.3 Var C

Var C is a well studied star; it was first observed by Hubble in 1926 and was among one of the original Hubble & Sandage variables that later became known as Luminous Blue Variables (Conti, 1984). Spectroscopically it resembles an early B-type supergiant or Of/late WN star during quiescence according to Humphreys and Davidson (1994), and during an LBV outburst it resembles a cool A-F type supergiant (Humphreys et al., 2014a) as a result of the star's winds becoming optically thick. Massey et al. (2007) use the spectra of Var C during quiescence as a benchmark for the classification of all "hot" LBVs in their paper, where the spectra is dominated by the Balmer hydrogen, He I and [Fe II] lines.

As for Clark et al. (2012), they made Var C one of three bona fide LBVs in their paper. The 2003 spectrum is dominated by several metallic absorption lines with just a weak Hβ emission. Combined with photometric data that suggested Var C was at maximum luminosity, Clark et al. (2012) concluded that this corresponded to a previously unknown outburst; thus casting doubt on the originally proposed ~ 40 year period of variability by Burggraf et al. (2011). The 2010 spectra from the same paper shows a noticeable change in the spectrum of Var C, with the re-emergence of strong [Fe II] and He I emission lines. This indicated that Var C had returned to a quiescent stage and more closely resembled the spectra by Massey et al. (2007) in 2007.

The spectra shown in Figure 5.3 takes the 2010 spectra from Clark et al. (2012) and compares it to new spectra from 2013. In this comparison it is noted that there are clear P Cygni profiles evident around the He I lines, and the profiles of the Balmer lines have also reduced since 2010. In addition to this, there is significant line broadening around the Hβ line resulting from increased Thompson scattering. This indicates that the wind properties of the star have changed, but there are two possible reasons for this. Either the wind temperature has changed, which

will change it's ionisation structure and hence the line strengths & profiles; or, the wind density has changed, which can affect the amount of electron scattering that occurs within the wind. In reality it is likely to be a combination of the two, but to determine this would require detailed stellar modelling which is beyond the scope of this thesis.

Figure 5.4 compares the 2013 spectra of Var C with that from B324. This is a cool yellow hypergiant which contains many low excitation metal absorption lines in its spectra, these are especially visible between $4500 - 4600\mathring{A}$, and some of these are also present in the Var C spectra from 2013, this indicates that the star has a cool photosphere capable of absorbing the metal lines. Additionally, what this spectra shows is that the absorption lines around the Hβ line are real, and are a result of residual photospheric lines.

In summary, what this new spectral data from 2013 shows is that Var C became more active in the years after Clark et al. (2012) observed it in 2010, and appears to have entered another "cool" phase of its S Dor variability cycle, further verifying the bona fide LBV classification attributed to it by Clark et al. (2012).

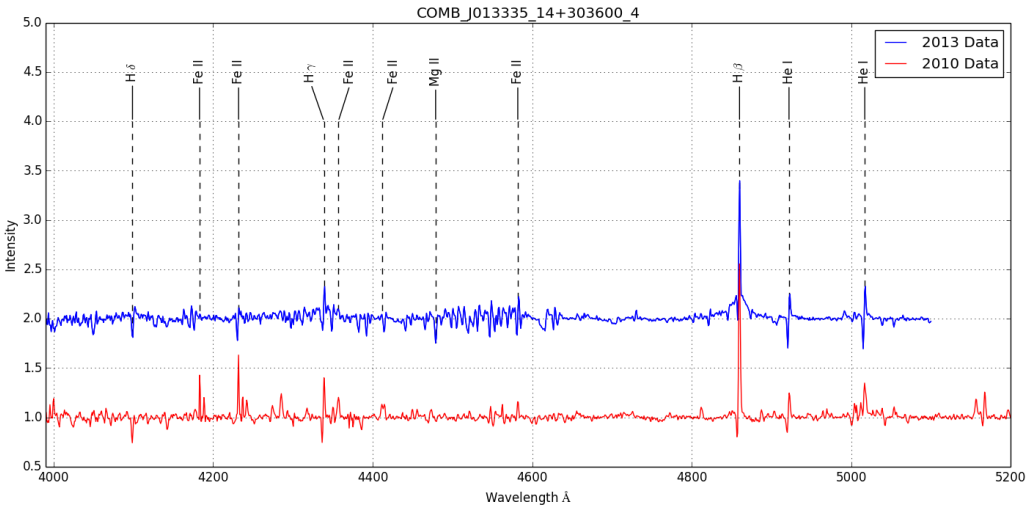

Figure 5.3: Spectra of LGGS J013335.14+303600.4 (also known as Var C), classified as a bona fide LBV by Clark et al. (2012).

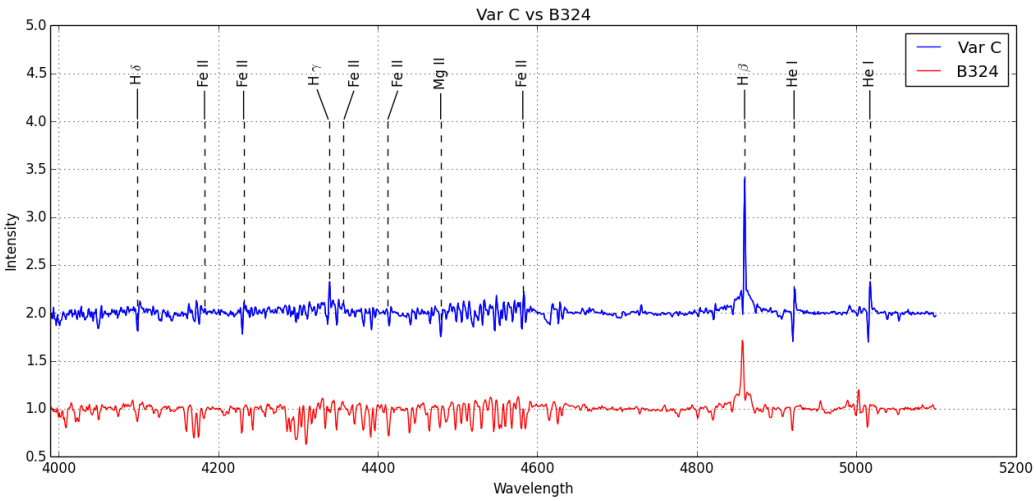

Figure 5.4: Comparison of the spectra from Var C and B324, which is a cool hypergiant and displays the cool metal absorption lines around $4500 - 4600\mathring{A}$ seen in Var C.

5.1.4 LGGS J013339.52+304540.5

This star was identified by Massey et al. (2007) as a P Cygni LBV candidate due to strong P Cygni components of the Balmer lines. This was a reclassification of the B0.5 I+WNE designation it had been assigned by Crowther et al. (1997), they noted that spectroscopic and photometric observations showed little signs of variability in the early 1990s. However, Massey et al. (2007) pointed out that these spectroscopic observations, in addition to their own 2006 specta, showed clear P Cygni profiles which had been overlooked.

Clark et al. (2012) took the low-resolution Crowther et al. (1997) spectra and compared them with new high resolution spectra taken in 1995 and 2010. What they noted was a dramatic change in the spectroscopic appearance of LGGS J013339.52+304540.5. This included the "disappearance of He I, He II and N II emission lines, a substantial weakening of the Balmer lines and the development of weak photospheric features such as: Si III".

The spectra presented in Figure 5.5 again compare the 2010 spectra taken by Clark et al. (2012) with the new spectra from 2013 and there appears to be little change between them. The P Cygni profiles are still evident on the Hβ and Hγ lines, whereas it appear the Hδ line has returned to absorption, something Massey et al. (2007) observed in their spectra from 1993. Also, it's worth noting that the He I lines are all still in absorption in the 2013 spectra, maintaining the change that Clark et al. (2012) described between their 1995 and 2010 spectra. In light of this, the author is confident that this star can now be classified as a bona fide LBV given the variability noted in previous observations and there being no new evidence to the contrary.

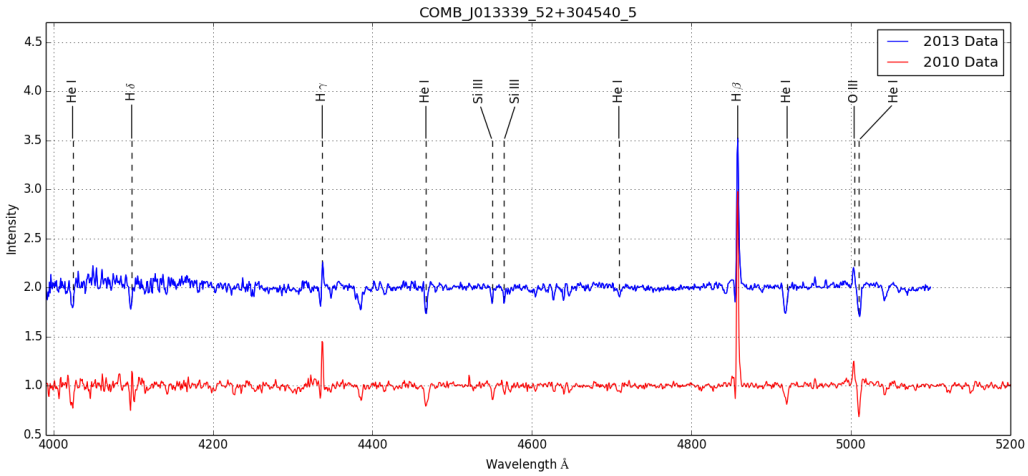

Figure 5.5: Spectra of LGGS J013339.52+304540.5, classified as a P Cygni LBV candidate by Clark et al. (2012).

5.1.5 LGGS J013341.28+302237.2

Similarly to the previous star, this star was also classified as a P Cygni LBV candidate by Massey et al. (2007). In their spectra from 2006 they noted that the Hγ Balmer line has equal absorption and emission components in its P Cygni profile, which was a departure from previous spectra obtained by Monteverde et al. (1996). And this feature continues in both the spectra presented by Clark et al. (2012) and in this thesis.

Clark et al. (2012) note that this is a "highly luminous object with a high mass loss rate" but that it also shows "no evidence for LBV-like variability over the past $\geq$17 years", which is unusual given that there is clear evidence of P Cygni components on the Balmer lines that indicate the presence of high velocity winds.

The spectra presented in this thesis is shown in Figure 5.6 and at first glance it appears that there are a few spurious lines that are too broad to be astrophysical in origin. The most likely cause of these is due to a fault in the reduction process; however, some details are still discernible. This includes the P Cygni profiles around the Balmer series lines $H\beta$ and $H\gamma$, as well as the nebular O III emission lines. Overall there is no significant change in the spectra between 2010 and 2013, meaning that this will remain as a P Cygni LBV candidate. The lack of variability in this short timescale isn't uncommon for LBV's; P Cygni itself hasn't varied significantly for 300 years but it is still classified as a bona fide LBV due to its 16$^{\text{th}}$ century eruption.

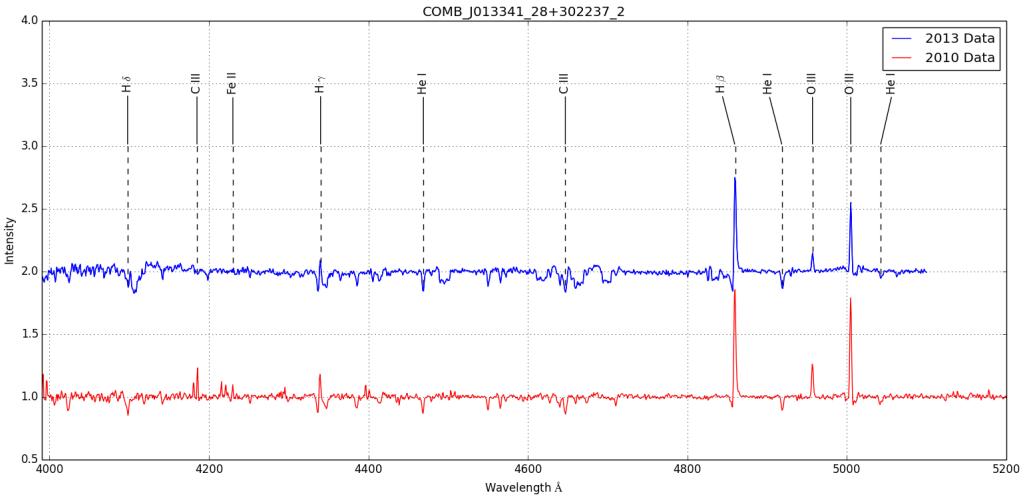

Figure 5.6: Spectra of LGGS J013341.28+302237.2, classified as a P Cygni LBV candidate by Clark et al. (2012).

5.1.6 LGGS J013350.12+304126.6

Also known as UIT 212 from Massey et al. (1996), LGGS J013350.12+304126.6 was classified as another "hot LBV candidate" by Massey et al. (2007) and as an Iron Star by Clark et al. (2012); they also noted that this star was very bright in the Infra-Red and the IR excess suggested this could be another sgB[e] star as well.

In their 2012 paper, Clark et al. (2012) present two more epochs of spectral data, one obtained in 2003 and the other in 2010, to compare with Massey 1996's 1995 spectrum. Over this 15 year time-span they noticed no significant variation beyond minor variations in emission line strengths. The spectra presented in this thesis in Figure 5.7 maintain this behaviour and the spectra from 2010 and 2013 look almost identical in every aspect. Therefore, it is straightforward to retain the Iron Star classification for this star.

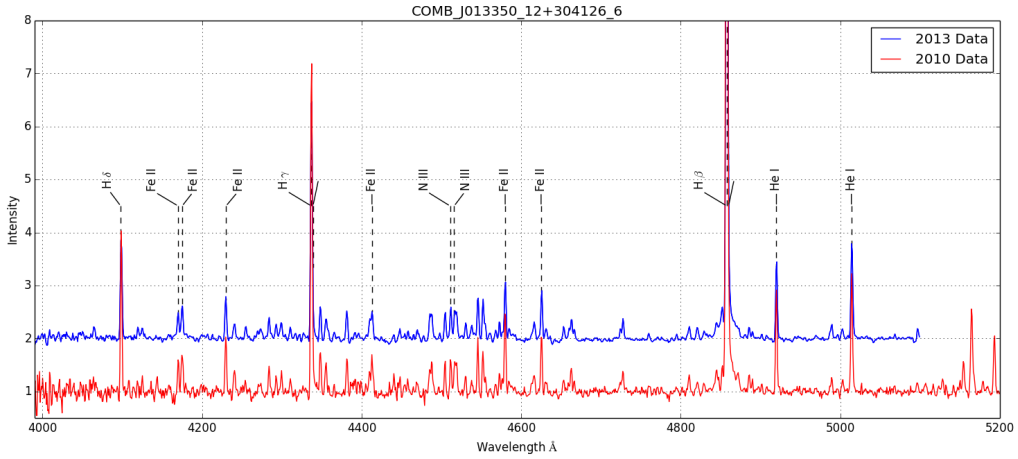

Figure 5.7: Spectra of LGGS J013350.12+304126.6, classified as an Iron Star by Clark et al. (2012).

5.1.7 LGGS J013357.73+301714.2

This star was classified as a "cool LBV candidate" by Massey et al. (2007) due to the presence of low excitation metal absorption features. What was most visibly evident in their spectra from 2006 was a strong P Cygni component to the $H\beta$ emission line, this was something that had all but disappeared in the 2010 spectra by Clark et al. (2012).

What the 2013 spectra displayed in Figure 5.8 shows is that this P Cygni profile around the $H\beta$ emission line has returned, which is evident compared to the 2010 spectra. What is also noticeable is a significant change in the $H\gamma$ absorption line (4338$\mathring{A}$) too. Lastly, it should be noted that the broad absorption features around the $H\beta$ line (4860$\mathring{A}$) are not astrophysical in origin, and are most likely caused by an error in the reduction process.

Although there is evidence of a P Cygni profile, the lack of any emission lines other than $H\beta$ suggests that this star should maintain the Blue Hypergiant (BHG) classification given by Clark et al. (2012), although clearly the wind (ionisation) structure is variable.

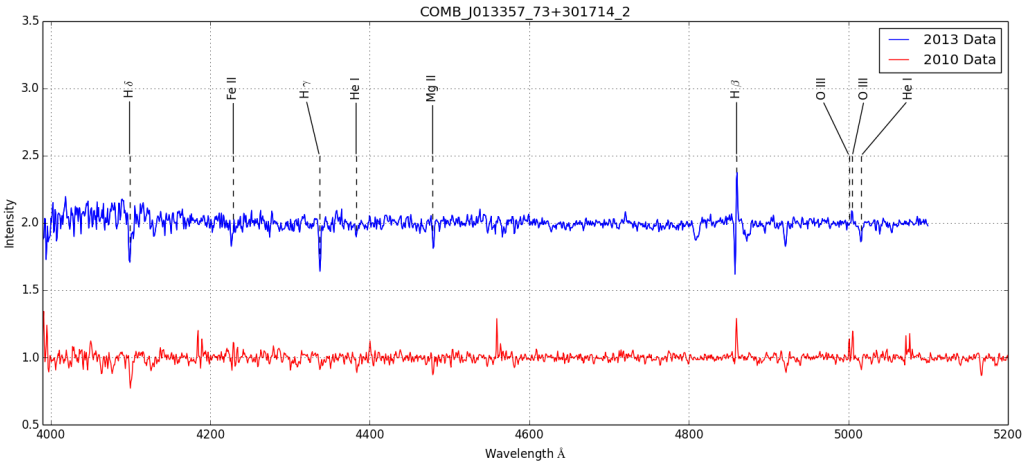

Figure 5.8: Spectra of LGGS J013357.73+301714.2, classified as a Blue Hypergiant by Clark et al. (2012).

5.1.8 LGGS J013406.63+304147.8

This is another star that was given the classification of "hot LBV candidate" by Massey et al. (2007) and of Iron Star by Clark et al. (2012). The classification by Massey dates back to their 1996 paper (Massey et al., 1996) in which it is referred to as UIT301.

Clark et al. (2012) commented that there was a lack of variability between the spectra from Massey et al. (1996) and their own in 2010, with only minor changes to the He I 4471$\mathring{A}$ emission line. When comparing this with the 2013 from this work (Figure 5.9) there is still little variation across the spectrum, with minor changes to the He I emission lines.

In addition to the spectra, archival Spitzer IR data was analysed by Clark et al. (2012) and this star was found to also possess a modest IR excess. This was explained by the presence of a circumstellar disc, but the exact cause of this disc remains uncertain; this is because radial velocity measurements by Sholukhova et al. (2004) concluded that this disc might have been generated by a short period binary, rather than rapid rotation as with classical B[e] stars.

By taking all three epochs of spectra into account, spanning 20 years in total, it is clear that this star has not shown any notable signs of variability and therefore will retain the Iron Star classification.

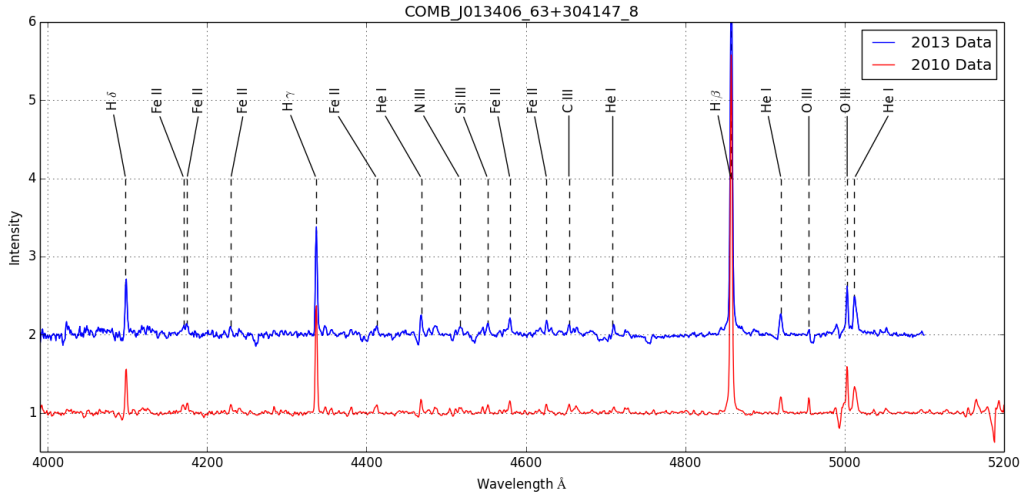

Figure 5.9: Spectra of LGGS J013406.63+304147.8, classified as an Iron Star by Clark et al. (2012).

5.1.9 LGGS J013416.07+303642.1

Also known as H108 (Corral, 1996), this was classified as a P Cygni LBV candidate by Massey et al. (2007) due to the strong P Cygni components around the He I lines and also the presence of N II emission lines, which are indicative of an enriched material at the surface.

The spectrum from 2006 also shows significant nebular contamination, something that is clearer in the higher resolution spectra taken by Clark et al. (2012) in 2010; this contamination was so bad it prevented them from correctly modelling the star.

As for the 2013 spectra shown in Figure 5.10, this is very similar to the 2010 spectra from Clark et al. (2012), although it must be noted that the spurious feature around $4440\mathring{A}$ was actually omitted in the published spectra because it is clearly not astrophysical in origin. There are little changes of note between these two spectra, the P Cygni profiles still remain around the He I lines, and the nebular contamination, namely [O III], is still strong around the $5000\mathring{A}$ mark. Therefore, this will remain classified as a P Cygni LBV candidate.

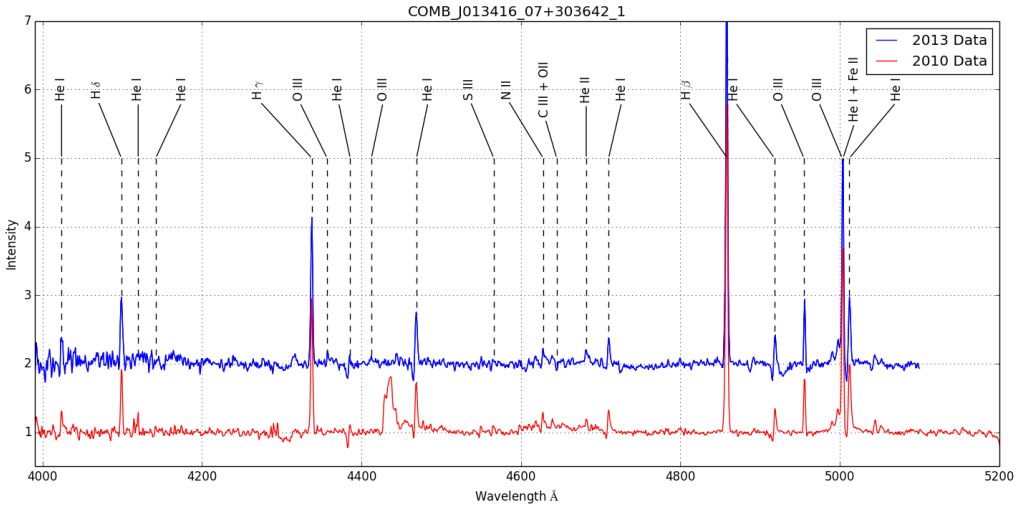

Figure 5.10: Spectra of LGGS J013416.07+303642.1, classified as a P Cygni LBV candidate by Clark et al. (2012).

5.1.10 LGGS J013422.91+304411.0

This was another star classified as a "cool LBV candidate" by Massey et al. (2007) owing to its spectroscopic appearance of a late-F/early-G type star due to the presence of cool metal absorption lines. However, Clark et al. (2012) preferred to use a morphological classification and so decided on the classification of Blue Hypergiant (BHG) for this star.

In their paper, Clark et al. (2012) describe this morphological classification based on a temperature diagnostic arising from the He I 4471$\mathring{A}$: Mg II 4481$\mathring{A}$ line ratio, whereby a strengthening of the Mg II absorption line relative to He I line is indicative of later spectra types. Indeed, they report that J013422.91+304411.0 varied from a $\sim$A0 spectral type in the 2006 spectra by Massey et al. (2007) to a $\sim$B5-8 type in 2010, due to the absence of He I absorption in the 2006 spectra.

The spectra from 2013 presented in this thesis (Figure 5.11) shows Mg II absorption has increased again, reducing the ratio and shifting the spectra type to later types.

Lastly, Clark et al. (2012) reported seeing a change in the $H\beta$ Balmer line from P Cygni-like to pure emission profile. In Figure 5.11, this is seen reversing again, with the re-emergence of a P Cygni profile by the time the observations were taken in 2013 and the presence of much more pronounced broadening features (wings) due to much stronger stellar winds. This is enough evidence to re-classify this star as an LBV due to the changes observed in the spectra.

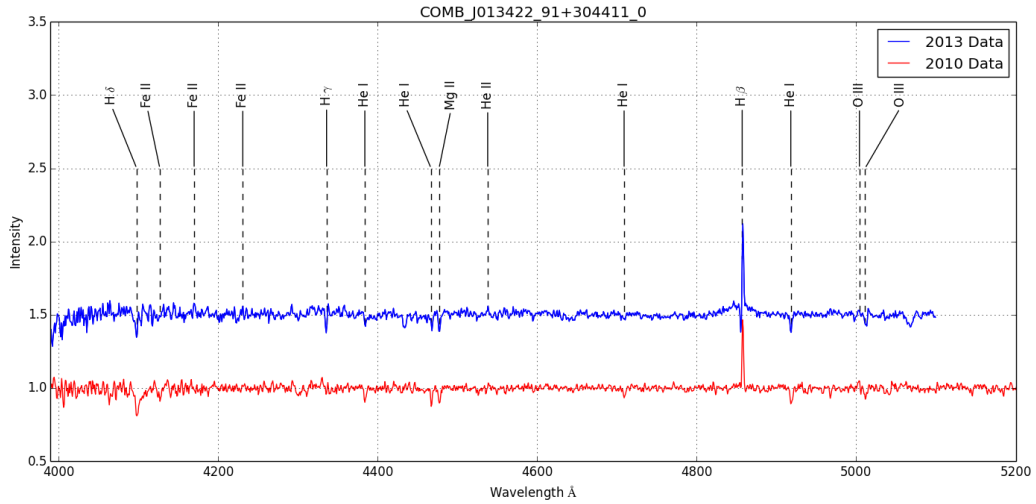

Figure 5.11: Spectra of LGGS J013422.91+304411.0, classified as a Blue Hypergiant by Clark et al. (2012). Note the significant broadening of the $H\beta$ emission line around 4860$\mathring{A}$.

5.1.11 LGGS J013429.64+303732.1

Classified as a "cool LBV candidate" by Massey et al. (2007), the spectra of this star show almost no emission features except a very narrow $H\beta$ emission atop a very broad component. They put forward the idea that this broad profile could be the result of a rapidly rotating disk or an optically thick wind, similar to Wolf-Rayets. And that the narrow emission could in fact be nebular in origin, but there are no other nebular lines, such as [O III], that would confirm this.

Similarly to the last star, Clark et al. (2012) classified this as a Blue Hypergiant due to its relatively cool spectra appearance and lack of emission lines. However, in addition to this spectra they also analysed archival mid-IR photometric observations of this star from the Spitzer telescope. From these observations they discovered that this particular star displayed pronounced long term photometric variability in the mid-IR. This has only been seen in two other M33 LBV candidates to date, Var C & Romano's Star; with the suspected cause being a combination of free-free wind emission & photospheric emission.

What their spectra from 2010 also showed was more variation in the Balmer series $H\beta$ line when compared to the Massey et al. (2007) spectra from 2006. Specifically, what they observed was an evolution of the $H\beta$ line from a single peak into a P Cygni profile superimposed onto the broad profile. However, the 2013 spectra presented in this thesis (Figure 5.12) shows this line profile has evolved again, and the P Cygni profile is no longer visible. This variation could be indicative of an LBV cycle, but what's more likely is that this is just part of the short period variations of Blue Hypergiant, which is due to the stochastic wind structure; therefore, this star will remain classified as a Blue Hypergiant.

It should be noted that there appears to be more spurious behaviour in the 2013 spectra from Figure 5.12 , owing to errors in the data reduction process. These broad absorption line features aren't astrophysical in origin.

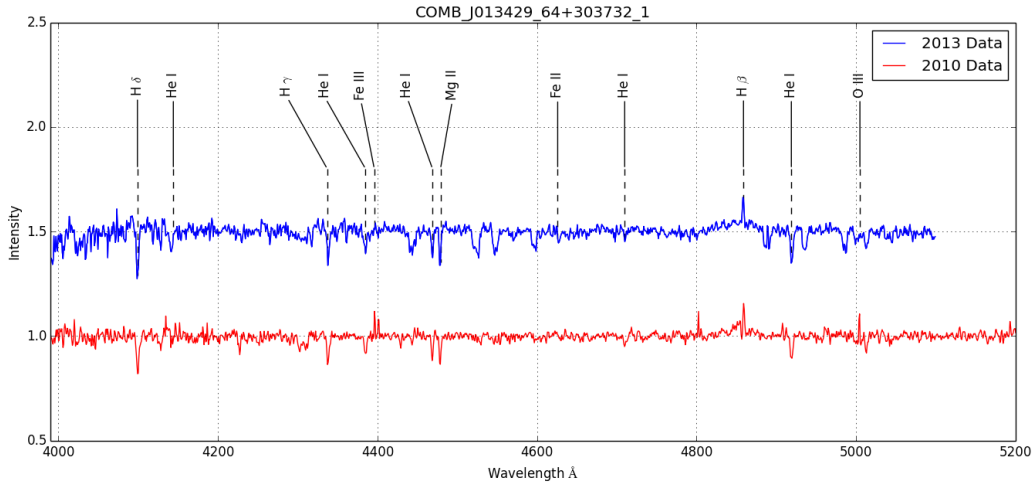

Figure 5.12: Spectra of LGGS J013429.64+303732.1, classified as a Blue Hypergiant by Clark et al. (2012).

5.1.12 LGGS J013459.47+303701.9

Based on their 2006 spectra, Massey et al. (2007) classified this as a "hot LBV candidate" due to the presence of strong Balmer series emission lines ($H\beta$,$H\gamma$ and $H\delta$), but they noted that this particular star had relatively weak Fe II lines.

Of the 15 variable candidates identified by Massey et al. (2007), the Clark et al. (2012) paper found that only one demonstrated coherent long term variability, that being J013459.47+303701.9, which they classified as an Iron star. Although this could be consistent with an LBV excursion, they concluded that as the star got bluer as it brightened, contrary to the expected behaviour of typical LBVs, it was unlikely to be one. However, there was also a suggestion that there was an intrinsic increase in reddening towards this particular region of M33.

The spectra from 2013 shown in Figure 5.13 resembles that of an Iron Star, with strong Balmer emission lines, Fe II lines and nebular [O III] lines. This is almost identical to the spectra presented by Massey et al. (2007) from 2006, with the ratio of the [O III] doublet at 4958-5007$\AA$ being indistinguishable from the one in 2013.

Unfortunately it appears that the spectra from 2010 for this star suffered from poor signal-to-noise observations, and therefore it appears featureless. Despite this poor spectra, it was still possible for Clark et al. (2012) to analyse the mid-IR photometric observations of this star. By producing a colour-colour plot of this mid-IR photometry, they were able to determine this star had a large mid-IR colour excess, consistent with other Iron Stars and similar to supergiant B[e] stars in the Large Magellanic Cloud (LMC). As has already been discussed, these two classifications might well be describing the same population of stars, that is a fast rotating star with a disk like structure at the equator, which is the cause of the mid-IR excess.

As the spectroscopic data from 2013 points to no changes in this star, the classification as an Iron Star will remain.

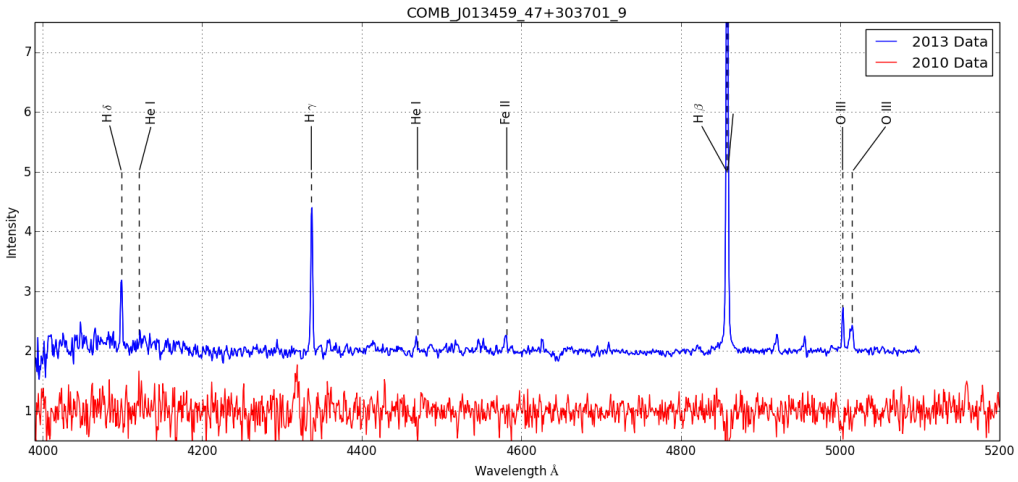

Figure 5.13: Spectra of LGGS J013459.47+303701.9, identified as an Iron Star by Clark et al. (2012).

5.1.13 Romano's Star

This star, known as Romano's Star, is a well known photometric and spectroscopic variable star in M33 and was was initially classified as an Ofpe/WN9 type star by Viotti et al. (2006). Massey et al. (2007) note that Ofpe/WN9 stars resemble the spectra of some LBVs at minimum light, and vice versa, and so Romano's Star was always considered an LBV candidate too.

Clark et al. (2012) took this further in their paper by re-classifying Romano's Star as a bona fide LBV, based on spectroscopic variability from a WN10 to WN9 star and consistent photometric data displaying a significant brightening within the same 7 month period. They also note that these Ofpe/WNL type stars are similar in spectral morphology to P Cygni stars, with the biggest difference is the absence of the P Cygni profile itself, due to higher temperatures and the presence of a weak He II line at 4686$\mathring{A}$.

What was unusual about the brightening of Romano's Star was that the bolometric luminosity appeared to increase at the same time, which as was shown in 2.2.2, is counter to the historical view that LBVs maintain a constant bolometric luminosity during an S Dor excursion. However, recent observations of LBVs such as AG Car (Groh et al., 2009) and S Dor have found that this bolometric magnitude decreases at visual maximum. And analysis by Clark et al. (2009) also found that the bolometric luminosity of the star AFGL2298 increased during an outburst. Therefore, it turns out Romano's Star is not as unusual as first thought, and the idea that LBVs maintain a constant bolometric magnitude during the S Dor cycle has now been repeatedly disproved.

It was noted by Clark et al. (2012) that the increase in bolometric luminosity of Romano's Star must be a result of increased energy output from within the star, seeing that a decrease in luminosity is usually associated with more energy being absorbed to support the expansion of the outer layers of the star. This disparity

in LBV behaviour could indicate that there are two distinct physical mechanisms underlying the behaviour of LBV stars, or it could just be related to the physical properties of LBVs such as age, mass or metallicity.

The spectra in this thesis, shown in Figure 5.14, shows that Romano's star has again varied in the three intervening years since the Clark et al. (2012) observations. One of these changes has been the return of the blended N II lines around 4640$\mathring{A}$, also seen in the Massey et al. (2007) spectra; and another has been the reduction in intensity of the Balmer lines ($H\beta, H\gamma \& H\delta$). But one of the most noticeable changes has been the large increase in the He II 4686$\mathring{A}$ emission line, which is indicative of the temperature increasing.

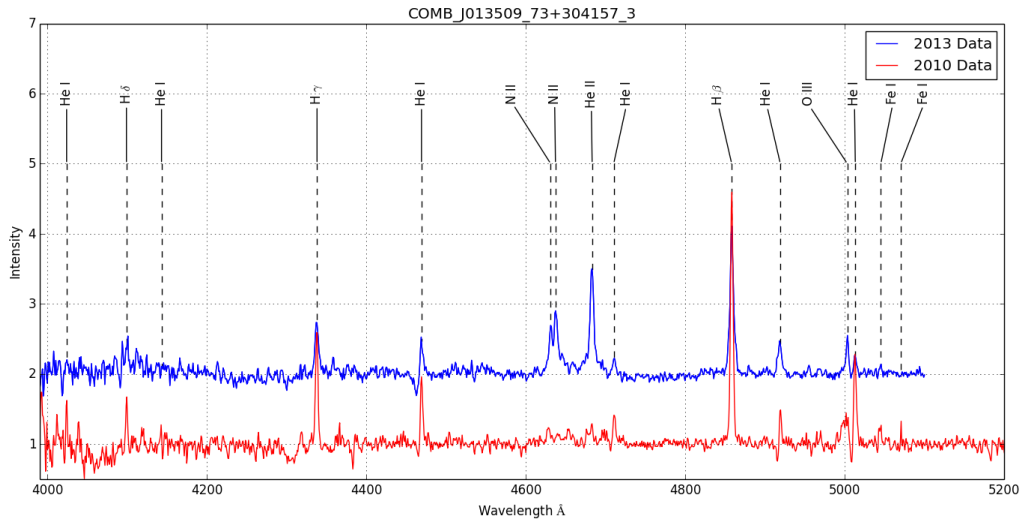

Figure 5.14: Spectra of LGGS J013509.73+304157.3, classified as a bona fide LBV star by Clark et al. (2012).

The most recent study of Romano's Star was made by Polcaro et al. (2016) and in their paper they collated historical photometric observations of Romano's star to

produce a lightcurve stretching back to 1901 and in addition to this, they studied all the published spectroscopic records too. What they found was that during 2002-2014 the spectra of the star varied between a WN10-11 to a WN8-9 during the visual maximum and minimum respectively. And this spectral change, closely correlated with the visual luminosity changes in the star. In light of this evidence and taking into account the bolometric luminosity and effective temperature, they suggest that Romano's star has finished it's last S Dor cycle and has now moved onto a Wolf-Rayet post-LBV phase (WNL).

There is still uncertainty surrounding the variability of WNL stars post-LBV and if stars such as Romano's Star that are still showing large luminosity variability have really finished their LBV phase or not. The difficulty arises because the WNL phase is a very short part of the evolution cycle of these massive stars; hence, why they are so rare and difficult to study.

The spectra from this thesis is consistent with this historic behaviour, and therefore there is no reason to disagree with this conclusion by Polcaro et al. (2016).

5.1.14 Summary Table

Below is Table 5.4 is a summary of all the new classifications made with respect to the preceding 13 subsections and the stars discussed therein. Only two stars were reclassified as a result of the analysis in this section, they were J013339.52+304540.5 and J013422.91+304411.0, which were both reclassified as bona fide LBVs.

LGGS J#	Other ID	Old Classification	New Classification
J013242.26+302114.1		Iron Star	Iron Star
J013324.62+302328.4		Iron Star	Iron Star
J013335.14+303600.4	Var C	LBV	LBV
J013339.52+304540.5	B517	P Cygni LBVc	LBV
J013341.28+302237.2	101-A	P Cygni LBVc	P Cygni LBVc
J013350.12+304126.6	UIT 212	Iron Star	Iron Star
J013357.73+301714.2		BHG	BHG
J013406.63+304147.8	UIT301	Iron Star	Iron Star
J013416.07+303642.1		P Cyg LBVc	P Cygni LBVc
J013422.91+304411.0		BHG	LBV
J013429.64+303732.1		BHG	BHG
J013459.47+303701.9		Iron Star	Iron Star
J013509.73+304157.3	Romano's Star	LBV	LBV

Table 5.4: A summary of the 13 LBV candidates after analysis, with old and new classifications.

Following on from this in the next section are a series of spectra grouped together by classification type. These spectra were all taken in 2013 but had no corresponding spectra from 2010.

5.2 Spectroscopic Analysis-Part 2

In this section are a collection of massive stars with spectroscopic data from 2013 but no corresponding data from 2010. These were identified after searching through the remaining 31 spectra obtained in 2013 that weren't already presented in section 5.1 and that showed some interesting features in their spectra. Due to time constraints, it was decided that they should all be grouped by type and shown alongside a prototypical star from that classification type, instead of a detailed analysis of each individual spectra. In addition to this, a list of unused spectra is also given.

5.2.1 Wolf-Rayets

Following on from section 5.1 and the discussion surrounding Romano's Star, it was thought prudent to check the spectra of Wolf-Rayet stars in M33 too, in case any of them showed signs of variability. Therefore, a selection of 8 stars thought to be Wolf-Rayet (WR) stars based on their spectroscopic appearance are presented here. The 8 stars are listed in Table 5.5, and their spectra is shown in Figure 5.15 compared to Romano's Star.

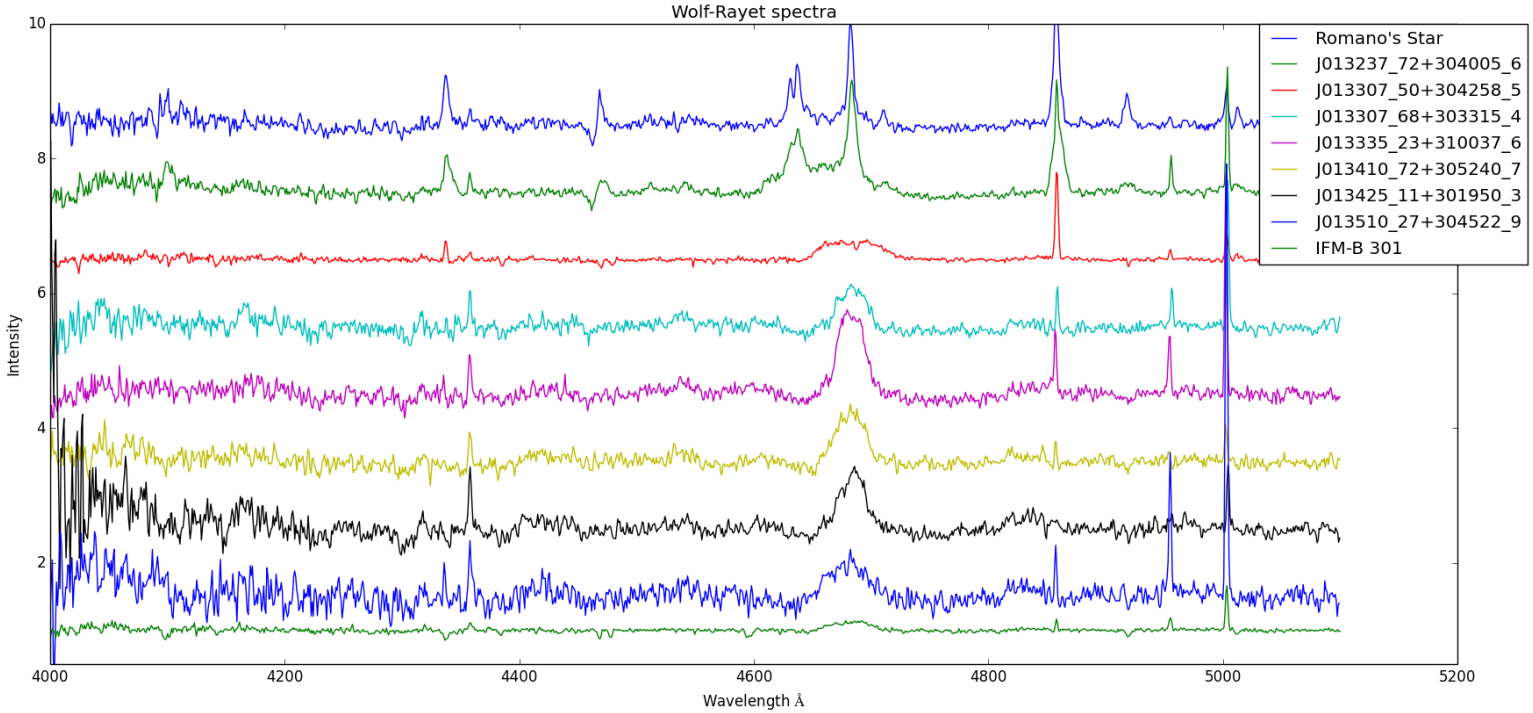

Figure 5.15: The spectra of 8 Wolf-Rayet candidates compared with the spectra of Romano's Star. The prominent lines are: N III doublet at 4634/4642$\mathring{A}$, He II at 4686$\mathring{A}$, $H\beta$ at 4860$\mathring{A}$ & [O III] at 5007$\mathring{A}$.

The key identifying feature of all these stars, and indeed of WRs in general, is the broad He II line around 4686$\mathring{A}$. Wolf-Rayets are associated with strong stellar winds, and they give rise to these broad emission line features; the stronger and faster the winds are, the broader these bumps appear. In addition to this, WN type Wolf-Rayets also show signs of a bump in their spectra around the 4634/4642$\mathring{A}$ N III doublet, which typically blends together to form what's known as the "blue bump". Conversely for WC type Wolf-Rayets, they are associated with a "red bump" around the C IV 5802/12$\mathring{A}$ doublet. Both of these bump features involve the products of the CNO cycle which are exposed as a result of the strong stellar winds (Gómez-González et al., 2016).

LGGS	Other ID	Classification
J013237.72+304005.6	UIT 003	Ofpe/WN9
J013307.50+304258.5		WN
J013307.68+303315.4		WN
J013335.23+310037.6		WN
J013311.44+304856.9	IFM-B 301	WN+OB Binary
J013410.72+305240.7		WN
J013425.11+301950.3		WN
J013510.27+304522.9		WN

Table 5.5: A list of all the Wolf-Rayet candidates.

Bibby and Crowther (2010) set out a classification of sub-categories for nitrogen rich Wolf-Rayets (WN) in their paper from 2010. For stars with spectra dominated by the N V lines 4603-20$\mathring{A}$ a classification of early type WR was assigned, also known as WNE or WN2-4. Secondly, for stars with spectra dominated by the N IV 4058$\mathring{A}$ and N III 4636-4641$\mathring{A}$ lines, these were classified as mid type Wolf-Rayets (WN5-6).

Lastly, for WN stars with spectra dominated by the N III 4634-41$\mathring{A}$, these were assigned the term late type WN, also known as WNL or WN7-9. But if only He II was detected in the spectra then they would be assumed to be a WNE subtype.

All of the spectra presented in Figure 5.15 show signs of this broad He II feature, some more so than others. Take J013237.72+304005.6 for example, this has a narrow but strong He II 4686$\mathring{A}$ line on top of a much broader emission feature which also contains the N III doublet as well. This spectra also closely resembles that of Romano's star, which as discussed in the previous section, is now thought to exist in a post-LBV phase as a WN8-9. So judging by the spectra alone, it could be argued that J013237.72+304005.6 is also a post-LBV WN star.

Two of these spectra, IMF-B 301 & J013307.50+304258.5 show only very slight bumps around this He II line; this could indicate a low wind density or it could just be contaminated by a second component continuum in the line of sight.

As for the Balmer series hydrogen lines ($H\beta$ & $H\gamma$), the narrow nature of these tend to indicate that they are in fact nebular emission lines and do not originate from the wind. With the exception of J013237.72+304005.6 which has a fairly broad $H\beta$ profile, this appears to be the case for all these WR candidates, which is not unexpected since Wolf-Rayets are supposed to be hydrogen-free.

5.2.2 Cool Hypergiants

Additionally, within this data set of spectra taken from 2013 it was found that there was a selection of 4 cool Hypergiants plus a cool LBV candidate, these are listed in Table 5.6 and their spectra is presented in Figure 5.16 and shown with B324 and Var C for comparison.

LGGS	Other ID	Classification
J013349.56+303941.6		Cool Hypergiant (Aof)
J013351.48+305252.9		Cool Hypergiant
J013355.47+310009.0		Cool Hypergiant
J013356.58+303826.6		Cool Hypergiant
J013415.42+302816.4		Cool LBVc

Table 5.6: List of 4 Cool Hypergiant stars and one cool LBV candidate. The prominent line around 4860$\mathring{A}$ is the $H\beta$ Balmer line and the lines between 4300-4600$\mathring{A}$ are all metal absorption lines.

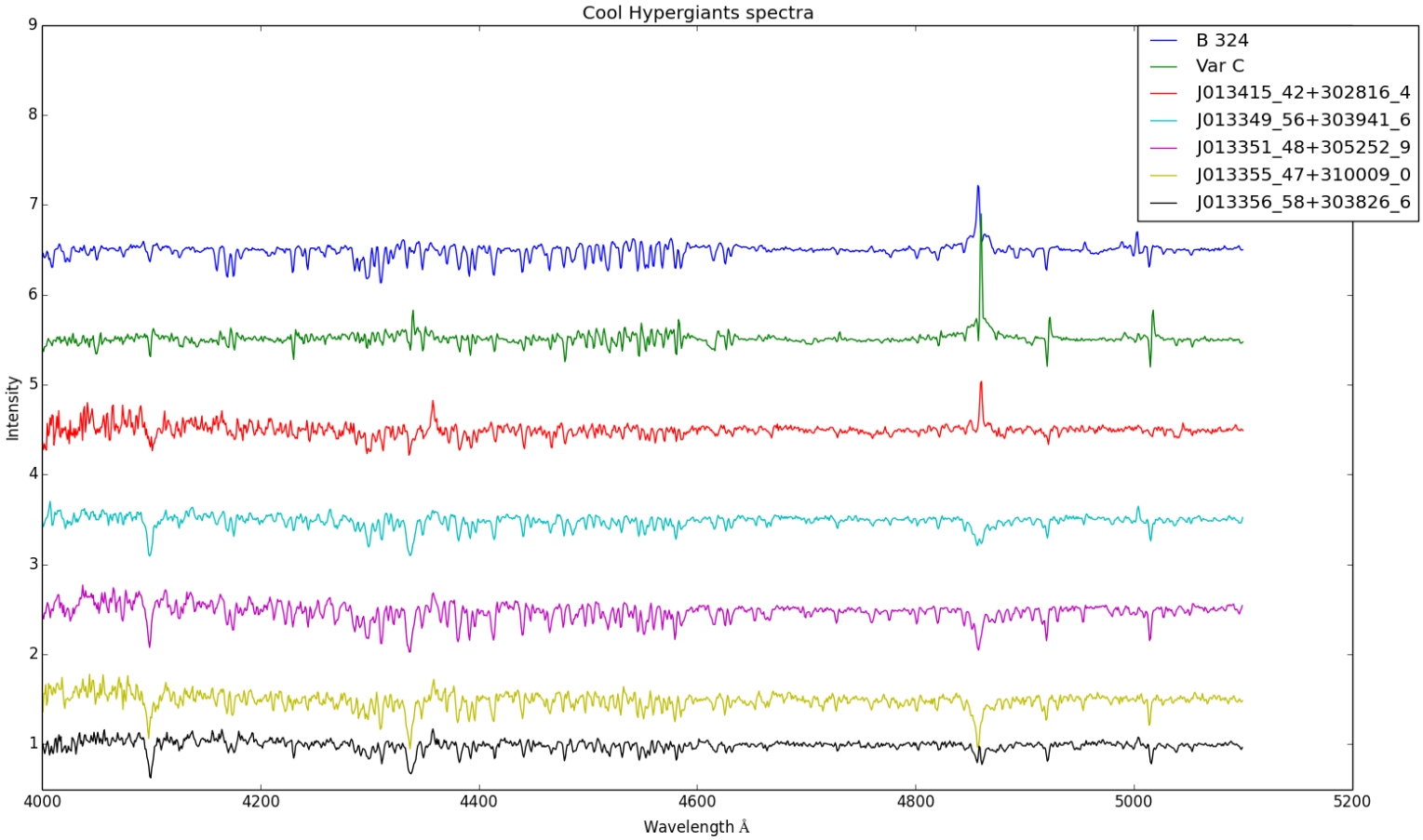

Figure 5.16: Spectra of 4 Cool Hypergiant candidates compared with the cool hypergiant B324.

What these stars all have in common in their spectra is the presence of low excitation metal lines in absorption between 4300-4600$\AA$. This is as a result of their cool photospheres which enables metal lines to be in a de-excited state, ready to absorb photons as they escape through the atmosphere. In addition to this, the 4 cool hypergiants all have the Balmer hydrogen lines in absorption, which means they must have a lower mass loss rate.

Included in Figure 5.16 are the spectra from two comparison stars, B324 & Var C. B324 is one of the most luminous blue stars in the Triangulum galaxy, occupying a region of the H-R diagram close to the classical Eddington limit. Analysis by Monteverde et al. (1996) showed that B324 has a possible spectral variability between an F0-F5 Ia to A5 Iae with line profile variation in the Balmer series, along with evidence of P Cygni profiles, which led them and previous groups to label B324 as an LBV.

Clark et al. (2012) suggested that the luminosity of this star is incompatible with a Yellow Hypergiant evolving across the red end of the H-R diagram, and it might instead better fit the classification of an LBV undergoing an outburst. Furthermore, the long term stability of this star over 20+ years tends to suggest it could be a Yellow Hypergiant, but an LBV undergoing an outburst over multiple decades isn't unheard of.

Take Var C for example, this is the other spectra from a known LBV shown in Figure 5.16. This star has had several periods of sustained luminosity increases, coincident with a cool phase of an S Dor cycle. And as shown by the close resemblance between their spectra in Figure 5.16, it can resemble a cool hypergiant during outburst, with rich absorption and emission lines.

Taking this into account, it was therefore possible to assign the classification of a cool LBV candidate to J013415.42+302816.4. This is a result of the presence of metallic absorption lines and Balmer emission lines in its spectrum, closely re-

LGGS J#	Other ID	Notes
013232.52+303022.4		Just noise (HII region?)
013245.41+303858.3	UIT008	Nebular and featureless
013250.70+304510.6		Essentially featureless
013315.43+302300.1		Essentially featureless
013333.49+304133.4		Nebular on BSG Continuum?
013345.15+303620.1		Featureless
013439.98+303839.4		Just noise or a cool star

Table 5.7: A table showing a list of targets with spectra obtained in 2013 but showed no significant features.

sembling that of B324 & Var C. The $H\beta$ emission line for example, is evidence for dense stellar winds emanating from the star at a high velocity; and coupled with the presence of metal lines that indicate a cool photosphere, there is more than enough evidence to classify this as an LBV candidate based on the spectroscopy alone.

As for the 4 cool hypergiants, these are likely to be A or F spectral type stars with surface temperatures around 6-8000K making them yellow-white in appearance.

5.2.3 Unused Spectra

Several spectra were disregarded because they were either dominated by noise or showed no significant spectral features. These are summarised in Table 5.7, and contain notes about why each one was disregarded. Typically this would either be due to nebular contamination or there was simply no spectral features visible.

For example, the spectra of UIT008 was found to contain strong narrow Balmer series emission lines but due to their narrow appearance they must originate in a nebular cloud, rather than in the stellar wind of a massive star.

5.3 Discussion

In summary, this chapter has presented new spectroscopic observations of 26 massive stars in the Triangulum galaxy (M33) to determine whether or not they resemble Luminous Blue Variable (LBV) stars. The first half of this chapter discussed comparison spectra from Clark et al. (2012) taken in 2010 and the new spectra taken in 2013, from this it was possible to determine that the stars J013339.52+304540.5 and J013422.91+304411.0 were both reclassified as bona fide LBV stars based on their spectroscopic appearance. In addition to this, in section 5.2.2, J013415.42+302816.4 was reclassified as a bona fide LBV based on it's resemblance with Var C during it's cool phase. This brings the total number of new LBVs identified in this thesis to 3, and brings the total number of confirmed LBVs in M33 to 45. In addition to this, it was also possible to assign new classifications to 4 Cool Hypergiants as a result of the spectra obtained in 2013.

What was also observed was the continuing variability of both Var C and Romano's Star, both considered bona fide LBVs. With respect to Var C, this was observed entering another "cool phase" of it's S Dor cycle in 2013 as a result of increased line broadening and stronger P Cygni absorption which both indicate increased mass-loss rates. And as for Romano's Star, this is thought to be near the end of it's LBV phase, or possibly already in a post-LBV WN phase, and several noticeable changes to it's spectra were observed. Most notably of these was the significant increase in the He II 4686$\mathring{A}$ emission line, which indicated an increase in the temperature of the star has occurred.

As for the new bona fide LBV stars, J013339.52+304540.5 and J013422.91+304411.0 both displayed variability in their spectra, including the presence of P Cygni profiles which indicated the presence of a strong circumstellar wind. In the case of J013415.42+302816.4, the presence of metallic absorption lines, along with Balmer hydrogen lines in emission, were enough evidence to reclassify this as

a bona fide LBV too.

With regards to the Cool Hypergiants, these four stars were found to have cool photospheres due to the presence of metal absorption lines. This puts them around the Yellow Hypergiant (YHG) phase of stellar evolution discussed in Chapter . These stars are all post main sequence stars of spectral type A-F and could either be evolving towards cooler temperatures or be post-red supergiants (RSGs) transitioning to warmer temperatures (Humphreys, 2007).

5.3.1 Further research

There are limitations to visually interpreting spectra and providing a qualitative analysis, because this is open to human interpretation and provides no numerical quantities for direct comparisons between stars. And although this is a good first approach to stellar classification, to obtain more detailed classifications requires quantitative analysis, such as determining the strength of emission/absorption lines or line ratios.

Furthermore, to calculate individual stellar parameters for each star requires detailed stellar atmosphere modelling that can take the input spectra, along with some assumptions such as metallicity & rotation, and produce a model spectra that matches. The resulting model can then be used to infer changes in the physical parameters such as bolometric luminosity, mass & temperature, in order to quantify the nature of the variability. Further spectral modelling also gives timescales of these changes, as well as the duty cycle of such events.

All this information is used to provide quantitative constraints on the underlying physics of this phenomenon and is also needed for the input into stellar evolution models. With expected mass loss rates of $> 10^{-5} M_{\odot}/yr$, the rate of mass loss from these stars plays a profound role in how stars transition from the hydrogen-rich Main Sequence to hydrogen-poor/hydrogen-free Wolf-Rayet phases.

Lastly, these models can be further refined with photometric observations of these massive star by providing more constraints on the spectral type, based on its photometric appearance (colour).

This work is beyond the scope of this thesis but it could be revisited in the future and follow a similar method to what Clark et al. (2012) used when they analysed Romano's Star by using the CMFGEN software (Hillier and Miller, 1998) to determine the stellar parameters of Romano's Star at different epochs. This software is able to determine the temperature and ionisation structure of the atmosphere, and the atomic level populations from the input spectra using detailed modelling based on solutions to the radiative transfer and statistical equilibrium equations in spherical geometry, and has been specifically developed to study massive stars such as Wolf-Rayets and Luminous Blue Variables.

Ultimately, by applying these models to stars it is possible to determine approximately where a star lies on its evolution path. Applying this to a population of massive stars, and it might be possible to get a better understanding of how these massive stars behave when they are undergoing period of such high mass loss.

This chapter has focused on the spectroscopic observations of LBV candidates in M33 but the next chapter will discuss photometric observations taken with PIRATE to compliment these spectra and build a better understanding of their behaviour over long timescales.

Chapter 6

Long term photometric monitoring of candidate LBVs in M33

This chapter presents the photometric observations of candidate LBV stars in M33, to complement the spectroscopic observations already discussed. However, this part of the project was initially designed to be a proof of concept, to examine whether or not small robotic telescopes, such as PIRATE, could be used to monitor extra-galactic targets, like massive stars in M33. And after the initial tests were completed satisfactorily, the main period of photometric observations began.

Photometric observations have long been used to supplement spectroscopic observations as another way of defining LBV stars based on their variability over long timescales as they are observationally cheap to acquire and there are many facilities around the globe.

These photometric observations with PIRATE were taken between 2016-2018 and the results of the observations are discussed in this chapter. Initial pilot observations commenced on the 24$^{\text{th}}$ November 2016 and utilised the OpenScience Observatories new online scheduler (OSO Scheduler), with a second observing season commencing on the 1$^{\text{st}}$ June 2017.

The method of using joint photometric and spectroscopic observations to analyse LBV candidates was used by Clark et al. (2012) and this chapter follows a similar method in data analysis. The list of stars that were the target of these observations were all taken from this paper, and these are presented in Table 6.1. Of the 18 stars considered in Clark et al. (2012), 13 had corresponding spectroscopic data taken in 2013 (see section 5.0.2) and 8 had good quality photometric data, taken by PIRATE.

LGGS	Other ID	Classification	Clear Variability
J013335.14+303600.4	Var C	LBV	No
J013339.52+304540.5	B517	P Cygni LBVc	Yes
J013341.28+302237.2	101-A	P Cygni LBVc	No
J013350.12+304126.6	UIT 212	Iron Star	No
J013416.10+303344.9	UIT 341	BHG	No
J013422.91+304411.0		BHG	No
J013424.78+303306.6		BHG	No
J013429.64+303732.1		BHG	No

Table 6.1: Summary of the 8 LBV candidates successfully imaged by PIRATE.

There are two main reasons why not all the LBV candidates in M33 could be monitored. Firstly, given that PIRATE's plate scale is 0.63"/pixel it makes it hard to identify individual sources in the galactic bulge of the galaxy, given that it is such a crowded field. And secondly the distance to these stars in M33 meant that these observations were already pushing the limits of what PIRATE could observe, and so some were too faint to detect and the rest had fairly poor signal-to-noise data but were still detectable.

6.1 Photometric Observations

Observations of M33 from Tenerife are dictated by the altitude of the galaxy above the observability horizon of the telescope at night time. M33 is located in the Northern Hemisphere and so can be seen for most of the year from Tenerife, as the plot in Figure 6.1 shows, but the optimum time to view this target is around October when it reaches maximum altitude in the sky, and thus the lowest airmass. However, as PIRATE is also a teaching telescope these duties come first and around late-October to mid-November & mid-March to early-April, the telescope is used almost exclusively by undergraduate students for activities in their modules. Therefore, any observations need to be taken outside these windows but when M33 is over 20° above the horizon for at least half an hour per night; this is determined by the altitude limit on PIRATE and the duration of the observing programme each night.

The first observing season started on the 24$^{\text{th}}$ November 2016 after the OSO Scheduler got up and running and regularly scheduled observations were made possible. Observations continued until the 4$^{\text{th}}$ January 2017 when the gravitational wave follow-up observations took priority. These observations were of relatively poor quality due to a number of factors, firstly there were poor weather conditions at the observatory site at that time of year, so there were several nights when no data was taken at all. And secondly, as the telescope was still in its commissioning phase, there were still a number of issues that had to be ironed out, such as generating good quality flat field images; these prevented good quality data reduction to take place.

For the second observing season, usable data was collected between 1$^{\text{st}}$ June and 1$^{\text{st}}$ November 2017; and this was the data that was eventually used in this chapter.

The observations themselves were grouped into observing blocks in the scheduler, these consisted of six 300s exposures of M33 in the B filter, and so it required a 30 minute observing slot each night to be observed, and if this wasn't available

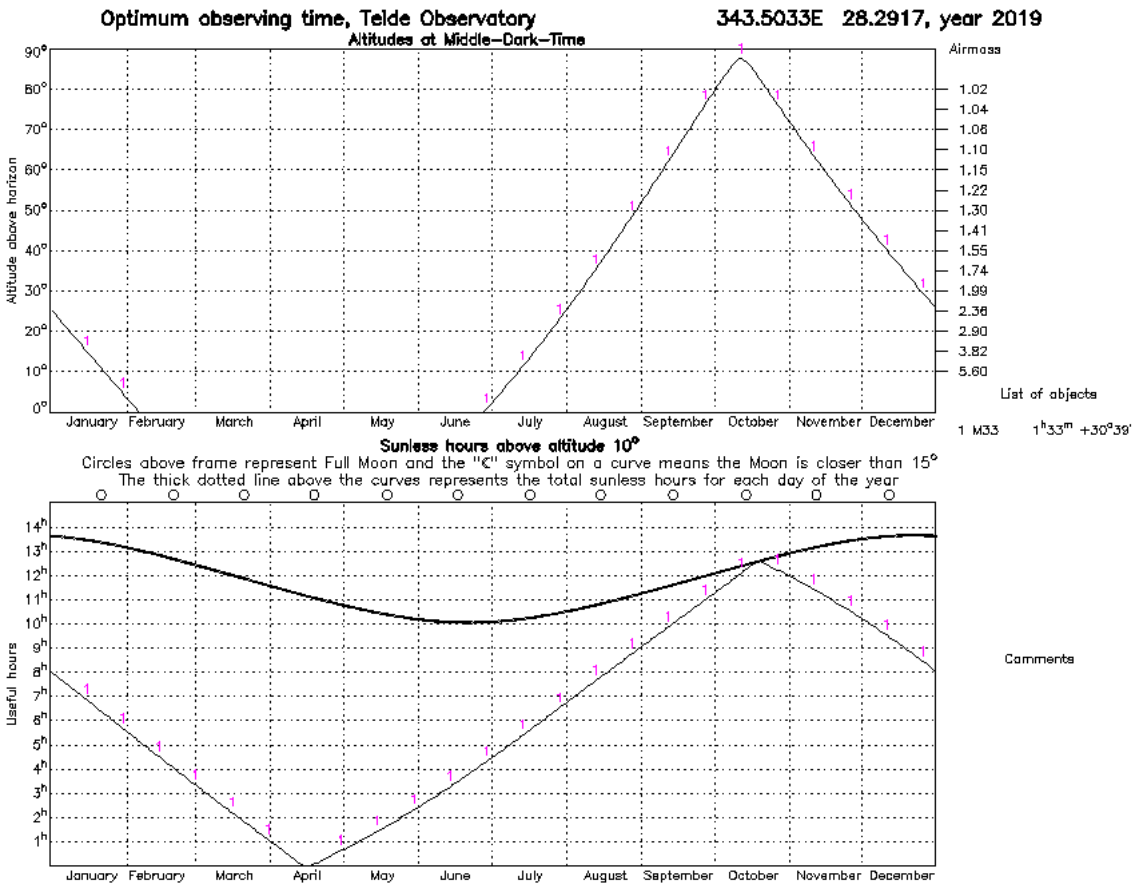

Figure 6.1: A Starobs plot showing the altitude of M33 in the sky throughout the year as seen from Teide Observatory. Plot courtesy of STARALT/Isaac Newton Group of Telescopes[1].

then no attempt would be made. But given the high priority of these observations they were almost always scheduled every night and only bad weather would prevent observations from being taken.

Photometric observations of LBVs have some benefits over their spectroscopic counterparts, firstly they are much easier to acquire as they do not require a telescope facility with a spectrograph, and as a consequence of this it follows that smaller aperture telescopes such as PIRATE can become plausible facilities for these observations. Indeed, a small robotic telescope like PIRATE can take repeat observations of the same target for months on end with little to no human input, and at a significantly lower cost than larger human operated observatories. This is important when trying to build up a long history of observations of an individual target, as obtaining spectra every night for months on end would be very expensive on a large observatory and also unlikely to be awarded observing time by a Time Allocation Committee when compared with other projects.

The main goal of this work was to continuously observe the same galaxy over and over again, to be able to monitor the behaviour of the massive stars or LBV candidates within it and look out for signs of an S Dor cycle or giant outburst of an LBV candidate star. However, these are very rare events and in reality it's only the low level variability that can be seen, which is right at the magnitude limit of PIRATE. But as the main goal was to detect and monitor these stars for large increases in luminosity, the PIRATE images provided sufficient quality in order to achieve this. As nothing resembling an S Dor outburst was detected during these observations, the secondary aim was to try and quantify any low level variability on much shorter timescales, hence what this chapter is primarily focused on.

It's thought that this low level variability most likely originates from instabilities within the star driving stochastic stellar wind events. However, photometric data alone is not enough to differentiate between this short lived stochastic wind

Figure 6.2: A true colour image of the Triangulum Galaxy, produced by stacking multiple images in different filters taken with the PIRATE telescope.

behaviour and longer term LBV trends such as the beginning of an S Dor phase. Based on the detailed photometric record of Var C, this would require much longer baselines (at least 2 years) or complementary spectroscopic data to determine when the star had undergone such a large change in temperature/radius.

6.2 Data Reduction and Analysis

Similarly to the images used in Chapter 4, the data taken in this chapter was reduced and analysed in a comparable way. The two main differences between these methods was that the M33 observations were taken in 1x1 binning and so required 1x1 binning calibration frames to calibrate the data; and secondly, although the lightcurves were generated in VaST again (see section 4.2.2), there was no requirement to employ a variability search method because the target stars were already known. So the VaST software was used in a slightly different way, by inputting the coordinates of all the target stars and just obtaining the lightcurves of this small selection.

Furthermore, VaST calculates the standard deviation of the data points of each lightcurve, which serves as a way of statistically quantifying the variability observed by the author.

The magnitudes given for all the lightcurve measurements were calibrated by VaST itself by comparing the observed fluxes with stars in the USNO catalogue of astrometric standards. However, these were not corrected for extinction due to the difficulty in obtaining an accurate value and time limitations in doing so.

Additionally, as PIRATE was using the Baader B filter at the time of these observations, the observed B filter fluxes will differ slightly to those taken with more common filters such as Johnson B or SDSS B filters (see Busuttil (2016) for more details). Therefore, all the lightcurves presented here appear slightly offset when compared directly to lightcurves obtained by other groups.

6.3 Lightcurves

Determining which lightcurves showed variability was done by a visual inspection of each lightcurve by the author. This enabled a first approximation for the variability based on the appearance of each lightcurve. The author employed a strict criteria to classify these as variable beyond any doubt, so while some lightcurves appear slightly variable, only the ones with variability clearly exceeding error bars were classified as variable. To support these assertions, the standard deviation (σ) values calculated by VaST were provided alongside each lightcurve, to illustrate the spread of values from the mean magnitude during the observing period.

Furthermore, to highlight the statistical significance of this variability, a lightcurve was constructed of a non-varying star in the same field, see Figure 6.3. This star was chosen as it had one of the lowest standard deviation values for stars of similar magnitude (of $\sigma = 0.064$) as the rest of the LBV candidates in this chapter; it was also one of lowest standard deviation lightcurves that wasn't poorly sampled, such as the one displayed in Figure 6.15.

In addition to this, this star's lightcurve was also put through the same periodogram software to look for signs of periodic variability. The periodogram in Figure 6.4 shows that for this star, even though it's got considerable scatter in the lightcurve, there's no signs of any periodic signal whatsoever.

Out of all the LBV candidates from Clark et al. (2012), only 8 were detected in the PIRATE images with good signal-to-noise data, and of those only 1 showed significant signs of variability, as outlined above. However, lightcurves for all 8 stars are presented in this chapter. It is important to note that all these images were taken in the B filter. For future observations it would be prudent to take multi-band observations to search for changes in colour, consistent with a star cooling as it expands.

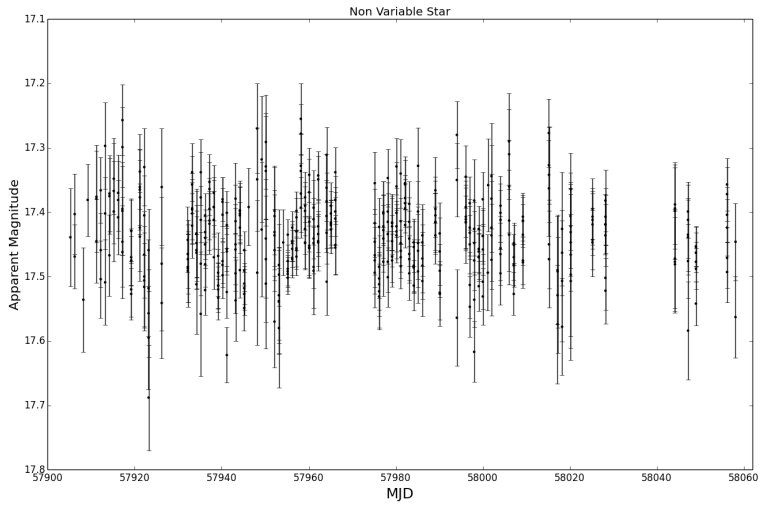

Figure 6.3: Lightcurve of a non-variable comparison star, showing a standard deviation of $\sigma = 0.064$.

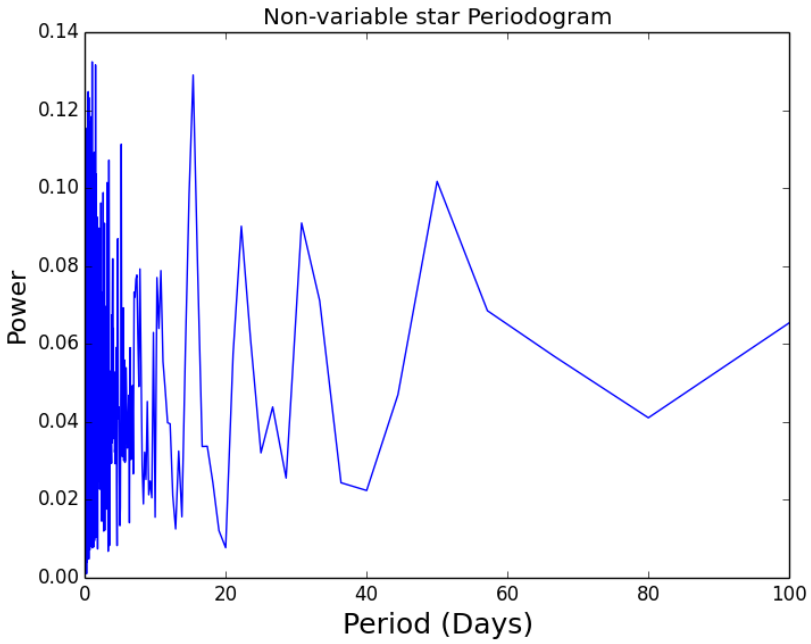

Figure 6.4: Periodogram of a non-varying star, showing no period in the data.

6.3.1 J013335.14+303600.4 (Var C)

As was discussed in section 5.1.3, this is a well studied star in M33 and was one of the very first LBVs observed in an external galaxy. As a result, there are many years of historic spectroscopic and photometric observations of Var C, dating back over 100 years in some instances (Burggraf et al., 2015).

The historical observations of Var C (shown in Figure 6.5) presented by Burggraf et al. (2015) in their paper date back to 1899, and continue until 2013 allowing them to look at the historical trend for Var C in great detail compared with other LBVs in M33.

In these long term observations, they observed Var C undergoing a prolonged period of constant luminosity of around B=17.5 for almost 20 years up to the mid-1930s, at which point the luminosity started to steadily increase up to a peak around 1947; which was the first recorded maximum of Var C, reaching B=15.4. This lasted for 3-5 years before declining to a luminosity slightly higher than it was pre-maximum. Two more minor luminosity increases were recorded in 1957 and 1963, but the long term trend was a constant luminosity of B$\sim$17 up until the mid-1980s.

At this point, Var C brightened again to a peak of B=15.4, which it maintained for approximately 4 years. After this maximum, the luminosity of Var C suddenly dropped by one magnitude in as little as 120 days. The star would then go on to spend most of the next 20 years in a cycle of short minor increases in luminosity, with one more maximum around 2002/2003 close to B=15.

The last reported observations in Burggraf et al. (2015) indicated that Var C was undergoing a sustained period of maximum luminosity from 2011-2013, with a peak luminosity of B=15.87 reported on the 1st September 2013. This leaves just under a 4 year gap between these observations and the ones obtained by the author, presented in Figure 6.6, that commenced on the 1st June 2017.

In this lightcurve taken by PIRATE the average B magnitude of Var C hovers

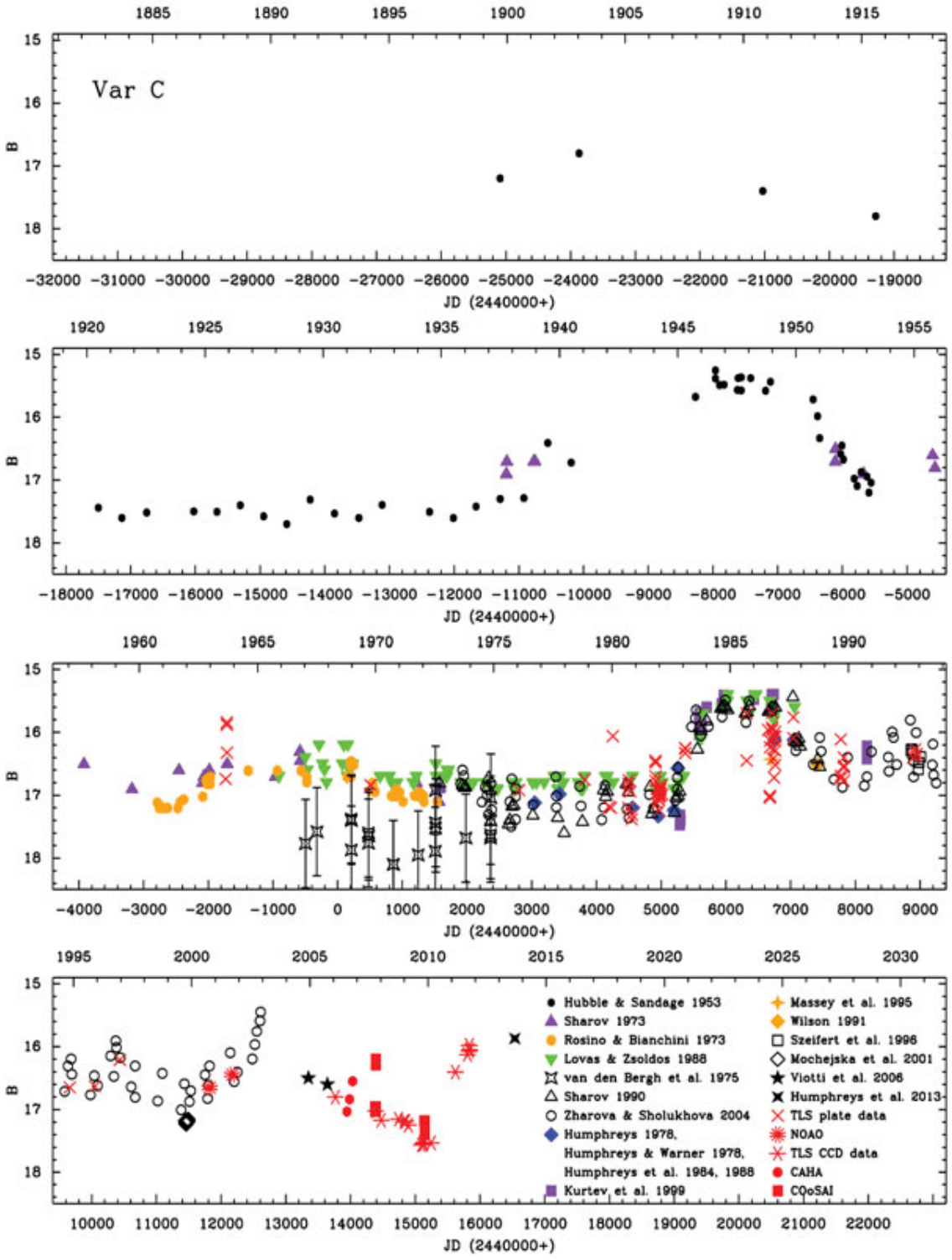

Figure 6.5: Long term lightcurve of Var C from 1899 to 2013, taken from Burggraf et al. (2015).

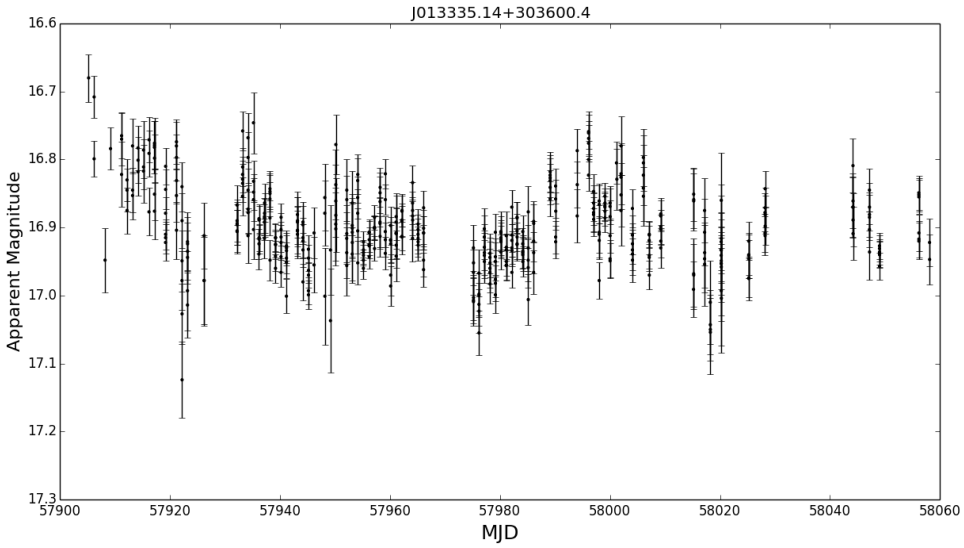

Figure 6.6: Lightcurve of Var C created with data obtained by PIRATE, showing a standard deviation of $\sigma = 0.059$. Classified as an LBV by Clark et al. (2012).

around 16.9 for almost the entirety of the 160 day observing season, and there were no signs of a significant brightening, indicative of an S Dor outburst. However the initial observations indicate a declining luminosity trend in the period leading up to these observations, which would be consistent with the last known magnitude of Var C; but this could also be part of short-term variability. And secondly, there is a slight periodical pattern to the data points, but this is largely within error bars, therefore it was decided that this star showed no signs of significant short term variability during this observing period.

A Lombe-Scargle periodogram was computed to determine a period of best fit to this data (Figure 6.7); however, there is little indication of a defined period outside of the 1 day period, connected to the period of observations.

In summary, it is believed that Var C has remained at or around a minimum in it's S Dor cycle for the duration of these observations, which is consistent with

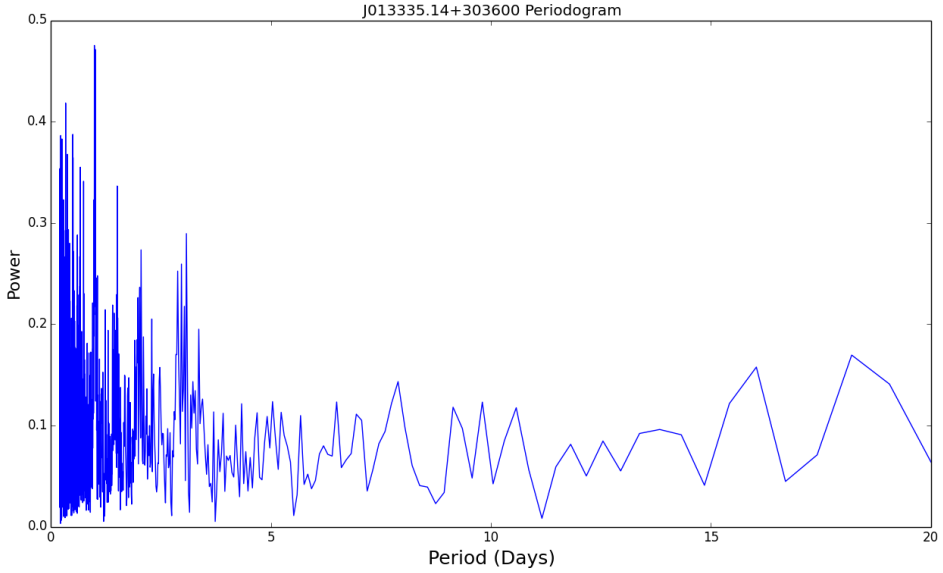

Figure 6.7: Periodogram of Var C, showing no clear period.

historical observations.

6.3.2 J013339.52+304540.5 (B517)

This star, otherwise known as B517 (Humphreys and Sandage, 1980), is classified as a P Cygni candidate by Massey et al. (2007) and Clark et al. (2012) but was re-classified in this thesis to be a bona fide LBV. This was as a result of the significant spectroscopic variability observed over three decades as well as the presence of P Cygni profiles appearing in some of the spectra.

These spectroscopic observations are supported by the photometric observations presented here (Figure 6.8) that show the star to increase in luminosity by up to 0.8 mag in as little as 7 days, and displaying some other small scale variations over the duration of the observing window. In addition to this, photometric data taken by Martin and Humphreys (2017) in their most recent observations published online[2] (see Figure 6.9) also pick up on this rapid variability around MJD 58000, although their observations are much more sparsely sampled.

Although these luminosity fluctuations are unlikely to be from an S Dor cycle, but they do indicate instabilities within the star, and these observations could be an indication of a sporadic outburst of strong stellar winds; this is backed up by the presence of P Cygni profiles in the spectra. As a result, the classification of a bona fide LBV has been further validated by these observations.

Rapid luminosity rises like this, could be mistaken for supernovae if their magnitude change were much higher; supernova impostors were already discussed in Chapter 1 but the lightcurves presented here provide some more evidence to this type of behaviour, due to the rapid rate in which the luminosity rises. However, it is not enough to indicate the star has begun an S Dor like outburst.

[2] `https://uisacad5.uis.edu/~jmart5/M31M33photcat/`

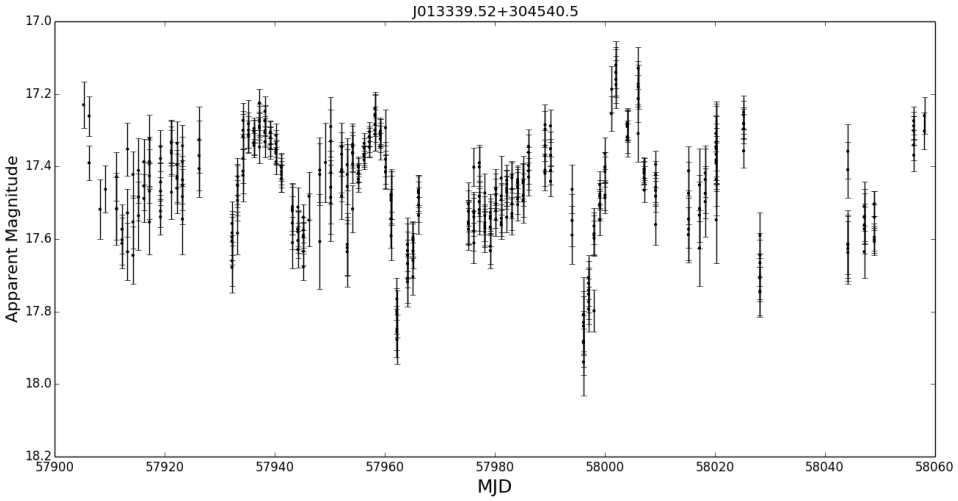

Figure 6.8: Lightcurve of B517 taken in the B filter with PIRATE, showing a standard deviation of $\sigma = 0.14$. Classified as a P Cygni LBVc by Clark et al. (2012).

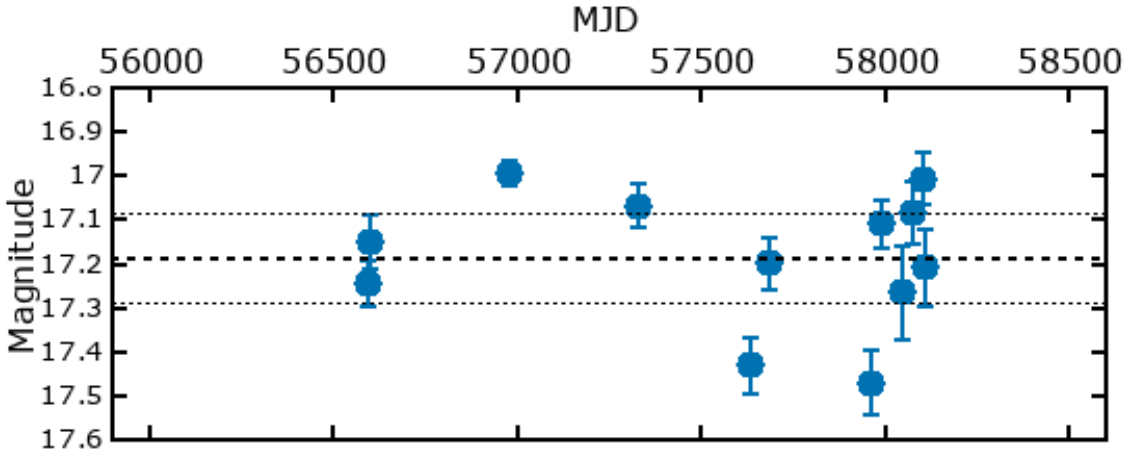

Figure 6.9: Lightcurve of B517 in the B filter, taken from Martin and Humphreys (2017) and their online catalogue[3], covering the period of observations reported in this thesis.

As with the previous star, a variability period search was performed in the form of a Lomb-Scargle periodogram and this is presented in Figure 6.10. As a result the most probable period was given as 33.36 days, but this was closely followed by periods of 16.69 days and 50.04 days. None of these period peaks were statistically significant enough to achieve a false alarm probability of 10% or lower, but they do give an indication of what the most likely timescales for this variability are.

One plausible explanation for this behaviour on short timescales is that this star is a type of α Cygni pulsator, which is common among LBV stars during quiescence. These stars exhibit non-radial pulsations, likely caused by opacity variations within the star (κ mechanism) Saio et al. (2013), which causes typical variations in brightness of $\sim 0.1 m_v$. Yet, the behaviour of B517 exceeds this, and so is unlikely to be as a result of α Cygni pulsators; so there might be another physical mechanism behind these rapid fluctuations.

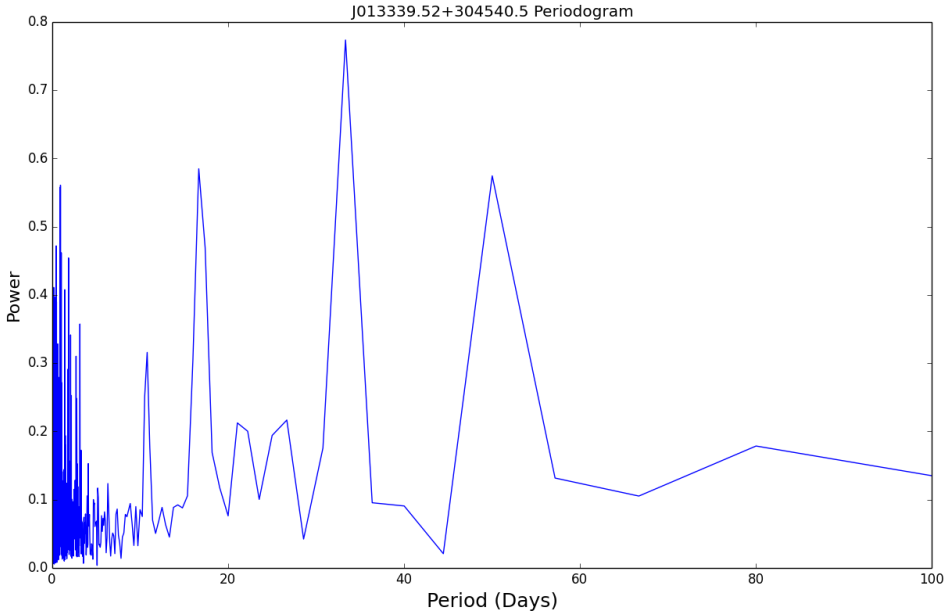

Figure 6.10: Periodogram of B517, showing a potential period of 33 days.

6.3.3 J013341.28+302237.2 (110-A)

Similarly to the previous star, this one was classified as a P Cygni candidate by Massey et al. (2007) and this particular star was noted for its high luminosity by Clark et al. (2012). However, they also noted was that this star lacked LBV-like variability over a 17 year period, which is reminiscent of P Cygni itself. The photometric observations presented here in Figure 6.11 also show few signs of significant luminosity change over the $\sim$ 4 months of photometric observations. While there is undoubtedly some variability present, after taking into account some of the large error bars it becomes harder to single out precise shifts in luminosity, and they are certainly not on the scale expected of an LBV undergoing an S Dor cycle.

This is further backed up by observations taken by Martin and Humphreys (2017) over the same time period, and for several years beforehand, which are shown in Figure 6.12. These show a near linear trend over a 4 year period leading up to the period of observations presented in Figure 6.11, thus supporting the conclusion that this star isn't photometrically variable at this time.

For consistency with other results published here, a periodogram was also computed for the lightcurve of this object; however, the results of this search showed no clear signs of a period and therefore it was decided not to include this graph.

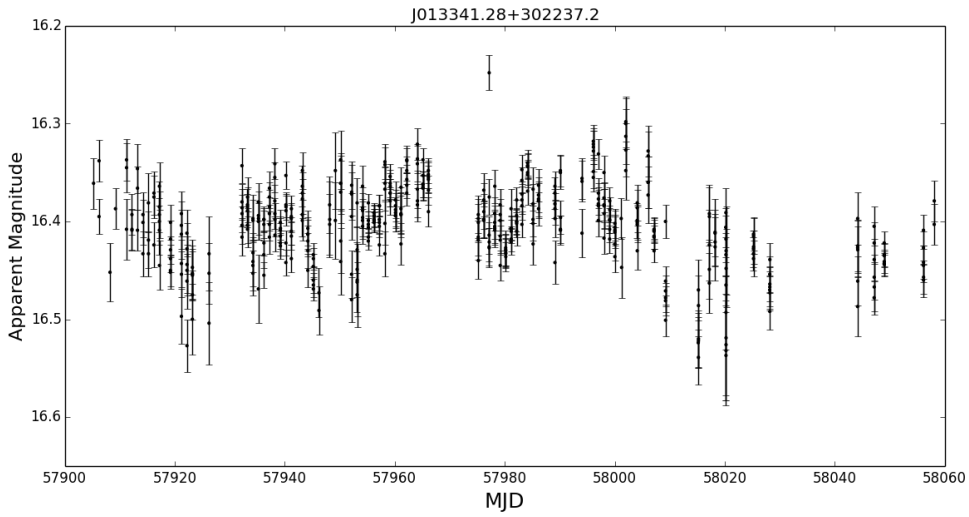

Figure 6.11: Lightcurve of 110-A taken in the B filter with PIRATE, with a standard deviation of $\sigma = 0.042$. Classified as a P Cygni LBVc by Clark et al. (2012).

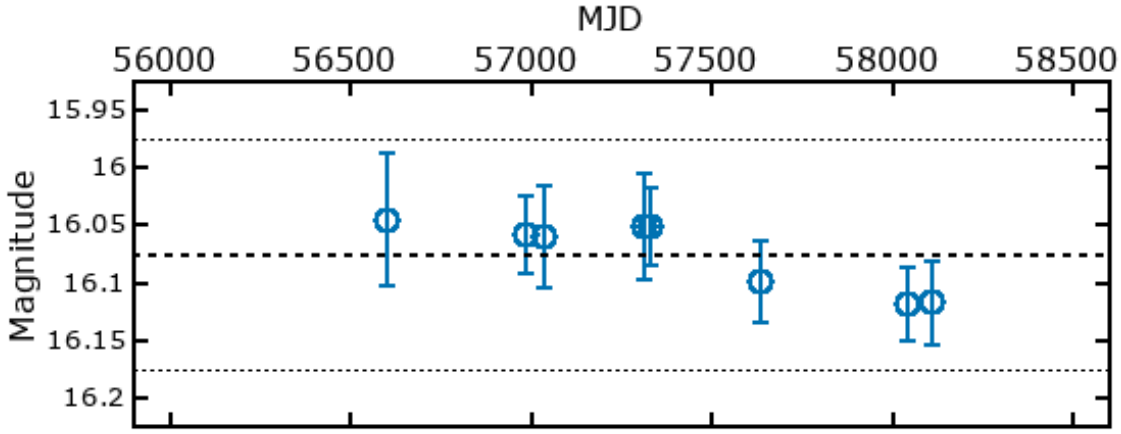

Figure 6.12: Lightcurve of 110-A in the B filter, again taken from Martin and Humphreys (2017) and their online catalogue.

6.3.4 J013350.12+304126.6 (UIT 212)

The star J013350.12+304126.6 (also known as UIT 212) was classified as a hot LBV candidate by Massey et al. (2007) and as an Iron Star by Clark et al. (2012). In section 5.1.6 it was shown that spectroscopic variations over 15 years had detected little change in the appearance of this star or the strength of the emission lines.

Subsequent photometric observations (see Figure 6.13) taken with PIRATE over the 5 month period between June-November 2017 also show little variation in the luminosity of this object in the B filter; with the exception of a slight rise in luminosity around the 58000 MJD mark. This was also observed by Martin and Humphreys (2017) in observations they have published online (which are seen in Figure 6.14). And similarly to the PIRATE observations, this appears to be a one off bump in what is an otherwise flat lightcurve. As this appears in both lightcurves, it is significant and could indicate the spike in the PIRATE data is actually a real effect. But to fully determine this, more high precision observations are required with a $\sim$1m class telescope.

However, the lightcurves in Figure 6.13 show no evidence for the beginning of an S Dor outburst, which was the primary aim of these observations, so this star must retain its classification as an Iron Star.

As with previous objects, a periodogram of UIT 212's lightcurve was performed; however, as it displayed no significant period, it was not necessary to publish the plot in this thesis.

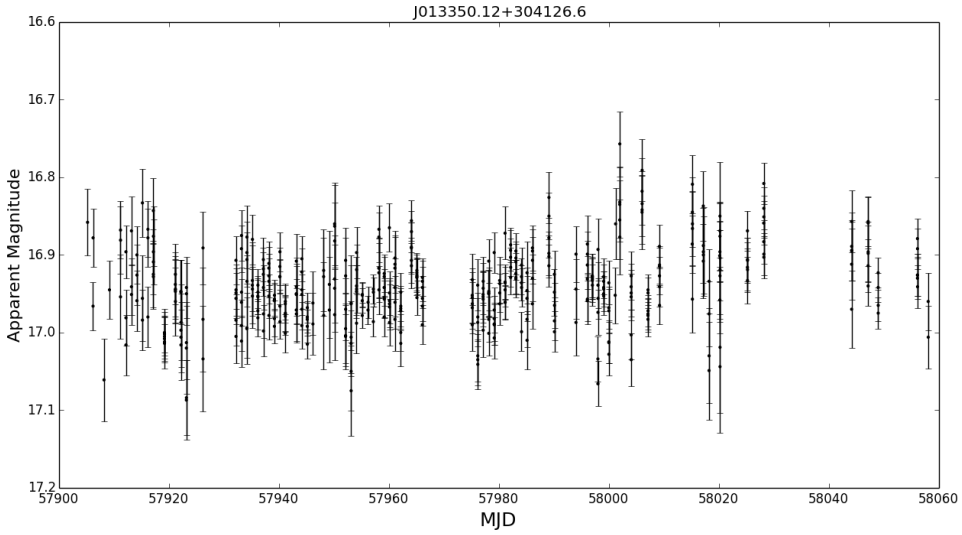

Figure 6.13: Lightcurve of UIT 212 taken in the B filter with PIRATE, showing a standard deviation of $\sigma = 0.049$. Classified as an Iron Star by Clark et al. (2012).

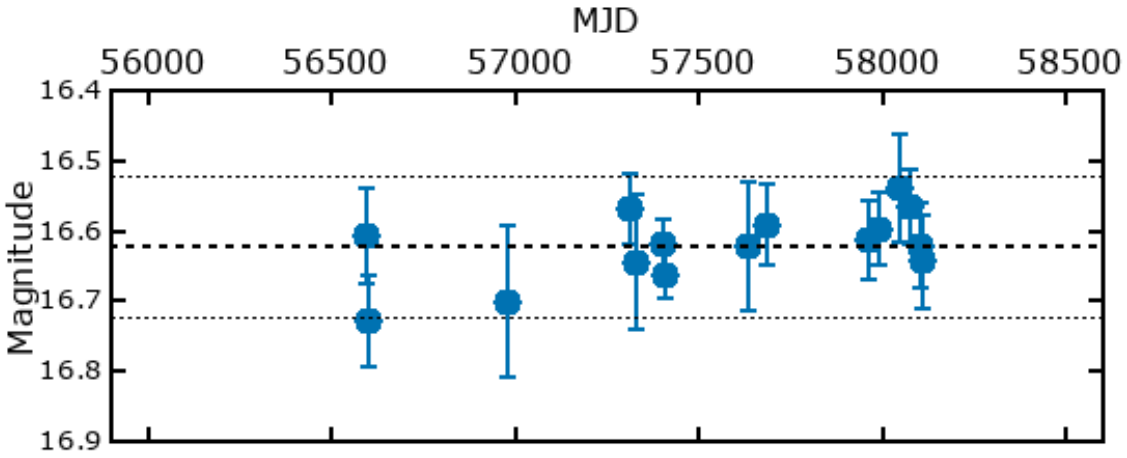

Figure 6.14: Lightcurve of UIT 212 in the B filter, also taken from Martin and Humphreys (2017) and their online catalogue.

6.3.5 J013416.10+303344.9 (UIT 341)

This star was classified as an LBV candidate by Massey et al. (2007), alongside Var B and Var C which were part of the original Hubble & Sandage variables. Also, Clark et al. (2012) classified this as an LBV candidate and commented on the resemblance of its spectrum with that of Var B & Var C, which included strong P Cygni Balmer and Fe II emission lines. This was the first time this object had been spectroscopically observed since Monteverde et al. (1996) first identified it as a possible LBV candidate.

No spectroscopic observations were obtained for this star in 2013, and so it wasn't discussed in chapter 5. But it was still added to the list of photometric targets in this chapter because it was published in Clark et al. (2012).

The lightcurve in Figure 6.15, shows a relatively poorly sampled lightcurve compared to other targets in this chapter. This is due to the location of this star within M33, where a large nebular expanse surrounds the star, making it difficult to resolve the individual PSF of this star and hence why there are fewer data points on this lightcurve. What these observations do not show, is direct evidence for the onset of a S Dor outburst and this LBV candidate is most likely undergoing quiescence or the "hot phase" of the S Dor cycle.

In comparison with the lightcurve in Figure 6.16, the PIRATE data has a larger spread in magnitudes and at a fainter level. This is because of two factors: the B filter on PIRATE has an unusual transmission curve, compared with standard filters and these observations haven't been corrected for galactic extinction. However, the true cause of this large spread in magnitudes cannot be determined from the PIRATE observations alone and so it requires more frequent observations to rule out a more rapid variation.

Lastly, a periodogram of UIT 341's lightcurve was computed, and it showed no definitive variability period above the background.

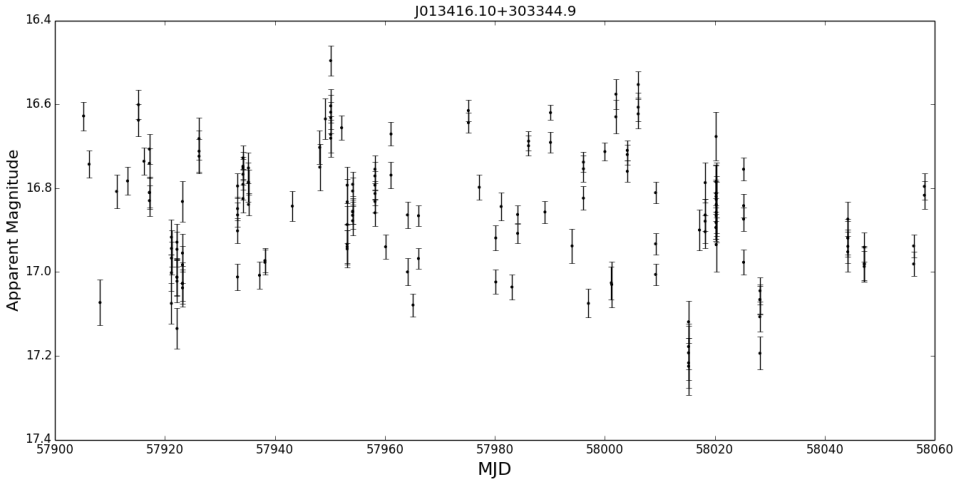

Figure 6.15: Lightcurve of UIT 341 taken in the B filter with PIRATE, showing a standard deviation of $\sigma = 0.146$. Classified as a bona fide LBV by Clark et al. (2012).

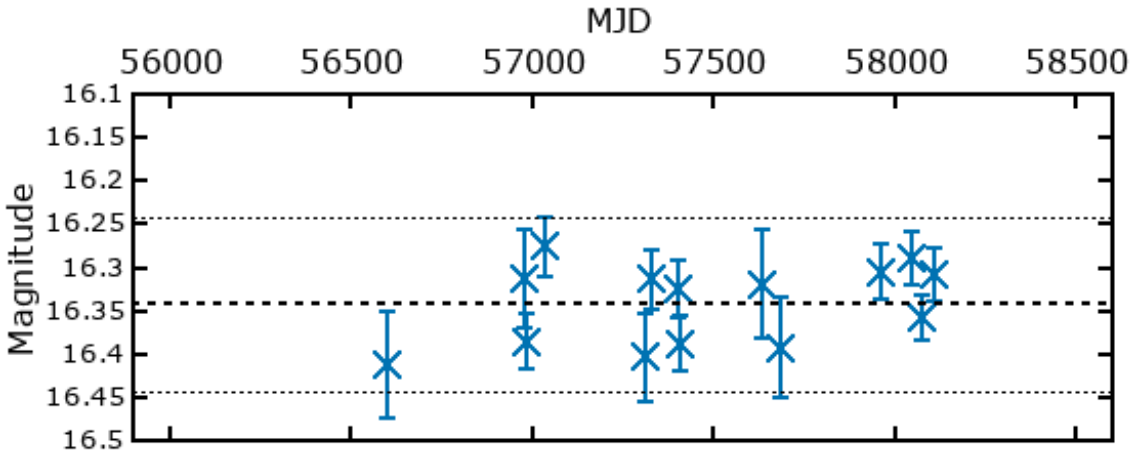

Figure 6.16: Lightcurve of UIT 314 in the B filter, also taken from Martin and Humphreys (2017) and their online catalogue.

6.3.6 J013422.91+304411.0

The source J013422.91+304411.0, was classified as a cool LBV candidate by Massey et al. (2007) and as a Blue Hypergiant by Clark et al. (2012). However, in the previous chapter of this thesis, it was decided to reclassify this star as a bona fide LBV due to the long term variability in it's spectra.

A lightcurve of the photometric observations of this star taken by PIRATE are presented in Figure 6.17 and it shows no clear variability over the period of observations. However, there are small variations over short timescales, which could be caused by the small pulsational instabilities attributed to α Cygni pulsators, as described in a previous subsection.

Observations by Martin and Humphreys (2017) (see lightcurve in Figure 6.18) around the same time period appear consistent with the PIRATE lightcurve, although this is not corrected for extinction. The trend of the lightcurve in Figure 6.18 seems to suggest that this star is on a gradual rise in luminosity over the last ~ 4 year period. If this is an LBV star, this could be an indication that it is about to move into the cool phase of an S Dor cycle that involves an increase in visual luminosity as the star cools and expands. In order to confirm this, it would require multi-band photometry to observe changes in the colour of the star in the future.

The absence of S Dor variability in the lightcurve of J013422.91+304411.0 itself does not rule it out as being an LBV, these cycles stretch over several years to decades, and there are indications of a rising luminosity trend in the photometric observations. But in the absence of a noticeable S Dor cycle it is harder to corroborate the spectroscopic observations & analysis that point towards this star being a bona fide LBV.

In keeping with previous stars, a periodogram of J013422.91+304411.0 was undertaken, but as it showed no clear variability period, the plot will not be published.

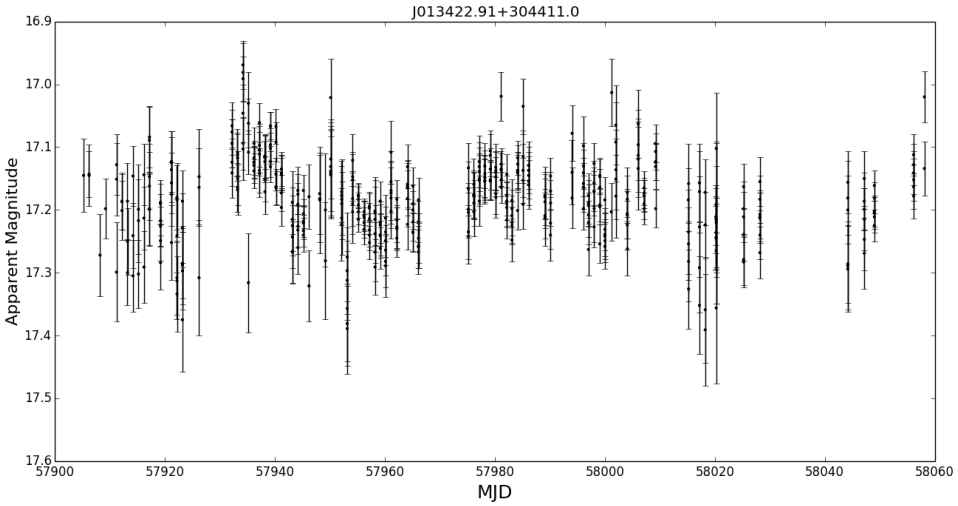

Figure 6.17: Lightcurve of LGGS J013422.91+304411.0 using data taken with PI-RATE in the B filter, showing a standard deviation of $\sigma = 0.065$. Classified as a Blue Hypergiant by Clark et al. (2012).

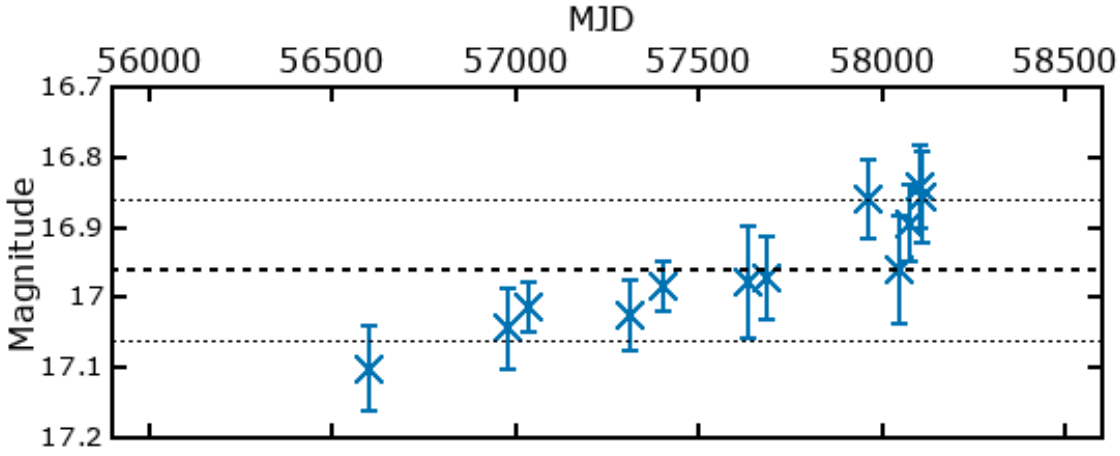

Figure 6.18: Lightcurve of LGGS J013422.91+304411.0 in the B filter, also taken from Martin and Humphreys (2017) and their online catalogue.

6.3.7 J013424.78+303306.6

Similarly to the previous star, J013424.78+303306.6 was originally classified as a cool LBV candidate by Massey et al. (2007) and as a Blue Hypergiant by Clark et al. (2012) due to the abundance of absorption and emission lines in its spectrum. However, as no corresponding spectrum taken of this star in 2013, it was not analysed in the previous chapter.

A lightcurve showing photometric observations of this star taken with PIRATE can be seen in Figure 6.19; the scatter of the lightcurve and size of the error bars is quite large which is due to reaching the observing limit of PIRATE. As a result, no definitive conclusion can be reached as to its variability. However, these observations do at least confirm that this star didn't undergo an S Dor outburst during this time, as no significant luminosity increase was detected.

To see where these observations lie in terms of the longer timescale variability, it is again worth comparing them with observations taken by Martin and Humphreys (2017) as recently as November 2018 (see Figure 6.20). These show that during the observing window of PIRATE, the luminosity of this star was around historic levels; however, in the weeks and months following there is a clear rise detected before returning to normal. Although these luminosity changes are only of the order 0.1 magnitudes, it is plausible to suggest that these small scale variations could be an indication of instabilities within the star, similar to α Cygni pulsators.

Ultimately these photometric observations are inconclusive, and do not give support to the idea that this might be an LBV star, but with a longer baseline of observations it might be possible to rule out this classification for definite. As with previous stars, a periodogram of J013424.78+303306.6 was computed, but as there was no significant variability in this star outside the error bars, the periodogram showed no clear period.

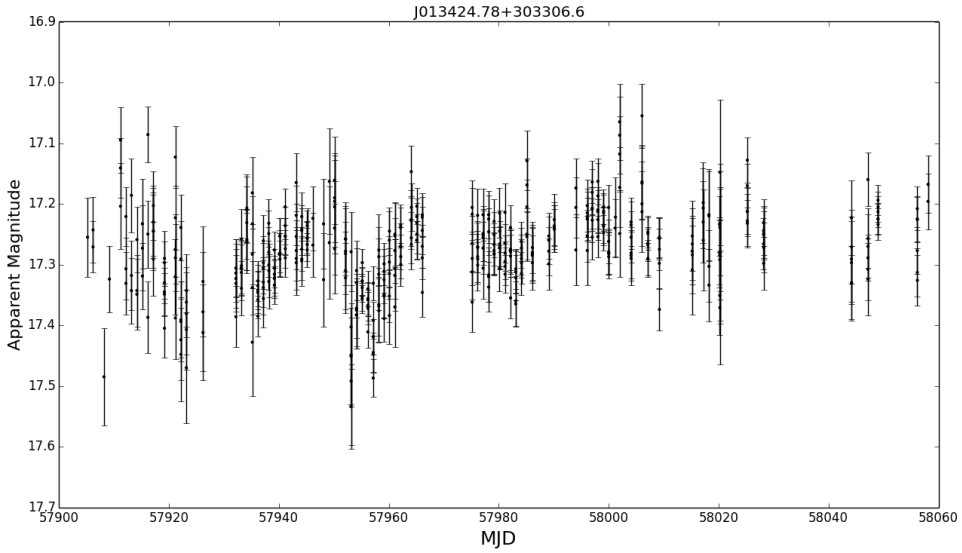

Figure 6.19: Lightcurve of LGGS J013424.78+303306.6 using data obtained with PIRATE, showing a standard deviation of $\sigma = 0.067$. Classified as a Blue Hypergiant by Clark et al. (2012).

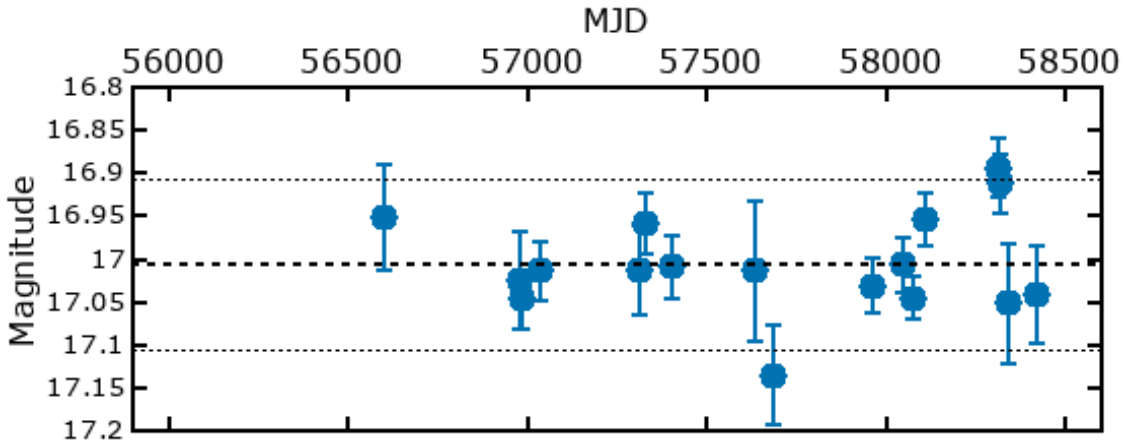

Figure 6.20: Lightcurve of LGGS J013424.78+303306.6 in the B filter, also taken from Martin and Humphreys (2017) and their online catalogue.

6.3.8 J013429.64+303732.1

Lastly, the star J013429.64+303732.1 was also classified as a cool LBV candidate by Massey et al. (2007) and as a Blue Hypergiant by Clark et al. (2012). This star was found to undergo long term photometric variability in archival mid-IR Spitzer images by Clark et al. (2012). This has only been seen in two previous M33 LBVs so far, namely Var C & Romano's Star. There are three potential causes for this variation: photospheric emission from a cool companion star, free-free continuum emission from a dense wind or thermal emission from a dusty circumstellar environment (Clark et al., 2012).

The images obtained by PIRATE were taken in the B filter, and didn't detect the same levels of variability as the Spitzer observations. Another explanation is that the star wasn't varying at the time of the PIRATE observations; these observations are depicted in Figure 6.21 as a lightcurve, produced over the 5 month period between June-November 2017. Although there are signs of some short scale variability, the low signal-to-noise observations make it impossible to discern them from the noise. As for signs of the S Dor cycle, no outburst was detected in these observations.

This can also be compared to the data taken by Martin and Humphreys (2017) and their recent observations. Their lightcurve in the B filter (see Figure 6.22) is similar to that from PIRATE, and it remains relatively flat over a long timescale. However, their observations taken in the I band show much larger fluctuations over the same period, this is shown in the lightcurve in Figure 6.23 and includes an increase in apparent magnitude by up to 0.6 compared to 0.1 fluctuations in the B filter. This is consistent with the mid-IR observations analysed by Clark et al. (2012) which indicates this star is highly variable at redder wavelengths, which could be caused by fluctuations in the dense stellar winds, among other things.

As with previous stars, a periodogram of this star was calculated but it showed no clear variability period in the data, and so therefore it wasn't published here.

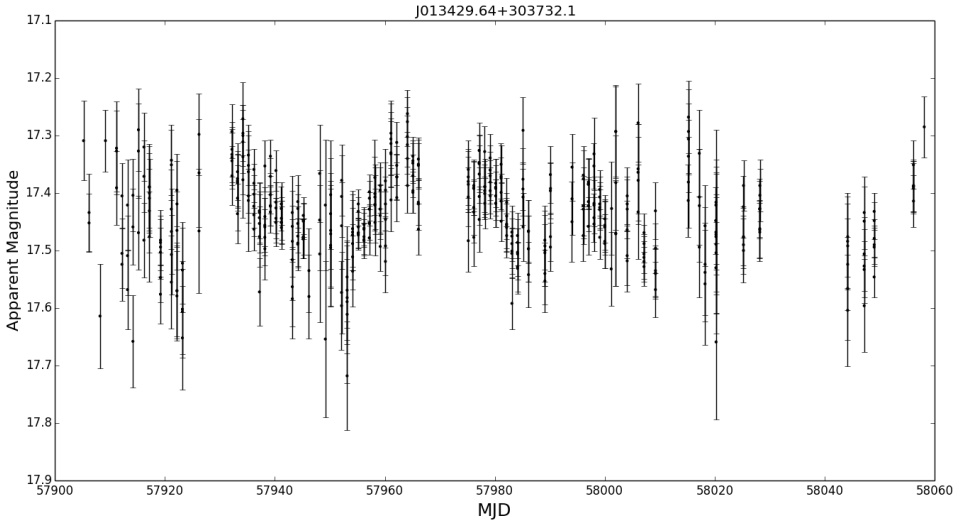

Figure 6.21: Lightcurve of LGGS J013429.64+303732.1 using data obtained by PI-RATE, showing a standard deviation of $\sigma = 0.075$. Classified as a Blue Hypergiant by Clark et al. (2012).

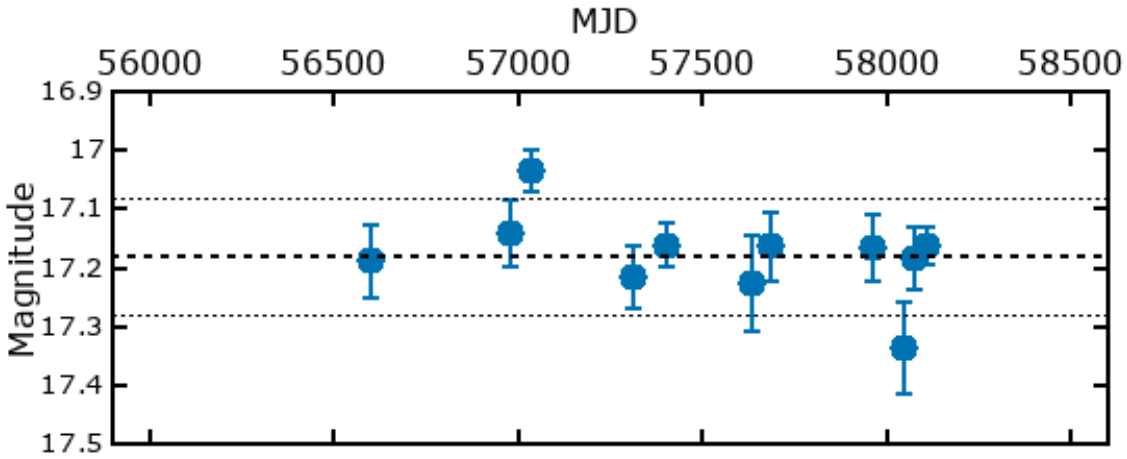

Figure 6.22: Lightcurve of LGGS J013429.64+303732.1 in the B filter, also taken from Martin and Humphreys (2017) and their online catalogue.

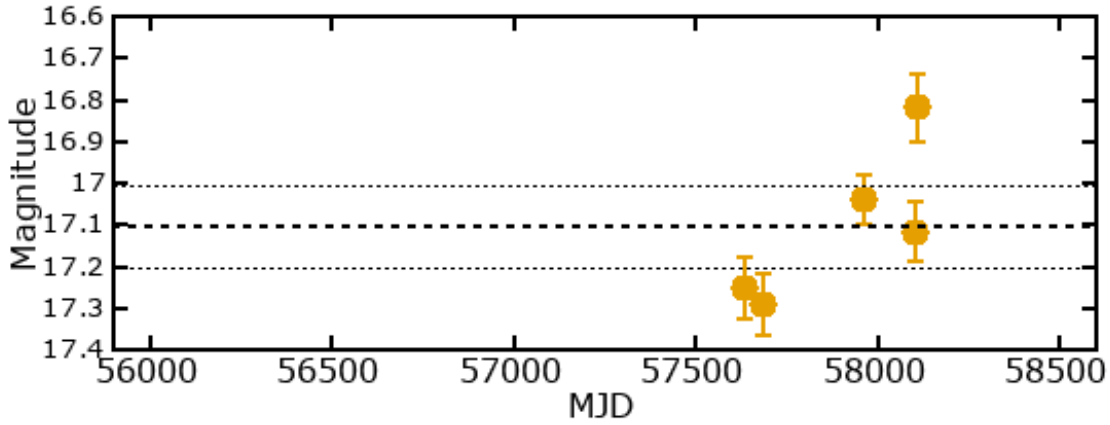

Figure 6.23: Lightcurve of LGGS J013429.64+303732.1 in the I filter, also taken from Martin and Humphreys (2017) and their online catalogue.

6.4 Summary

To summarise, this chapter has presented new photometric observations of 8 LBV candidates, taken from the list of 18 presented in Clark et al. (2012). The initial target of these observations was to monitor these LBV candidates for signs of significant luminosity increases that would be indicative of an S Dor cycle commencing. However in the absence of this, a secondary use of these observations was to probe variations on shorter timescales. Analysis of these 8 objects showed only one to undergo significant variability over the period of observations; this was J013339.52+304540.5 which showed variations of up to 0.8 mag. The others displayed some variation but due to the observing limitations of PIRATE, none were statistically significant enough above background noise.

The observations themselves were taken over a 4 month period from 1st June to 1st November 2017 and were solely taken using the B filter with PIRATE.

All these observations were also compared with historical observations taken by Martin and Humphreys (2017) and uploaded to an online database[4]. This was useful to help compare the observations presented in this thesis and put them in context with longer timescales.

6.4.1 Discussion

In the short 160 day window of observations taken with PIRATE, there was no evidence for a significant change in luminosity that would indicate a giant LBV outburst or the beginnings of an S Dor cycle for any of these stars. Instead, the low-scale photometric variability seen in one of these objects is thought to arise from instabilities within the star, and is separate from the global shift in temperature/radius that is behind the S Dor cycle.

[4] `https://uisacad5.uis.edu/~jmart5/M31M33photcat/`

Furthermore, what these observations did demonstrate is that with modern detectors and a high altitude observing site, it is possible to use a small robotic telescope to monitor extragalactic massive stars in nearby local group galaxies, such as the Triangulum galaxy, for signs of an S Dor outburst which would be typical LBV behaviour. This opens up a new window of opportunity to astronomers looking to increase their sample size for a relatively low cost. Moreover, these small robotic telescopes not only offer cost advantages but also the ability to take many more repeat observations compared with larger observatory sites where observing time is at a premium. The ability to take more frequent observations with these facilities also opens up a new region of parameter space to be be investigated, by looking for much shorter timescale variations.

However, there were limitations to this work, as only 8 stars could be clearly imaged from the target list; this was due to a few reasons. Firstly, the central region of M33 is a very crowded field, and even with 1x1 binning of images, there was a significant number of blended stars and high background light, which made the extraction of individual sources difficult. And secondly, in order to obtain these images PIRATE was taking 300s exposures, which at the time was the limit of guided observations determined by the pointing model on the mount; observations longer than this were at risk of having the point spread function (PSF) become significantly distorted. Lastly, the apparent magnitude of most LBV candidates in M33 was close to, or below, the operational limit of the 17-inch PIRATE telescope due to the aperture size and seeing conditions, which in Tenerife average 0.76“ across the year (Munoz-Tunon et al., 1997). With multiple stacked exposures it would be possible to increase the signal-to-noise of these images, but that would be at the expense of higher cadence. To have the best chance of observing shorter timescale variability requires a larger $\sim$1m class telescope that would not operate as close to its observing limit as PIRATE has done.

6.4.2 Connections with Gravitational Wave progenitors

Lastly, this section cannot be complete without returning to the connections between LBV stars and gravitational waves and their merger events. This was already discussed in section 2.2.5, which touched upon the connections between LBVs and Type IIn supernovae (SN) and recently superluminous-supernovae (SLSN).

The strongest feature connecting LBVs with SLSN is the presence of a dense circumstellar medium, thought to be the cause of the increased luminosity of SLSN; this could be formed as a result of prolonged periods of high mass-loss rates, which is why LBV stars are the prime candidates because of their S Dor cycles and giant outbursts. SLSN would produce a "burst" of gravitational radiation when they explode, which is one of the two event types that LIGO is searching for. This has close ties with the other work in this thesis on following up gravitational wave alerts, which could included both burst alerts and CBC alerts.

PIRATE is ideal for following up both kinds of transient events due to its autonomous design, and in the near future there is the possibility of recreating the multi-messenger follow up of GW170817 with a supernova event instead. This would involve a LIGO/Virgo detection of a burst signal, followed up by photometric confirmation of a new supernova source in a nearby galaxy, which could then be observed by optical telescopes across the globe, including PIRATE. And further research could then be done using archival data to try and determine the progenitor to the supernova, and if it was a high mass-loss star such as an LBV.

The topic of discussion now moves away from photometric observations of LBVs and instead turns to the conclusions and future outlooks of all the work presented thus far in the thesis.

Chapter 7

Conclusions

This chapter provides a summary of all the previous chapters, including the key results and findings. Furthermore, it presents recommendations for improvements and lists the potential for follow-up work in the future.

7.1 Summary

The central question running throughout this thesis was "Can a small-aperture robotic telescope be used to follow up time-critical and variable astronomical events, and what can we learn from these observations?". This was split into two main goals, with the first being to participate in the follow up of gravitational wave alerts released by LIGO/Virgo with the aim of detecting an optical counterpart. And the second was to perform long term monitoring of several massive stars in the nearby Triangulum Galaxy (M33), that were classified as candidate Luminous Blue Variable (LBV) stars.

The direct observation of an EM counterpart had never been done before when this project started, and so it made this a much more difficult task because the only predictions that existed were solely reliant on theoretical modelling, so it wasn't

certain if PIRATE would even be able to detect these faint sources. However, as it turned out with the detection of GW170817, PIRATE would have just about been powerful enough to image the optical counterpart in its early hours, but unfortunately this event was unobservable from Tenerife. And although PIRATE did not observe this, or any other counterparts, it did produce upper limits. What these results have provided is proof that the initial concept of this project works, and answers the question posed right at the start of the thesis in that small-aperture telescope, like PIRATE, can be used for follow up of time critical astronomical events.

In contrast, the monitoring of LBV candidates in M33 had some success, but it was at the limits of PIRATE's capability and a larger aperture telescope would be needed to monitor all 18 candidates laid out in Clark et al. (2012). However, PIRATE was able to successfully monitor 8 sources for signs of an S Dor outburst, and further analysis showed that at least one of these stars showed signs of variability on day-to-day timescales. In addition to this, spectroscopic data of the same LBV candidates in M33 was analysed and resulted in the re-classification of 3 stars as bona fide LBVs and 4 as Cool Hypergiants.

The two elements are of this thesis are not just tied together by the use of PIRATE, but they also have a direct scientific link too. As LBV stars are thought to be progenitors of Super Luminous Supernova (SLSN), these events generate large bursts of gravitational radiation, and if one occurred close enough, it could be detected by LIGO. This gives the work in studying LBV stars and their evolutionary journey greater importance, and if such an event were detected by LIGO it could open up the massive star community to a new field of astronomy, just like the binary neutron star merger has.

7.1.1 Gravitational Wave follow-up method

Chapter 3 focused on the methods used to enable PIRATE to follow up gravitational wave alerts from LIGO. This centred around creating a new pipeline that could run autonomously and conduct follow-up observations of these alerts without the need for human interaction at the OU. These alerts were generated by the LIGO alert pipeline, using various search algorithms, and distributed via the Gamma-ray Coordination Network (GCN). The alerts came in a variety of types which could be filtered by the end user depending on what astrophysical objects they wanted to observe. The two main categories were compact binary coalescence (CBC) and bursts, these covered the merger of binary systems and cataclysmic explosions respectively.

Early on, it was decided that PIRATE would try to observe all these alerts unfiltered, mainly because the total expected number of these alerts during the second LIGO observing run (O2) was highly uncertain, and also following up all alerts allowed for more opportunities to test and refine the new alert pipeline for PIRATE. In section 3.1.1 & 3.1.2 these two types of alert are described in detail, but in summary the CBC alerts were more promising due to the ability to model the expected waveforms very well (using General Relativity models) and also the high SNR for these events compared to the short weak signal from burst events.

The alerts themselves are described in section 3.1.3 and they contain the event time & type as well as the important sky localisation map, otherwise known as a skymap. These skymaps are generated in a HEALpix format that produces pixels on the sky of equal area, thus mapping the probability distribution across the sky equally. The skymaps produced by LIGO are generated by the individual search pipelines based on the data produced by the interferometers and can vary in area substantially depending on the strength and orientation of the signal, but most importantly, the number of interferometers that detected it. Furthermore, there

can be 4 types of alerts sent via the GCN network to users, these are: Preliminary, Initial, Update and Test alert.

The PIRATE alert pipeline was a new alert pipeline written by the author in Python and is based upon the tutorial script by Singer (2015). This pipeline is split into three main parts, firstly it uses a Python package called pygcn to connect to the GCN network and this allows it to continuously listen for any incoming gravitational wave alerts 24/7. As the LIGO alerts were private during O2, this had to be done via a private port number on the GCN servers, using a unique user key to access it. Secondly, the most important stage of the pipeline involves processing the individual alerts and turning the skymap generated by LIGO into a set of individual observing fields for the telescope. The processing strategy for this thesis was to target the highest probability pixels of the skymap, producing a list of 30-40 fields in the highest probability region of the skymap for PIRATE to follow up. Finally, it was the responsibility of the last part of the pipeline to upload these new observing fields to the telescope, via the OSO scheduler, for immediate observation. This required giving the pipeline control over the scheduler to enable it to stop all current observations and allow the gravitational wave observations to take precedence over them for the rest of the night.

To facilitate the smooth operation of this script, the author worked in close collaboration with Edward Hand on developing the OSO scheduler and also with Sybilla Technologies in their ongoing improvements to their ABOT control software. This ultimately allowed for the author to autonomously request immediate use of the telescope in the event of receiving an alert from LIGO which involved adapting both systems to be able to handle such a time dependant request.

7.1.2 Results from O2 observing run with PIRATE

The O2 observing run itself ran from 30th November 2016 to the 25th August 2017 and involved the distribution of 14 alerts in total by the LIGO/Virgo collaboration to EM follow-up partners, although some were ultimately retracted (see Table 4.1).

Of these 14 alerts, PIRATE was able to follow-up 10 to some degree, but only 4 had sufficient data to be analysed fully, namely G296853, GW170814, G298936 & G299232. For the alerts that weren't observed, the primary reason was that no part of the skymap for these alerts was visible from Tenerife but telescope availability was also a factor in one event. For the 6 alerts that were observed but weren't fully analysed, there were two main reasons for this. Either the alerts were retracted before analysis was started or the quality or duration of the follow-up images was not sufficiently good enough to analyse. As for the 4 gravitational wave alerts that were followed up and analysed, PIRATE obtained 1155 individual exposures, covering 59 observing fields and taken over 24 nights in total.

To prepare these images for analysis, they first had to undergo calibration using dark, bias and flatfield frames. This was done using an image reduction pipeline built in-house by another telescope user at The Open University, and it follows standard image calibration procedures. Following on, the images were all fed thought the Variability Search Toolkit (VaST) which works by identifying all the individual sources in a frame using SExtractor, and catalogues each object's pixel coordinates and instrumental magnitude. From this it produces a series of lightcurves, one for every source in the image, and then VaST computes multiple variability statistics to measure the smoothness and scatter of the data points in each lightcurve.

For this work the ratio of the mean square successive difference to the variance (η) was used as the variability index, this is heavily weighted to the variation of successive data points, and so is a good way to identify long term trends from short term scatter in a lightcurve. Once VaST had identified lightcurves with a high $1/\eta$

value, the author then manually classified these into one of four categories based on the lightcurves morphology, with the ultimate goal of finding a source whose lightcurve fits the morphology of a transient.

The results of the variability search with VaST are summarised in Table 4.6, which shows the frequency of lightcurve morphology classes that were identified in the follow up of the 4 alerts from LIGO/Virgo, with a total of 259 objects being classified across the 59 fields. The majority of these were classified as long period variables, with only one lightcurve resembling a transient. Upon further investigation it was found that this source was actually a known star (Gaia star 0545555925600166 40), and was likely too faint to pick up in the initial SIMBAD/GCVS cross-reference. Among the objects that were cross referenced in SIMBAD & GCVS though were a: W UMa eclipsing binary (RTS J012032.0-174732), Mira variable (U Scl) and rotationally variable star (CD-24 564).

Evidently with the one transient candidate ruled out, it meant that there were no EM counterparts identified in the follow-up of these 4 alerts down to a magnitude limit between R=16.8-17.5 . This was not unexpected as all these 4 events involved the merger of two black holes, and they are not thought to produce an EM counterpart beyond their event horizons. However, this result does not mean they don't exist, it just places upper limits on their optical magnitude. In total, over 70 EM observing partners participated in O2 and reported follow-up observations, not only to these 4 events but the 14 total alerts released by LIGO; these are summarised in Abbott et al. (2019). Furthermore, as a consequence of the follow-up partnership with other EM facilities, PIRATE was able to follow-up a Type IIb supernova for over 65 days and catch a significant amount of data both pre & post luminosity peak.

Following on from this work on gravitational wave follow-up was work involving Luminous Blue Variable stars, who's evolutionary path is still highly uncertain but

that has links to gravitational waves in that they are thought to be progenitors of Super Luminous Supernova, an event that could eventually be picked up by LIGO in the near future.

7.1.3 Analysis of spectra from candidate LBVs in M33

To begin the Luminous Blue Variable analysis, new spectroscopic observations were presented and compared to archival observations in an attempt to reclassify some massive stars in the Triangulum Galaxy (M33). This work was based upon the work by Clark et al. (2012) and predating that of Massey et al. (2007). This relied upon using spectroscopy to identify any LBV candidates in nearby galaxies such as Andromeda and Triangulum. In Massey et al. (2007) they estimated there were up to 37 known or candidate LBVs in M33 and this was further added to in 2016 by the release of Massey et al. (2016) which increased this number to 42.

In Clark et al. (2012), a total of 18 candidate LBVs in M33 were presented, with accompanying spectroscopic and IR photometric analysis. For the analysis in this thesis, 13 stars that had corresponding spectra taken in 2013 were used, this was then compared with the spectra taken in 2010 by Clark et al. (2012).

After the analysis of these 13 stars, 2 were reclassified as bona fide LBVs, these were J013339.52+304540.5 and J013422.91+304411.0. This was as a result of close analysis of their spectra and comparison with earlier archival spectra that showed that these stars had varied and the presence of P Cygni profiles on some prominent emission lines was enough to reclassify them.

Other bona fide LBVs such as Var C and Romano's Star were also discussed in detail, and this centred around their variability. There are a number of ways in which these stars can appear to vary spectroscopically, that is by the changes in the line strengths themselves, or even a reversal from emission to absorption or vice versa; in addition to this, characteristics such as P Cygni profiles and line broadening help to

identify stars undergoing a period of very strong stellar winds. This thesis showed that Romano's star has continued to vary since the observations presented in Clark et al. (2012), evident by the return of strong N II emission lines; furthermore, Var C was observed to vary with increased line broadening around the Hβ emission line, this is a result of increased Thompson scattering, caused by a denser stellar wind.

Additional spectroscopic observations were presented from 2013, this time without corresponding spectra from Clark et al. (2012). As a result, they were grouped together by classification type and this split the stars into two main categories, Wolf-Rayets and Cool Hypergiants. The Wolf-Rayets were identified primarily by the broad He II line around 4686$\mathring{A}$ in their spectra, this results from dense fast stellar winds that are associated with Wolf-Rayet stars. As for the Cool Hypergiants, all four were given this new classification based on the presence of low excitation metal absorption lines between 4300-4600$\mathring{A}$ in their spectra. These come about due to the cooler photospheres of these stars which allows metals to exist in a de-excited state. In addition to this, one star displayed a very similar spectrum to the other Cool Hypergiants but crucially it showed the Hβ line in emission. This indicates it is highly likely to be an LBV undergoing an outburst in the cool phase of the S Dor cycle, and its spectrum closely resembles Var C & B324, both of which are confirmed LBVs.

Additionally, there were several spectra from 2013 that were not considered further due to numerous reasons, the foremost of those were featureless spectra or spectra heavily dominated by noise from other sources.

This work showed the close links between these different types of stars and the fine lines that separates them, which shows why classifying them is extremely difficult. As it's been shown, LBVs resemble two very different types of star depending on what phase of the S Dor cycle they are in. This is why it is important to gather both spectroscopic and photometric observations in the study of these stars. Fur-

thermore, it is also necessary to conduct atmospheric modelling of these massive stars in order to fully understand what the spectra is saying about the characteristics of each star, something which there wasn't time for in this project.

7.1.4 Long term monitoring of candidate LBVs in M33

Complimenting these spectroscopic observations of LBV candidates in M33 were photometric observations taken with PRIATE over a 5 month period. These were used to monitor several candidate LBVs in the galaxy in order to detect any visible change in luminosity, indicative of an S Dor outburst. As photometric observations are cheaper and easier to obtain, they provide the backbone of observations in astronomy, and are supplemented by occasional spectroscopic observations to confirm the behaviour of a star at any given time.

The observations were only taken in the B filter and were designed to monitor the luminosity of these stars over several weeks, to look for any signs of an S Dor cycle or even a giant LBV outburst. In total 8 stars were monitored between 1st June and 1st November 2017 in the M33 galaxy. These observations were automatically scheduled on PIRATE using the OSO Scheduler and were acquired during a time window with which both the telescope was available and the target galaxy was high enough in the night sky.

What the results from these observations found was that none of the eight stars studied displayed signs of an S Dor outburst, which would strongly support their classification as a bona fide LBV. However, due to the high cadence of these observations, the author was able to investigate small scale variability in these stars on short timescales. As most of these stars were close to PIRATE's magnitude limit it was difficult to differentiate between noise and true variation; therefore only one star (B517) was said to show significant signs of small scale variability. The most favourable explanation for the behaviour of this star was attributed to a type of

variable called an α Cygni pulsator, which occurs when some parts of the star are expanding while other parts are contracting, creating pulses that cause small scale luminosity fluctuations.

But what this work showed was that with modern detector technology a small robotic telescope such as PIRATE can be used to perform photometric monitoring of individual sources in external galaxies, in order to oversee them for signs of significant variability. And all this can be done at a much reduced cost than traditional observatories.

Although the evolutionary behaviour of massive stars is still not fully understood, and the fundamental processes powering LBV outbursts are still uncertain, the ability to monitor several candidates in a single galaxy over several months to years, could provide valuable insight into how these stars behave; furthermore, the ability to monitor these targets at much shorter timescales (day-to-day) opens up the possibility of probing a new area of parameter space, one that hasn't yet been fully investigated. In order to do that effectively, this work has shown that it would require a 1m class telescope to obtain the signal-to-noise ratio required for such faint sources.

7.2 Recommendations for improvement

This section aims to address ways in which a similar project could be improved in the future, and the key recommendations from this one.

The gravitational wave follow-up work would have benefited from a working pipeline sooner, this would have removed the reliance on a human user to trigger the follow-up alerts with PIRATE, but this would only have helped in a few situations given that a lot of alerts were received during the daytime, when rapid observations were not possible. In addition to having a working pipeline sooner, the one biggest

improvement would be to carry out a more targeted search routine, when following up the alerts; so instead of searching the highest probability area of the skymap, the observations could be targeted at a list of galaxies within that area instead. Using the area and distance estimates from LIGO, it is possible to determine a volume of space where the signal most likely originated from, and then target individual galaxies within that search volume.

Another recommended change is to take images in several filters, instead of just using the R filter. This would have resulted in a trade off between area covered or cadence of observations, but if a counterpart were found, it would have provided valuable colour information about the object, and subsequently what physical process might have been generating the luminosity.

In addition to this, it could have theoretically been possible to observe the historic kilonova event associated with GW170817 with PIRATE had the telescope been pushed below its altitude limit (20°); however, this isn't recommended without human oversight and any images obtained in this way would suffer from very high airmass.

On the analysis side of things, the process of identifying sources could be improved by cross-matching the sources with larger databases, such as VizieR, instead of relying on the ones used by VaST. This could prevent a large number of known stars being passed on to the manual identification process as unknown sources. This itself could also be improved, by removing the human element of the classification process, and relying on pure statistical methods only to search for transients in the data set.

In regards to the work on Luminous Blue Variables, there are several suggested improvements that could be made in the future. Firstly, in regards to the spectroscopic analysis, given more time it would have been beneficial to analyse each of the Wolf-Rayet and Cool Hypergiant stars individually; and compare them with

any archival data for reference. As for the photometric observations, similarly to the gravitational wave follow-up they could also have benefited from multi-filter observations. This would have allowed a determination of the colour of these stars as well as a magnitude, from which a temperature estimation could have been made. This would have helped to better understand the point at which these stars sat on their evolutionary path.

Another possible improvement to the long term monitoring of LBV candidates could have been achieved by stacking the observations from each night together, to produce a higher signal-to-noise (SNR) image and ultimately allow the detection of fainter LBV candidates. Unfortunately due to time constraints this was not possible, but it was the original intention of the author to take up to 6 images per night for this very purpose, given the faint nature of extragalactic stars.

Moreover, another improvement that could be implemented if a similar project were to be performed again would be the quantitative analysis of candidate LBV lightcurves. Due to time constraints, this work had to be curtailed in order to meet the end deadline; however, there is enough data from just 5 months observations to allow lots of quantitative analysis to take place. This would involve calculating a line of best fit to the data and associated chi-squared consistency check. In addition to this, the stacking of images would provide higher SNR data which would hopefully enable better source extraction and lower error bars in the lightcurve data.

7.3 Future Outlook

Lastly, this section focuses on the future outlook of PIRATE and any potential follow on work or offshoot projects as a result of the work in this thesis.

One obvious such project would be to continue the gravitational wave follow-up work into the 3rd observing run (O3), which now includes public alerts and further

improved detector sensitivities. The aim of this work could be to focus on the rapid follow-up of a counterpart to a binary neutron star merger, as the expectation is that several will be detected during the 12 month long observing run. This wouldn't necessarily focus on the primary search for the object, because many more facilities will be joining in with this search now that the alerts are public; but instead this work could focus on the detailed follow up of a source once it has been reported to the EM community. This would utilise PIRATE's robotic nature, and allow extensive follow-up observations to be taken from days to months following the event.

There are also long term plans to integrate PIRATE into an ABOT driven global telescope network, such as Las Cumbres Observatory. This has many benefits over a single telescope in one location, the greatest of these being the ability to monitor the night sky 24 hours a day with at least one telescope always in darkness.

As for PIRATE itself, the long term aim is to upgrade the Optical Tube Assembly to a 1m aperture, this was always the intention since PIRATE was relocated to Tenerife because both the mount and dome were built to handle a 1m class telescope. Such a telescope would be able to fully utilise the optimal observing conditions in Tenerife for research purposes, and allow COAST to take the existing PIRATE OTA for use teaching undergraduate students.

As for the work on Luminous Blue Variables, the spectroscopic data used in this thesis is already 6 years old and new spectra of all these targets are well overdue. It is important to gather frequent spectra of these targets to be able to monitor any change in their behaviour, especially as most S Dor cycles last less than 10 years. New spectra would help to continue the trend of observations started in the 1990s, and help to re-classify more candidates as bonafide LBVs.

Finally, as already pointed out in section 5.3.1, there are limitations to the quantitative analysis performed in Chapter 5; and to be able to fully utilise these spectroscopic observations detailed stellar atmosphere modelling needs to be performed

in order to determine the physical parameters of these stars, such as: bolometric luminosity, mass & temperature. Such a project could use the CMFGEN software (Hillier and Miller, 1998), which was designed specifically for massive stars such as Wolf-Rayets and Luminous Blue Variables.

Appendix A

Pipeline

```
# Python standard library imports
import tempfile
import shutil
import sys
import glob
import time

# Third-party imports
import subprocess
import gcn
import gcn.handlers
import gcn.notice_types
import requests
import healpy as hp
import numpy as np
import astropy.coordinates
```

```
import astropy.time
import astropy.units as u
import matplotlib.pyplot as plt
from astropy.table import Table
from astropy.io import ascii
import math
from math import cos, sin, acos, degrees, radians, sqrt


def get_skymap(root):
    """
    Look up URL of sky map in VOEvent XML document,
    download sky map, and parse FITS file.
    """
    # Read out URL of sky map.
    # This will be something like
    # https://gracedb.ligo.org/apibasic/events/M131141/files
       /bayestar.fits.gz
    skymap_url = root.find(
        ".//What/Param[@name='SKYMAP_URL_FITS_BASIC']").
            attrib['value']
    print skymap_url

    # Send HTTP request for sky map
    response = requests.get(skymap_url, stream=True)

    # Uncomment to save VOEvent payload to file
    #open('example.xml', 'w').write(payload)
```

```
    # Raise an exception unless the download succeeded (HTTP
        200 OK)
    response.raise_for_status()

    # Create a temporary file to store the downloaded FITS
        file
    with tempfile.NamedTemporaryFile() as tmpfile:
        # Save the FITS file to the temporary file
        shutil.copyfileobj(response.raw, tmpfile)
        tmpfile.flush()

        # Uncomment to save FITS payload to file
        fitsfile = '%s.fits.gz' % root.find("./What/Param[
            @name='GraceID']").attrib['value']
        shutil.copyfileobj(response.raw, open(fitsfile,'wb')
            )

        # Read HEALPix data from the temporary file
        hpx, header = hp.read_map(tmpfile.name, h=True,
            verbose=False)
        header = dict(header)

    # Done!
    return hpx, header

def tabletest(hpx, header,root):
```

```
dpix = len(hpx)
nside = hp.npix2nside(dpix)
npix_array=np.arange(dpix)
theta, phi = hp.pix2ang(nside, np.arange(dpix))
radecs = astropy.coordinates.SkyCoord(
    ra=phi*u.rad, dec=(0.5*np.pi - theta)*u.rad)
x=Table([npix_array,hpx,radecs.ra,radecs.dec], names=(
        'Pixel_Number','Probability', 'RA', 'Dec'))
x2=x[x['Dec']>-40*u.degree]
ipix_max = np.argmax(hpx)
maximum=hpx[ipix_max]
minimum = maximum-(maximum/15)
x3=x2[x2['Probability']>minimum]
x3.sort('Probability') #Orders rows in ascending
    probability
x3.reverse()    #Reverses the order so highest
    probability is at the top

csvfile1 = '%s_initial.csv' % root.find("./What/Param[
    @name='GraceID']").attrib['value']
ascii.write(x3, csvfile1, format='csv', fast_writer=
    False, overwrite=True)

observed=np.zeros((1,4))#this creates an empty array to
    save the pixels to.
with open(csvfile1,"r")as csv:
    y=0
```

```
for line in csv:
    if y==0:#ignore the first line of the data that
       contains the headers
            y=y+1
    elif y==1:
            line=line.split(",")
            observed[0,0]=int(line[0])
            observed[0,1]=float(line[1])
            observed[0,2]=float(line[2])
            observed[0,3]=float(line[3])
            y=y+1 #this checks the 1st pixel with
                all other pixels in the csv
    else:
            observedline=np.zeros((1,4))
            add=0
            line=line.split(",")
            RA=float(line[2])
            DEC=float(line[3])
            for x in range(len(observed)):#now we
               have to compare RA & Dec of every
               pixel to the "observed" array
                RAa=observed[x,2]
                DECa=observed[x,3]
                theta = degrees(acos(sin(radians(DEC
                   ))*sin(radians(DECa)) + cos(
                   radians(DEC))*cos(radians(DECa))*
                   cos(radians(RA-RAa))))
```

```
                    h = math.pow(theta,2)
                    o = math.pow((DEC-DECa),2)
                    y = abs(h-o)
                    a = sqrt(y)
                    DECahigh=DECa+0.7
                    DECalow=DECa-0.7
                    if ((a>0.7)or(DEC>DECahigh)or(DEC<
                        DECalow)):
                        add=1
                        observedline[0,0]=int(line[0])
                        observedline[0,1]=float(line[1])
                        observedline[0,2]=float(line[2])
                        observedline[0,3]=float(line[3])
                    else:
                        add=0
                        break
                if add==1:
                        observed=np.append(observed,
                            observedline,axis=0)
                y=y+1
observed=observed[observed[:,2].argsort()] #sort final
    table values by RA

csvfile2 = '%s_final.csv' % root.find("./What/Param[
    @name='GraceID']").attrib['value']
ascii.write(observed, csvfile2, format='csv',
    fast_writer=False, overwrite=True)
```

```
    ascii.write(observed, 'observations.csv', format='csv',
       fast_writer=False, overwrite=True)
    print "I have worked"
    return csvfile2

def OSO_API_uploader(csvfile2):

    x=0
    with open(csvfile2, "r") as csv:
            for line in csv:
                    RA=0.0
                    DEC=0.0
                    if x == 0:
                            pass
                    else:
                            line = line.split(',')
                            RA = float(line[2])/15.0
                            DEC = line[3]
                            prio= 1001-x
                            #Data to be sent to the API
                            params = {
                                    'key': '51272
                                       f354a2b2131534d2a####
                                       ',
                                    'name': 'Kappa_%d' % x,
                                    'observatory': 'pirate',
                                    'isTimed': 'false',
```

```
                    'ra': RA,
                    'dec': DEC,
                    'atoms': 'R:100',
                    'priority':prio,
                    'binning': 1,
                    'altLimit': 20,
                    'repeats': 2,
                    'immediate': 'true',
                    'maxRepeats': 3,}

                response = requests.post('http
                    ://trillian.open.ac.uk:3021/
                    relay/addRequest', data=
                    params)

                output =response.text
                print("Your upload to the OSO
                    API was:%s"%output)
                time.sleep(0.5)

            x=x+1
clear = {
        'key': '51272f354a2b2131534d2a####',
        'observatory': 'pirate',}

response = requests.post('http://trillian.open.ac.uk
    :3021/relay/clearQueue', data=clear)
```

```
    end = response.text
    print("Clear Queue command was:%s"%end)
# Function to call every time a GCN is received.
# Run only for notices of type LVC_INITIAL or LVC_UPDATE.
@gcn.handlers.include_notice_types(
    gcn.notice_types.LVC_INITIAL,
    gcn.notice_types.LVC_UPDATE,
    gcn.notice_types.LVC_TEST)
def process_gcn(payload, root):
    # Print the alert
    print('Got VOEvent:')
    print(payload)
    #Save alert to file using GraceID name
    filename = '%s.xml' % root.find("./What/Param[@name='
        GraceID']").attrib['value']
    open(filename, 'w').write(payload)
    open('payload.xml', 'w').write(payload)

    # Respond only to 'test' events.
    # VERY IMPORTANT! Replce with the following line of code
    # to respond to only real 'observation' events.
    if root.attrib['role'] != 'observation': return
    #if root.attrib['role'] != 'test': return
    hpx2,header2=get_skymap(root)
    csvfile2=tabletest(hpx2, header2,root)
    OSO_API_uploader(csvfile2)
    subprocess.call(['./Mail.sh'])
```

```
# Listen for GCNs until the program is interrupted (killed
    or interrupted with control-C).
gcn.listen(host="68.169.57.253",port=8096, handler=
    process_gcn)
```

Appendix B

Observing Manual

In this manual is additional information relating to the implementation and use of the PIRATE alert pipepine and related process's.

B.1 PIRATE Alert Pipeline

The PIRATE alert pipeline was based upon a tutorial script written by Leo Singer (Singer, 2015). Any initial queries could be solved by checking out the tutorial webpage[1] or Leo Singers GitHub account [2]. However, below are a short collection of common issues or small changes that might be required if this script were to be used again in the future.

1. As this script is almost 2 years old now, there is likely to be changes required to run it again. One of the biggest such changes will be in how the alerts are accessed/distributed, as from O3 onwards, they will all be publicly available. This might render some aspects of this script, such as the .netrc file,

[1] `http://nbviewer.jupyter.org/github/lpsinger/ligo-virgo-emfollowup-tutorial/blob/master/ligo-virgo-emfollowup-tutorial.ipynb`

[2] `https://github.com/lpsinger`

unnecessary in the future.

2. Manually change the pre-determined name of the observations (e.g. Sigma) each time an alert has been processed to avoid a new alert overriding the existing observations.

3. If an alert is received in the daytime, it can be useful to run the "tabletest" function more than once to refine the number of observations. This can be achieved by tweaking the probability threshold, currently set at 6.67%.

4. The minimum separation between fields that has been set in the script is 0.7 degrees, which equates to 42 arcminutes. This is only just smaller than the size of the PIRATE FoV of 43 arcminutes. This was done in order to ensure maximum coverage without the need to ensure every single field overlapped. This can be reduced in the future to ensure every field overlaps with another one; or, in the event that the PIRATE FoV changes (due to new hardware), this value will have to be altered accordingly.

5. Connection with OSO Scheduler via API might change in the future, so check HTTP addressed carefully. But any new user will require a new API key to enable command line uploads to the OSO Scheduler.

6. After the script has run, the last subprocess called "Mail.sh" is performed. This runs a bash file from Python that automatically emails the author and other users to notify them that an alert has been received & processed successfully. It also includes an attachment of all the observing requests sent to the scheduler in CSV format, which can be human read to look for any mistakes. These email addresses will need to be updated for the new user.

B.2 OSO Scheduler Requests

As mentioned in 3.3.2, there are two ways in which observing requests can be uploaded to the scheduler, this is either via a web form, or by using a command line interface to send requests via an API; this method requires an API key for identification purposes. Regardless of the method, all requests must contain basic observing parameters, these include: object name, target coordinates, filters, exposure time, binning, repeats and user priority. These can be seen in Figure B.1 which was taken from the OSO schedule website, showing the online web form version for creating requests.

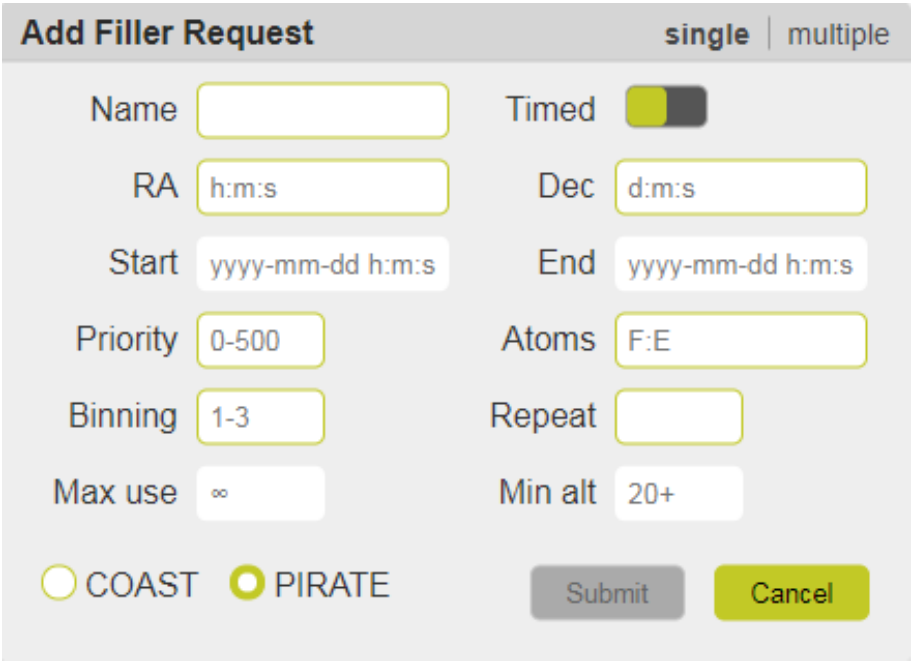

Figure B.1: Observation request web form on the OSO website.

Users submitting requests via this online form are able to delete their requests from the queue by a simple one-click process. However, for API users, this requires submitting a HTTP POST request to remove it from the scheduler, and this must contain the users unique API key.

Appendix C

VaST Variability Indices Comparison

Below is a comparison of nine different variability indices used by VaST. The data used for this test was taken from the MASTER OT Type IIb supernova follow-up observations, and the object itself is highlighted in red in each figure.

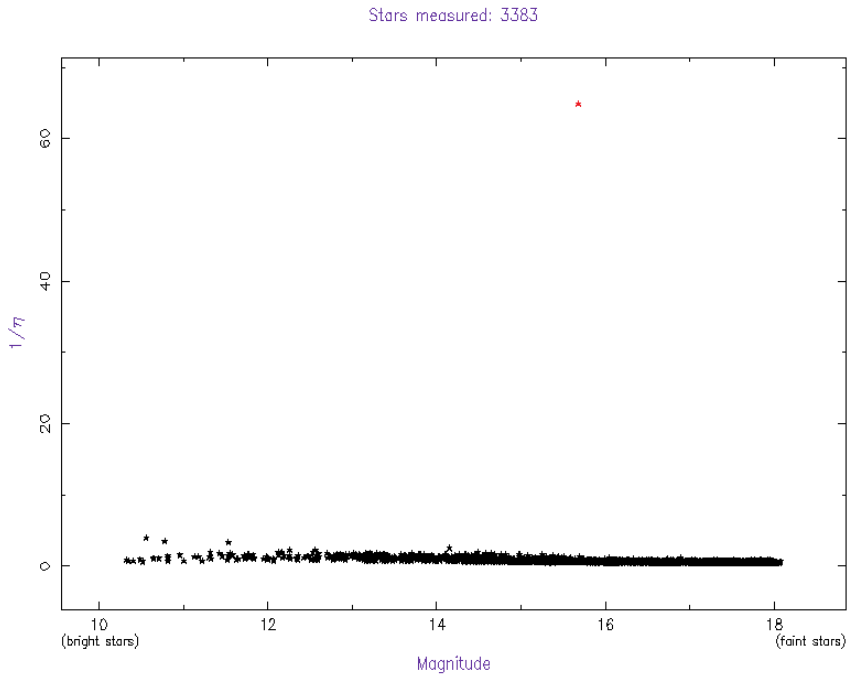

Figure C.1: Ratio of the mean square successive difference to the variance-variability index. With the SN highlighted in red.

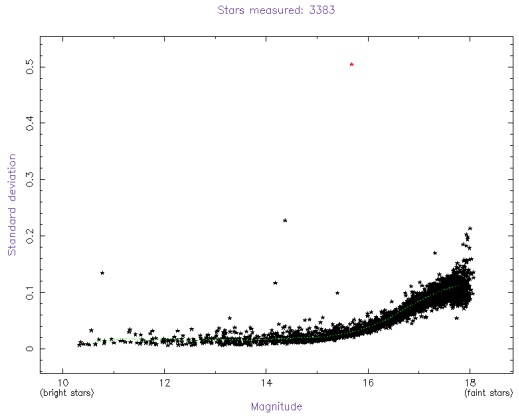

(a) Standard deviation-variability index.

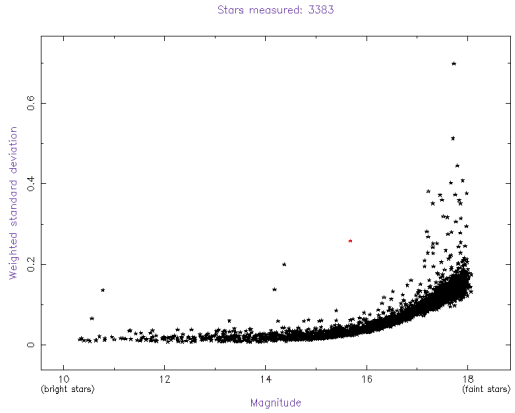

(b) Weighted standard deviation-variability index.

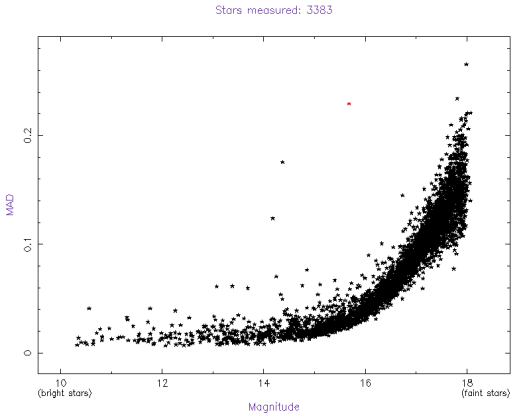

(c) Median Absolute Average (MAD)-variability index.

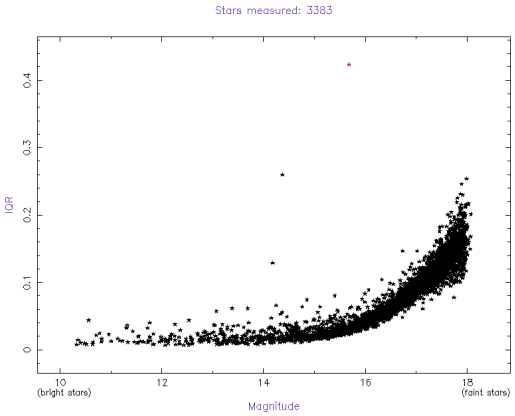

(d) Interquartile Range-variability index.

Figure C.2: Comparison of four more variability indices with the supernova data set. SN is highlighted in red.

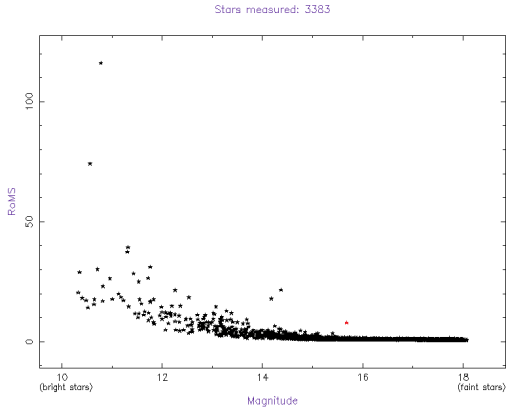

(a) Robust Median Statistic (RoMS)-variability index.

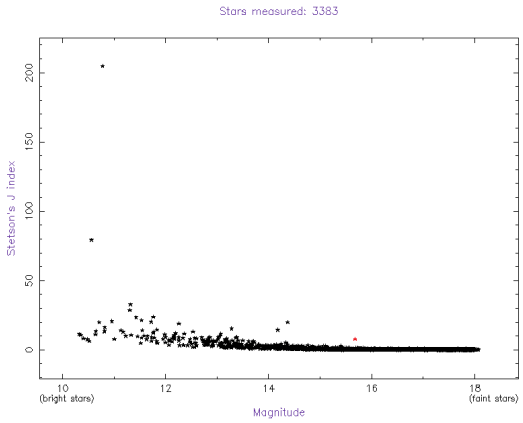

(b) Stetson's J index-variability index.

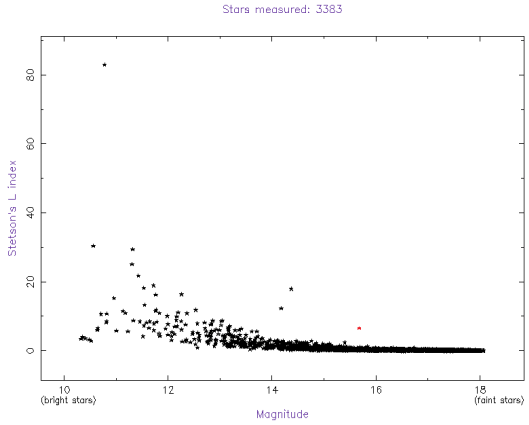

(c) Stetson's L index-variability index.

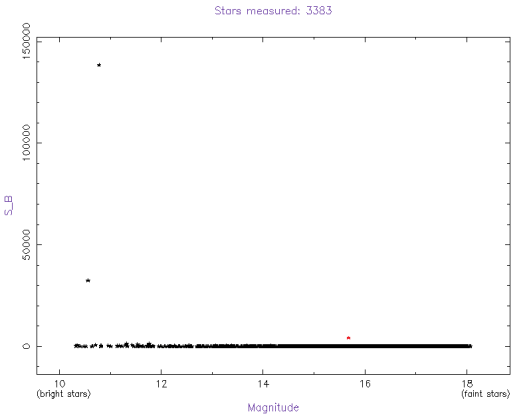

(d) Variability Detection Statistic (S_B)-variability index.

Figure C.3: Comparison of the final four variability indices with the supernova data set. SN is highlighted in red.

Appendix D

Tables containing objects of interest identified by VaST

D.1 Sigma

Field	Object ID	$1/\eta$	m_R	δm	Ra Dec	Classification (SIMBAD Identifier)
Sigma_1						
	out20274.dat	1.19	16.76	0.05	01:07:20.00 -28:47:28.5	2dFGRS TGS292Z041 – Galaxy
	out00106.dat	1.16	12.83	0.01	01:06:18.62 -28:48:33.1	Bok I 153B – Star
Sigma_2						
	out00254.dat	1.33	14.14	0.01	01:04:25.32 -27:56:18.7	Variable star, bright
	out20064.dat	1.25	16.18	0.03	01:05:55.54 -28:05:31.7	Faint star
	out00244.dat	1.17	15.37	0.01	01:06:37.96 -27:57:45.8	Faint star
	out00174.dat	1.16	15.71	0.02	01:05:27.46 -27:53:38.3	2MASS J01052747-2753377 – Star
	out00156.dat	1.16	15.87	0.02	01:04:32.70 -27:50:49.0	Very faint, large error
	out00040.dat	1.15	12.74	0.01	01:04:30.22 -27:33:20.4	2MASS J01043020-2733202 – Star
Sigma_3						
	out00051.dat	1.15	14.30	0.01	01:04:44.79 -26:33:42.5	RGO 877 – Star
	out20064.dat	1.14	16.41	0.03	01:05:29.80 -26:35:59.9	Faint star
	out20002.dat	1.06	12.90	0.01	01:05:44.54 -26:25:04.9	Long period variable
Sigma_4						
	out00125.dat	1.28	14.71	0.01	01:07:11.59 -25:40:06.7	Variable

Table D.1 continued from previous page

Field	Object ID	$1/\eta$	m_R	δm	Ra Dec	Classification (SIMBAD Identifier)
	out20113.dat	1.2	16.37	0.02	01:05:49 -25:52:29	2dFGRS TGS145Z036 – Galaxy
Sigma_5						
	out00154.dat	1.3	11.98	0.01	01:07:06.84 -24:34:51.3	Long period variable
	out00227.dat	1.22	13.67	0.01	01:07:58.36 -24:40:00.3	Variable
	out20085.dat	1.15	16.52	0.03	01:06:09.22 -24:34:17.7	Faint
	out00023.dat	1.15	13.75	0.01	01:08:41.82 -24:09:49.2	Variable
	out00004.dat	1.1	13.88	0.01	01:08:20.35 -24:06:44.4	Long period variable
Sigma_6						
	out00211.dat	1.5	9.94	0.01	01:07:00.21 -23:26:46.1	TYC 6425-345-1 – Star
	out00071.dat	1.42	12.04	0.01	01:09:22.92 -23:05:22.5	TYC 6425-727-1 – Star
	out00253.dat	1.32	9.89	0.01	01:07:02.38 -23:26:51.5	TYC 6425-632-1 – Star
	out00271.dat	1.29	9.76	0.01	01:06:59.75 -23:28:26.9	HD 6653 – Star
	out00133.dat	1.22	12.73	0.01	01:06:44.62 -23:17:32.5	Variable
Sigma_7						
	out00005.dat	1.91	12.75	0.01	01:09:59.35 -21:50:39.8	Long period variable
	out00143.dat	1.16	15.71	0.03	01:08:42.91 -22:11:44.8	Faint star
	out00086.dat	1.1	14.93	0.01	01:08:49.53 -22:02:33.4	Variable

Table D.1 continued from previous page

Field	Object ID	$1/\eta$	m_R	δm	Ra Dec	Classification (SIMBAD Identifier)
	out00212.dat	1.1	13.70	0.01	01:09:34.06 -22:27:35.7	Variable
Sigma_8						
	out00237.dat	1.51	15.86	0.02	01:11:42.25 -28:13:09.6	Very long period variable
	out20122.dat	1.42	16.39	0.04	01:11:48.66 -28:11:58.3	Faint star
	out20098.dat	1.29	16.27	0.04	01:11:53.29 -28:10:38.4	Long period variable
	out20052.dat	1.28	16.22	0.03	01:09:38.48 -28:15:29.0	Faint Star
Sigma_9						
	out20108.dat	1.48	16.33	0.04	01:11:33.32 -27:01:55.9	Faint Star
	out00127.dat	1.2	13.09	0.01	01:11:33.27 -27:01:56.0	Variable
	out20001.dat	1.02	12.23	0.01	01:12:22.42 -26:59:51.0	2MASS J01122240-2659507 – Star
Sigma_10						
	out00050.dat	1.3	13.74	0.01	01:11:36.24 -28:44:26.2	GEN# +8.61290229 – Star
Sigma_11						
	out00162.dat	1.72	12.55	0.01	01:11:36.40 -30:06:28.3	Long Period Variable- U Scl (GCVS)
	out20347.dat	1.6	16.03	0.03	01:11:53.42 -30:08:00.8	Faint star
	out00116.dat	1.56	15.52	0.02	01:09:18.88 -29:59:14.2	Long Period Variable
Sigma_12						

Table D.1 continued from previous page

Field	Object ID	$1/\eta$	m_R	δm	Ra Dec	Classification (SIMBAD Identifier)
	out20313.dat	3.4	16.42	0.05	01:12:17.56 -21:00:58.5	Faint star
	out00245.dat	2.2	12.55	0.01	01:10:50.93 -21:16:10.9	Variable
	out00261.dat	1.9	16.49	0.04	01:09:57.08 -21:17:52.7	Faint star
Sigma_13						
	out20055.dat	1.16	16.21	0.03	01:10:23.50 -25:27:25.6	Faint Star
Sigma_14						
	out00199.dat	2.75	9.97	0.01	01:11:38.00 -24:53:22.5	CD-25 473 – Star
	out00044.dat	1.32	15.31	0.03	01:11:27.57 -24:23:20.7	Variable
	out00186.dat	1.25	16.00	0.03	01:11:38.32 -24:56:20.8	Variable
Sigma_15						
	out00146.dat	1.6	13.30	0.01	01:14:08.13 -23:33:00.7	Long Period Variable
	out00222.dat	1.59	13.93	0.01	01:14:15.98 -23:41:35.2	Long Period Variable
Sigma_16						
	out00086.dat	1.91	14.69	0.01	01:11:42.41 -19:49:26.9	Long Period Variable
	out00230.dat	1.81	15.26	0.02	01:13:00.62 -20:12:59.0	Variable
	out20289.dat	1.8	16.51	0.05	01:14:18.81 -20:01:19.4	Long Period Variable
Sigma_17						

Table D.1 continued from previous page

Field	Object ID	$1/\eta$	m_R	δm	Ra Dec	Classification (SIMBAD Identifier)
	out00064.dat	4.1	13.25	0.01	01:15:02.98 -18:35:57.7	Long Period Variable
	out00173.dat	1.88	13.26	0.01	01:14:19.54 -18:50:46.7	Variable
	out20271.dat	1.71	16.48	0.03	01:15:11.43 -19:09:39.7	Faint star
	out00078.dat	1.69	13.66	0.01	01:16:32.72 -18:37:22.9	Long Period Variable
Sigma_18						
	out00290.dat	1.85	16.12	0.02	01:15:16.22 -22:28:07.1	Long Period Variable
	out00137.dat	1.8	12.49	0.01	01:13:51.13 -22:16:31.3	Variable
	out00024.dat	1.55	11.91	0.01	01:13:44.88 -22:02:36.1	TYC 5853-792-1 – Star
	out00058.dat	1.51	12.10	0.01	01:16:29.64 -22:07:32.9	TYC 5853-560-1 – Star
Sigma_19						
	out20085.dat	2.29	12.24	0.01	01:17:15.55 -26:52:30.2	Variable
	out20116.dat	1.3	16.36	0.04	01:15:08.93 -27:02:21.2	Faint star
	out20256.dat	1.22	15.95	0.03	01:14:11.78 -26:46:56.5	Variable
	out20432.dat	1.22	16.44	0.03	01:16:16.09 -27:08:19.6	Faint star
Sigma_20						
	out00217.dat	1.4	15.45	0.02	01:17:11.92 -21:30:27.9	Variable
	out00178.dat	1.3	15.44	0.01	01:16:35.90 -21:16:50.4	Variable

Table D.1 continued from previous page

Field	Object ID	$1/\eta$	m_R	δm	Ra Dec	Classification (SIMBAD Identifier)
	out00209.dat	1.16	14.33	0.01	01:14:48.09 -21:32:31.7	Variable
Sigma_21						
	out00015.dat	2.77	9.37	0.01	01:14:26.89 -27:48:31.4	CD-28 378 – Star
	out00253.dat	1.68	12.98	0.01	01:17:15.58 -28:14:22.6	BPS CS 29518-0032 – Star
	out20045.dat	1.33	16.13	0.03	01:14:49.00 -28:06:48.6	Variable
Sigma_22						
	out20132.dat	2.49	16.38	0.05	01:16:45.29 -25:36:31.0	Long Period Variable
	out00154.dat	1.49	15.18	0.01	01:17:11.09 -26:02:46.8	Variable
	out00108.dat	1.41	14.27	0.01	01:15:11.11 -25:54:05.8	2dFGRS TGS147Z222 – Galaxy
	out20116.dat	1.39	16.10	0.03	01:15:38.75 -26:17:00.6	Faint Star
Sigma_23						
	out00092.dat	2.77	12.97	0.01	01:17:56.95 -17:25:40.0	Long Period Variable
	out00225.dat	2.16	10.93	0.01	01:17:59.81 -17:49:16.4	TYC 5851-652-1 – Star
	out00080.dat	2.02	16.24	0.04	01:16:13.08 -17:24:17.0	Faint Star
Sigma_24						
	out00141.dat	1.41	16.30	0.03	01:16:04.34 -24:47:14.4	LEDA 786203 – Galaxy
	out20107.dat	1.37	16.30	0.03	01:17:44.73 -24:33:01.7	Faint Star

Table D.1 continued from previous page

Field	Object ID	$1/\eta$	m_R	δm	Ra Dec	Classification (SIMBAD Identifier)
	out20130.dat	1.22	16.50	0.03	01:17:29.84 -24:27:50.7	Faint Star
Sigma_25						
	out00048.dat	3.28	8.98	0.01	01:18:24.85 -23:24:17.1	CD-24 564 – Rotationally variable Star
	out20158.dat	1.86	16.61	0.04	01:17:36.89 -23:52:47.9	ROSC 475N50 2 – Galaxy in Cluster of Galaxies
	out00101.dat	1.85	13.71	0.01	01:16:50.01 -23:32:32.6	Long Period Variable
	out00003.dat	1.76	14.11	0.01	01:17:49.09 -23:17:17.5	Long Period Variable
Sigma_26						
	out00193.dat	2.08	10.19	0.01	01:16:35.65 -20:10:32.9	TYC 5853-1929-1 – Star
	out00262.dat	1.46	10.99	0.01	01:16:45.05 -20:16:10.8	TYC 5853-1369-1 – Star
	out00186.dat	1.44	13.88	0.01	01:18:05.09 -20:09:21.3	Variable
Sigma_27						
	out00044.dat	1.7	13.82	0.01	01:19:04.82 -22:15:45.8	Variable
	out00018.dat	1.48	14.83	0.01	01:19:00.76 -22:12:10.8	Variable
	out00200.dat	1.45	15.55	0.06	01:21:17.84 -22:48:02.2	ESO 476-5 – Emission-line galaxy
Sigma_28						
	out00036.dat	2.23	14.25	0.01	01:21:15.17 -18:43:44.6	Variable
	out00038.dat	2.15	13.76	0.01	01:21:21.06 -18:43:53.7	Variable

Table D.1 continued from previous page

Field	Object ID	$1/\eta$	m_R	δm	Ra Dec	Classification (SIMBAD Identifier)
	out00039.dat	2.11	13.26	0.01	01:20:54.18 -18:44:17.9	Variable
Sigma_29						
	out00110.dat	2.42	13.35	0.03	01:20:32.09 -17:47:32.5	CRTS J012032.0-174732 – W UMa type binary
	out00022.dat	2.02	13.63	0.01	01:22:07.77 -17:32:20.1	TYC 5852-308-1 – Star
	out00157.dat	1.73	15.41	0.01	01:21:35.38 -17:54:59.2	Long Period Variable
	out00108.dat	1.61	16.39	0.03	01:21:10.26 -17:46:42.9	Long Period Variable
Sigma_30						
	out00119.dat	1.7	16.24	0.04	01:20:25.24 -21:19:42.1	Faint Star
	out20106.dat	1.54	16.29	0.03	01:19:35.62 -21:23:09.5	Faint Star
	out00107.dat	1.49	12.16	0.01	01:21:55.96 -21:17:43.9	UCAC2 23280266 – Star
	out00218.dat	1.47	16.19	0.03	01:19:45.46 -21:38:12.9	LEDA 825767 – Galaxy
Sigma_31						
	out00008.dat	1.91	12.20	0.01	01:24:05.54 -16:26:58.9	TYC 5852-2127-1 – Star
	out20235.dat	1.59	16.37	0.03	01:23:23.43 -16:50:13.2	Faint star
	out00220.dat	1.52	16.02	0.03	01:24:00.81 -16:53:04.4	Faint star
	out00086.dat	1.4	12.28	0.01	01:23:48.33 -16:37:00.4	Long Period Variable
Sigma_32						

Table D.1 continued from previous page

Field	Object ID	$1/\eta$	m_R	δm	Ra Dec	Classification (SIMBAD Identifier)
	out20267.dat	1.65	16.66	0.05	01:21:41.76 -20:27:30.0	Faint Star
	out20058.dat	1.37	14.10	0.01	01:21:21.85 -20:29:10.5	Long Period Variable
	out00098.dat	1.32	14.70	0.01	01:24:15.84 -20:08:12.2	TYC 5854-693-1 – Star
Sigma_33						
	out00261.dat	2.19	11.62	0.01	01:25:11.27 -18:28:18.0	TYC 5852-180-1 – Star
	out00004.dat	1.74	16.21	0.04	01:25:22.02 -17:51:13.9	Long Period Variable
	out00002.dat	1.47	13.35	0.01	01:26:06.70 -17:50:40.2	Variable
Sigma_34						
	out00138.dat	1.9	12.74	0.01	01:28:26.84 -17:05:27.9	Variable
	out00022.dat	1.55	16.40	0.03	01:26:45.50 -16:48:55.9	Faint Star
	out00094.dat	1.51	13.08	0.01	01:28:06.16 -16:59:01.6	Variable

Table D.1: Comprehensive list of all the objects of interest detected across all 34 fields of the Sigma follow-up observations to candidate alert G296853. The Object ID is automatically generated by VaST and $1/\eta$ is the variability index.

D.2 Nu

Field	Object ID	$1/\eta$	m_R	δm	Ra Dec	Classification (SIMBAD Identifier)
Nu_8						
	out00511.dat	2.78	16.34	0.05	03:14:26.83 -34:54:54.8	Long Period Variable
	out00285.dat	1.53	16.50	0.09	03:13:44.84 -34:47:15.5	Long Period Variable
	out00218.dat	1.51	16.45	0.07	03:14:28.21 -34:42:08.9	Faint Star
Nu_11						
	out00261.dat	2.24	16.95	0.07	03:14:05.11 -33:41:44.0	Long period variable?
	out00191.dat	2.12	13.40	0.06	03:16:14.09 -33:35:14.9	2MASS J03161395-3336024 – Star
	out00109.dat	1.93	16.05	0.05	03:14:32.42 -33:29:28.2	2dFGRS TGS524Z120 – Galaxy
Nu_13						
	out00009.dat	2.33	15.49	0.02	03:17:01.66 -32:20:27.3	Long Period Variable
	out00338.dat	2.14	16.44	0.04	03:17:22.67 -32:43:33.7	Long Period Variable
	out00191.dat	1.98	15.53	0.03	03:14:27.51 -32:35:36.1	Transient
	out00201.dat	1.94	15.99	0.05	03:17:19.77 -32:35:30.9	Faint Star
Nu_16						
	out00248.dat	2.7	15.34	0.04	03:17:12.24 -31:33:38.4	Long Period Variable
	out00153.dat	1.93	15.40	0.04	03:17:03.07 -31:24:44.0	Long Period Variable

Table D.2 continued from previous page

Field	Object ID	$1/\eta$	m_R	δm	Ra Dec	Classification (SIMBAD Identifier)
	out00380.dat	1.8	13.32	0.02	03:18:01.21 -31:55:16.7	Long Period Variable
Nu_17						
	out00011.dat	2.06	16.34	0.06	03:19:11.54 -34:32:18.9	Long Period Variable
	out00073.dat	1.87	16.95	0.07	03:17:14.10 -34:37:04.3	Faint Star
	out00320.dat	1.79	15.33	0.02	03:18:27.91 -34:55:05.5	Variable
Nu_19						
	out00489.dat	3.38	16.79	0.07	03:20:01.15 -34:07:44.1	Faint Star
	out00570.dat	2.29	15.60	0.01	03:19:30.79 -34:02:09.2	Long Period Variable
	out00193.dat	2.27	15.97	0.03	03:20:29.08 -33:44:23.1	Variable
	out00009.dat	2.18	16.20	0.05	03:20:00.64 -33:30:04.5	Long Period Variable
	out00378.dat	2.17	13.75	0.01	03:19:48.04 -33:57:53.5	Variable
Nu_21						
	out00018.dat	2.48	13.78	0.01	03:22:27.79 -32:28:58.9	Long Period Variable
	out00466.dat	2.45	16.67	0.01	03:20:51.43 -33:02:55.8	Variable
	out00490.dat	1.86	12.80	0.01	03:20:44.87 -33:03:44.4	Variable
Nu_24						

Table D.2 continued from previous page

Field	Object ID	$1/\eta$	m_R	δm	Ra Dec	Classification (SIMBAD Identifier)
	out00120.dat	3.49	15.18	0.02	03:20:55.48 -31:38:22.8	Long Period Variable
	out00013.dat	3.48	14.75	0.02	03:22:30.64 -31:28:57.4	Long Period Variable
	out00007.dat	3.26	13.88	0.02	03:22:30.52 -31:28:30.9	Long Period Variable
	out00163.dat	2.76	15.38	0.02	03:20:56.67 -31:40:27.2	Long Period Variable
	out00338.dat	2.54	15.56	0.03	03:23:21.12 -31:54:19.5	2dFGRS TGS472Z146 – Galaxy
	out00528.dat	2.2	12.80	0.01	03:22:29.27 -31:58:30.8	Long Period Variable
	out00115.dat	2.04	15.60	0.03	03:22:52.94 -31:37:19.0	Faint Star
Nu_25						
	out00497.dat	2.37	15.13	0.02	03:21:50.24 -31:04:06.5	Long Period Variable
	out00131.dat	2.11	15.41	0.02	03:22:40.40 -30:37:46.9	Long Period Variable
	out00541.dat	2.09	14.64	0.01	03:24:15.82 -30:59:48.5	Long Period Variable
Nu_28						
	out00094.dat	2.46	15.78	0.08	03:23:14.74 -29:32:41.5	Long Period Variable
	out00083.dat	2.39	16.22	0.03	03:23:20.00 -29:31:38.1	Faint Star
	out00031.dat	2.17	14.33	0.02	03:24:22.50 -29:27:11.3	Variable
Nu_29						
	out00167.dat	2.36	15.42	0.02	03:26:05.11 -34:02:02.0	Long Period Variable

Table D.2 continued from previous page

Field	Object ID	$1/\eta$	m_R	δm	Ra Dec	Classification (SIMBAD Identifier)
	out00259.dat	2.12	15.57	0.06	03:25:47.75 -34:07:56.9	Faint Star
	out00569.dat	1.99	15.93	0.05	03:23:58.86 -34:24:21.2	Long Period Variable
	out00203.dat	1.89	15.56	0.02	03:24:14.58 -34:05:30.5	LEDA 667314 – Galaxy
Nu_30						
	out00490.dat	2.34	16.42	0.04	03:26:57.71 -33:26:56.1	Faint Star
	out00460.dat	2.11	16.74	0.04	03:24:40.19 -33:20:02.5	Faint Star
Nu_33						
	out00463.dat	4.94	15.12	0.02	03:27:34.59 -32:17:17.5	Long Period Variable
	out00091.dat	3.9	15.84	0.04	03:26:58.49 -31:56:01.6	Long Period Variable
	out00518.dat	2.5	10.66	0.01	03:26:37.27 -32:20:08.8	TYC 7021-102-1 – High proper-motion Star
	out00369.dat	2.29	13.25	0.05	03:28:06.54 -32:17:09.8	NGC 1339 – Galaxy in Group of Galaxies
	out00420.dat	2.28	16.65	0.08	03:27:55.66 -32:27:31.8	Faint Star
	out00210.dat	2.26	16.09	0.04	03:27:55.58 -32:03:48.4	Faint Star
	out00044.dat	2.13	16.18	0.02	03:28:31.19 -31:51:34.8	Faint Star
	out00485.dat	2.12	14.30	0.01	03:25:55.24 -32:25:39.6	Long Period Variable
	out00554.dat	2.03	14.76	0.03	03:25:49.71 -32:20:15.8	Variable
	out00315.dat	2.02	15.19	0.02	03:28:57.17 -32:11:58.1	Long Period Variable

Table D.2 continued from previous page

Field	Object ID	$1/\eta$	m_R	δm	Ra Dec	Classification (SIMBAD Identifier)
Nu_34						
	out00242.dat	3.13	13.47	0.01	03:27:19.31 -31:04:39.6	Long Period Variable
	out00274.dat	2.59	11.45	0.01	03:27:37.70 -31:06:11.5	TYC 7021-811-1 – Star
	out00542.dat	2.08	12.21	0.03	03:28:52.16 -31:19:20.1	Long Period Variable
	out00169.dat	2.06	11.51	0.02	03:28:11.83 -30:59:20.9	TYC 7021-782-1 – Star
	out00060.dat	2.04	11.83	0.01	03:28:27.65 -30:50:27.1	TYC 7021-860-1 – Star
	out00529.dat	2	16.09	0.05	03:27:26.28 -31:17:25.5	Long Period Variable

Table D.2: Comprehensive list of all the objects of interest detected across all 14 fields of the Nu follow-up observations to the gravitational wave GW170814.

D.3 Iota

Field	Object ID	$1/\eta$	m_R	δm	Ra Dec	Classification (SIMBAD Identifier)
Iota_1						
	out01982.dat	3.24	16.41	0.05	04:22:51.08 +49:46:29.4	Faint star
	out00316.dat	3.17	15.48	0.02	04:22:41.36 +50:05:33.4	Long Period Variable
	out01635.dat	3.02	16.59	0.05	04:20:58.45 +49:50:01.5	Long Period Variable
	out00611.dat	2.92	14.87	0.01	04:23:06.77 +50:02:22.6	Long Period Variable
	out00631.dat	2.9	13.74	0.01	04:23:02.88 +50:02:02.1	Long Period Variable
	out00863.dat	2.82	16.57	0.01	04:22:26.48 +49:59:28.6	Faint star
	out03316.dat	2.77	15.40	0.01	04:23:47.93 +49:35:50.8	Variable
	out01765.dat	2.67	16.41	0.03	04:21:09.38 +49:48:42.9	Faint star
	out00284.dat	2.62	16.59	0.05	04:21:56.97 +50:05:52.0	Faint star
	out02585.dat	2.61	16.61	0.04	04:23:21.96 +49:28:19.8	Faint star
Iota_2						
	out02066.dat	4.17	16.87	0.04	04:24:41.75 +48:39:48.3	Faint Star
	out02331.dat	3.89	15.58	0.01	04:25:14.27 +48:43:51.4	Long Period Variable
	out02320.dat	2.71	15.04	0.01	04:25:13.43 +48:43:39.2	Long Period Variable
	out00441.dat	2.67	16.36	0.03	04:22:54.37 +49:08:28.4	Variable

Table D.3 continued from previous page

Field	Object ID	$1/\eta$	m_R	δm	Ra Dec	Classification (SIMBAD Identifier)
	out20356.dat	2.54	16.84	0.05	04:25:40.89 +48:46:36.1	Long Period Variable
	out20698.dat	2.45	16.93	0.08	04:24:22.53 +48:55:00.2	Long Period Variable
	out00322.dat	2.45	13.46	0.01	04:22:55.84 +49:10:29.0	Long Period Variable
	out01203.dat	2.4	16.70	0.03	04:22:57.10 +48:54:48.7	Long Period Variable
	out01319.dat	2.39	16.10	0.02	04:25:56.22 +48:53:36.0	Variable
	out00053.dat	2.32	16.70	0.05	04:25:48.24 +49:16:10.8	Long Period Variable
Iota_3						
	out00350.dat	2.96	15.99	0.03	04:28:15.76 +49:58:31.9	TYC 3337-1159-1 – Star
	out02102.dat	2.56	15.82	0.02	04:26:26.16 +49:22:40.9	Long Period Variable
	out00635.dat	2.52	16.58	0.04	04:25:37.28 +49:53:33.7	Variable
	out01761.dat	2.51	12.58	0.01	04:28:33.23 +49:38:17.7	Long Period Variable
	out02612.dat	2.46	15.14	0.01	04:29:11.86 +49:28:22.7	Long Period Variable
	out20308.dat	2.45	16.94	0.05	04:25:38.69 +49:26:57.5	Long Period Variable
	out01390.dat	2.4	15.43	0.03	04:27:58.06 +49:43:51.8	Variable
	out01482.dat	2.4	16.09	0.02	04:27:07.78 +49:42:20.4	Long Period Variable
	out00255.dat	2.33	15.54	0.02	04:26:11.37 +49:59:24.5	Long Period Variable
	out00356.dat	2.25	16.67	0.05	04:28:57.00 +49:58:40.7	Long Period Variable

Table D.3 continued from previous page

Field	Object ID	$1/\eta$	m_R	δm	Ra Dec	Classification (SIMBAD Identifier)
	out01172.dat	2.25	16.36	0.03	04:25:27.40 +49:45:58.4	Long Period Variable
	out00991.dat	2.23	13.45	0.01	04:28:47.99 +49:48:54.8	Long Period Variable
	out00470.dat	2.23	15.84	0.02	04:27:21.62 +49:56:38.7	Long Period Variable
	out00656.dat	2.22	17.01	0.07	04:27:23.58 +49:53:50.5	Faint star
Iota_4						
	out01764.dat	3.22	13.79	0.01	04:27:55.76 +50:24:12.8	Long Period Variable
	out00508.dat	3.03	16.06	0.03	04:30:04.55 +50:43:12.9	Faint Star
	out01096.dat	2.98	16.45	0.03	04:30:32.70 +50:34:22.0	Faint Star
	out00467.dat	2.72	15.22	0.01	04:27:32.11 +50:42:56.9	HD 27968 – Star
	out02724.dat	2.66	16.65	0.03	04:30:48.86 +50:19:36.2	Faint Star
	out01117.dat	2.55	16.15	0.02	04:28:24.23 +50:33:23.0	Long Period Variable
	out02388.dat	2.54	14.51	0.01	04:28:04.46 +50:21:05.4	Long Period Variable
	out00820.dat	2.52	16.54	0.03	04:29:10.81 +50:38:22.4	Long Period Variable
	out02320.dat	2.46	16.20	0.02	04:29:24.24 +50:12:15.2	Faint Star
	out20811.dat	2.45	16.76	0.05	04:28:11.24 +50:14:49.0	Faint Star
	out02174.dat	2.45	16.49	0.05	04:27:36.42 +50:09:48.2	Faint Star
	out00331.dat	2.44	13.09	0.01	04:27:13.02 +50:44:42.5	Long Period Variable

Table D.3 continued from previous page

Field	Object ID	$1/\eta$	m_R	δm	Ra Dec	Classification (SIMBAD Identifier)
Iota_5						
	out01033.dat	3.57	14.85	0.08	04:30:19.08 +49:44:00.8	2MASS04301894+4944024
	out00483.dat	2.78	16.22	0.02	04:32:01.49 +49:51:26.4	Long Period Variable
	out02283.dat	2.78	16.51	0.02	04:31:49.09 +49:27:31.3	Long Period Variable
	out00114.dat	2.7	16.72	0.04	04:31:12.96 +49:56:00.0	Faint Star
	out01312.dat	2.7	11.11	0.01	04:33:19.53 +49:40:59.3	TYC 3350-827-1 – Star
	out01969.dat	2.65	15.35	0.01	04:30:43.73 +49:30:52.8	Long Period Variable
	out00550.dat	2.58	16.79	0.06	04:33:05.70 +49:50:51.7	Faint Star
	out20138.dat	2.44	16.63	0.05	04:30:04.64 +49:41:40.3	Faint Star
	out00952.dat	2.38	16.33	0.02	04:29:32.42 +49:44:52.8	Faint Star
	out02227.dat	2.29	15.77	0.02	04:31:29.12 +49:18:01.7	Long Period Variable
	out02427.dat	2.25	16.06	0.03	04:30:35.70 +49:20:24.8	Long Period Variable
	out01263.dat	2.18	16.21	0.02	04:31:30.16 +49:41:43.4	Long Period Variable
	out02274.dat	2.16	16.66	0.03	04:32:23.54 +49:19:22.9	Faint Star

Table D.3: Comprehensive list of all the objects of interest detected across the 5 fields of the Iota follow-up observations to candidate alert G298936.

D.4 Kappa

Field	Object ID	$1/\eta$	m_R	δm	Ra Dec	Classification (SIMBAD Identifier)
Kappa_1						
	out00600.dat	3.87	10.74	0.01	02:01:43.69 +38:44:28.6	TYC 2829-403-1 – Star
	out00077.dat	1.9	14.23	0.01	02:04:01.53 +38:59:49.3	Variable
	out00443.dat	1.72	13.49	0.01	02:01:54.24 +38:49:08.4	Variable
	out00326.dat	1.71	13.3	0.01	02:01:12.40 +38:52:10.6	Variable
	out00834.dat	1.7	13.94	0.01	02:02:56.87 +38:38:19.0	Variable
	out00770.dat	1.68	12.16	0.01	02:01:58.25 +38:39:30.8	Variable
Kappa_2						
	out01440.dat	2.64	12.72	0.01	02:02:52.67 +39:15:25.0	Long Period Variable
	out00958.dat	2.23	14.78	0.01	02:04:30.18 +39:20:54.5	Variable
	out20002.dat	1.58	13.44	0.01	02:02:38.93 +39:16:45.5	Variable
	out01255.dat	1.42	16.48	0.02	02:05:24.13 +39:10:55.0	Variable
	out00937.dat	1.36	13.38	0.01	02:02:52.49 +39:20:34.8	Long Period Variable
	out00070.dat	1.33	16.53	0.02	02:04:25.99 +39:46:06.0	Long Period Variable
	out01196.dat	0.6	13.26	0.04	02:05:12.70 +39:10:24.7	V0755 Andromeda – W Uma type binary
Kappa_3						

Table D.4 continued from previous page

Field	Object ID	$1/\eta$	m_R	δm	Ra Dec	Classification (SIMBAD Identifier)
	out00020.dat	1.79	12.61	0.01	02:04:26.08 +40:33:17.6	Vairable
	out20662.dat	1.42	17.29	0.03	02:06:18.80 +39:57:35.6	Faint Star
Kappa_4						
	out01239.dat	3	12.53	0.01	02:05:54.62 +40:43:26.9	V* AH And – Variable Star of Mira Cet type
	out00456.dat	2.32	12.06	0.01	02:06:41.50 +41:08:46.4	Variable
	out00384.dat	2.14	14.04	0.01	02:08:00.34 +41:11:28.6	Variable
	out00502.dat	1.87	16.47	0.02	02:07:59.84 +41:08:29.0	2MASX J02075993+4108290 – Galaxy
Kappa_5						
	out01495.dat	2.2	16.74	0.04	02:09:22.74 +41:38:59.0	Variable (Faint)
	out00680.dat	1.99	15.44	0.02	02:07:38.37 +41:52:53.8	Variable
	out20043.dat	1.88	16.34	0.07	02:10:20.99 +41:45:37.6	Variable
	out01461.dat	1.74	13.99	0.01	02:06:58.36 +41:32:27.5	Variable
	out01563.dat	1.7	14.39	0.01	02:08:26.15 +41:35:13.3	Long Period Varibale
	out01330.dat	1.69	14.9	0.03	02:10:14.77 +41:31:18.6	UGC 1661 – Galaxy in Group of Galaxies
Kappa_6						
	out00167.dat	2.45	15.95	0.3	02:08:40.21 +42:53:34.6	2MASX J02084017+4253336 – Galaxy
	out00900.dat	1.8	13.26	0.01	02:09:16.90 +42:38:21.0	Long Period Variable

Table D.4 continued from previous page

Field	Object ID	$1/\eta$	m_R	δm	Ra Dec	Classification (SIMBAD Identifier)
	out00233.dat	1.72	14.45	0.01	02:10:15.89 +42:52:39.7	Variable
	out01398.dat	1.62	12.11	0.01	02:08:29.43 +42:16:45.6	Variable

Table D.4: Comprehensive list of all the objects of interest detected across the 6 fields of the Kappa follow-up observations to candidate alert G299232.

Appendix E

Lightcurves

Lightcurves from Sigma follow-up.

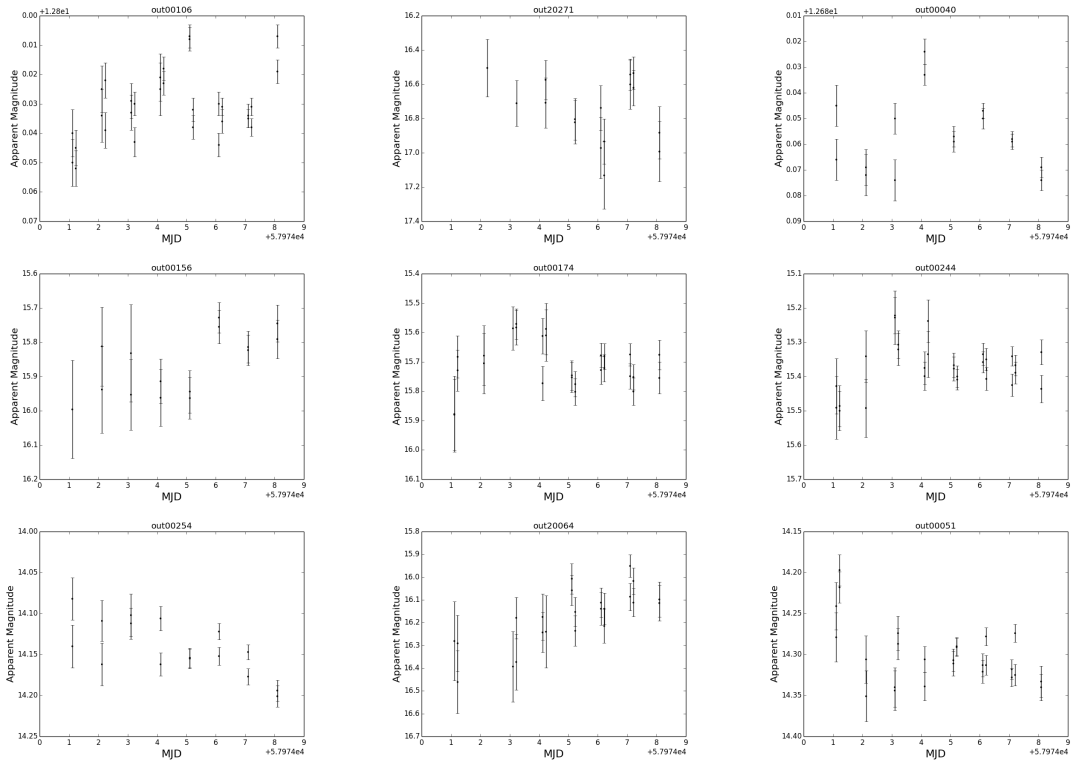

Figure E.1: Sigma 1, Sigma 2 and Sigma 3 lightcurves.

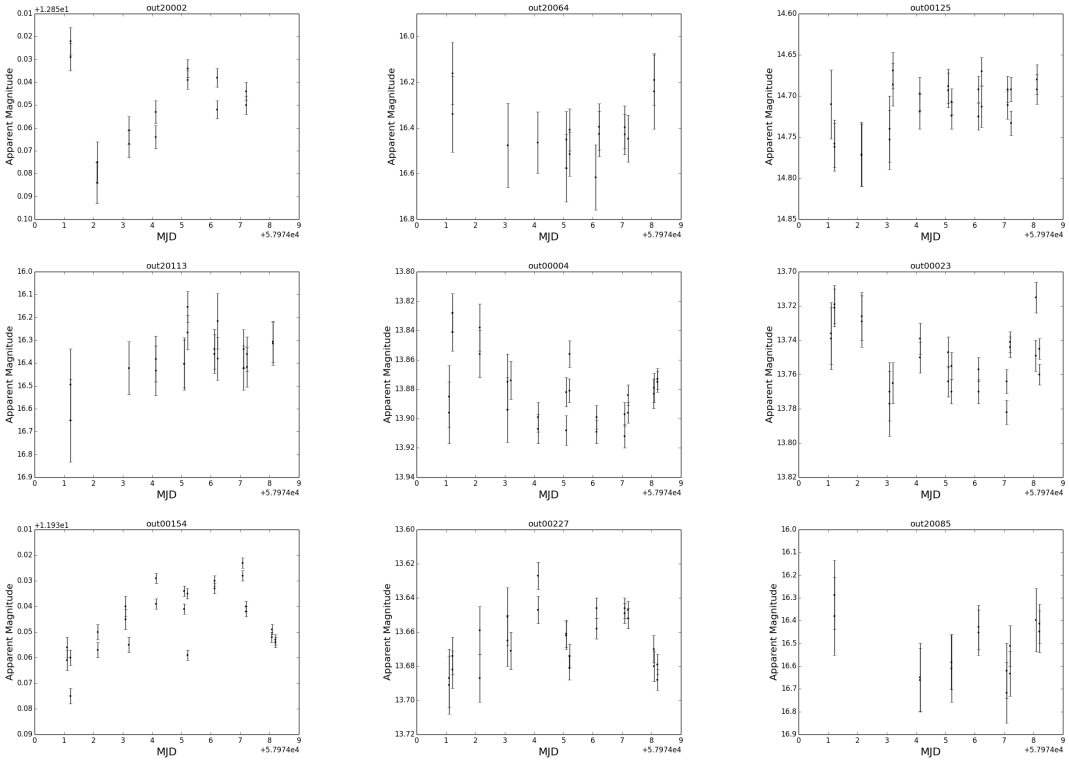

Figure E.2: Sigma 3 cont., Sigma 4 and Sigma 5 lightcurves.

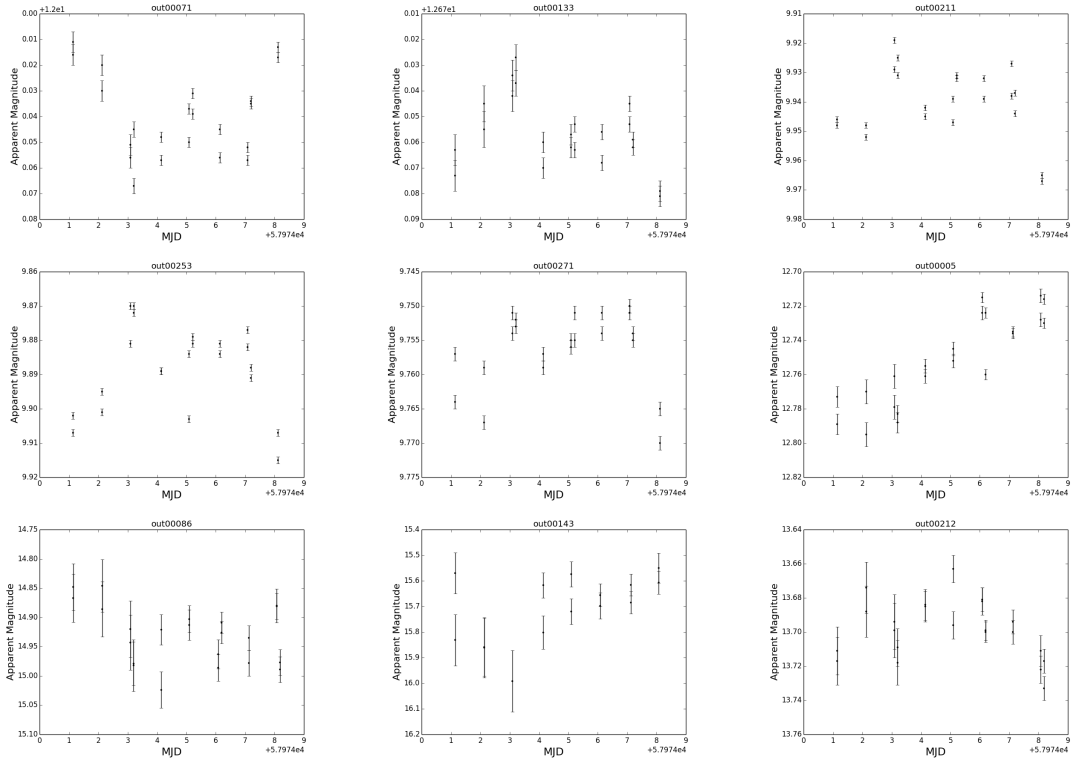

Figure E.3: Sigma 6 and Sigma 7 lightcurves.

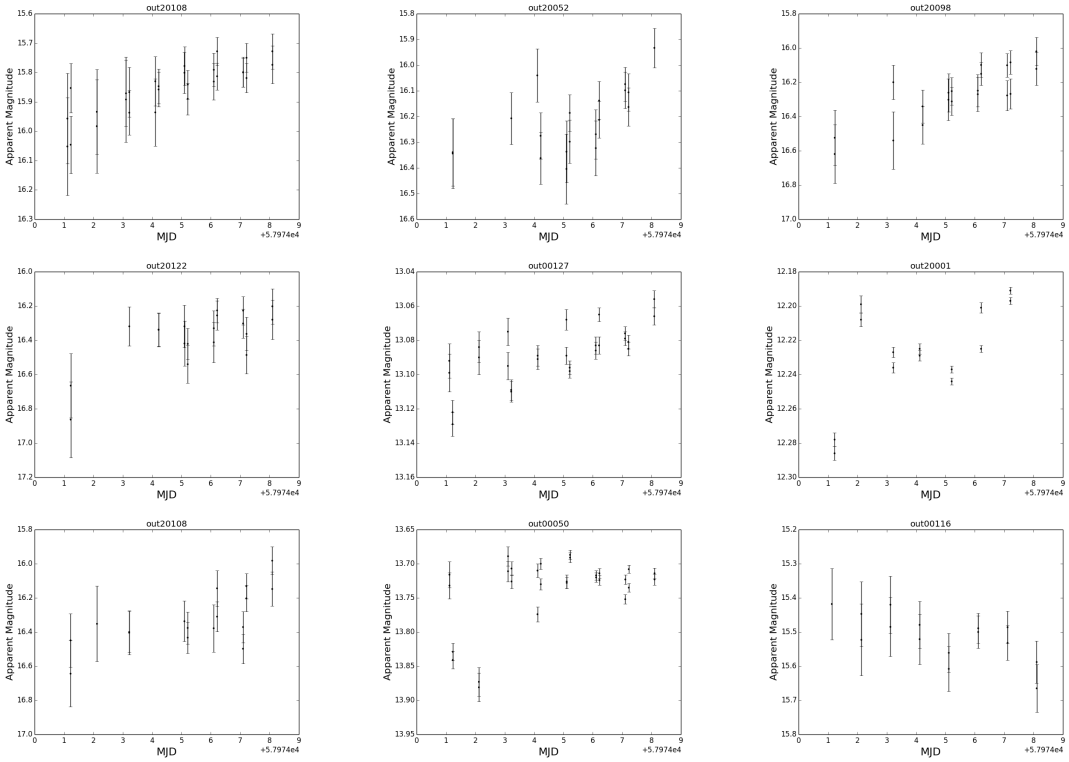

Figure E.4: Sigma 8, Sigma 9, Sigma 10 and Sigma 11 lightcurves.

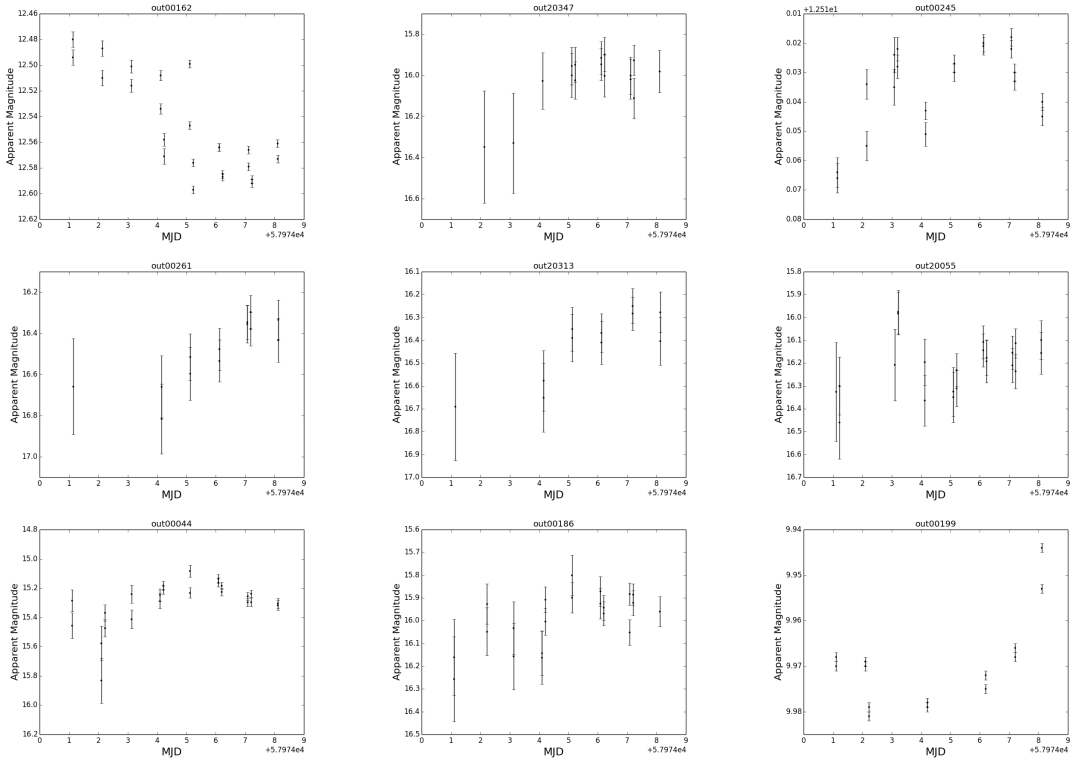

Figure E.5: Sigma 11 cont., Sigma 12, Sigma 13 and Sigma 14 lightcurves.

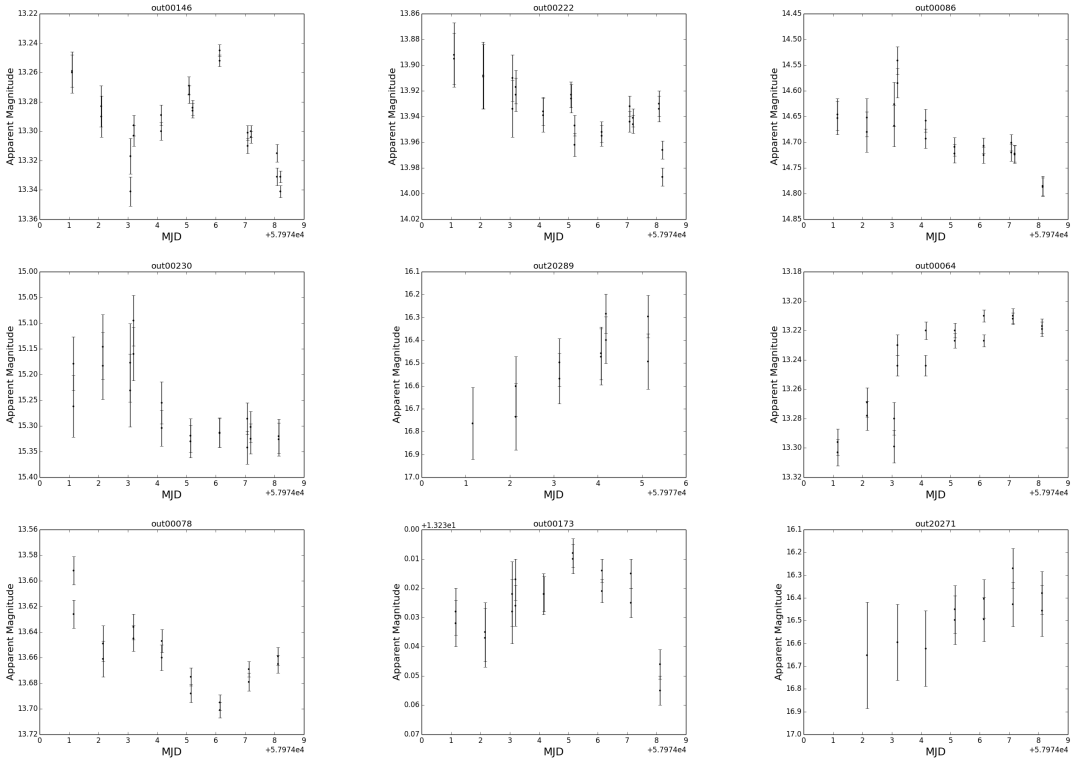

Figure E.6: Sigma 15, Sigma 16, and Sigma 17 lightcurves.

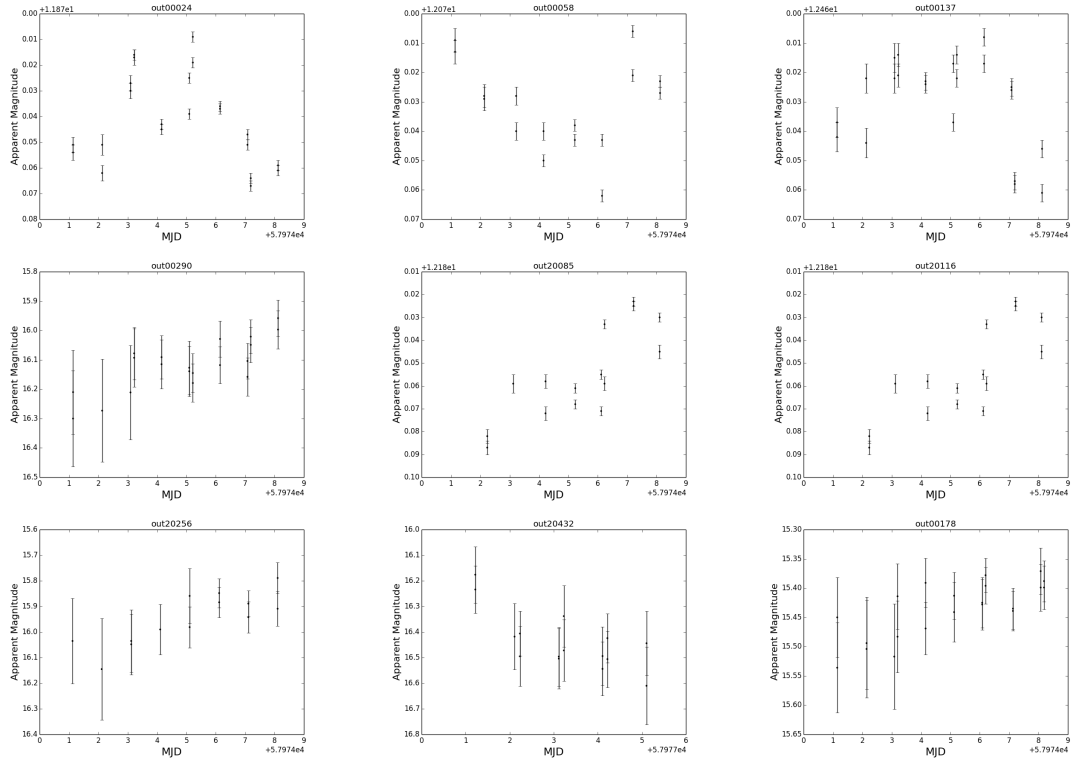

Figure E.7: Sigma 18, Sigma 19, and Sigma 20 lightcurves.

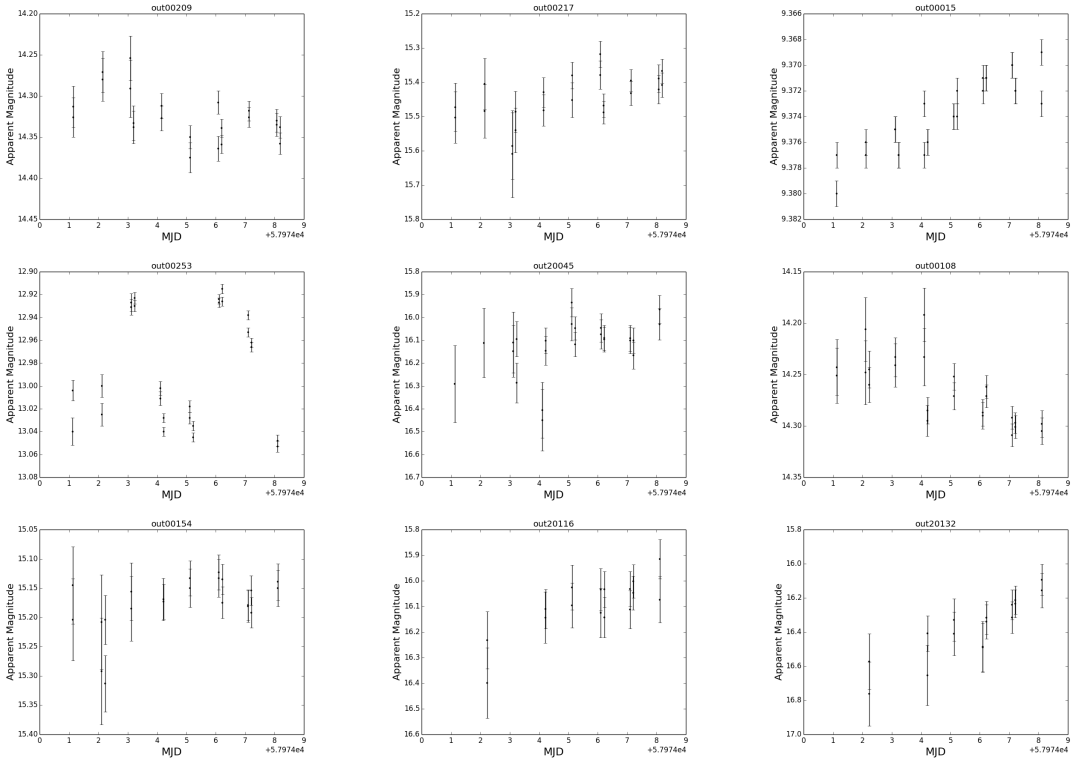

Figure E.8: Sigma 20 cont., Sigma 21, and Sigma 22 lightcurves.

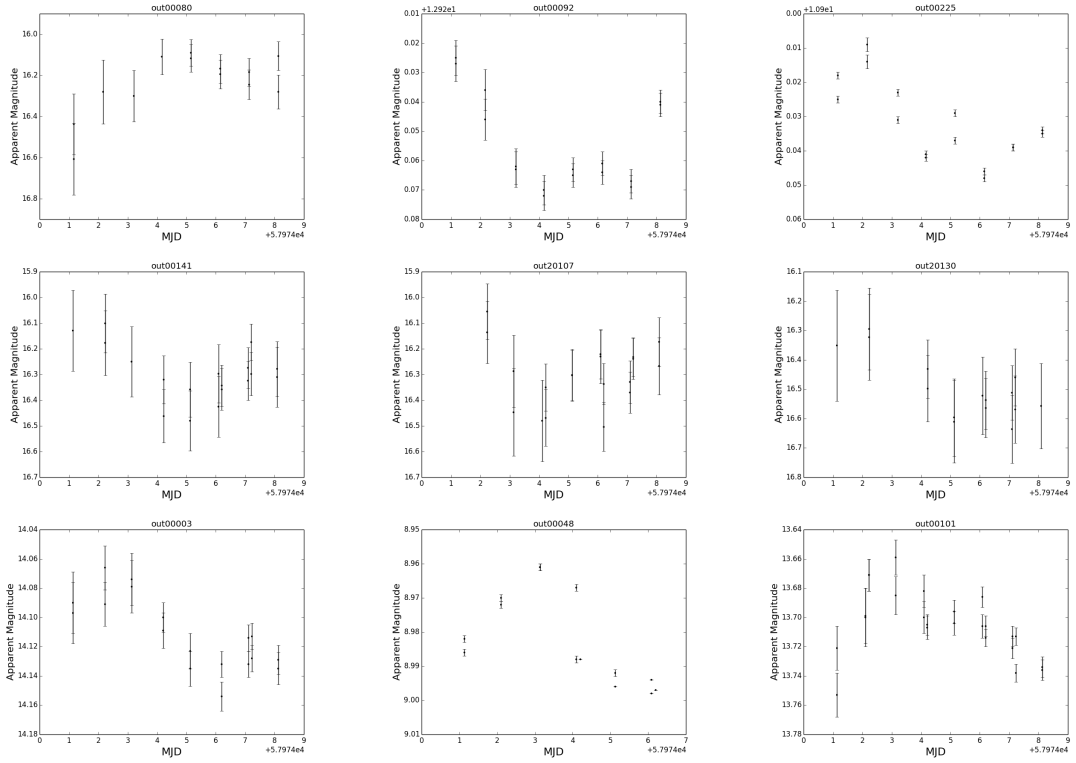

Figure E.9: Sigma 23, Sigma 24, and Sigma 25 lightcurves.

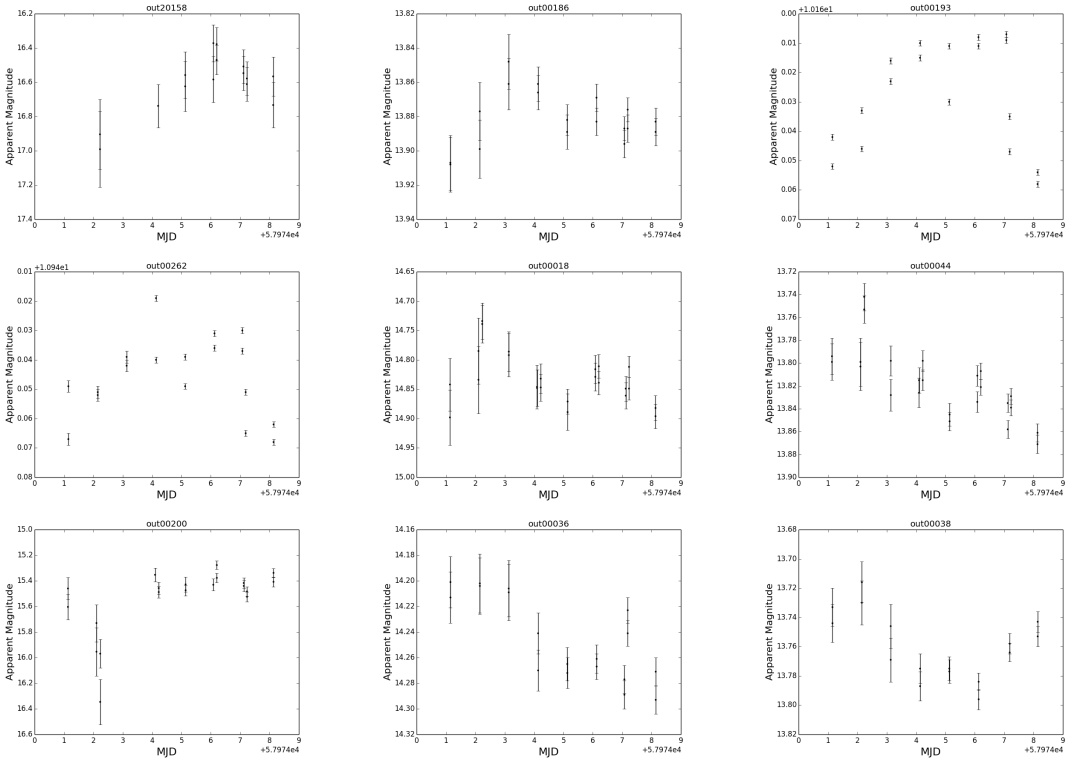

Figure E.10: Sigma 25 cont., Sigma 26, Sigma 27 and Sigma 28 lightcurves.

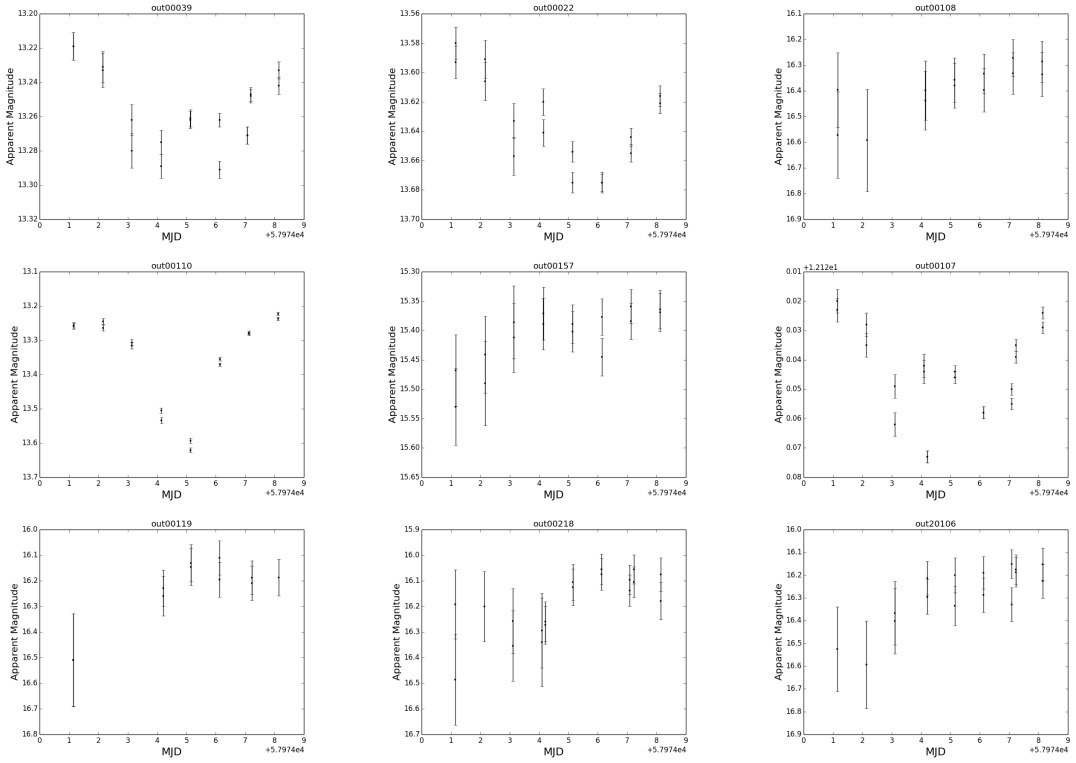

Figure E.11: Sigma 28 cont., Sigma 29,and Sigma 30 lightcurves.

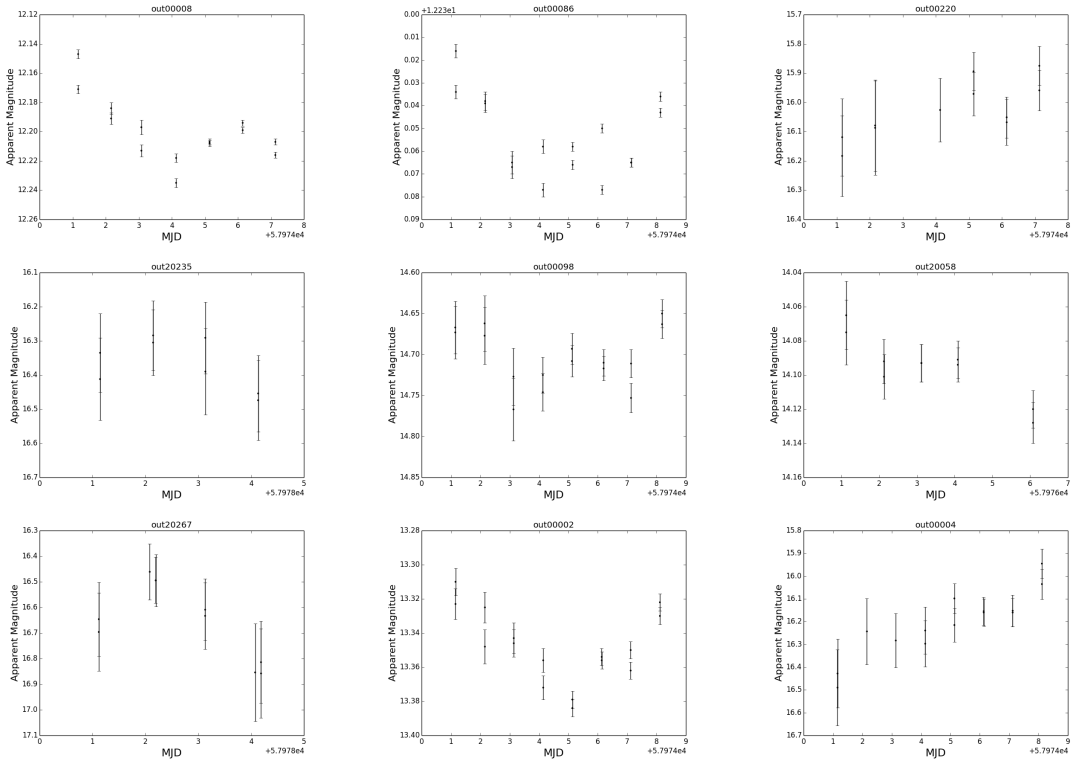

Figure E.12: Sigma 31 Sigma 32,and Sigma 33 lightcurves.

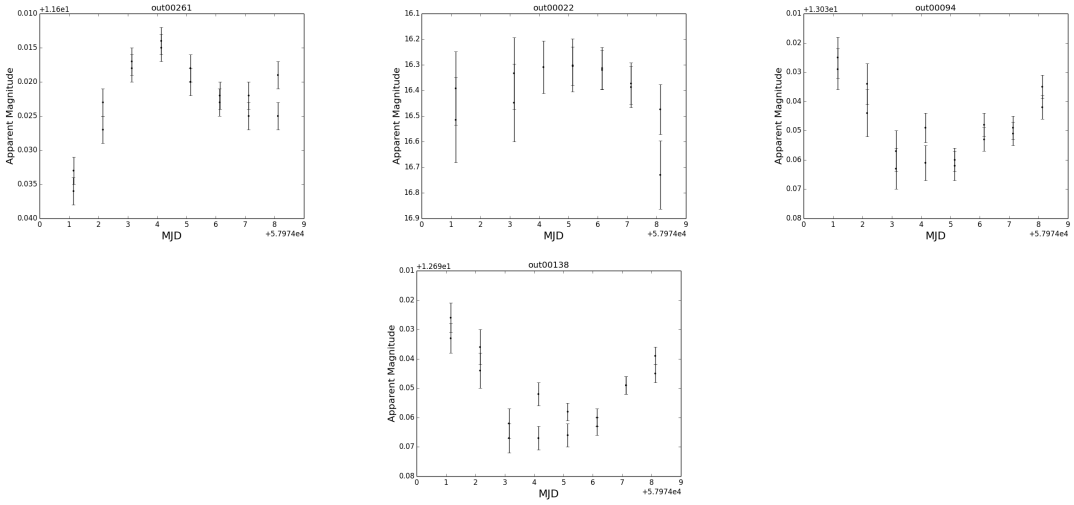

Figure E.13: Sigma 33 cont. and Sigma 34 lightcurves.

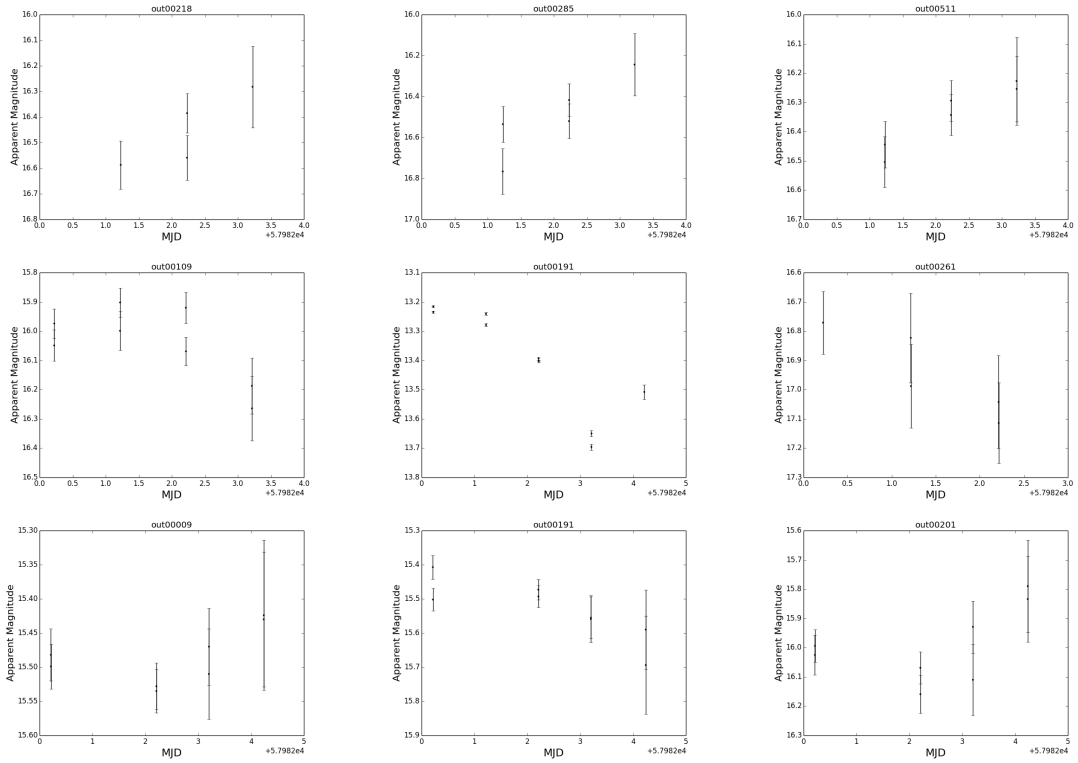

Figure E.14: Nu 8, Nu 11 and Nu 13 lightcurves.

Lightcurves from Nu follow-up.

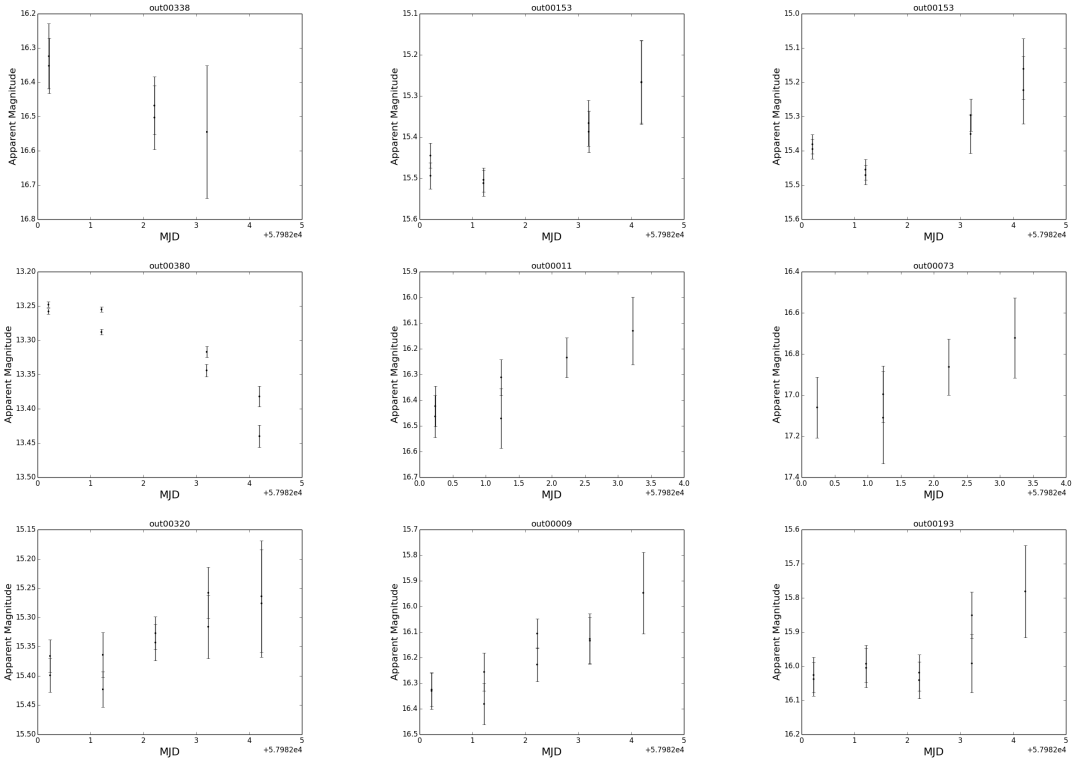

Figure E.15: Nu 13 cont., Nu 16, Nu 17 and Nu 19 lightcurves.

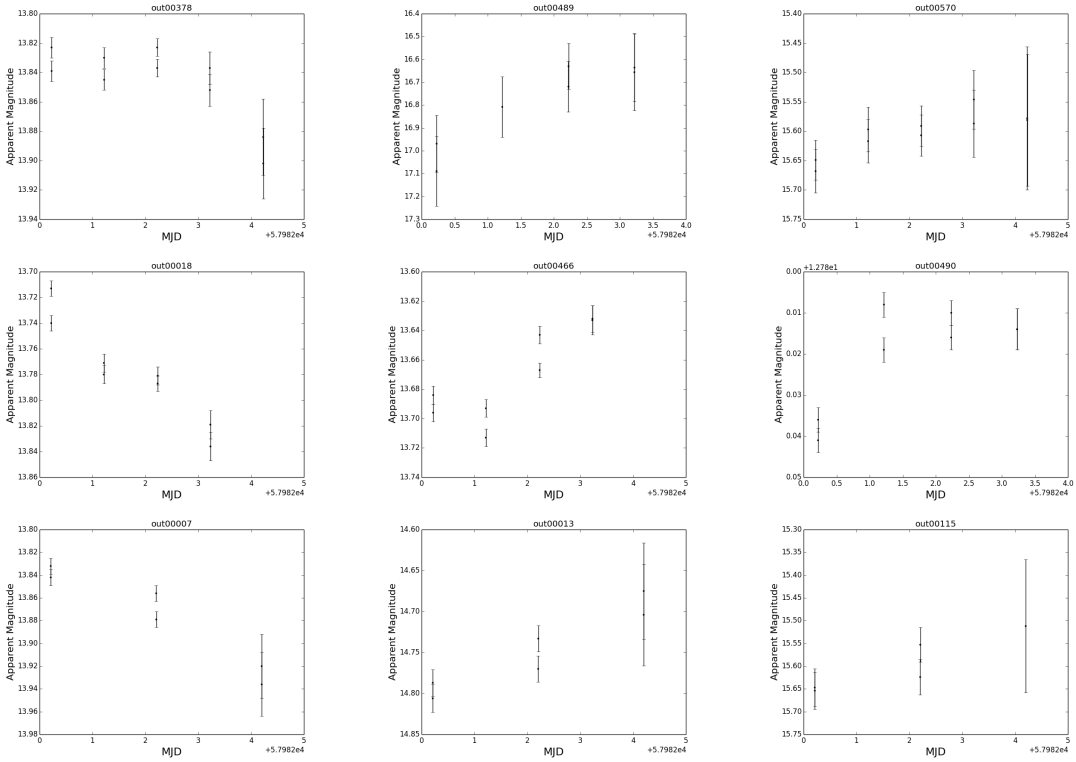

Figure E.16: Nu 19 cont., Nu 21 and Nu 24 lightcurves.

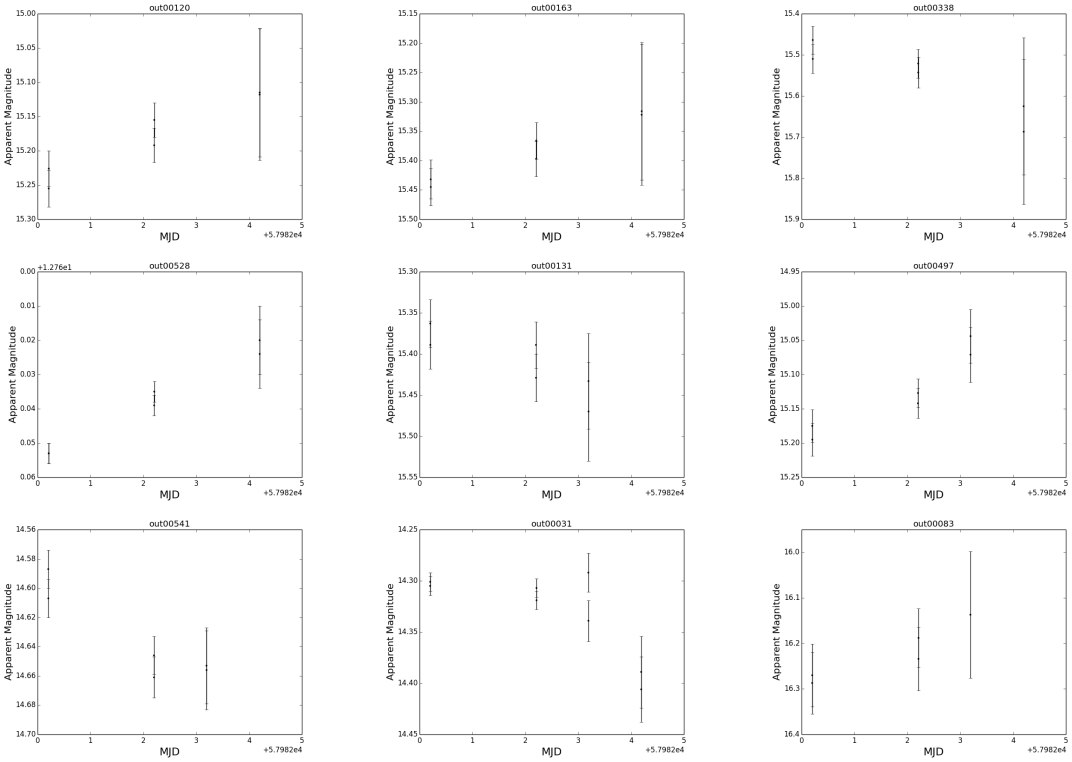

Figure E.17: Nu 24 cont., Nu 25 and Nu 28 lightcurves.

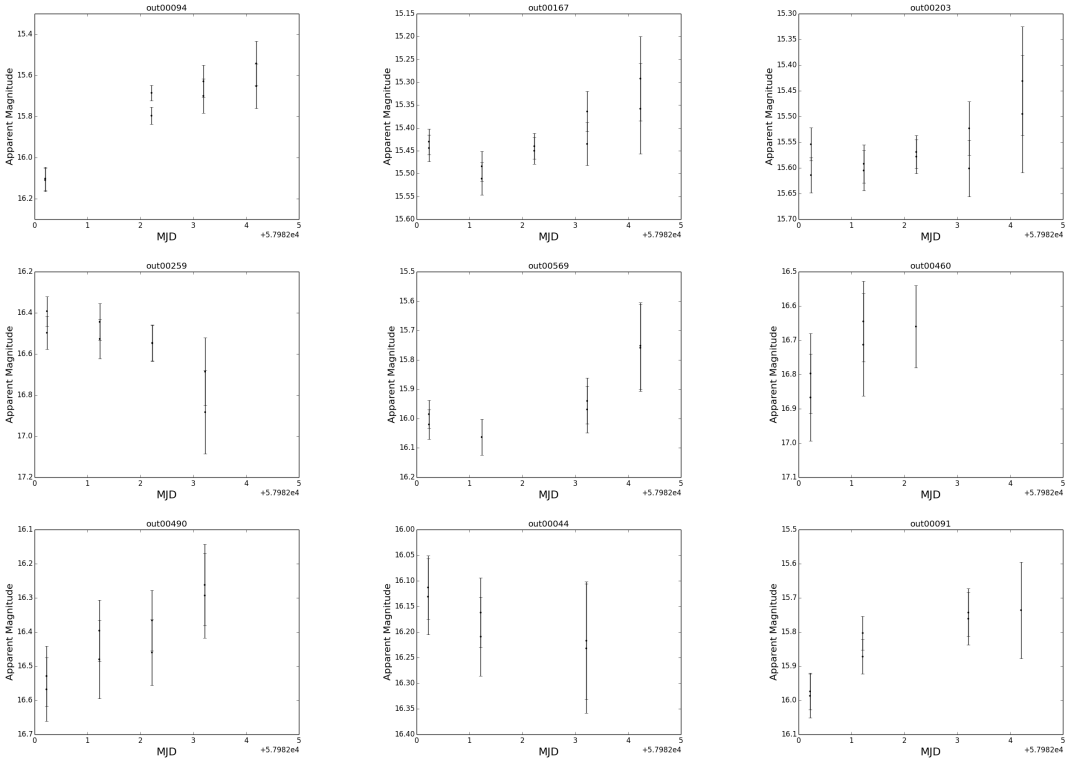

Figure E.18: Nu 28 cont., Nu 29, Nu 30 and Nu 33 lightcurves.

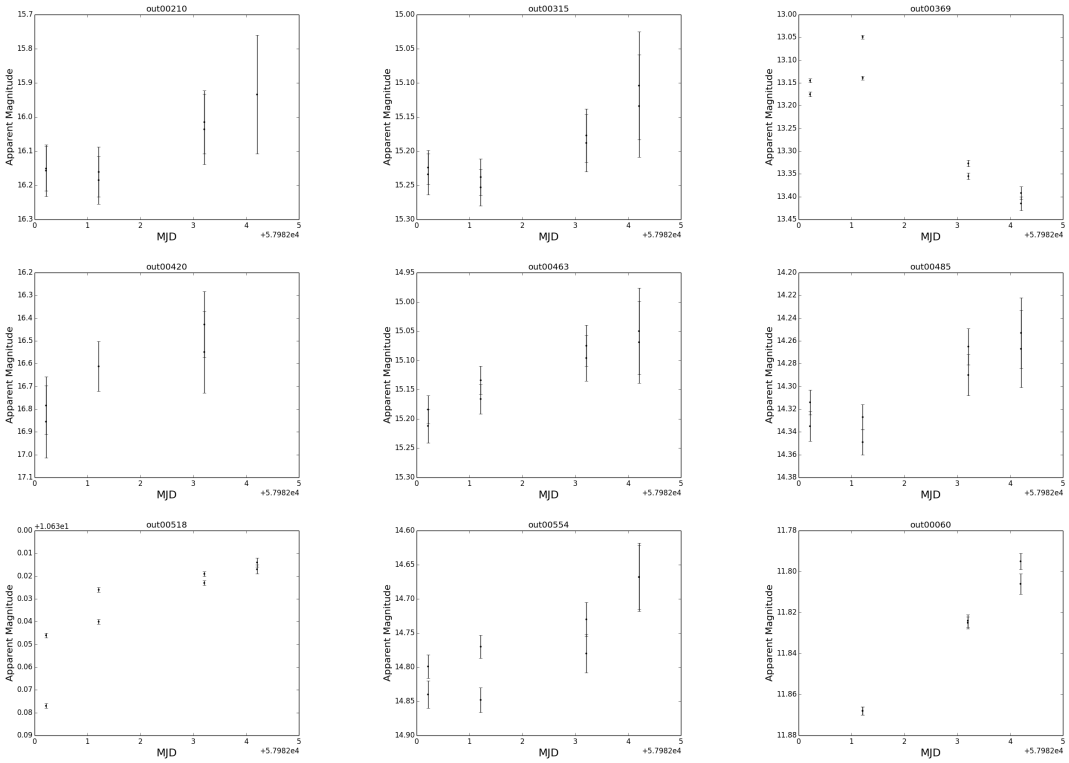

Figure E.19: Nu 33 cont. and Nu 34 lightcurves.

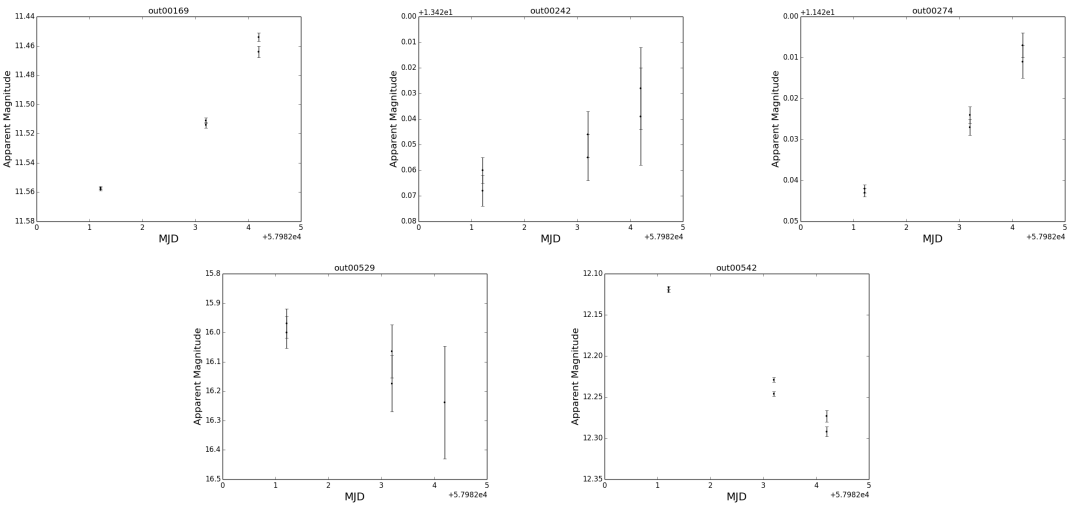

Figure E.20: Nu 33 cont. and Nu 34 lightcurves.

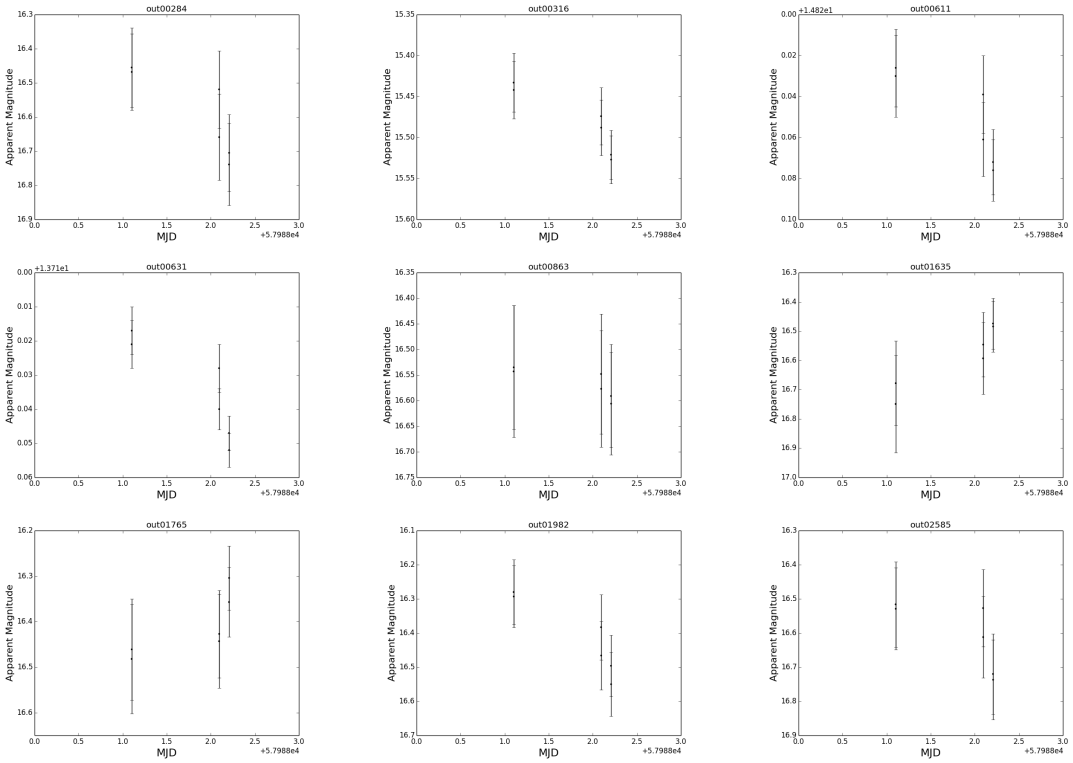

Figure E.21: Iota 1 lightcurves.

Lightcurves from the Iota follow up.

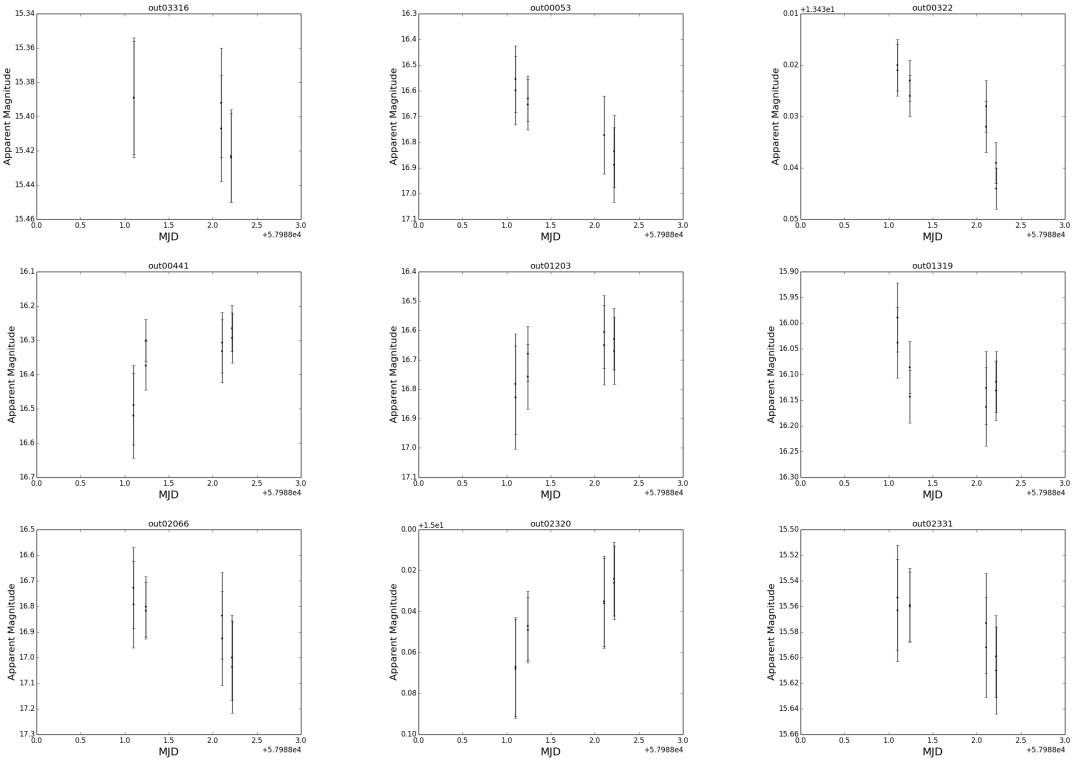

Figure E.22: Iota 1 cont. and Iota 2 lightcurves.

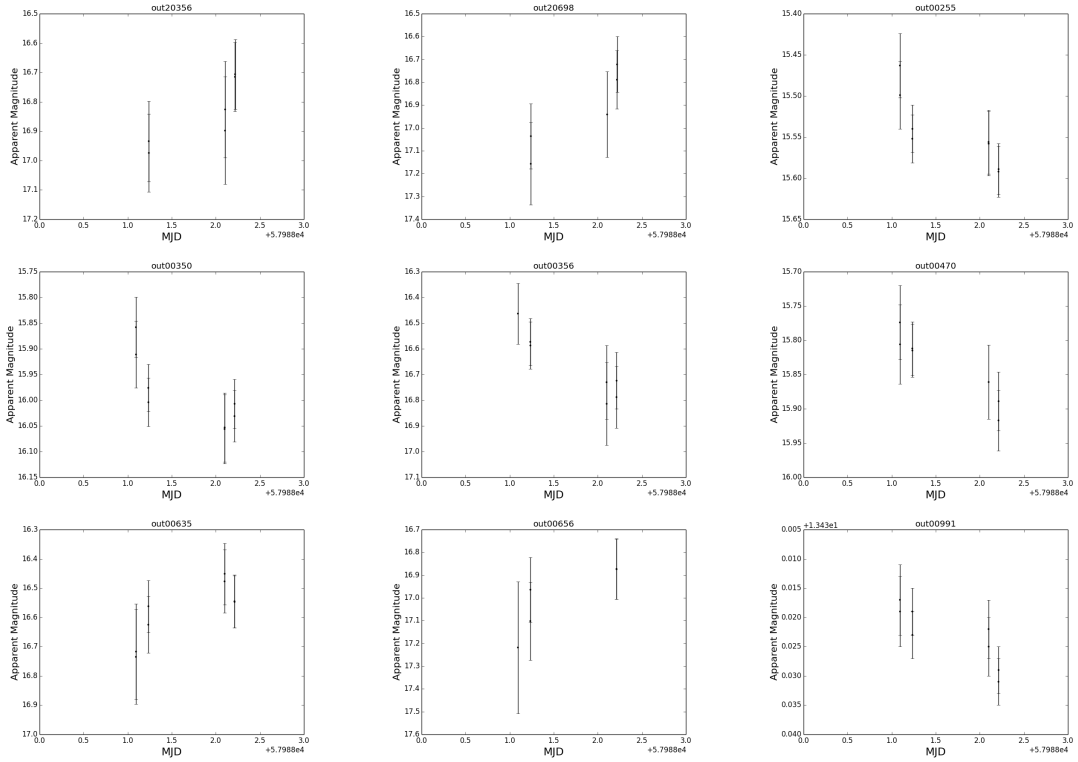

Figure E.23: Iota 2 cont. and Iota 3 lightcurves.

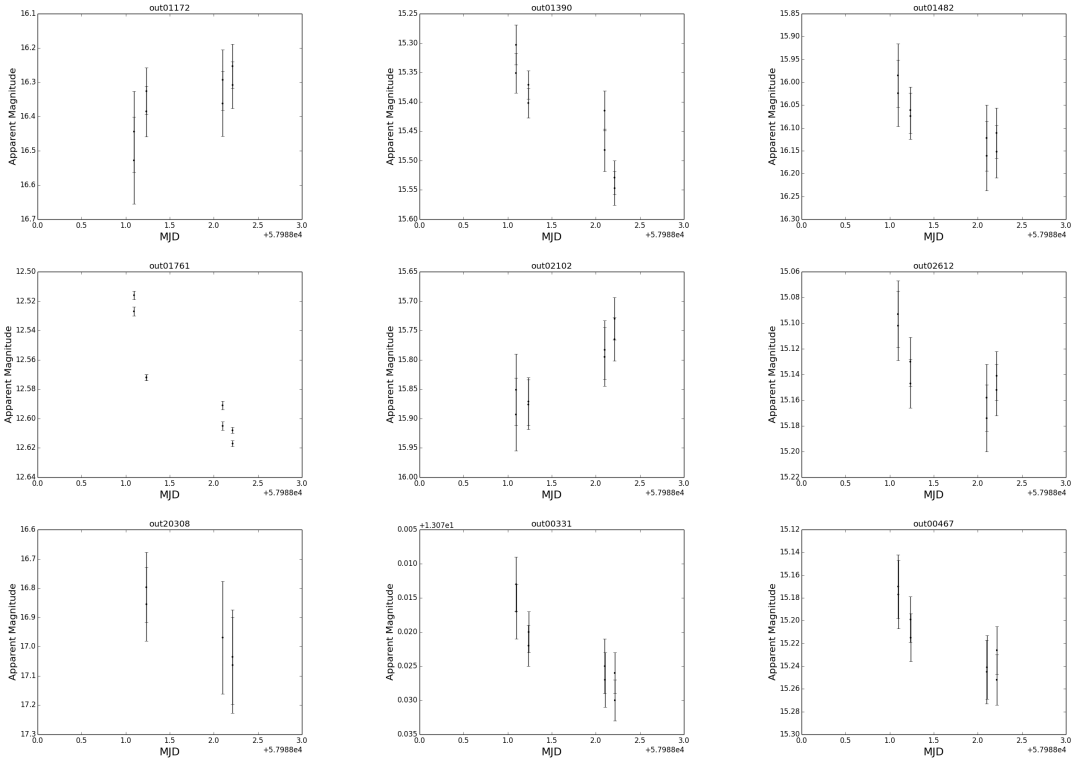

Figure E.24: Iota 3 cont. and Iota 4 lightcurves.

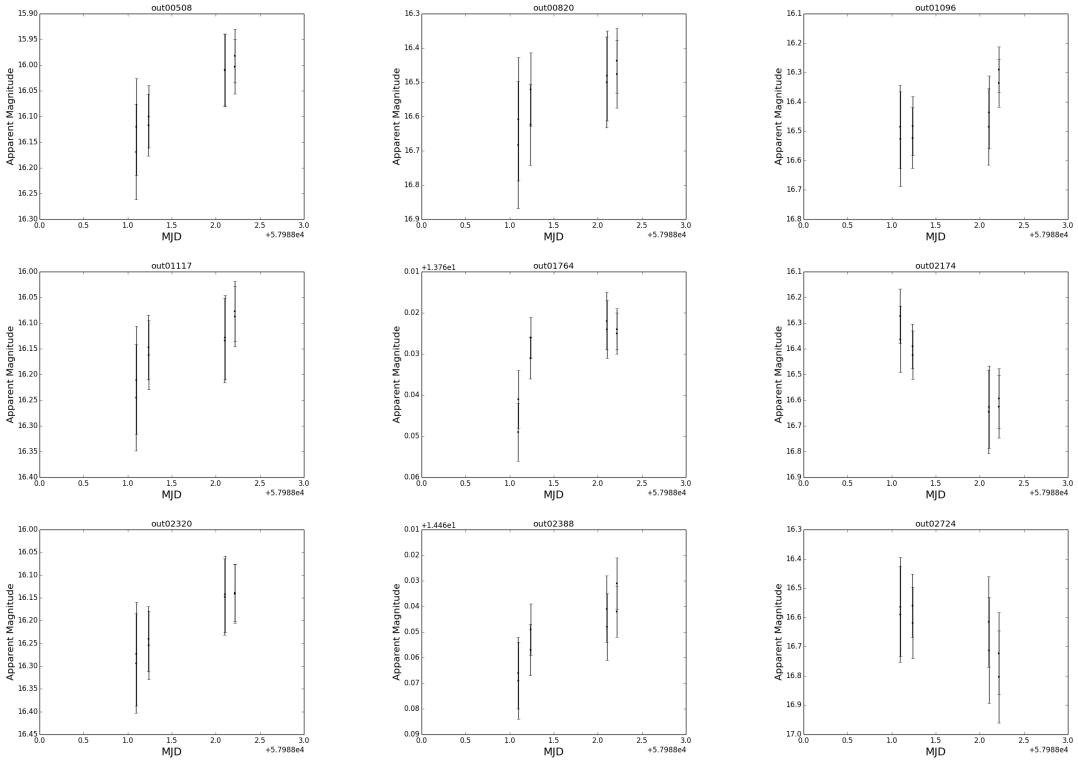

Figure E.25: Iota 4 cont. lightcurves.

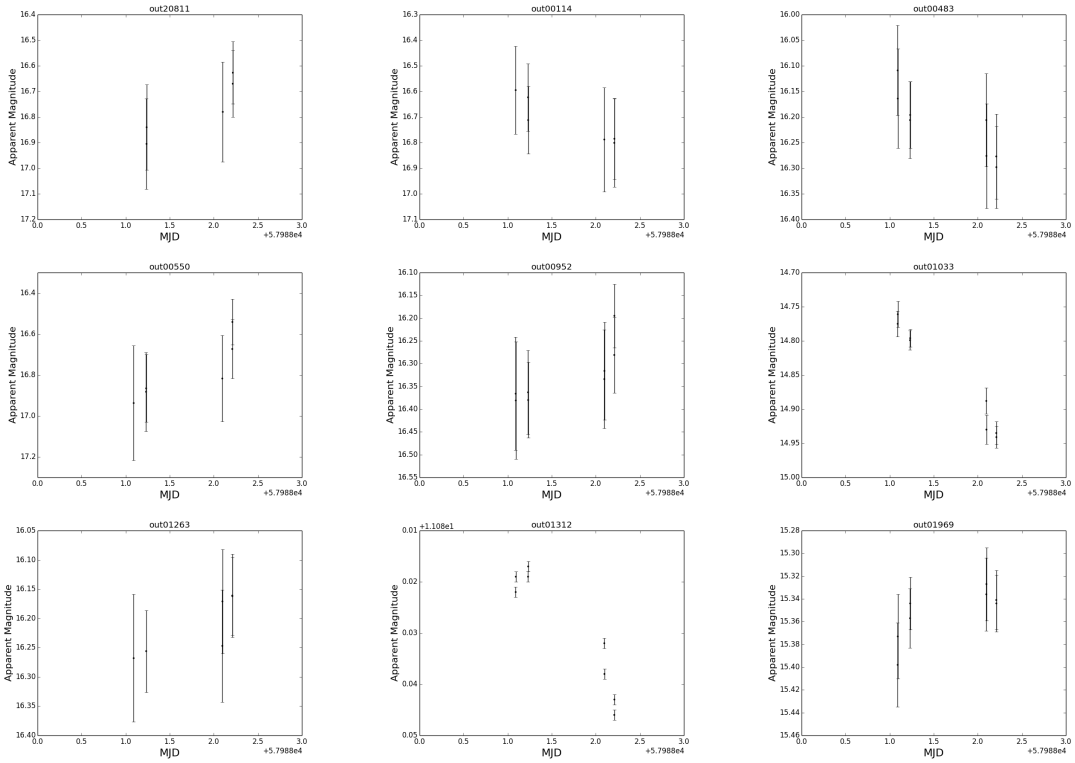

Figure E.26: Iota 4 cont. and Iota 5 lightcurves.

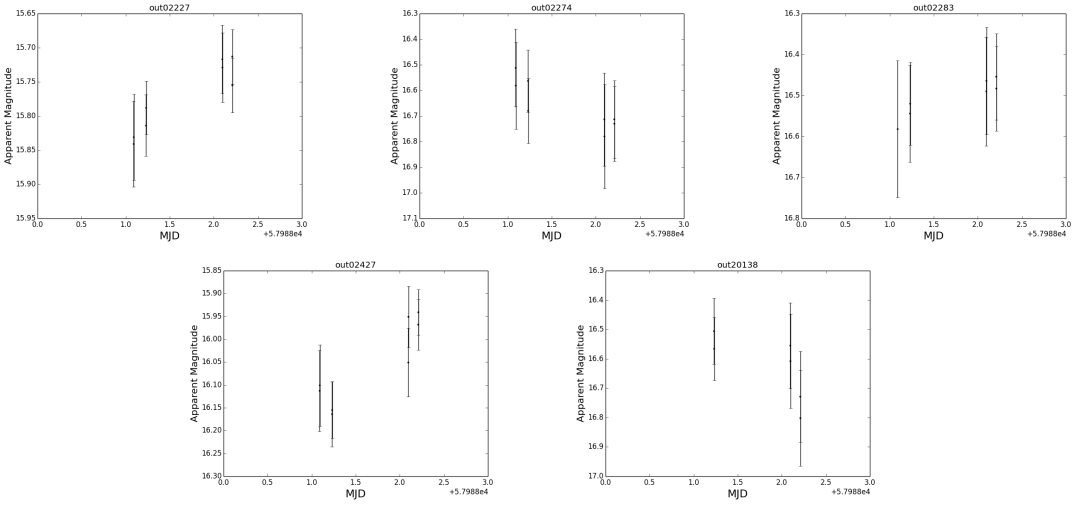

Figure E.27: Iota 5 cont. lightcurves.

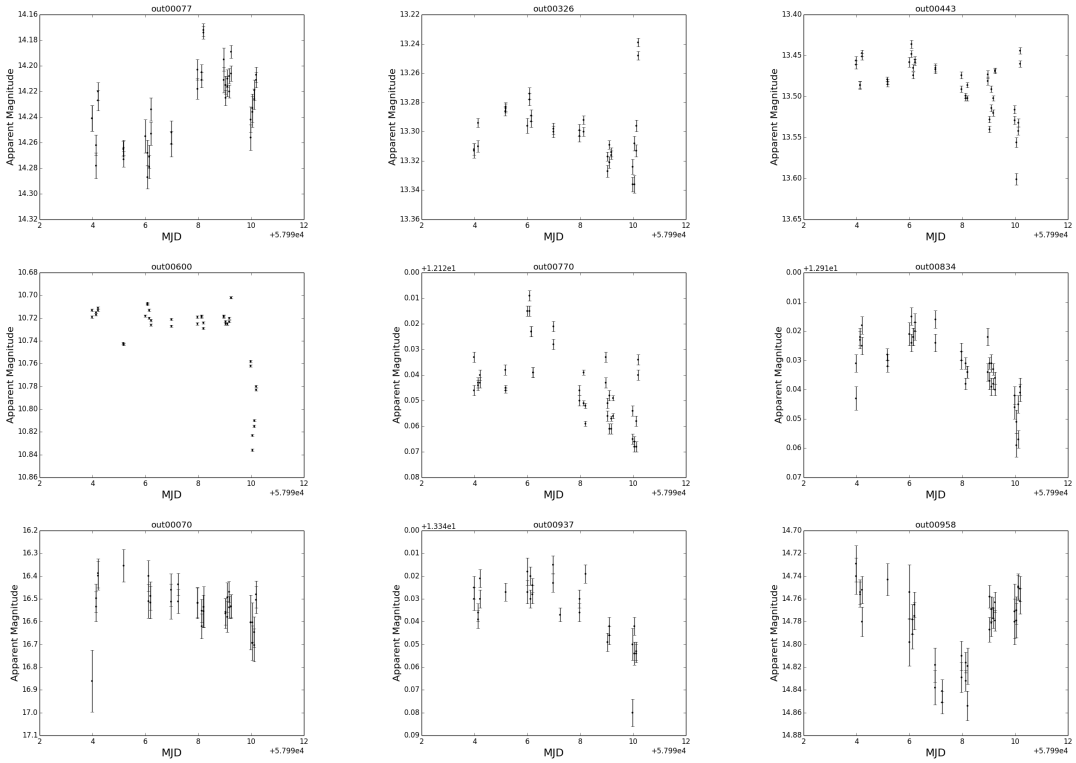

Figure E.28: Kappa 1 and Kappa 2 lightcurves.

Lightcurves from the Kappa follow-up.

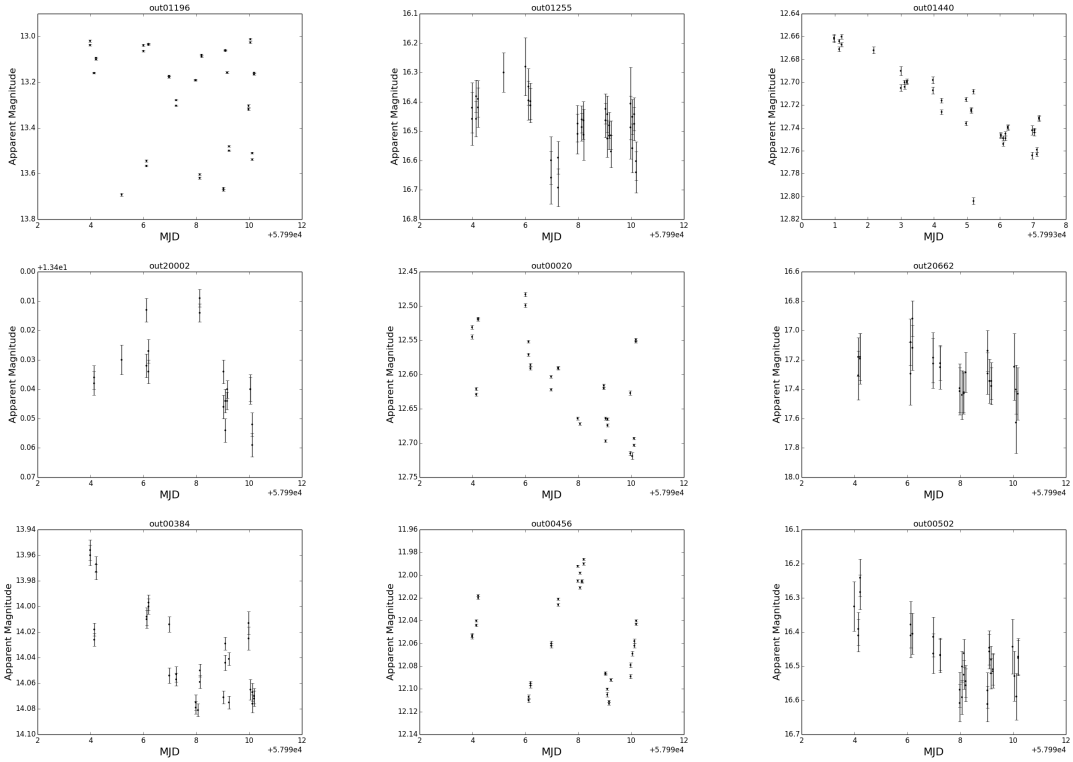

Figure E.29: Kappa 2 cont., Kappa 3 and Kappa 4 lightcurves.

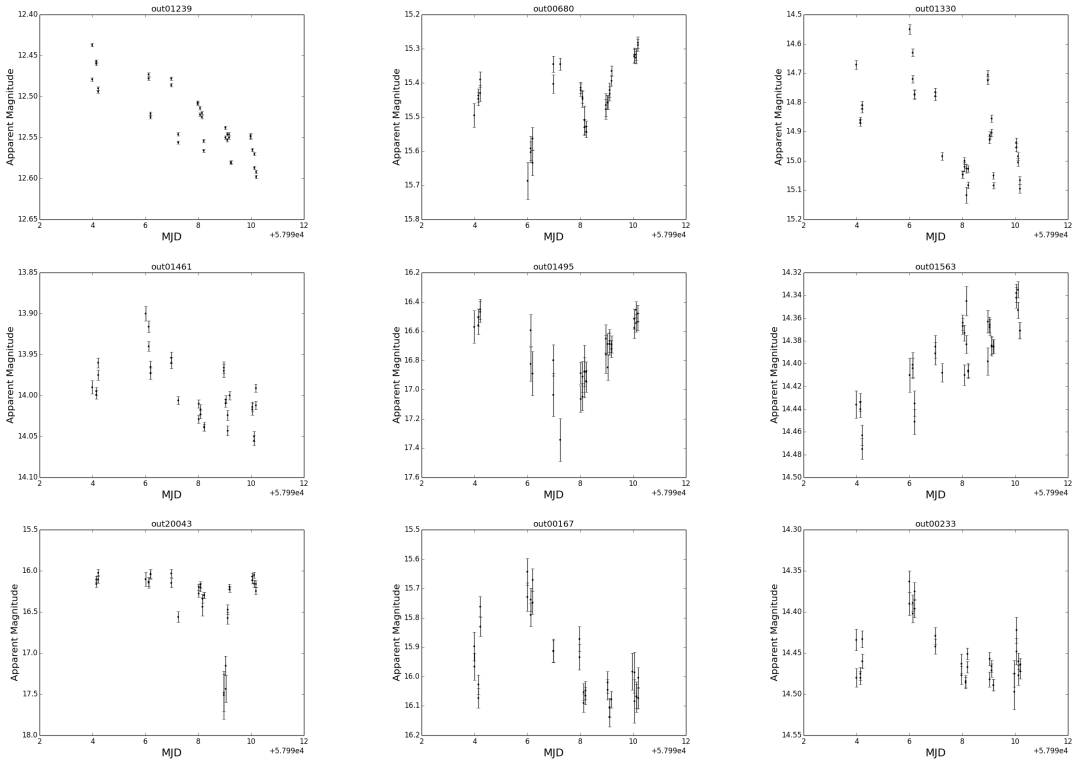

Figure E.30: Kappa 4 cont., Kappa 5 and Kappa 6 lightcurves.

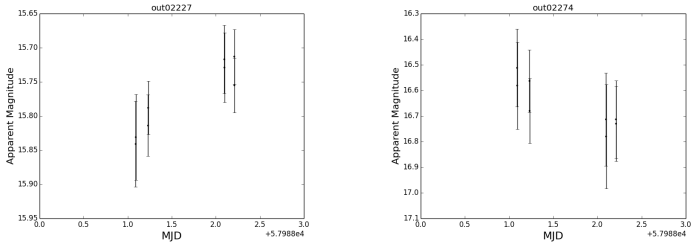

Figure E.31: Kappa 6 cont. lightcurves.

Appendix F

Variability Indices from VaST

Variability Indices from the Sigma, Nu, Iota and Kappa follow-ups

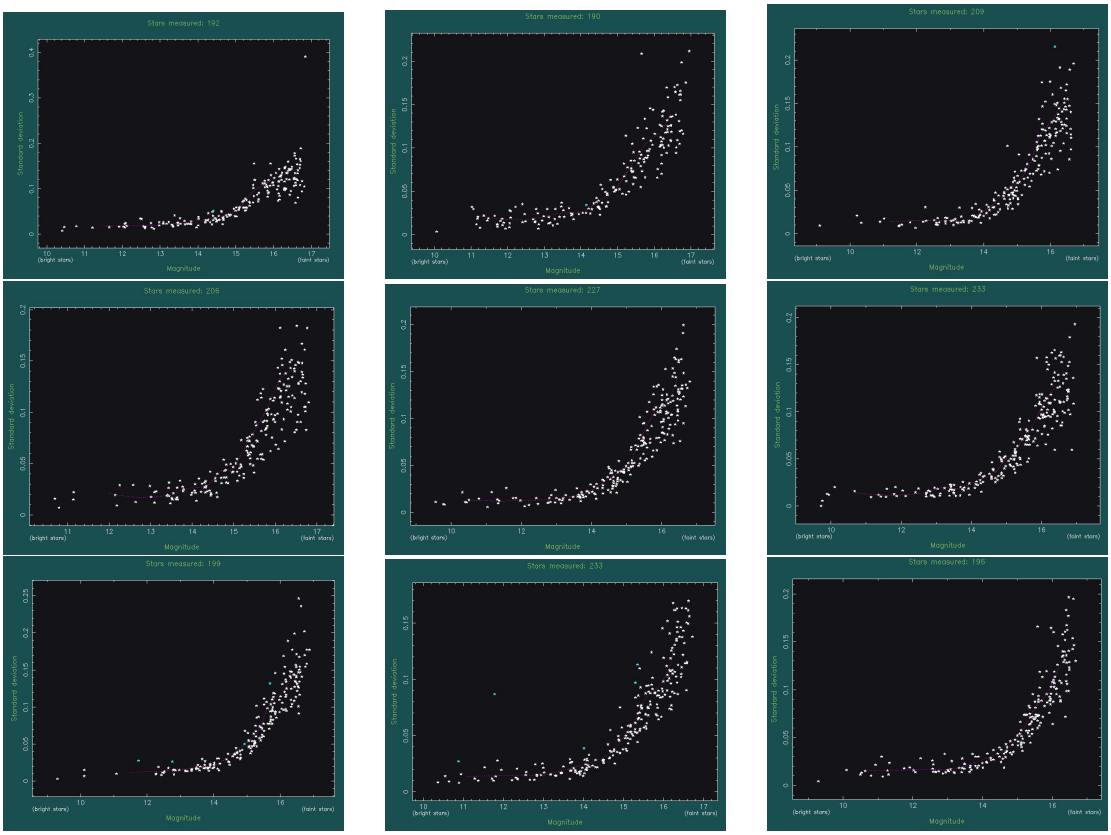

Figure F.1: Sigma 1-9, Standard Deviation variability indices.

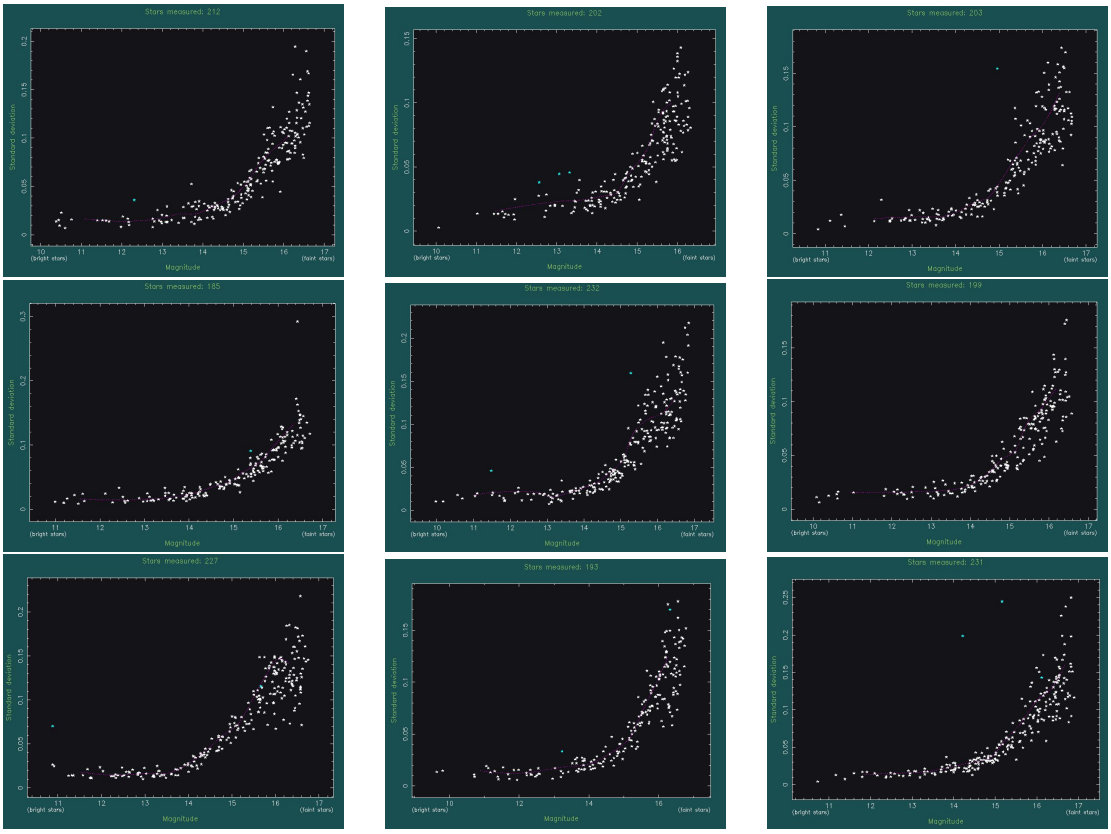

Figure F.2: Sigma 10-18, Standard Deviation variability indices.

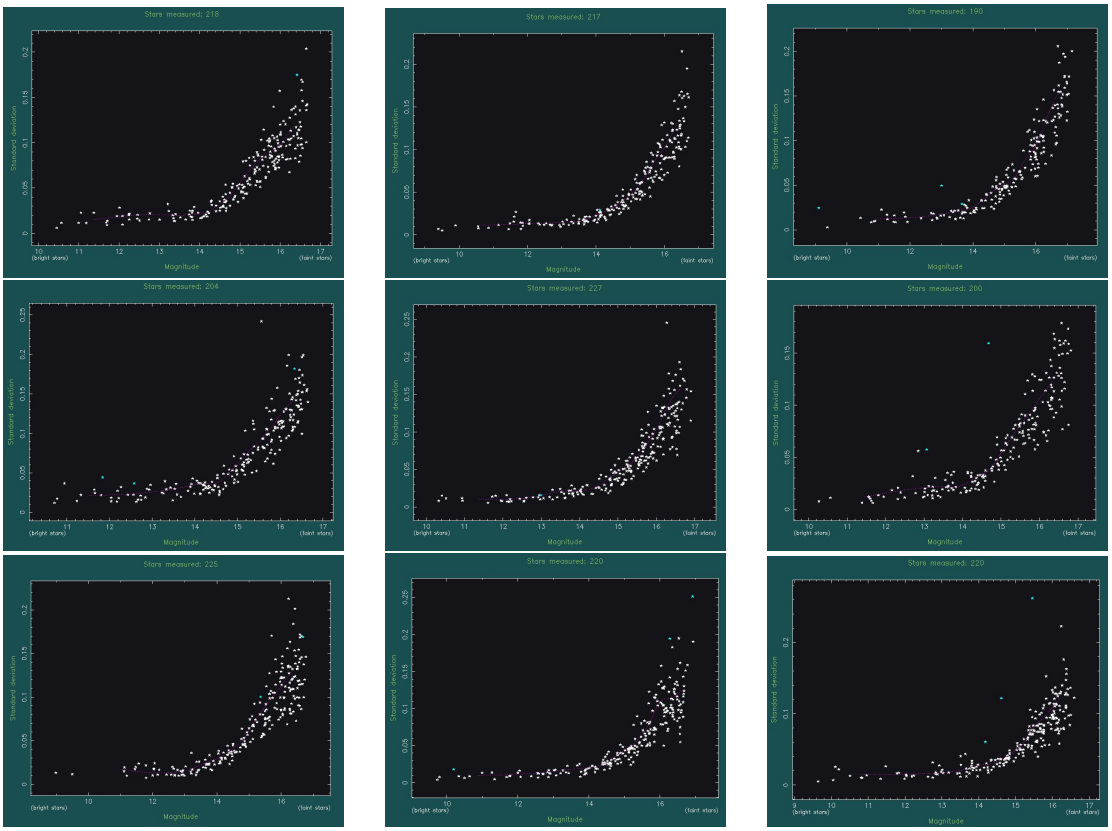

Figure F.3: Sigma 19-27, Standard Deviation variability indices.

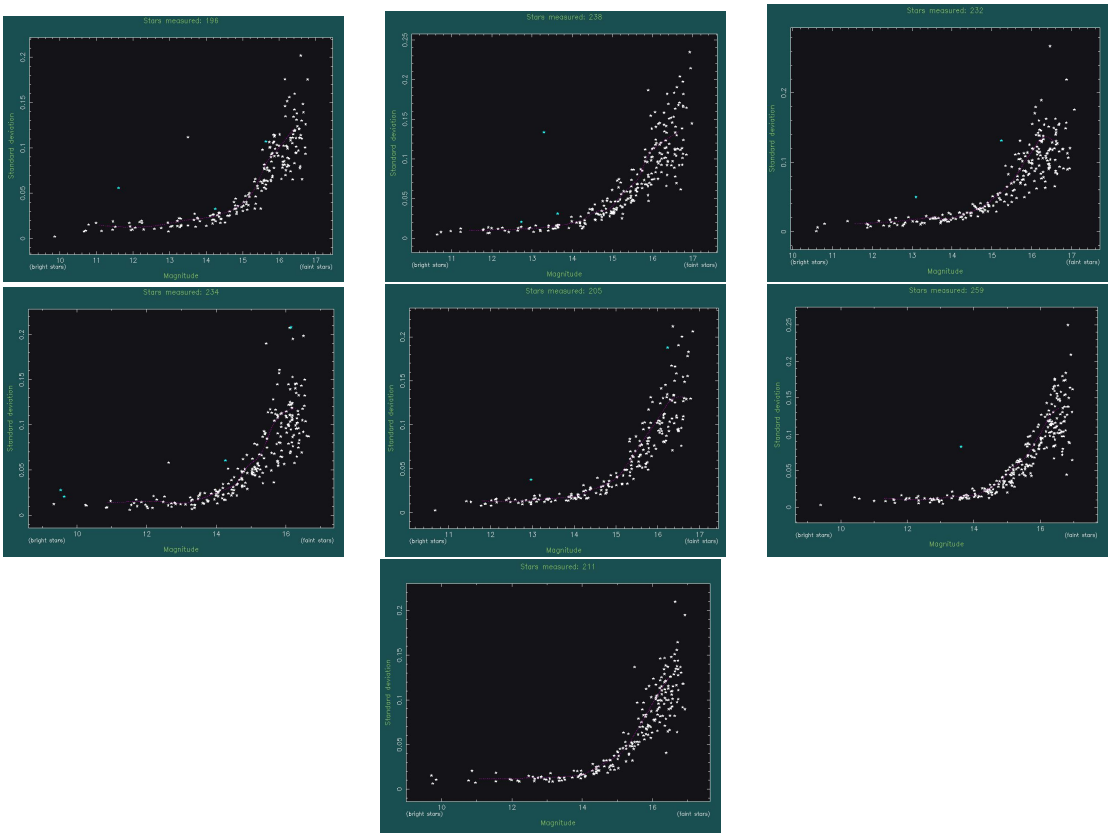

Figure F.4: Sigma 28-34, Standard Deviation variability indices.

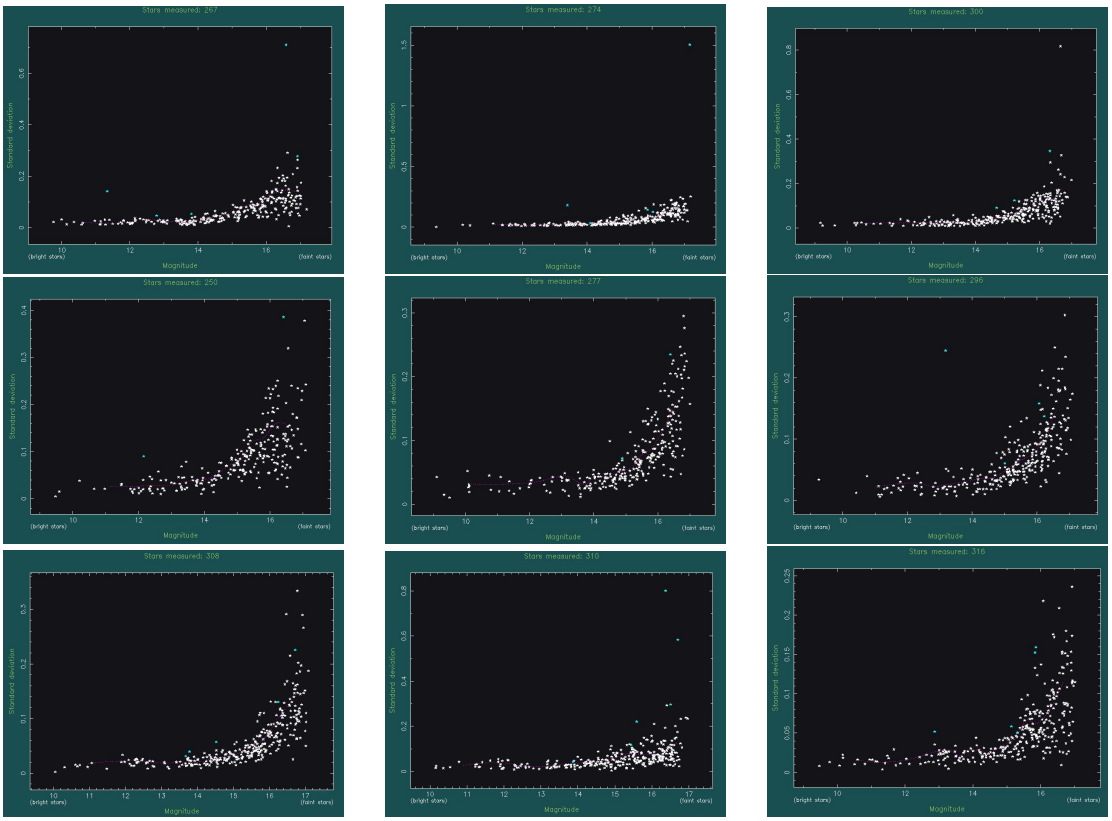

Figure F.5: Nu 8, 11, 13, 16, 17, 19, 21, 24 and 25 Standard Deviation variability indices.

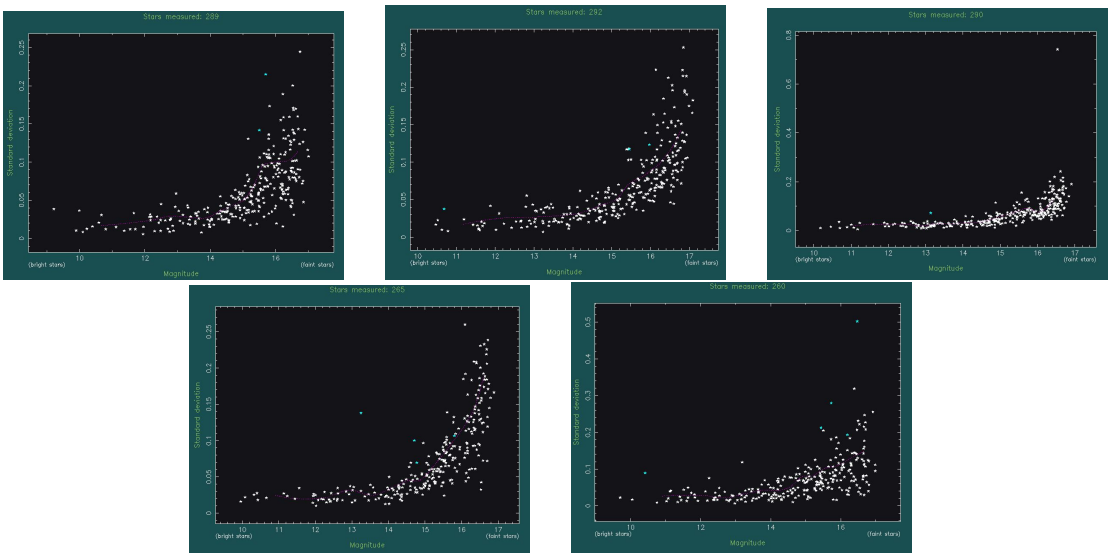

Figure F.6: Nu 28, 29, 30, 33 and 34 Standard Deviation variability indices.

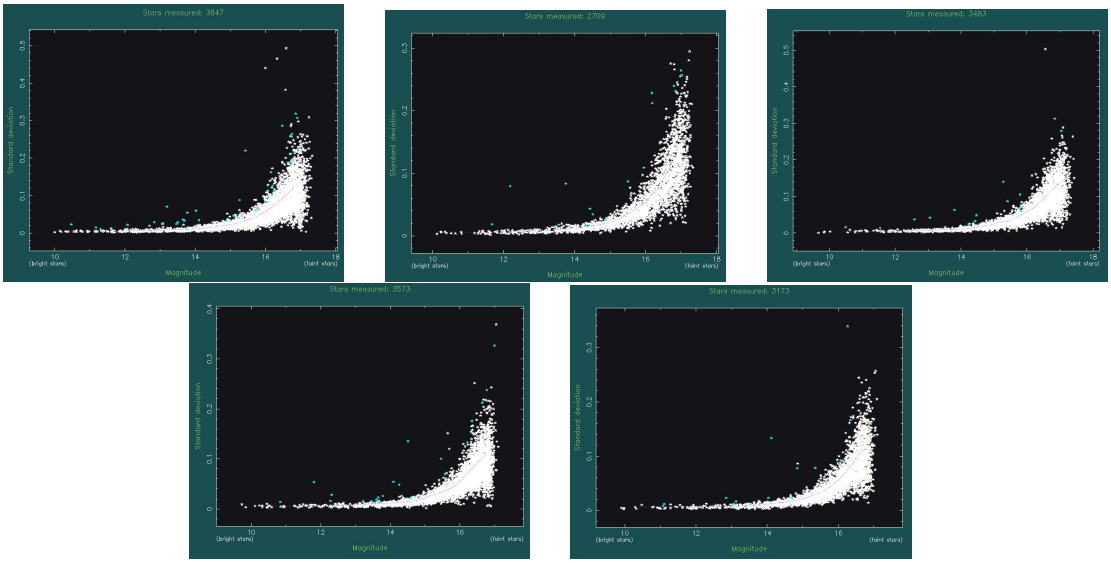

Figure F.7: Iota 1-5 Standard Deviation variability indices.

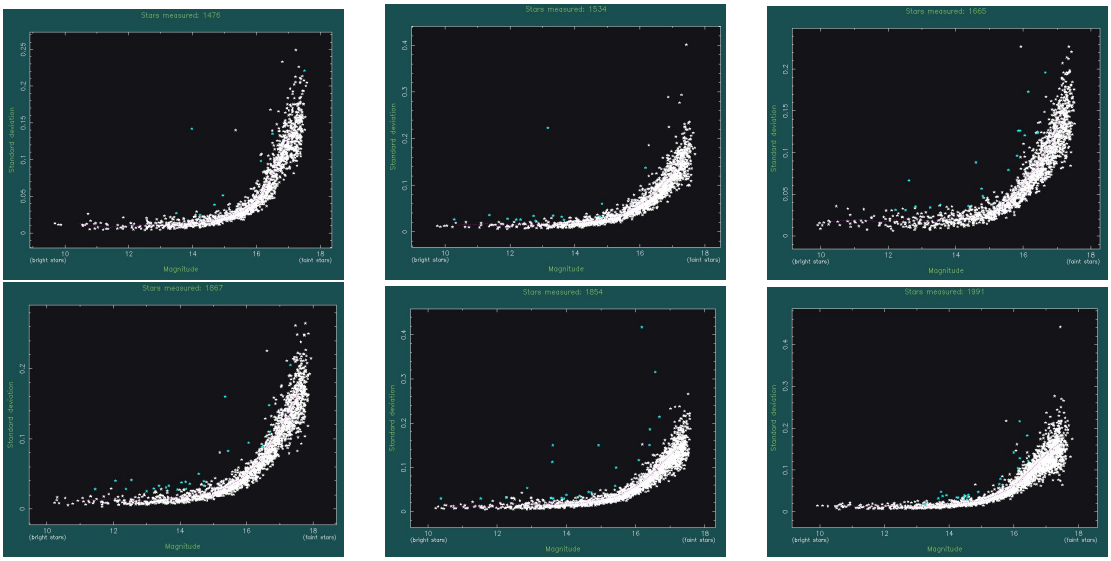

Figure F.8: Kappa 1-6 Standard Deviation variability indices.

Following on are 4 tables containing lists of the faintest stars in each field observed with PIRATE and the corresponding Signal to Noise Ratios (SNR).

Field	Magnitude	SD	SNR
Sigma 1	16.82	0.105	10.36
Sigma 2	16.97	0.212	5.13
Sigma 3	16.63	0.196	5.55
Sigma 4	16.77	0.182	5.98
Sigma 5	16.58	0.163	6.67
Sigma 6	16.99	0.193	5.63
Sigma 7	16.84	0.177	6.14
Sigma 8	16.60	0.156	6.97
Sigma 9	16.60	0.195	5.58
Sigma 10	16.64	0.147	7.39
Sigma 11	16.30	0.124	8.77
Sigma 12	16.68	0.133	8.17
Sigma 13	16.60	0.145	7.50
Sigma 14	16.79	0.204	5.33
Sigma 15	16.44	0.140	7.76
Sigma 16	16.58	0.173	6.29
Sigma 17	16.73	0.152	7.15
Sigma 18	16.88	0.198	5.49
Sigma 19	16.66	0.142	7.66
Sigma 20	16.69	0.161	6.75
Sigma 21	17.19	0.200	5.44
Sigma 22	16.58	0.156	6.97
Sigma 23	16.90	0.154	7.06

Field	Magnitude	SD	SNR
Sigma 24	16.69	0.173	6.29
Sigma 25	16.78	0.146	7.45
Sigma 26	16.91	0.190	5.72
Sigma 27	16.56	0.123	8.84
Sigma 28	16.74	0.176	6.18
Sigma 29	16.98	0.145	7.50
Sigma 30	17.04	0.176	6.18
Sigma 31	16.50	0.150	7.25
Sigma 32	16.87	0.206	5.28
Sigma 33	16.99	0.162	6.71
Sigma 34	16.87	0.195	5.58

Table F.1: List of the faintest detectable star in the Sigma fields.

Field	Magnitude	SD	SNR
Nu 8	17.07	0.278	3.91
Nu 11	17.16	0.254	4.28
Nu 13	16.89	0.216	5.03
Nu 16	17.11	0.243	4.48
Nu 17	16.94	0.198	5.49
Nu 19	17.05	0.174	6.25
Nu 21	17.05	0.188	5.78
Nu 24	16.91	0.234	4.65
Nu 25	16.96	0.174	6.25
Nu 28	16.89	0.143	7.60
Nu 29	17.01	0.183	5.94
Nu 30	16.89	0.190	5.72
Nu 33	16.72	0.226	4.81
Nu 34	16.85	0.256	4.25

Table F.2: List of the faintest detectable star in the Nu fields.

Field	Magnitude	SD	SNR
Iota 1	17.24	0.206	5.28
Iota 2	17.28	0.211	5.15
Iota 3	17.32	0.203	5.36
Iota 4	17.02	0.172	6.32
Iota 5	16.98	0.153	7.08

Table F.3: List of the faintest detectable star in the Iota fields.

Field	Magnitude	SD	SNR
Kappa 1	17.59	0.205	5.30
Kappa 2	17.62	0.0212	5.13
Kappa 3	17.47	0.185	5.88
Kappa 4	17.93	0.215	5.06
Kappa 5	17.54	0.188	5.78
Kappa 6	17.69	0.207	5.25

Table F.4: List of the faintest detectable star in the Kappa fields.

Appendix G

Bibliography

Aadland, E., P. Massey, K. F. Neugent, and M. R. Drout
2018. Shedding Light on the Isolation of Luminous Blue Variables. AJ, 156:294.

Aartsen, M. G., M. Ackermann, J. Adams, J. A. Aguilar, M. Ahlers, M. Ahrens, D. Altmann, T. Anderson, C. Arguelles, T. C. Arlen, and et al.
2014. Multimessenger search for sources of gravitational waves and high-energy neutrinos: Initial results for LIGO-Virgo and IceCube. *Phys. Rev. D*, 90(10):102002.

Aasi, J., J. Abadie, B. P. Abbott, R. Abbott, T. D. Abbott, M. Abernathy, T. Accadia, F. Acernese, C. Adams, T. Adams, and et al.
2013. Parameter estimation for compact binary coalescence signals with the first generation gravitational-wave detector network. Phys. Rev. D, 88(6):062001.

Abadie, J., B. P. Abbott, R. Abbott, T. D. Abbott, M. Abernathy, T. Accadia, F. Acernese, C. Adams, R. Adhikari, C. Affeldt, M. Agathos, K. Agatsuma, P. Ajith, B. Allen, E. Amador Ceron, D. Amariutei, S. B. Anderson, W. G. Anderson, K. Arai, M. A. Arain, M. C. Araya, S. M. Aston, P. Astone, D. Atkinson, P. Aufmuth, C. Aulbert, B. E. Aylott, S. Babak, P. Baker, G. Ballardin,

S. Ballmer, J. C. B. Barayoga, D. Barker, F. Barone, B. Barr, L. Barsotti, M. Barsuglia, M. A. Barton, I. Bartos, R. Bassiri, M. Bastarrika, A. Basti, J. Batch, J. Bauchrowitz, T. S. Bauer, M. Bebronne, D. Beck, B. Behnke, M. Bejger, M. G. Beker, A. S. Bell, A. Belletoile, I. Belopolski, M. Benacquista, J. M. Berliner, and et al.

2012. All-sky search for gravitational-wave bursts in the second joint ligo-virgo run. *Phys. Rev. D*, 85:122007.

Abadie, J., B. P. Abbott, R. Abbott, T. D. Abbott, M. Abernathy, T. Accadia, F. Acernese, C. Adams, R. X. Adhikari, C. Affeldt, and et al.

2012. Search for Gravitational Waves Associated with Gamma-Ray Bursts during LIGO Science Run 6 and Virgo Science Runs 2 and 3. ApJ, 760:12.

Abadie, J., B. P. Abbott, R. Abbott, T. Accadia, F. Acernese, R. Adhikari, P. Ajith, B. Allen, G. Allen, E. Amador Ceron, R. S. Amin, S. B. Anderson, W. G. Anderson, F. Antonucci, M. A. Arain, M. Araya, K. G. Arun, Y. Aso, S. Aston, P. Astone, P. Aufmuth, C. Aulbert, S. Babak, P. Baker, G. Ballardin, S. Ballmer, D. Barker, F. Barone, B. Barr, P. Barriga, L. Barsotti, M. Barsuglia, M. A. Barton, I. Bartos, R. Bassiri, M. Bastarrika, T. S. Bauer, B. Behnke, M. G. Beker, A. Belletoile, M. Benacquista, J. Betzwieser, P. T. Beyersdorf, S. Bigotta, I. A. Bilenko, G. Billingsley, S. Birindelli, R. Biswas, M. A. Bizouard, E. Black, J. K. Blackburn, L. Blackburn, D. Blair, B. Bland, M. Blom, C. Boccara, O. Bock, T. P. Bodiya, R. Bondarescu, F. Bondu, L. Bonelli, R. Bonnand, R. Bork, M. Born, S. Bose, L. Bosi, B. Bouhou, S. Braccini, C. Bradaschia, P. R. Brady, V. B. Braginsky, J. E. Brau, J. Breyer, D. O. Bridges, A. Brillet, M. Brinkmann, V. Brisson, M. Britzger, A. F. Brooks, D. A. Brown, and et al.

2010a. All-sky search for gravitational-wave bursts in the first joint ligo-geo-virgo run. *Phys. Rev. D*, 81:102001.

Abadie, J., B. P. Abbott, R. Abbott, T. Accadia, F. Acernese, R. Adhikari, P. Ajith, B. Allen, G. Allen, E. A. Ceron, R. S. Amin, S. B. Anderson, W. G. Anderson, F. Antonucci, S. Aoudia, M. A. Arain, M. Araya, K. G. Arun, Y. Aso, S. Aston, P. Astone, P. Aufmuth, C. Aulbert, S. Babak, P. Baker, G. Ballardin, S. Ballmer, D. Barker, F. Barone, B. Barr, P. Barriga, L. Barsotti, M. Barsuglia, M. A. Barton, I. Bartos, R. Bassiri, M. Bastarrika, T. S. Bauer, B. Behnke, M. G. Beker, A. Belletoile, M. Benacquista, J. Betzwieser, P. T. Beyersdorf, S. Bigotta, I. A. Bilenko, G. Billingsley, S. Birindelli, R. Biswas, M. A. Bizouard, E. Black, J. K. Blackburn, L. Blackburn, D. Blair, B. Bland, M. Blom, C. Boccara, O. Bock, T. P. Bodiya, R. Bondarescu, F. Bondu, L. Bonelli, R. Bonnand, R. Bork, M. Born, S. Bose, L. Bosi, S. Braccini, C. Bradaschia, P. R. Brady, V. B., and T. L. S. C. . T. V. Collaboration

2010b. Search for gravitational-wave inspiral signals associated with short gamma-ray bursts during ligo's fifth and virgo's first science run. *The Astrophysical Journal*, 715(2):1453.

Abbott, B., R. Abbott, R. Adhikari, A. Ageev, J. Agresti, P. Ajith, B. Allen, J. Allen, R. Amin, S. B. Anderson, W. G. Anderson, M. Araya, H. Armandula, M. Ashley, F. Asiri, P. Aufmuth, C. Aulbert, S. Babak, R. Balasubramanian, S. Ballmer, B. C. Barish, C. Barker, D. Barker, M. Barnes, B. Barr, M. A. Barton, K. Bayer, R. Beausoleil, and et al.

2005. Upper limits from the LIGO and TAMA detectors on the rate of gravitational-wave bursts. *Phys. Rev. D*, 72:122004.

Abbott, B., R. Abbott, R. Adhikari, A. Ageev, J. Agresti, P. Ajith, B. Allen, J. Allen, R. Amin, S. B. Anderson, W. G. Anderson, M. Araya, H. Armandula, M. Ashley, F. Asiri, P. Aufmuth, C. Aulbert, S. Babak, R. Balasubramanian, S. Ballmer, B. C. Barish, C. Barker, D. Barker, M. Barnes, B. Barr, M. A. Barton, K. Bayer,

R. Beausoleil, and et al.

2006. Joint LIGO and TAMA300 search for gravitational waves from inspiralling neutron star binaries. *Phys. Rev. D*, 73:102002.

Abbott, B., R. Abbott, R. Adhikari, A. Ageev, B. Allen, R. Amin, S. B. Anderson, W. G. Anderson, M. Araya, H. Armandula, and et al.

2004a. Detector description and performance for the first coincidence observations between LIGO and GEO. *Nuclear Instruments and Methods in Physics Research A*, 517:154–179.

Abbott, B., R. Abbott, R. Adhikari, A. Ageev, B. Allen, R. Amin, S. B. Anderson, W. G. Anderson, M. Araya, H. Armandula, and et al.

2004b. Setting upper limits on the strength of periodic gravitational waves from PSR J1939+2134 using the first science data from the GEO 600 and LIGO detectors. *Phys. Rev. D*, 69(8):082004.

Abbott, B., R. Abbott, R. Adhikari, A. Ageev, B. Allen, R. Amin, S. B. Anderson, W. G. Anderson, M. Araya, H. Armandula, and et al.

2005. Upper limits on gravitational wave bursts in ligo's second science run. *Phys. Rev. D*, 72:062001.

Abbott, B., R. Abbott, R. Adhikari, A. Ageev, B. Allen, R. Amin, S. B. Anderson, W. G. Anderson, M. Araya, H. Armandula, and et al.

2006. Search for gravitational-wave bursts in ligo's third science run. *Classical and Quantum Gravity*, 23(8):S29.

Abbott, B., R. Abbott, R. Adhikari, A. Ageev, B. Allen, R. Amin, S. B. Anderson, W. G. Anderson, M. Araya, H. Armandula, and et al.

2007. Search for gravitational-wave bursts in ligo data from the fourth science run. *Classical and Quantum Gravity*, 24(22):5343.

Abbott, B., R. Abbott, R. Adhikari, A. Ageev, B. Allen, R. Amin, S. B. Anderson, W. G. Anderson, M. Araya, H. Armandula, and et al.
2009. All-sky ligo search for periodic gravitational waves in the early fifth-science-run data. *Phys. Rev. Lett.*, 102:111102.

Abbott, B. P., R. Abbott, T. D. Abbott, M. R. Abernathy, F. Acernese, K. Ackley, C. Adams, T. Adams, P. Addesso, R. X. Adhikari, V. B. Adya, C. Affeldt, M. Agathos, K. Agatsuma, N. Aggarwal, O. D. Aguiar, L. Aiello, A. Ain, P. Ajith, B. Allen, A. Allocca, P. A. Altin, S. B. Anderson, W. G. Anderson, K. Arai, M. C. Araya, C. C. Arceneaux, J. S. Areeda, N. Arnaud, K. G. Arun, S. Ascenzi, G. Ashton, M. Ast, S. M. Aston, P. Astone, P. Aufmuth, and C. Aulbert
2016. Gw151226: Observation of gravitational waves from a 22-solar-mass binary black hole coalescence. *Phys. Rev. Lett.*, 116:241103.

Abbott, B. P., R. Abbott, T. D. Abbott, M. R. Abernathy, F. Acernese, K. Ackley, C. Adams, T. Adams, P. Addesso, R. X. Adhikari, and et al.
2016a. Localization and Broadband Follow-up of the Gravitational-wave Transient GW150914. ApJ, 826:L13.

Abbott, B. P., R. Abbott, T. D. Abbott, M. R. Abernathy, F. Acernese, K. Ackley, C. Adams, T. Adams, P. Addesso, R. X. Adhikari, and et al.
2016b. Observation of Gravitational Waves from a Binary Black Hole Merger. *Physical Review Letters*, 116(6):061102.

Abbott, B. P., R. Abbott, T. D. Abbott, M. R. Abernathy, F. Acernese, K. Ackley, C. Adams, T. Adams, P. Addesso, R. X. Adhikari, and et al.
2016c. Observing gravitational-wave transient GW150914 with minimal assumptions. Phys. Rev. D, 93(12):122004.

Abbott, B. P., R. Abbott, T. D. Abbott, M. R. Abernathy, F. Acernese, K. Ackley,

C. Adams, T. Adams, P. Addesso, R. X. Adhikari, and et al.
2016d. Prospects for Observing and Localizing Gravitational-Wave Transients with Advanced LIGO and Advanced Virgo. *Living Reviews in Relativity*, 19.

Abbott, B. P., R. Abbott, T. D. Abbott, S. Abraham, F. Acernese, K. Ackley, C. Adams, R. X. Adhikari, V. B. Adya, C. Affeldt, M. Agathos, K. Agatsuma, N. Aggarwal, O. D. Aguiar, L. Aiello, A. Ain, P. Ajith, G. Allen, A. Allocca, M. A. Aloy, P. A. Altin, A. Amato, A. Ananyeva, S. B. Anderson, W. G. Anderson, S. V. Angelova, S. Antier, S. Appert, K. Arai, M. C. Araya, J. S. Areeda, M. Arène, N. Arnaud, K. G. Arun, S. Ascenzi, G. Ashton, S. M. Aston, P. Astone, F. Aubin, P. Aufmuth, K. AultONeal, C. Austin, V. Avendano, A. Avila-Alvarez, S. Babak, and P. Bacon
2019. Low-Latency Gravitational Wave Alerts for Multi-Messenger Astronomy During the Second Advanced LIGO and Virgo Observing Run. *arXiv e-prints*, P. arXiv:1901.03310.

Abbott, B. P., R. Abbott, T. D. Abbott, F. Acernese, K. Ackley, C. Adams, T. Adams, P. Addesso, R. X. Adhikari, V. B. Adya, and et al.
2017a. GW170104: Observation of a 50-Solar-Mass Binary Black Hole Coalescence at Redshift 0.2. *Physical Review Letters*, 118(22):221101.

Abbott, B. P., R. Abbott, T. D. Abbott, F. Acernese, K. Ackley, C. Adams, T. Adams, P. Addesso, R. X. Adhikari, V. B. Adya, and et al.
2017b. GW170608: Observation of a 19 Solar-mass Binary Black Hole Coalescence. ApJ, 851:L35.

Abbott, B. P., R. Abbott, T. D. Abbott, F. Acernese, K. Ackley, C. Adams, T. Adams, P. Addesso, R. X. Adhikari, V. B. Adya, and et al.
2017c. GW170814: A Three-Detector Observation of Gravitational Waves from a Binary Black Hole Coalescence. *Physical Review Letters*, 119(14):141101.

Abbott, B. P., R. Abbott, T. D. Abbott, F. Acernese, K. Ackley, C. Adams, T. Adams, P. Addesso, R. X. Adhikari, V. B. Adya, and et al.
2017d. GW170817: Observation of Gravitational Waves from a Binary Neutron Star Inspiral. *Physical Review Letters*, 119(16):161101.

Adams, T., D. Buskulic, V. Germain, G. M. Guidi, F. Marion, M. Montani, B. Mours, F. Piergiovanni, and G. Wang
2016. Low-latency analysis pipeline for compact binary coalescences in the advanced gravitational wave detector era. *Classical and Quantum Gravity*, 33(17):175012.

Akerlof, C. W., R. L. Kehoe, T. A. McKay, E. S. Rykoff, D. A. Smith, D. E. Casperson, K. E. McGowan, W. T. Vestrand, P. R. Wozniak, J. A. Wren, M. C. B. Ashley, M. A. Phillips, S. L. Marshall, H. W. Epps, and J. A. Schier
2003. The ROTSE-III Robotic Telescope System. PASP, 115:132–140.

Allan, A., R. B. Denny, and J. Swinbank
2016. *VOEvent Transport Protocol*. International Virtual Observatory Alliance.

Allen, B., W. G. Anderson, P. R. Brady, D. A. Brown, and J. D. E. Creighton
2012. FINDCHIRP: An algorithm for detection of gravitational waves from inspiraling compact binaries. Phys. Rev. D, 85:122006.

ANTARES Collaboration, A. Albert, M. André, M. Anghinolfi, G. Anton, M. Ardid, J.-J. Aubert, T. Avgitas, B. Baret, J. Barrios-Martí, S. Basa, B. Belhorma, V. Bertin, S. Biagi, R. Bormuth, S. Bourret, M. C. Bouwhuis, H. Brânzaş, R. Bruijn, J. Brunner, J. Busto, A. Capone, L. Caramete, J. Carr, S. Celli, R. Cherkaoui El Moursli, T. Chiarusi, M. Circella, J. A. B. Coelho, A. Coleiro, R. Coniglione, H. Costantini, P. Coyle, A. Creusot, A. F. Díaz, A. Deschamps, G. De Bonis, C. Distefano, I. Di Palma, A. Domi, C. Donzaud, D. Dornic,

D. Drouhin, T. Eberl, I. El Bojaddaini, N. El Khayati, D. Elsässer, A. Enzenhöfer, A. Ettahiri, F. Fassi, I. Felis, L. A. Fusco, P. Gay, V. Giordano, H. Glotin, T. Grégoire, R. G. Ruiz, K. Graf, S. Hallmann, H. van Haren, A. J. Heijboer, Y. Hello, J. J. Hernández-Rey, J. Hößl, J. Hofestädt, C. Hugon, G. Illuminati, C. W. James, M. de Jong, M. Jongen, M. Kadler, O. Kalekin, U. Katz, D. Kießling, A. Kouchner, M. Kreter, I. Kreykenbohm, V. Kulikovskiy, C. Lachaud, R. Lahmann, D. Lefèvre, E. Leonora, M. Lotze, S. Loucatos, M. Marcelin, A. Margiotta, A. Marinelli, J. A. Martínez-Mora, R. Mele, K. Melis, T. Michael, P. Migliozzi, A. Moussa, S. Navas, E. Nezri, M. Organokov, G. E. Păvălaş, C. Pellegrino, C. Perrina, P. Piattelli, V. Popa, T. Pradier, L. Quinn, C. Racca, G. Riccobene, A. Sánchez-Losa, M. Saldaña, I. Salvadori, D. F. E. Samtleben, M. Sanguineti, P. Sapienza, F. Schüssler, C. Sieger, M. Spurio, T. Stolarczyk, M. Taiuti, Y. Tayalati, A. Trovato, D. Turpin, C. Tönnis, B. Vallage, V. Van Elewyck, F. Versari, D. Vivolo, A. Vizzoca, J. Wilms, J. D. Zornoza, and J. Zúñiga

2017. All-sky Search for High-Energy Neutrinos from Gravitational Wave Event GW170104 with the ANTARES Neutrino Telescope. *ArXiv e-prints*.

Arcavi, I., G. Hosseinzadeh, D. A. Howell, C. McCully, D. Poznanski, D. Kasen, J. Barnes, M. Zaltzman, S. Vasylyev, D. Maoz, and S. Valenti

2017. Optical emission from a kilonova following a gravitational-wave-detected neutron-star merger. Nature, 551:64–66.

Arnett, D.

1996. *Supernovae and Nucleosynthesis: An Investigation of the History of Matter from the Big Bang to the Present*.

Asplund, M., N. Grevesse, A. J. Sauval, and P. Scott

2009. The Chemical Composition of the Sun. ARA&A, 47:481–522.

Astone, P., S. Frasca, and G. Pizzella

2000. Background estimation in a gravitational wave experiment. *International Journal of Modern Physics D*, 9.

Astropy Collaboration, T. P. Robitaille, E. J. Tollerud, P. Greenfield, M. Droettboom, E. Bray, T. Aldcroft, M. Davis, A. Ginsburg, A. M. Price-Whelan, W. E. Kerzendorf, A. Conley, N. Crighton, K. Barbary, D. Muna, H. Ferguson, F. Grollier, M. M. Parikh, P. H. Nair, H. M. Unther, C. Deil, J. Woillez, S. Conseil, R. Kramer, J. E. H. Turner, L. Singer, R. Fox, B. A. Weaver, V. Zabalza, Z. I. Edwards, K. Azalee Bostroem, D. J. Burke, A. R. Casey, S. M. Crawford, N. Dencheva, J. Ely, T. Jenness, K. Labrie, P. L. Lim, F. Pierfederici, A. Pontzen, A. Ptak, B. Refsdal, M. Servillat, and O. Streicher

2013. Astropy: A community Python package for astronomy. *Astronomy and Astrophysics*, 558:A33.

Bailer-Jones, C. A. L., J. Rybizki, M. Fouesneau, G. Mantelet, and R. Andrae

2018. Estimating Distance from Parallaxes. IV. Distances to 1.33 Billion Stars in Gaia Data Release 2. AJ, 156:58.

Barthelmy, S.

2015. GCN notices. NASA (Website). URL: http://gcn.gsfc.nasa.gov/lvc.htmltc1.

Belczynski, K., D. E. Holz, T. Bulik, and R. O'Shaughnessy

2016. The first gravitational-wave source from the isolated evolution of two stars in the 40-100 solar mass range. Nature, 534:512–515.

Bertin, E. and S. Arnouts

1996. SExtractor: Software for source extraction. A&AS, 117:393–404.

Bibby, J. L. and P. A. Crowther

2010. A Very Large Telescope imaging and spectroscopic survey of the Wolf-Rayet population in NGC7793. MNRAS, 405:2737–2753.

Boss, A. P. and S. A. Keiser

2010. Who Pulled the Trigger: A Supernova or An Asymptotic Giant Branch Star? ApJ, 717:L1–L5.

Buonanno, A. and T. Damour

2000. Transition from inspiral to plunge in binary black hole coalescences. Phys. Rev. D, 62(6):064015.

Burggraf, B., K. Weis, D. J. Bomans, and M. Henze

2011. Var C: (Semi-)Periodic Long-Term Variability. *Bulletin de la Societe Royale des Sciences de Liege*, 80:356–360.

Burggraf, B., K. Weis, D. J. Bomans, M. Henze, H. Meusinger, O. Sholukhova, A. Zharova, A. Pellerin, and A. Becker

2015. Var C: Long-term photometric and spectral variability of a luminous blue variable in M 33. A&A, 581:A12.

Busuttil, R.

2016. *Investigating exoplanets and transients using small-aperture telescopes*. PhD thesis, The Open University, Milton Keynes.

Camp, J. B. and N. J. Cornish

2004. Gravitational Wave Astronomy. *Annual Review of Nuclear and Particle Science*, 54:525–577.

Cannon, A. J. and E. C. Pickering

1918. The Henry Draper catalogue 0h, 1h, 2h, and 3h. *Annals of Harvard College Observatory*, 91:1–290.

Cannon, K., R. Cariou, A. Chapman, M. Crispin-Ortuzar, N. Fotopoulos, M. Frei, C. Hanna, E. Kara, D. Keppel, L. Liao, S. Privitera, A. Searle, L. Singer, and

A. Weinstein

2012. Toward Early-warning Detection of Gravitational Waves from Compact Binary Coalescence. ApJ, 748:136.

Canton T. D., T. et al.

2014. Implementing a search for aligned-spin neutron star-black hole systems with advanced ground based gravitational wave detectors. *Phys. Rev.*, D90(8):082004.

Chromey, F. R. and D. A. Hasselbacher

1996. The Flat Sky: Calibration and Background Uniformity in Wide Field Astronomical Images. PASP, 108:944.

Chu, Q., E. J. Howell, A. Rowlinson, H. Gao, B. Zhang, S. J. Tingay, M. Boër, and L. Wen

2016. Capturing the electromagnetic counterparts of binary neutron star mergers through low-latency gravitational wave triggers. *Mon. Not. R. Astron. Soc.*, 459:121–139.

Clark, J. S., N. Castro, M. Garcia, A. Herrero, F. Najarro, I. Negueruela, B. W. Ritchie, and K. T. Smith

2012. On the nature of candidate luminous blue variables in M 33. *Astronomy and Astrophysics*, 541:A146.

Clark, J. S., P. A. Crowther, V. M. Larionov, I. A. Steele, B. W. Ritchie, and A. A. Arkharov

2009. Bolometric luminosity variations in the luminous blue variable ¡ASTROBJ¿AFGL2298¡/ASTROBJ¿. A&A, 507:1555–1565.

Clark, J. S., M. P. Egan, P. A. Crowther, D. R. Mizuno, V. M. Larionov, and

A. Arkharov

2003. Dusty ring nebulae around new candidate Luminous Blue Variables. A&A, 412:185–198.

Clark, J. S., V. M. Larionov, and A. Arkharov

2005. On the population of galactic Luminous Blue Variables. *Astronomy and Astrophysics*, 435:239–246.

Clark, J. S., M. E. Lohr, F. Najarro, H. Dong, and F. Martins

2018. The Arches cluster revisited. I. Data presentation and stellar census. A&A, 617:A65.

Connaughton, V., E. Burns, A. Goldstein, L. Blackburn, M. S. Briggs, N. Christensen, C. M. Hui, D. Kocevski, T. Littenberg, J. E. McEnery, J. Racusin, P. Shawhan, J. Veitch, C. A. Wilson-Hodge, P. N. Bhat, E. Bissaldi, W. Cleveland, M. M. Giles, M. H. Gibby, A. von Kienlin, R. M. Kippen, S. McBreen, C. A. Meegan, W. S. Paciesas, R. D. Preece, O. J. Roberts, M. Stanbro, and P. Veres

2018. On the Interpretation of the Fermi-GBM Transient Observed in Coincidence with LIGO Gravitational-wave Event GW150914. ApJ, 853:L9.

Conti, P. S.

1984. Basic Observational Constraints on the Evolution of Massive Stars. In *Observational Tests of the Stellar Evolution Theory*, A. Maeder and A. Renzini, eds., volume 105 of *IAU Symposium*, P. 233.

Copperwheat, C. M. and I. A. Steele

2017. GCN Circular 21755. GRB Coordinates Network.

Cornish, N. J. and T. B. Littenberg

2015. Bayeswave: Bayesian inference for gravitational wave bursts and instrument glitches. *Classical and Quantum Gravity*, 32(13):135012.

Corral, L. J.

1996. LBV-Type Stars in M33. AJ, 112:1450.

Coulter, D. A., R. J. Foley, C. D. Kilpatrick, M. R. Drout, A. L. Piro, B. J. Shappee, M. R. Siebert, J. D. Simon, N. Ulloa, D. Kasen, B. F. Madore, A. Murguia-Berthier, Y.-C. Pan, J. X. Prochaska, E. Ramirez-Ruiz, A. Rest, and C. Rojas-Bravo

2017. Swope Supernova Survey 2017a (SSS17a), the optical counterpart to a gravitational wave source. *Science*, 358:1556–1558.

Crowther, P.

2012. Birth, life and death of massive stars. *Astronomy and Geophysics*, 53(4):4.30–4.36.

Crowther, P. A.

2004. Fundamental parameters of massive stars. In *EAS Publications Series*, M. Heydari-Malayeri, P. Stee, and J.-P. Zahn, eds., volume 13 of *EAS Publications Series*, Pp. 1–20.

Crowther, P. A., T. Szeifert, O. Stahl, and F. J. Zickgraf

1997. B 517 - Another very late WNL star in M 33. A&A, 318:543–547.

Cutri, R. M., M. F. Skrutskie, S. van Dyk, C. A. Beichman, J. M. Carpenter, T. Chester, L. Cambresy, T. Evans, J. Fowler, J. Gizis, E. Howard, J. Huchra, T. Jarrett, E. L. Kopan, J. D. Kirkpatrick, R. M. Light, K. A. Marsh, H. McCallon, S. Schneider, R. Stiening, M. Sykes, M. Weinberg, W. A. Wheaton, S. Wheelock, and N. Zacarias

2003. VizieR Online Data Catalog: 2MASS All-Sky Catalog of Point Sources (Cutri+ 2003). *VizieR Online Data Catalog*, P. II/246.

D'Avanzo, P.

2015. Short gamma-ray bursts: A review. *Journal of High Energy Astrophysics*, 7:73 – 80. Swift 10 Years of Discovery, a novel approach to Time Domain Astronomy.

Davidson, K. and R. M. Humphreys, eds.

2012a. *Eta Carinae and the Supernova Impostors*, volume 384 of *Astrophysics and Space Science Library*.

Davidson, K. and R. M. Humphreys

2012b. The Great Eruption of η Carinae. Nature, 486:E1.

de Mink, S. E., H. Sana, N. Langer, R. G. Izzard, and F. R. N. Schneider

2014. The Incidence of Stellar Mergers and Mass Gainers among Massive Stars. ApJ, 782:7.

Drever, R. W. P., J. Hough, R. Bland, and G. W. Lessnoff

1973. Search for Short Bursts of Gravitational Radiation. Nature, 246:340–344.

Dwarkadas, V. V.

2011. On luminous blue variables as the progenitors of core-collapse supernovae, especially Type IIn supernovae. MNRAS, 412:1639–1649.

Einstein, A.

1905. Zur Elektrodynamik bewegter Körper. (German) [On the electrodynamics of moving bodies]. *Annalen der Physik (1900) (series 4)*, 322(10):891–921.

Einstein, A.

1916. Die Grundlagen der Allgemeinene Relativitätstheorie. (German) [The foundations of the Theory of General Relativity]. *Annalen der Physik (1900) (series 4)*, 354(7):769–822.

Einstein, A.

1918. Über Gravitationswellen. (German) [On gravitational waves]. *Ständiger Beobachter der Preussischen Akademie der Wissenschaften, Part 1*, Pp. 154–167.

Ekström, S., C. Georgy, P. Eggenberger, G. Meynet, N. Mowlavi, A. Wyttenbach, A. Granada, T. Decressin, R. Hirschi, U. Frischknecht, C. Charbonnel, and A. Maeder

2012. Grids of stellar models with rotation. I. Models from 0.8 to 120 M at solar metallicity (Z = 0.014). A&A, 537:A146.

Emery, S.

2017. GCN Circular 21758. GRB Coordinates Network.

Essick, R., S. Vitale, E. Katsavounidis, G. Vedovato, and S. Klimenko

2015. Localization of Short Duration Gravitational-wave Transients with the Early Advanced LIGO and Virgo Detectors. ApJ, 800:81.

Fairhurst, S.

2014. Improved source localization with LIGO-India. In *Journal of Physics Conference Series*, volume 484 of *Journal of Physics Conference Series*, P. 012007.

Fenech, D. M., J. S. Clark, R. K. Prinja, S. Dougherty, F. Najarro, I. Negueruela, A. Richards, B. W. Ritchie, and H. Andrews

2018. An ALMA 3 mm continuum census of Westerlund 1. A&A, 617:A137.

Filippenko, A. V.

1997. Optical Spectra of Supernovae. ARA&A, 35:309–355.

Freedman, W. L., B. F. Madore, B. K. Gibson, L. Ferrarese, D. D. Kelson, S. Sakai, J. R. Mould, R. C. Kennicutt, Jr., H. C. Ford, J. A. Graham, J. P. Huchra,

S. M. G. Hughes, G. D. Illingworth, L. M. Macri, and P. B. Stetson
2001. Final Results from the Hubble Space Telescope Key Project to Measure the Hubble Constant. ApJ, 553:47–72.

Gaia Collaboration, T. Prusti, J. H. J. de Bruijne, A. G. A. Brown, A. Vallenari, C. Babusiaux, C. A. L. Bailer-Jones, U. Bastian, M. Biermann, D. W. Evans, L. Eyer, F. Jansen, C. Jordi, S. A. Klioner, U. Lammers, L. Lindegren, X. Luri, F. Mignard, D. J. Milligan, C. Panem, V. Poinsignon, D. Pourbaix, S. Randich, G. Sarri, P. Sartoretti, H. I. Siddiqui, C. Soubiran, V. Valette, F. van Leeuwen, N. A. Walton, C. Aerts, F. Arenou, M. Cropper, R. Drimmel, E. Høg, D. Katz, M. G. Lattanzi, W. O'Mullane, E. K. Grebel, A. D. Holland, C. Huc, X. Passot, L. Bramante, C. Cacciari, J. Castañeda, L. Chaoul, N. Cheek, F. De Angeli, C. Fabricius, R. Guerra, J. Hernández, A. Jean-Antoine-Piccolo, E. Masana, R. Messineo, N. Mowlavi, K. Nienartowicz, D. Ordóñez- Blanco, P. Panuzzo, J. Portell, P. J. Richards, M. Riello, G. M. Seabroke, P. Tanga, F. Thévenin, J. Torra, S. G. Els, G. Gracia- Abril, G. Comoretto, M. Garcia-Reinaldos, T. Lock, E. Mercier, M. Altmann, R. Andrae, T. L. Astraatmadja, I. Bellas-Velidis, K. Benson, J. Berthier, R. Blomme, G. Busso, B. Carry, A. Cellino, G. Clementini, S. Cowell, O. Creevey, J. Cuypers, M. Davidson, J. De Ridder, A. de Torres, L. Delchambre, A. Dell'Oro, C. Ducourant, Y. Frémat, M. García-Torres, E. Gosset, J. L. Halbwachs, N. C. Hambly, D. L. Harrison, M. Hauser, D. Hestroffer, S. T. Hodgkin, H. E. Huckle, A. Hutton, G. Jasniewicz, S. Jordan, M. Kontizas, A. J. Korn, A. C. Lanzafame, M. Manteiga, A. Moitinho, K. Muinonen, J. Osinde, E. Pancino, T. Pauwels, J. M. Petit, A. Recio-Blanco, A. C. Robin, L. M. Sarro, C. Siopis, M. Smith, K. W. Smith, A. Sozzetti, W. Thuillot, W. van Reeven, Y. Viala, U. Abbas, A. Abreu Aramburu, S. Accart, J. J. Aguado, P. M. Allan, W. Allasia, G. Altavilla, M. A. Álvarez, J. Alves, R. I. Anderson, A. H. Andrei, E. Anglada Varela, E. Antiche, T. Antoja, S. Antón, B. Ar-

cay, A. Atzei, L. Ayache, N. Bach, S. G. Baker, L. Balaguer-Núñez, C. Barache, C. Barata, A. Barbier, F. Barblan, M. Baroni, D. Barrado y Navascués, M. Barros, M. A. Barstow, U. Becciani, M. Bellazzini, G. Bellei, A. Bello García, V. Belokurov, P. Bendjoya, A. Berihuete, L. Bianchi, O. Bienaymé, F. Billebaud, N. Blagorodnova, S. Blanco-Cuaresma, T. Boch, A. Bombrun, R. Borrachero, S. Bouquillon, G. Bourda, H. Bouy, A. Bragaglia, M. A. Breddels, N. Brouillet, T. Brüsemeister, B. Bucciarelli, F. Budnik, P. Burgess, R. Burgon, A. Burlacu, D. Busonero, R. Buzzi, E. Caffau, J. Cambras, H. Campbell, R. Cancelliere, T. Cantat-Gaudin, T. Carlucci, J. M. Carrasco, M. Castellani, P. Charlot, J. Charnas, P. Charvet, F. Chassat, A. Chiavassa, M. Clotet, G. Cocozza, R. S. Collins, P. Collins, G. Costigan, F. Crifo, N. J. G. Cross, M. Crosta, C. Crowley, C. Dafonte, Y. Damerdji, A. Dapergolas, P. David, M. David, P. De Cat, F. de Felice, P. de Laverny, F. De Luise, R. De March, D. de Martino, R. de Souza, J. Debosscher, E. del Pozo, M. Delbo, A. Delgado, H. E. Delgado, F. di Marco, P. Di Matteo, S. Diakite, E. Distefano, C. Dolding, S. Dos Anjos, P. Drazinos, J. Durán, Y. Dzigan, E. Ecale, B. Edvardsson, H. Enke, M. Erdmann, D. Escolar, M. Espina, N. W. Evans, G. Eynard Bontemps, C. Fabre, M. Fabrizio, S. Faigler, A. J. Falcão, M. Farràs Casas, F. Faye, L. Federici, G. Fedorets, J. Fernández-Hernández, P. Fernique, A. Fienga, F. Figueras, F. Filippi, K. Findeisen, A. Fonti, M. Fouesneau, E. Fraile, M. Fraser, J. Fuchs, R. Furnell, M. Gai, S. Galleti, L. Galluccio, D. Garabato, F. García-Sedano, P. Garé, A. Garofalo, N. Garralda, P. Gavras, J. Gerssen, R. Geyer, G. Gilmore, S. Girona, G. Giuffrida, M. Gomes, A. González-Marcos, J. González-Núñez, J. J. González-Vidal, M. Granvik, A. Guerrier, P. Guillout, J. Guiraud, A. Gúrpide, R. Gutiérrez-Sánchez, L. P. Guy, R. Haigron, D. Hatzidimitriou, M. Haywood, U. Heiter, A. Helmi, D. Hobbs, W. Hofmann, B. Holl, G. Holland, J. A. S. Hunt, A. Hypki, V. Icardi, M. Irwin, G. Jevardat de Fombelle, P. Jofré, P. G. Jonker, A. Jorissen,

F. Julbe, A. Karampelas, A. Kochoska, R. Kohley, K. Kolenberg, E. Kontizas, S. E. Koposov, G. Kordopatis, P. Koubsky, A. Kowalczyk, A. Krone-Martins, M. Kudryashova, I. Kull, R. K. Bachchan, F. Lacoste-Seris, A. F. Lanza, J. B. Lavigne, C. Le Poncin-Lafitte, Y. Lebreton, T. Lebzelter, S. Leccia, N. Leclerc, I. Lecoeur-Taibi, V. Lemaitre, H. Lenhardt, F. Leroux, S. Liao, E. Licata, H. E. P. Lindstrøm, T. A. Lister, E. Livanou, A. Lobel, W. Löffler, M. López, A. Lopez-Lozano, D. Lorenz, T. Loureiro, I. MacDonald, T. Magalhães Fernandes, S. Managau, R. G. Mann, G. Mantelet, O. Marchal, J. M. Marchant, M. Marconi, J. Marie, S. Marinoni, P. M. Marrese, G. Marschalkó, D. J. Marshall, J. M. Martín-Fleitas, M. Martino, N. Mary, G. Matijevič, T. Mazeh, P. J. McMillan, S. Messina, A. Mestre, D. Michalik, N. R. Millar, B. M. H. Miranda, D. Molina, R. Molinaro, M. Molinaro, L. Molnár, M. Moniez, P. Montegriffo, D. Monteiro, R. Mor, A. Mora, R. Morbidelli, T. Morel, S. Morgenthaler, T. Morley, D. Morris, A. F. Mulone, T. Muraveva, I. Musella, J. Narbonne, G. Nelemans, L. Nicastro, L. Noval, C. Ordénovic, J. Ordieres-Meré, P. Osborne, C. Pagani, I. Pagano, F. Pailler, H. Palacin, L. Palaversa, P. Parsons, T. Paulsen, M. Pecoraro, R. Pedrosa, H. Pentikäinen, J. Pereira, B. Pichon, A. M. Piersimoni, F. X. Pineau, E. Plachy, G. Plum, E. Poujoulet, A. Prša, L. Pulone, S. Ragaini, S. Rago, N. Rambaux, M. Ramos-Lerate, P. Ranalli, G. Rauw, A. Read, S. Regibo, F. Renk, C. Reylé, R. A. Ribeiro, L. Rimoldini, V. Ripepi, A. Riva, G. Rixon, M. Roelens, M. Romero-Gómez, N. Rowell, F. Royer, A. Rudolph, L. Ruiz-Dern, G. Sadowski, T. Sagristà Sellés, J. Sahlmann, J. Salgado, E. Salguero, M. Sarasso, H. Savietto, A. Schnorhk, M. Schultheis, E. Sciacca, M. Segol, J. C. Segovia, D. Segransan, E. Serpell, I. C. Shih, R. Smareglia, R. L. Smart, C. Smith, E. Solano, F. Solitro, R. Sordo, S. Soria Nieto, J. Souchay, A. Spagna, F. Spoto, U. Stampa, I. A. Steele, H. Steidelmüller, C. A. Stephenson, H. Stoev, F. F. Suess, M. Süveges, J. Surdej, L. Szabados, E. Szegedi-Elek, D. Tapiador, F. Taris, G. Tauran, M. B.

Taylor, R. Teixeira, D. Terrett, B. Tingley, S. C. Trager, C. Turon, A. Ulla, E. Utrilla, G. Valentini, A. van Elteren, E. Van Hemelryck, M. van Leeuwen, M. Varadi, A. Vecchiato, J. Veljanoski, T. Via, D. Vicente, S. Vogt, H. Voss, V. Votruba, S. Voutsinas, G. Walmsley, M. Weiler, K. Weingrill, D. Werner, T. Wevers, G. Whitehead, Ł. Wyrzykowski, A. Yoldas, M. Žerjal, S. Zucker, C. Zurbach, T. Zwitter, A. Alecu, M. Allen, C. Allende Prieto, A. Amorim, G. Anglada-Escudé, V. Arsenijevic, S. Azaz, P. Balm, M. Beck, H. H. Bernstein, L. Bigot, A. Bijaoui, C. Blasco, M. Bonfigli, G. Bono, S. Boudreault, A. Bressan, S. Brown, P. M. Brunet, P. Bunclark, R. Buonanno, A. G. Butkevich, C. Carret, C. Carrion, L. Chemin, F. Chéreau, L. Corcione, E. Darmigny, K. S. de Boer, P. de Teodoro, P. T. de Zeeuw, C. Delle Luche, C. D. Domingues, P. Dubath, F. Fodor, B. Frézouls, A. Fries, D. Fustes, D. Fyfe, E. Gallardo, J. Gallegos, D. Gardiol, M. Gebran, A. Gomboc, A. Gómez, E. Grux, A. Gueguen, A. Heyrovsky, J. Hoar, G. Iannicola, Y. Isasi Parache, A. M. Janotto, E. Joliet, A. Jonckheere, R. Keil, D. W. Kim, P. Klagyivik, J. Klar, J. Knude, O. Kochukhov, I. Kolka, J. Kos, A. Kutka, V. Lainey, D. LeBouquin, C. Liu, D. Loreggia, V. V. Makarov, M. G. Marseille, C. Martayan, O. Martinez-Rubi, B. Massart, F. Meynadier, S. Mignot, U. Munari, A. T. Nguyen, T. Nordlander, P. Ocvirk, K. S. O'Flaherty, A. Olias Sanz, P. Ortiz, J. Osorio, D. Oszkiewicz, A. Ouzounis, M. Palmer, P. Park, E. Pasquato, C. Peltzer, J. Peralta, F. Péturaud, T. Pieniluoma, E. Pigozzi, J. Poels, G. Prat, T. Prod'homme, F. Raison, J. M. Rebordao, D. Risquez, B. Rocca-Volmerange, S. Rosen, M. I. Ruiz-Fuertes, F. Russo, S. Sembay, I. Serraller Vizcaino, A. Short, A. Siebert, H. Silva, D. Sinachopoulos, E. Slezak, M. Soffel, D. Sosnowska, V. Straižys, M. ter Linden, D. Terrell, S. Theil, C. Tiede, L. Troisi, P. Tsalmantza, D. Tur, M. Vaccari, F. Vachier, P. Valles, W. Van Hamme, L. Veltz, J. Virtanen, J. M. Wallut, R. Wichmann, M. I. Wilkinson, H. Ziaeepour, and S. Zschocke

2016. The Gaia mission. A&A, 595:A1.

Goldstein, A., P. Veres, E. Burns, L. Blackburn, M. S. Briggs, N. Christensen, W. H. Cleveland, V. Connaughton, T. Dal Canton, R. Hamburg, C. M. Hui, P. A. Jenke, D. Kocevski, R. D. Preece, K. Siellez, J. Veitch, C. A. Wilson-Hodge, N. Bhat, E. Bissaldi, M. H. Gibby, M. M. Giles, A. von Kienlin, B. Mailyan, C. A. Meegan, W. S. Paciesas, O. J. Roberts, M. Stanbro, (Fermi-LAT Collaboration, M. Ackermann, M. Ajello, W. B. Atwood, L. Baldini, G. Barbiellini, D. Bastieri, R. Bellazzini, R. D. Blandford, E. D. Bloom, R. Bonino, E. Bottacini, T. J. Brandt, J. Bregeon, P. Bruel, R. Buehler, T. H. Burnett, S. Buson, R. A. Cameron, P. A. Caraveo, E. Cavazzuti, C. Cecchi, E. Charles, A. Chekhtman, J. Chiang, G. Chiaro, S. Ciprini, L. R. Cominsky, D. Costantin, S. Cutini, F. D'Ammando, F. de Palma, R. Desiante, S. W. Digel, N. Di Lalla, M. Di Mauro, L. Di Venere, C. Favuzzi, E. C. Ferrara, A. Franckowiak, Y. Fukazawa, S. Funk, P. Fusco, F. Gargano, D. Gasparrini, N. Giglietto, M. Giomi, F. Giordano, M. Giroletti, T. Glanzman, D. Green, I. A. Grenier, J. E. Grove, L. Guillemot, S. Guiriec, A. K. Harding, E. Hays, D. Horan, G. Jóhannesson, T. Kamae, S. Kensei, M. Kuss, G. La Mura, S. Larsson, L. Latronico, J. Li, F. Longo, F. Loparco, M. N. Lovellette, P. Lubrano, J. D. Magill, S. Maldera, A. Manfreda, M. N. Mazziotta, J. E. McEnery, M. Meyer, P. F. Michelson, T. Mizuno, A. A. Moiseev, M. E. Monzani, E. Moretti, A. Morselli, I. V. Moskalenko, M. Negro, E. Nuss, T. Ohsugi, N. Omodei, M. Orienti, E. Orlando, J. F. Ormes, M. Palatiello, V. S. Paliya, D. Paneque, J. S. Perkins, M. Persic, M. Pesce-Rollins, V. Petrosian, F. Piron, T. A. Porter, G. Principe, J. L. Racusin, S. Rainò, R. Rando, M. Razzano, S. Razzaque, A. Reimer, O. Reimer, T. Reposeur, P. M. Saz Parkinson, C. Sgrò, E. J. Siskind, F. Spada, G. Spandre, P. Spinelli, D. J. Suson, J. G. Thayer, J. B. Thayer, D. F. Torres, E. Troja, G. Vianello, K. Wood, and M. Wood
2017a. Fermi Observations of the LIGO Event GW170104. ApJ, 846:L5.

Goldstein, A., P. Veres, E. Burns, M. S. Briggs, R. Hamburg, D. Kocevski, C. A. Wilson-Hodge, R. D. Preece, S. Poolakkil, O. J. Roberts, C. M. Hui, V. Connaughton, J. Racusin, A. von Kienlin, T. Dal Canton, N. Christensen, T. Littenberg, K. Siellez, L. Blackburn, J. Broida, E. Bissaldi, W. H. Cleveland, M. H. Gibby, M. M. Giles, R. M. Kippen, S. McBreen, J. McEnery, C. A. Meegan, W. S. Paciesas, and M. Stanbro

2017b. An Ordinary Short Gamma-Ray Burst with Extraordinary Implications: Fermi-GBM Detection of GRB 170817A. ApJ, 848:L14.

Gomez, E. L. and M. T. Fitzgerald

2017. Robotic telescopes in education. *The Astronomical Review*, 13:28–68.

Gómez-González, V. M. A., Y. D. Mayya, and D. Rosa- González

2016. Wolf-Rayet stars in M81: detection and characterization using GTC/OSIRIS spectra and HST/ACS images. MNRAS, 460:1555–1566.

Górski, K. M., E. Hivon, A. J. Banday, B. D. Wandelt, F. K. Hansen, M. Reinecke, and M. Bartelmann

2005. HEALPix: A Framework for High-Resolution Discretization and Fast Analysis of Data Distributed on the Sphere. *ApJ*, 622:759–771.

Gräfener, G., S. P. Owocki, and J. S. Vink

2012. Stellar envelope inflation near the Eddington limit. Implications for the radii of Wolf-Rayet stars and luminous blue variables. A&A, 538:A40.

Granot, J.

2007. The Structure and Dynamics of GRB Jets. In *Revista Mexicana de Astronomia y Astrofisica, vol. 27*, volume 27 of *Revista Mexicana de Astronomia y Astrofisica Conference Series*, Pp. 140–165.

Groh, J. H., D. J. Hillier, A. Damineli, P. A. Whitelock, F. Marang, and C. Rossi
2009. On the Nature of the Prototype Luminous Blue Variable Ag Carinae. I. Fundamental Parameters During Visual Minimum Phases and Changes in the Bolometric Luminosity During the S-Dor Cycle. ApJ, 698:1698–1720.

Groh, J. H., G. Meynet, and S. Ekström
2013. Massive star evolution: luminous blue variables as unexpected supernova progenitors. A&A, 550:L7.

Groh, J. H., G. Meynet, S. Ekström, and C. Georgy
2014. The evolution of massive stars and their spectra. I. A non-rotating 60 M star from the zero-age main sequence to the pre-supernova stage. A&A, 564:A30.

Hasler, M.
2003. Gravitational waves inauguration of the franco-italian virgo detector. Technical report, CNRS, Campus Gérard-Mégie , 3 rue Michel-Ange - F-75794 Paris, cedex 16.

Hillier, D. J. and D. L. Miller
1998. The Treatment of Non-LTE Line Blanketing in Spherically Expanding Outflows. ApJ, 496:407–427.

Hiriart, D., J. Valdez, B. Martínez, B. García, A. Cordova, E. Colorado, G. Guisa, J. L. Ochoa, J. M. Nuñez, U. Ceseña, R. Cunniffe, D. Murphy, W. Lee, I. H. Park, and A. J. Castro-Tirado
2016. The BOOTES-5 telescope at San Pedro Martir National Astronomical Observatory, Mexico. In *Revista Mexicana de Astronomia y Astrofisica Conference Series*, volume 48 of *Revista Mexicana de Astronomia y Astrofisica Conference Series*, Pp. 114–117.

Hirschi, R., G. Meynet, and A. Maeder

2004. Stellar evolution with rotation. XII. Pre-supernova models. A&A, 425:649–670.

Hobbs, G.

2011. Pulsars as gravitational wave detectors. *Astrophysics and Space Science Proceedings*, 21:229.

Hobbs, G., A. Archibald, Z. Arzoumanian, D. Backer, M. Bailes, N. D. R. Bhat, M. Burgay, S. Burke-Spolaor, D. Champion, I. Cognard, W. Coles, J. Cordes, P. Demorest, G. Desvignes, R. D. Ferdman, L. Finn, P. Freire, M. Gonzalez, J. Hessels, A. Hotan, G. Janssen, F. Jenet, A. Jessner, C. Jordan, V. Kaspi, M. Kramer, V. Kondratiev, J. Lazio, K. Lazaridis, K. J. Lee, Y. Levin, A. Lommen, D. Lorimer, R. Lynch, A. Lyne, R. Manchester, M. McLaughlin, D. Nice, S. Oslowski, M. Pilia, A. Possenti, M. Purver, S. Ransom, J. Reynolds, S. Sanidas, J. Sarkissian, A. Sesana, R. Shannon, X. Siemens, I. Stairs, B. Stappers, D. Stinebring, G. Theureau, R. van Haasteren, W. van Straten, J. P. W. Verbiest, D. R. B. Yardley, and X. P. You

2010. The International Pulsar Timing Array project: using pulsars as a gravitational wave detector. *Classical and Quantum Gravity*, 27(8):084013.

Hobbs, G. B., M. Bailes, N. D. R. Bhat, S. Burke-Spolaor, D. J. Champion, W. Coles, A. Hotan, F. Jenet, L. Kedziora-Chudczer, J. Khoo, K. J. Lee, A. Lommen, R. N. Manchester, J. Reynolds, J. Sarkissian, W. van Straten, S. To, J. P. W. Verbiest, D. Yardley, and X. P. You

2009. Gravitational-Wave Detection Using Pulsars: Status of the Parkes Pulsar Timing Array Project. *Publications of the Astron. Soc. of Australia*, 26:103–109.

Høg, E., C. Fabricius, V. V. Makarov, S. Urban, T. Corbin, G. Wycoff, U. Bastian,

P. Schwekendiek, and A. Wicenec

2000. The Tycho-2 catalogue of the 2.5 million brightest stars. A&A, 355:L27–L30.

Holmes, S., U. Kolb, C. A. Haswell, V. Burwitz, R. J. Lucas, J. Rodriguez, S. M. Rolfe, J. Rostron, and J. Barker

2011. PIRATE: A Remotely Operable Telescope Facility for Research and Education. *Publications of the ASP*, 123:1177–1187.

Hornung, H.

2016. Tracking down the gentle tremble. Technical report, Max Planck Society, Callinstrabe 38, 30167 Hannover, Germany.

Howell, S. B.

2006. *Handbook of CCD Astronomy*, volume 5.

Huchra, J. P., L. M. Macri, K. L. Masters, T. H. Jarrett, P. Berlind, M. Calkins, A. C. Crook, R. Cutri, P. Erdoğdu, E. Falco, T. George, C. M. Hutcheson, O. Lahav, J. Mader, J. D. Mink, N. Martimbeau, S. Schneider, M. Skrutskie, S. Tokarz, and M. Westover

2012. The 2MASS Redshift SurveyDescription and Data Release. ApJS, 199:26.

Humphreys, R. M.

2007. The Circumstellar Environments of the Cool Hypergiants: Implications for the Mass Loss Mechanism. In *Revista Mexicana de Astronomia y Astrofisica Conference Series*, volume 30 of *Revista Mexicana de Astronomia y Astrofisica Conference Series*, Pp. 6–11.

Humphreys, R. M. and K. Davidson

1994. The luminous blue variables: Astrophysical geysers. *Publications of the ASP*, 106:1025–1051.

Humphreys, R. M., K. Davidson, M. S. Gordon, K. Weis, B. Burggraf, D. J. Bomans, and J. C. Martin

2014a. The Wind of Variable C in M33. ApJ, 782:L21.

Humphreys, R. M., M. S. Gordon, J. C. Martin, K. Weis, and D. Hahn

2017. Luminous and Variable Stars in M31 and M33. IV. Luminous Blue Variables, Candidate LBVs, B[e] Supergiants, and the Warm Hypergiants: How to Tell Them Apart. ApJ, 836:64.

Humphreys, R. M. and A. Sandage

1980. On the stellar content and structure of the spiral Galaxy M33. ApJS, 44:319–381.

Humphreys, R. M., K. Weis, K. Davidson, D. J. Bomans, and B. Burggraf

2014b. Luminous and Variable Stars in M31 and M33. II. Luminous Blue Variables, Candidate LBVs, Fe II Emission Line Stars, and Other Supergiants. ApJ, 790:48.

Hunter, J. D.

2007. Matplotlib: A 2d graphics environment. *Computing In Science & Engineering*, 9(3):90–95.

Hutsemékers, D., N. L. J. Cox, and C. Vamvatira-Nakou

2013. A massive parsec-scale dust ring nebula around the yellow hypergiant Hen 3-1379. A&A, 552:L6.

IAC

2017. New robotic facilities at the teide observatory. Instituto de Astrofísica de Canarias, Vía Láctea, 38200 - La Laguna (Tenerife), Spain.

International Gravitational Event Collaboration

2003. Methods and results of the IGEC search for burst gravitational waves in the years 1997–2000. *ArXiv Astrophysics e-prints*.

Jonker, P.

2017. GCN Circular 21737. GRB Coordinates Network.

Kennefick, D.

2007. *Traveling at the Speed of Thought: Einstein and the Quest for Gravitational Waves*. Princeton University Press.

Keppel, D. G.

2009. *Signatures and dynamics of compact binary coalescences and a search in LIGO's S5 data*. PhD thesis, California Institute of Technology. CaltechETD:etd-05202009-115750.

Klimenko, S., G. Vedovato, M. Drago, F. Salemi, V. Tiwari, G. A. Prodi, C. Lazzaro, K. Ackley, S. Tiwari, C. F. Da Silva, and G. Mitselmakher

2016. Method for detection and reconstruction of gravitational wave transients with networks of advanced detectors. Phys. Rev. D, 93(4):042004.

Klotz, A., M. Boër, J. Eysseric, Y. Damerdji, M. LaasBourez, C. Pollas, and F. Vachier

2008. Robotic Observations of the Sky with TAROT: 2004-2007. PASP, 120:1298.

Kolb, U.

2014. The PIRATE Facility: at the crossroads of research and teaching. In *Revista Mexicana de Astronomia y Astrofisica Conference Series*, volume 45 of *Revista Mexicana de Astronomia y Astrofisica Conference Series*, Pp. 16–19.

Kolb, U., M. Brodeur, N. Braithwaite, and S. Minocha

2018. A Robotic Telescope For University-Level Distance Teaching. *ArXiv e-prints*.

KU collaboration

2017a. GCN Circular 21723. GRB Coordinates Network.

KU collaboration

2017b. GCN Circular 21755. GRB Coordinates Network.

Lamers, H. J. G. L. M.

2013. Mass Loss and Evolution of Massive Stars. In *370 Years of Astronomy in Utrecht*, G. Pugliese, A. de Koter, and M. Wijburg, eds., volume 470 of *Astronomical Society of the Pacific Conference Series*, P. 97.

LIGO Scientific Collaboration, J. Aasi, B. P. Abbott, R. Abbott, T. Abbott, M. R. Abernathy, K. Ackley, C. Adams, T. Adams, P. Addesso, and et al.

2015. Advanced LIGO. *Classical and Quantum Gravity*, 32(7):074001.

LIGO Scientific Collaboration, Virgo Collaboration, J. Abadie, B. P. Abbott, R. Abbott, T. D. Abbott, M. Abernathy, T. Accadia, F. Acernese, C. Adams, and et al.

2012. Implementation and testing of the first prompt search for gravitational wave transients with electromagnetic counterparts. A&A, 539:A124.

LIGO Scientific Collaboration & Virgo Collaboration

2017a. GCN Circular 20364. GRB Coordinates Network. URL: `https://gcn.gsfc.nasa.gov/other/G268556.gcn3`.

LIGO Scientific Collaboration & Virgo Collaboration

2017b. GCN Circular 20486. GRB Coordinates Network.

LIGO Scientific Collaboration & Virgo Collaboration

2017c. GCN Circular 20689. GRB Coordinates Network.

LIGO Scientific Collaboration & Virgo Collaboration

2017d. GCN Circular 20738. GRB Coordinates Network.

LIGO Scientific Collaboration & Virgo Collaboration
2017e. GCN Circular 20763. GRB Coordinates Network.

LIGO Scientific Collaboration & Virgo Collaboration
2017f. GCN Circular 20840. GRB Coordinates Network.

LIGO Scientific Collaboration & Virgo Collaboration
2017g. GCN Circular 20982. GRB Coordinates Network.

LIGO Scientific Collaboration & Virgo Collaboration
2017h. GCN Circular 20983. GRB Coordinates Network.

LIGO Scientific Collaboration & Virgo Collaboration
2017i. GCN Circular 21060. GRB Coordinates Network.

LIGO Scientific Collaboration & Virgo Collaboration
2017j. GCN Circular 21264. GRB Coordinates Network.

LIGO Scientific Collaboration & Virgo Collaboration
2017k. GCN Circular 21281. GRB Coordinates Network.

LIGO Scientific Collaboration & Virgo Collaboration
2017l. GCN Circular 21431. GRB Coordinates Network.

LIGO Scientific Collaboration & Virgo Collaboration
2017m. GCN Circular 21474. GRB Coordinates Network.

LIGO Scientific Collaboration & Virgo Collaboration
2017n. GCN Circular 21656. GRB Coordinates Network.

LIGO Scientific Collaboration & Virgo Collaboration
2017o. GCN Circular 21661. GRB Coordinates Network.

LIGO Scientific Collaboration & Virgo Collaboration
2017p. GCN Circular 21693. GRB Coordinates Network.

LIGO Scientific Collaboration & Virgo Collaboration
2017q. GCN Circular 21751. GRB Coordinates Network.

LIGO Scientific Collaboration & Virgo Collaboration
2017r. GCN Circular 21770. GRB Coordinates Network.

Lindley, D.
2005. Focus: A fleeting detection of gravitational waves. *Phys.Rev.Focus.*

Lipunov, V.
2017a. GCN Circular 21719. GRB Coordinates Network.

Lipunov, V.
2017b. GCN Circular 21720. GRB Coordinates Network.

Lipunov, V.
2017c. GCN Circular 21736. GRB Coordinates Network.

Lipunov, V.
2017d. GCN Circular 21749. GRB Coordinates Network.

Lipunov, V.
2017e. GCN Circular 21755. GRB Coordinates Network.

Lipunov, V.
2017f. GCN Circular 21780. GRB Coordinates Network.

Lipunov, V., V. Kornilov, E. Gorbovskoy, N. Tiurina, A. Kuznetsov, P. Balanutsa, V. Chazov, O. Gress, D. Kuvshinov, V. Vladimirov, D. Buckley, R. Rebolo, M. Serra-Ricart, R. Podesta, H. Levato, N. Budnev, K. Ivanov, A. Tlatov,

A. Gabovich, and V. Yurkov

2016. MASTER Global Robotic Net: new sites and new result. In *Revista Mexicana de Astronomia y Astrofisica Conference Series*, volume 48 of *Revista Mexicana de Astronomia y Astrofisica Conference Series*, Pp. 42–47.

Maeder, A. and P. S. Conti

1994. Massive Star Populations in Nearby Galaxies. ARA&A, 32:227–275.

Maeder, A. and G. Meynet

2008. Mass Loss and the Evolution of Massive Stars. In *Mass Loss from Stars and the Evolution of Stellar Clusters*, A. de Koter, L. J. Smith, and L. B. F. M. Waters, eds., volume 388 of *Astronomical Society of the Pacific Conference Series*, P. 3.

Malafarina, D. and P. S. Joshi

2016. Electromagnetic counterparts to gravitational waves from black hole mergers and naked singularities. *ArXiv e-prints*.

Martin, J. C. and R. M. Humphreys

2017. Multi-epoch BVRI Photometry of Luminous Stars in M31 and M33. AJ, 154:81.

Massey, P.

2013. Massive stars in the galaxies of the Local Group. New A Rev., 57:14–27.

Massey, P., L. Bianchi, J. B. Hutchings, and T. P. Stecher

1996. The UV-brightest Stars of M33 and Its Nucleus: Discovery, Photometry, and Optical Spectroscopy. ApJ, 469:629.

Massey, P., R. T. McNeill, K. A. G. Olsen, P. W. Hodge, C. Blaha, G. H. Jacoby,

R. C. Smith, and S. B. Strong

2007. A Survey of Local Group Galaxies Currently Forming Stars. III. A Search for Luminous Blue Variables and Other Hα Emission-Line Stars. AJ, 134:2474–2503.

Massey, P., K. F. Neugent, and B. M. Smart

2016. A Spectroscopic Survey of Massive Stars in M31 and M33. AJ, 152:62.

Metzger, B. D.

2017. Kilonovae. *Living Reviews in Relativity*, 20:3.

Metzger, B. D. and E. Berger

2012. What is the Most Promising Electromagnetic Counterpart of a Neutron Star Binary Merger? *ApJ*, 746:48.

Mirabel, I. F.

2016. The Formation of Stellar Black Holes. *ArXiv e-prints*.

Monteverde, M. I., A. Herrero, D. J. Lennon, and R. P. Kudritzki

1996. Spectroscopic observations of AB supergiants in M 33. A&A, 312:24–32.

Moore, C. J., R. H. Cole, and C. P. L. Berry

2015. Gravitational-wave sensitivity curves. *Classical and Quantum Gravity*, 32(1):015014.

Moriya, T. J., E. I. Sorokina, and R. A. Chevalier

2018. Superluminous Supernovae. Space Sci. Rev., 214:59.

Morris, S. L.

1994. Two mathematical expansions of the Roche equipotentials. PASP, 106:154–155.

Muijres, L. E.

2010. *The physics of line-driven winds of hot massive stars*. PhD thesis, University of Amsterdam.

Munoz-Tunon, C., J. Vernin, and A. M. Varela

1997. Night-time image quality at Roque de LOS Muchachos Observatory. *Astronomy and Astrophysics Supplement Series*, 125:183–193.

Nitz, A. H., T. Dent, T. Dal Canton, S. Fairhurst, and D. A. Brown

2017. Detecting binary compact-object mergers with gravitational waves: Understanding and Improving the sensitivity of the PyCBC search. *Astrophys. J.*, 849(2):118.

Nugis, T. and H. J. G. L. M. Lamers

2000. Mass-loss rates of Wolf-Rayet stars as a function of stellar parameters. A&A, 360:227–244.

Polcaro, V. F., O. Maryeva, R. Nesci, M. Calabresi, A. Chieffi, S. Galleti, R. Gualandi, R. Haver, O. F. Mills, W. H. Osborn, A. Pasquali, C. Rossi, T. Vasilyeva, and R. F. Viotti

2016. GR 290 (Romanos Star). II. Light History and Evolutionary State. AJ, 151:149.

Prodi, G. A., V. Martinucci, R. Mezzena, A. Vinante, S. Vitale, I. S. Heng, Z. A. Allen, W. O. Hamilton, W. W. Johnson, M. P. McHugh, G. Santostasi, and et al.

2000. Initial Operation of the International Gravitational Event Collaboration. *International Journal of Modern Physics D*, 9:237–245.

Reitz, K.

2011. Requests. `https://github.com/requests/requests`.

Rieke, G. H. and M. J. Lebofsky

1985. The interstellar extinction law from 1 to 13 microns. ApJ, 288:618–621.

Rivinius, T., A. C. Carciofi, and C. Martayan

2013. Classical Be stars. Rapidly rotating B stars with viscous Keplerian decretion disks. A&A Rev., 21:69.

Roberts, D.

2017. GCN Circular 21888. GRB Coordinates Network. URL: `https://gcn.gsfc.nasa.gov/other/G297595.gcn3`.

Roberts, D., U. Kolb, and M. Morrell

2017. GCN Circular 21752. GRB Coordinates Network.

Rodríguez, N. and C. del Puerto

2015. Educational outreach. Instituto de Astrofísica de Canarias, Vía Láctea, 38200 - La Laguna (Tenerife), Spain.

Rose, M. B. and E. G. Hintz

2007. A Search for Low-Amplitude Variability in Six Open Clusters Using the Robust Median Statistic. AJ, 134:2067–2078.

Rosslowe, C. K. and P. A. Crowther

2018. A deep near-infrared spectroscopic survey of the Scutum-Crux arm for Wolf-Rayet stars. MNRAS, 473:2853–2870.

Rossum, G.

1995. Python reference manual. Technical report, python, Amsterdam, The Netherlands, The Netherlands.

Saio, H., C. Georgy, and G. Meynet

2013. Evolution of blue supergiants and α Cygni variables: puzzling CNO surface abundances. MNRAS, 433:1246–1257.

Salaris, M. and S. Cassisi

2005. *Evolution of Stars and Stellar Populations*.

Salpeter, E. E.

1955. The Luminosity Function and Stellar Evolution. ApJ, 121:161.

Samus', N. N., E. V. Kazarovets, O. V. Durlevich, N. N. Kireeva, and E. N. Pastukhova

2017. General catalogue of variable stars: Version GCVS 5.1. *Astronomy Reports*, 61:80–88.

Sana, H., S. E. de Mink, A. de Koter, N. Langer, C. J. Evans, M. Gieles, E. Gosset, R. G. Izzard, J.-B. Le Bouquin, and F. R. N. Schneider

2012. Binary Interaction Dominates the Evolution of Massive Stars. *Science*, 337:444.

Savchenko, V., C. Ferrigno, E. Bozzo, A. Bazzano, S. Brandt, J. Chenevez, T. J.-L. Courvoisier, R. Diehl, L. Hanlon, A. von Kienlin, E. Kuulkers, P. Laurent, F. Lebrun, A. Lutovinov, A. Martin-Carillo, S. Mereghetti, J. P. Roques, R. Sunyaev, and P. Ubertini

2017. INTEGRAL Observations of GW170104. ApJ, 846:L23.

Savchenko, V., C. Ferrigno, S. Mereghetti, L. Natalucci, and E. Kuulkers

2016. INTEGRAL upper limits on gamma-ray emission associated with the gravitational wave event GW150914. In *XMM-Newton: The Next Decade*, P. 117.

Schlegel, E. M.

1990. A new subclass of Type II supernovae? MNRAS, 244:269–271.

Shin, M.-S., M. Sekora, and Y.-I. Byun

2009. Detecting variability in massive astronomical time series data - I. Application of an infinite Gaussian mixture model. MNRAS, 400:1897–1910.

Sholukhova, O., S. Fabrika, M. Roth, and T. Becker

2004. B 416 – a B[e]-SUPERGIANT in Interacting Binary? *Baltic Astronomy*, 13:156–158.

Sholukhova, O. N., S. N. Fabrika, A. F. Valeev, and A. N. Sarkisian

2018. LBV Candidates in M31 and M33. Overview of 20 Years of the 6-m Telescope: Observations and Results. *Astrophysical Bulletin*, 73:413–424.

Singer, L.

2016. Advanced-LIGO Electromagnetic Followup: Proposed Changes to O2 Alerts. LV-EM Forum Telecons. [Online-Private; announced 2-June-2016].

Singer, L.

2018. Pygcn. `https://github.com/lpsinger/pygcn`.

Singer, L. P.

2015. Ligo-virgo em follow-up tutorial. Jupyter Notebook (Web-page). This document is LIGO-G1500442-v10.

Singer, L. P. and L. R. Price

2016. Rapid Bayesian position reconstruction for gravitational-wave transients. Phys. Rev. D, 93(2):024013.

Smith, J. R. and LIGO Scientific Collaboration

2009. The path to the enhanced and advanced LIGO gravitational-wave detectors. *Classical and Quantum Gravity*, 26(11):114013.

Smith, N.

2014. Mass Loss: Its Effect on the Evolution and Fate of High-Mass Stars. *Annual Review of Astron. and Astrophys.*, 52:487–528.

Smith, N., J. E. Andrews, A. Rest, F. B. Bianco, J. L. Prieto, T. Matheson, D. J. James, R. C. Smith, G. M. Strampelli, and A. Zenteno

2018. Light echoes from the plateau in Eta Carinae's Great Eruption reveal a two-stage shock-powered event. MNRAS, 480:1466–1498.

Smith, N., M. Ganeshalingam, R. Chornock, A. V. Filippenko, W. Li, J. M. Silverman, T. N. Steele, C. V. Griffith, N. Joubert, N. Y. Lee, T. B. Lowe, M. P. Mobberley, and D. M. Winslow

2009. SN 2008S: A Cool Super-Eddington Wind in a Supernova Impostor. ApJ, 697:L49–L53.

Smith, N., W. Li, J. M. Silverman, M. Ganeshalingam, and A. V. Filippenko

2011. Luminous blue variable eruptions and related transients: diversity of progenitors and outburst properties. MNRAS, 415:773–810.

Smith, N. and S. P. Owocki

2006. On the Role of Continuum-driven Eruptions in the Evolution of Very Massive Stars and Population III Stars. ApJ, 645:L45–L48.

Smith, R. and E. Thrane

2018. Optimal search for an astrophysical gravitational-wave background. *Phys. Rev. X*, 8:021019.

Sokolovsky, K. V., P. Gavras, A. Karampelas, S. V. Antipin, I. Bellas-Velidis, P. Benni, A. Z. Bonanos, A. Y. Burdanov, S. Derlopa, D. Hatzidimitriou, A. D. Khokhryakova, D. M. Kolesnikova, S. A. Korotkiy, E. G. Lapukhin, M. I. Moretti, A. A. Popov, E. Pouliasis, N. N. Samus, Z. Spetsieri, S. A. Veselkov, K. V. Volkov,

M. Yang, and A. M. Zubareva

2017. Comparative performance of selected variability detection techniques in photometric time series data. MNRAS, 464:274–292.

Sokolovsky, K. V. and A. A. Lebedev

2018. VaST: A variability search toolkit. *Astronomy and Computing*, 22:28–47.

Steele, I. A.

2004. The liverpool telescope. *Astronomische Nachrichten*, 325(6-8):519–521.

Steinicke, W.

2005. Einstein and Gravitational Waves. *Astronomische Nachrichten*, 326:640–641.

Stetson, P. B.

1996. On the Automatic Determination of Light-Curve Parameters for Cepheid Variables. PASP, 108:851.

Sybilski, P. W., R. Pawłaszek, S. K. Kozłowski, M. Konacki, M. Ratajczak, and K. G. Hełminiak

2014. Software for autonomous astronomical observatories: challenges and opportunities in the age of big data. In *Software and Cyberinfrastructure for Astronomy III*, volume 9152 of Proc. SPIE, P. 91521C.

Tanaka, M.

2016. Kilonova/Macronova Emission from Compact Binary Mergers. *Advances in Astronomy*, 2016:634197.

Taylor, J. H. and J. M. Weisberg

1989. Further experimental tests of relativistic gravity using the binary pulsar PSR 1913 + 16. *ApJ*, 345:434–450.

The LIGO Scientific Collaboration and The Virgo Collaboration
2016. GW150914: The Advanced LIGO Detectors in the Era of First Discoveries. *ArXiv e-prints*.

Thorne, K. and R. Weiss
2016. A Brief History of LIGO. Technical report, California Institute of Technology/LIGO, LIGO Laboratory, MC 100-36, California Institute of Technology, Pasadena, CA 91125.

Tóth, J., P. Zigo, D. Kalmančok, J. Šimon, L. Kornoš, J. Világi, R. Rudawska, M. Serra-Ricart, J. C. Perez, and J. Licandro
2015. 5 months of AMOS on the Canary Islands. In *International Meteor Conference Mistelbach, Austria*, J.-L. Rault and P. Roggemans, eds., Pp. 63–65.

Usman, S. A. et al.
2016. The PyCBC search for gravitational waves from compact binary coalescence. *Class. Quant. Grav.*, 33(21):215004.

Valenti, S., David, J. Sand, S. Yang, E. Cappellaro, L. Tartaglia, A. Corsi, S. W. Jha, D. E. Reichart, J. Haislip, and V. Kouprianov
2017. The Discovery of the Electromagnetic Counterpart of GW170817: Kilonova AT 2017gfo/DLT17ck. ApJ, 848:L24.

Van Der Walt, S., S. C. Colbert, and G. Varoquaux
2011. The NumPy array: a structure for efficient numerical computation. *ArXiv e-prints*.

van Genderen, A. M.
2001. S Doradus variables in the Galaxy and the Magellanic Clouds. A&A, 366:508–531.

Veitch, J., V. Raymond, B. Farr, W. Farr, P. Graff, S. Vitale, B. Aylott, K. Blackburn, N. Christensen, M. Coughlin, W. Del Pozzo, F. Feroz, J. Gair, C.-J. Haster, V. Kalogera, T. Littenberg, I. Mandel, R. O'Shaughnessy, M. Pitkin, C. Rodriguez, C. Röver, T. Sidery, R. Smith, M. Van Der Sluys, A. Vecchio, W. Vousden, and L. Wade

2015. Parameter estimation for compact binaries with ground-based gravitational-wave observations using the LALInference software library. Phys. Rev. D, 91(4):042003.

Verrecchia, F., M. Tavani, A. Ursi, A. Argan, C. Pittori, I. Donnarumma, A. Bulgarelli, F. Fuschino, C. Labanti, M. Marisaldi, Y. Evangelista, G. Minervini, A. Giuliani, M. Cardillo, F. Longo, F. Lucarelli, P. Munar-Adrover, G. Piano, M. Pilia, V. Fioretti, N. Parmiggiani, A. Trois, E. Del Monte, L. A. Antonelli, G. Barbiellini, P. Caraveo, P. W. Cattaneo, S. Colafrancesco, E. Costa, F. D'Amico, M. Feroci, A. Ferrari, A. Morselli, L. Pacciani, F. Paoletti, A. Pellizzoni, P. Picozza, A. Rappoldi, and S. Vercellone

2017. AGILE Observations of the Gravitational-wave Source GW170104. ApJ, 847:L20.

Viotti, R. F., C. Rossi, V. F. Polcaro, F. Montagni, R. Gualandi, and L. Norci

2006. The present status of four luminous variables in M 33. A&A, 458:225–234.

von Neumann, J.

1941. Distribution of the ratio of the mean square successive difference to the variance. *Ann. Math. Statist.*, 12(4):367–395.

Waldman, S. J.

2011. The Advanced LIGO Gravitational Wave Detector. *ArXiv e-prints*.

Watson, A. M.

2017. GCN Circular 21742. GRB Coordinates Network.

Weber, J.

1960. Detection and generation of gravitational waves. *Phys. Rev.*, 117:306–313.

Weber, J.

1968. Gravitational-wave-detector events. *Phys. Rev. Lett.*, 20:1307–1308.

Weber, J.

1969. Evidence for discovery of gravitational radiation. *Phys. Rev. Lett.*, 22:1320–1324.

Weis, K. and W. J. Duschl

2002. Outflow from and asymmetries in the nebula around the LBV candidate Sk-69^{o}279. *Astronomy and Astrophysics*, 393:503–510.

Wenger, M., F. Ochsenbein, D. Egret, P. Dubois, F. Bonnarel, S. Borde, F. Genova, G. Jasniewicz, S. Laloë, S. Lesteven, and R. Monier

2000. The SIMBAD astronomical database. The CDS reference database for astronomical objects. A&AS, 143:9–22.

Williams, G. G., P. A. Milne, H. S. Park, S. D. Barthelmy, D. H. Hartmann, A. Updike, and K. Hurley

2008. The Robotic Super-LOTIS Telescope: Results Future Plans. In *American Institute of Physics Conference Series*, M. Galassi, D. Palmer, and E. Fenimore, eds., volume 1000 of *American Institute of Physics Conference Series*, Pp. 535–538.

Woosley, S. E., A. Heger, and T. A. Weaver

2002. The evolution and explosion of massive stars. *Reviews of Modern Physics*, 74:1015–1071.

Zhang, M., G. Á. Bakos, K. Penev, Z. Csubry, J. D. Hartman, W. Bhatti, and M. de Val-Borro

2016. Precision Multiband Photometry with a DSLR Camera. *Publications of the Astronomical Society of the Pacific*, 128:035001.

Zickgraf, F.-J., B. Wolf, O. Stahl, C. Leitherer, and G. Klare

1985. The hybrid spectrum of the LMC hypergiant R126. A&A, 143:421–430.